Finite element models for the study of hydrogen embrittlement of steel structures

Daniella Lopes Pinto

To cite this version:

Daniella Lopes Pinto. Finite element models for the study of hydrogen embrittlement of steel structures. Solid mechanics [physics.class-ph]. Université Paris sciences et lettres, 2025. English. ⟨NNT : 2025UPSLM022⟩. ⟨tel-05240581v2⟩

HAL Id: tel-05240581

https://hal.science/tel-05240581v2

Submitted on 19 Feb 2026

HAL is a multi-disciplinary open access archive for the deposit and dissemination of scientific research documents, whether they are published or not. The documents may come from teaching and research institutions in France or abroad, or from public or private research centers.

L'archive ouverte pluridisciplinaire **HAL**, est destinée au dépôt et à la diffusion de documents scientifiques de niveau recherche, publiés ou non, émanant des établissements d'enseignement et de recherche français ou étrangers, des laboratoires publics ou privés.

Autorisation HAL

HAL Authorization

PSL
UNIVERSITÉ PARIS

THÈSE DE DOCTORAT
DE L'UNIVERSITÉ PSL

Préparée à MINES Paris

Modèles éléments finis pour l'étude de la fragilisation par l'hydrogène des structures en acier

Finite element models for the study of hydrogen embrittlement of steel structures

Soutenue par
Daniella LOPES PINTO
Le 7 mars 2025

École doctorale n°621
Ingénierie des Systèmes, Matériaux, Mécanique, Énergétique

Spécialité
Mécanique

Composition du jury :

Djimedo KONDO Professeur des universités, Sorbonne Université	*Président*
Yann CHARLES Professeur des universités, Université Sorbonne Paris Nord	*Rapporteur*
Jianying HE Professeure, Norwegian University of Science and Technology	*Rapporteuse*
Quentin AUZOUX Ingénieur de recherche, CEA Saclay	*Examinateur*
Yazid MADI Professeur, Mines Paris	*Examinateur*
Nikolay OSIPOV Ingénieur, Transvalor S.A.	*Examinateur*
Jacques BESSON Directeur de recherche, Mines Paris, CNRS	*Directeur de thèse*

MINES PARIS | PSL

To my grandmother Maria Eugenia,
for your endless love, support and encouragement.

Acknowledgments

The dream of pursuing a PhD in France began several years ago when I did not speak a word of French, yet the idea of studying in the hexagon and collaborating with industrial partners fascinated me. The journey to reach this point has been long, but I am grateful to say that many people have been part of it, and I would like to express my sincere gratitude.

First and foremost, I would like to thank my thesis director, Jacques Besson, for your patience, availability, and for sharing your invaluable knowledge with me over the past three years. It is impossible to quantify how much I have learned from you. Thank you for being not only a scientific role model but also a truly remarkable person.

I am honored to have my work evaluated by the members of the jury. Firstly, thanks to Djimedo Kondo for accepting being the president of the jury. A special thanks to Yann Charles and Jianying He for dedicating your precious time and agreeing to serve as the reporteurs for this thesis. Thanks to Quentin Auzoux for the interesting comments and kind remarks.

I would like to express my gratitude to Transvalor for the partnership on this thesis, especially the Z-set team: Nikolay, Stephane, Basava, Mohamed, and Wajih. It has been a pleasure to work with all of you. Your kindness, availability, and support made the experience truly enjoyable. The time spent at the office with you was always a pleasure.

I would like to thank all the members of the MESSIAH project. Yazid, thank you for your help, discussions, and kindness. A heartfelt thanks to Luciano, Said, and Pilar for your friendship, which made this journey so much more pleasant. I also want to thank our industrial partners: Transvalor, EDF, GRTgaz, Mannesmann, and Air Liquide, for making this project possible and for the insightful discussions and suggestions.

I would like to thank Laurent Lacourt, who was my academic advisor during the first year, for your invaluable help. Thanks to Amar, my industrial advisor for a year and a half, for your constant availability and guidance, particularly with Z-set.

I would like to thank all my colleagues at the Centre des Matériaux, for the great exchanges, the nice working environment, and the good moments spent with each of you.

Lastly, I want to express my deepest gratitude to my close ones. Thank you, Vincent, for your love, care, and unwavering support, especially during the toughest moments, and for sharing your life with me. To my friends: Amanda, Mariana, Matteus, Alexandre, Gustavo, André, and Eduardo, thank you for your true friendship and for always being there for me, despite the physical distance. And to my grandmother Maria Eugenia and my aunt Luciana, thank you for your love, encouragement, and belief in me, which made this dream a reality.

Contents

List of Figures

List of Tables

1

Introduction

Abstract This chapter offers an overview of the study's context and objectives, emphasizing the impact of hydrogen embrittlement (HE) on industrial materials. It discusses the challenges hydrogen poses to energy infrastructure, particularly in the context of Europe's commitment to achieving carbon neutrality. The chapter introduces the MESSIAH Chair initiative, which proposes to use sub-size specimens for non-destructive testing, enabling the assessment of hydrogen's effects on mechanical properties without interrupting service. Additionally, it outlines the key objectives of the thesis, which include developing a numerical framework to simulate HE, predicting the impact of hydrogen on material properties, and modeling hydrogen diffusion within materials.

Résumé Ce chapitre donne un aperçu du contexte et des objectifs de l'étude, en mettant l'accent sur l'impact de la fragilisation par l'hydrogène (FPH) sur les matériaux industriels. Il aborde les défis que pose l'hydrogène aux infrastructures énergétiques, en particulier dans le contexte de l'engagement de l'Europe à atteindre la neutralité carbone. Le chapitre présente l'initiative de la chaire MESSIAH, qui propose d'utiliser des éprouvettes de taille réduite pour les essais non-destructifs, ce qui permet d'évaluer les effets de l'hydrogène sur les propriétés mécaniques sans interrompre le service. En outre, il décrit les principaux objectifs de la thèse, qui comprennent le développement d'un modèle numérique pour simuler la FPH, la prédiction de l'impact de l'hydrogène sur les propriétés des matériaux et la modélisation de la diffusion de l'hydrogène à l'intérieur des matériaux.

Contents

1.1 Context

Industrial power generation and transmission structures are designed to operate for more than 40 years. Consequently, a comprehensive understanding of material degradation and performance trends over long periods is essential. This knowledge is fundamental to ensuring the continued safety and reliability of these critical assets.

As part of the energy transition, Europe has made a strong commitment to the use of sustainable energy sources, setting ambitious goals to achieve carbon neutrality by 2050. Hydrogen, produced from water electrolysis using renewable energy sources, is emerging as a promising clean and renewable energy vector. It holds the potential to help decarbonize the energy sector and meet climate objectives (Abbasi and Abbasi, 2011; Meibom and Karlsson, 2010).

However, there is a significant challenge associated with the use of hydrogen. It can easily diffuse through metals and accumulate in areas of high stress, leading to premature failure. This failure is characterized by a reduction in ductility and toughness, a phenomenon known as Hydrogen Embrittlement (HE) (Ferreira et al., 1999; Hirth, 1980; Sofronis and McMeeking, 1989).

In order to monitor the material changes over the lifetime of installations and to assess their suitability for hydrogen transport, the MESSIAH Chair proposes the use of miniature specimens. These specimens are machined from coupons extracted from these installations. The advantage of using these miniature specimens is that they allow for quasi-non-destructive testing. This approach avoids the need for service interruption or subsequent repairs to the equipment in question, which often involve significant cost and operational constraints. In addition, these specimens can be used for production control testing, equipment approval, and new material development when limited material is available.

The miniature specimens will include tensile and notched bars, Charpy specimens, and fracture mechanics specimens such as Compact Tension (CT) and Single Edge Notch Tensile (SENT) specimens, which must be miniaturized. The results obtained from these miniature specimens will be compared to those obtained from "standard" specimens. This comparison, along with the results from the uncharged material, will facilitate the qualification of the effect of hydrogen on mechanical properties and failure. Figure 1.1 contains a representation of the described procedure and the specimens used in the study.

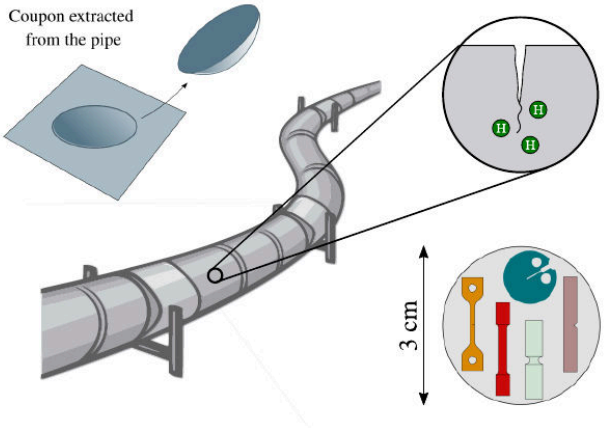

Figure 1.1: Schematic of the procedure proposed by the MESSIAH Chair.

The MESSIAH Chair brings together a manufacturer of steel tubes for energy transport, Mannesmann, with three key players in the field of energy production and transport: GRTgaz, EdF and Air Liquide. In addition, a software developer, Transvalor, which is a CIFRE partner in this thesis, is in charge of the numerical implementations carried out during the project.

1.2 A brief state of the art

To accurately model hydrogen embrittlement, several factors must be considered: plasticity, hydrogen diffusion kinetics within a stress gradient, hydrogen trapping, and the deleterious effects of hydrogen on the mechanical properties of the material. In particular, a damage mechanism influenced by hydrogen concentration must be considered to simulate the accelerated evolution of damage.

Several models have been proposed in the literature to represent and predict the degradation effects of hydrogen on metals. One widely used model is the cohesive zone modeling (CZM), which has been used in numerous studies of continuum-level hydrogen embrittlement simulations (Ahn et al., 2007; Jemblie et al., 2017; Olden et al., 2008; Xia et al., 2019). In this approach, cohesive elements are introduced along a predefined crack path. The effect of hydrogen embrittlement is then modeled by decreasing the cohesive strength with increasing hydrogen concentration.

Alternatively, the phase field approach has been used in recent research (Martínez-Pañeda et al., 2018). In this method, the material is represented by continuous fields, where each point in space corresponds to the local state of the material. A phase field variable is introduced to distinguish between different phases or states of the material. The evolution of the phase field variable (and other fields) over time is governed by a set of coupled partial differential equations (PDEs). This formulation is based on minimizing the total free energy of the system, which includes contributions from chemical, interfacial, and mechanical energy.

The GTN (Gurson-Tvergaard-Needleman) model (Tvergaard and Needleman, 1984) is a widely used micromechanical model in the field of damage and ductile failure. It was developed to predict the initiation, growth, and coalescence of voids in ductile materials, which can lead to eventual material failure. In the literature, this model has also been modified to account for hydrogen embrittlement, where damage is accelerated/increased due to the presence of hydrogen in the material (Depraetere et al., 2021; Lin et al., 2022; Yu et al., 2019).

1.3 Objectives

The aim of this thesis is to improve the understanding of hydrogen embrittlement (HE) mechanisms and to develop a robust and efficient numerical framework. The main research objectives of this work are:

- Develop a numerical framework for simulating hydrogen embrittlement (HE) using a nonlocal Gurson-Tvergaard-Needleman (GTN) model that integrates plasticity, damage, and hydrogen diffusion.

- Predict the effect of hydrogen on the mechanical properties of the material and the hydrogen distribution within the specimen, using experimental test results to calibrate the model parameters.

- Simulate both the absorption and desorption of hydrogen in the structure, taking into account the various trapping sites present.

- Simulate the experimental tests using miniaturized specimens in air atmospheres to analyzed the effect of the specimen's size and thickness on the toughness results.

In parallel to this work, an experimental study of hydrogen embrittlement in steels was carried out by Luciano Meirelles Santana, another PhD student and member of the MESSIAH Chair.

1.4 Outline

This work is organized as follows: Chapter 2 provides a comprehensive bibliographic review of key topics essential for understanding hydrogen embrittlement (HE), including ductile failure mechanisms, regularized damage models, locking-free finite element methods, hydrogen embrittlement in steels, and mechanical testing on sub-size specimens. Chapter 3 introduces the study of hydrogen embrittlement in steels through pressurized disk tests, combining experimental testing and simulations to analyze the impact of hydrogen on various mechanical tests under different pressure rise rates. Chapter 4 focuses on the simulation of hydrogen uptake during a tensile test, examining the effects of absorbed hydrogen content at different strain levels, strain rates, and dwell times, while comparing experimental and numerical results. Chapter 5 presents a comprehensive model that couples plasticity, damage, and hydrogen diffusion to simulate a dataset of various mechanical tests. Finally, Chapter 6 reports both experimental and numerical results from fracture toughness tests on sub-size and standard specimens, analyzing the influence of specimen thickness and size on the toughness results.

2

Bibliography: Ductile failure and hydrogen embrittlement

Abstract This chapter presents a comprehensive bibliographic review of key topics essential for understanding hydrogen embrittlement (HE). It begins with an examination of ductile failure mechanisms and the existing models that aim to replicate these phenomena. Next, it addresses the issues of strain and damage localization, along with the methods developed to mitigate these challenges. The chapter also explores the concept of volumetric locking in finite element modeling and discusses the techniques developed to overcome this issue. It then delves into the HE problem, presenting the mechanisms that attempt to explain this phenomenon. The chapter covers hydrogen transport equations and reviews the models in the literature used to simulate HE and hydrogen-assisted failure. Finally, it introduces the topic of mechanical testing on sub-size specimens, with a focus on fracture toughness tests, relevant standards, and the influence of specimen thickness on toughness.

Résumé Ce chapitre présente une revue bibliographique des sujets clés essentiels pour comprendre la fragilisation par l'hydrogène (FPH). Il commence par examiner des mécanismes de rupture ductile et des modèles existants visant à reproduire ces phénomènes. Ensuite, il aborde les problèmes de localisation de la déformation et de l'endommagement, ainsi que les méthodes développées pour les mitiger. Le chapitre explore également le concept de verrouillage volumétrique dans la modélisation par éléments finis et discute des techniques développées pour surmonter cette problématique. Il s'intéresse ensuite au problème de la FPH, en présentant les mécanismes qui tentent d'expliquer ce phénomène. Le chapitre traite des équations de transport de l'hydrogène et examine les modèles dans la littérature utilisés pour simuler la FPH et la rupture assistée par l'hydrogène. Enfin, il introduit le sujet des essais mécaniques sur des éprouvettes de taille réduite, en mettant l'accent sur les tests de ténacité à la rupture, les normes pertinentes et l'influence de l'épaisseur des éprouvettes sur la ténacité.

Contents

2.1 Ductile failure

In simplified terms, materials can be classified as ductile or brittle based on their behavior. Ductile materials, such as metals and polymers, exhibit large deformations before failure, while brittle materials like ceramics, glasses, and concretes fail suddenly with minimal deformation. However, this classification is not absolute, as a material's behavior can vary significantly with temperature changes and external factors, such as corrosion and irradiation.

Numerical simulations are widely used in industrial applications, especially in situations where conducting full-scale experiments is impractical. For example, when examining extensive gas pipeline tears over several meters, numerical simulations are a valuable tool for predicting crack propagation, assessing structural stability, and analyzing stress distributions.

This work focuses on ductile failure, a mode of material failure typically occurring at high strain levels. This section provides a comprehensive literature review, highlighting various models used to simulate this phenomenon.

2.1.1 Mechanisms of ductile failure

Ductile failure is typically divided into three stages: void nucleation, growth, and coalescence. Voids initiate at material defects, such as second-phase particles or inclusions, by decohesion of the particle-matrix interface or by particle cracking. Then, under significant plastic strain, void growth takes place in regions of high-stress triaxiality[1]. Figure 2.1 gives several examples of ductile failure for an aluminum alloy (2000 series) and various steel grades.

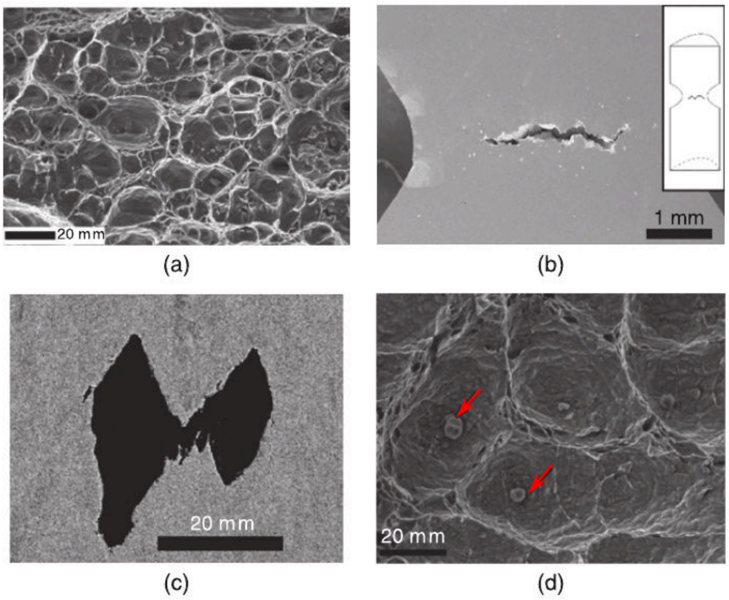

Figure 2.1: Examples of ductile failure by internal necking on voids initiated at primary inclusions. (a) AI 2024 (Bron et al., 2004): void initiation on coarse intermetallic particles containing Fe and Si. (b) A508 steel (Tanguy, 2001): formation of macroscopic crack by void coalescence in a notched bar. (c) X52 steel (Benzerga, 2000): void coalescence by internal necking. (d) X100 steel (Luu, 2006): void initiation on spherical CaS inclusions (red arrows).

When voids reach a critical size, they coalesce to form microcracks that eventually propagate to form a macroscopic crack, culminating in macroscopic failure. Figure 2.2 shows the two most common coalescence modes (V. Nguyen et al., 2020):

- *Internal necking:* Caused by the internal necking of the ligament between adjacent voids. This mode is dominant in high-stress triaxiality states.
- *Internal shearing:* Caused by micro-shear bands that are oblique to the direction, connecting adjacent voids. Often observed in low-stress triaxiality states.

The ductile fracture process typically involves significant plastic strains. Therefore, when using the Finite Element Method (FEM) for numerical simulations of this process, it is imperative to adopt a finite strain framework.

2.1.2 Models of ductile failure

Since the 1970s, numerous models have been proposed to describe ductile damage, which are critical for understanding and predicting crack initiation and growth at the microstructural level of materials. These models can be divided into two main approaches: global and local.

The global approaches are based on energy considerations. A notable example is Rice's integral model (Rice, 1968). However, this model has several limitations: it can only address pre-existing

---

[1] The stress triaxiality, denoted by η, is defined as $\eta = \frac{1}{3}\sigma_{ii}/\sigma_{eq}$, where σ_{ii} is the trace of the stress tensor and σ_{eq} is the von Mises equivalent stress.

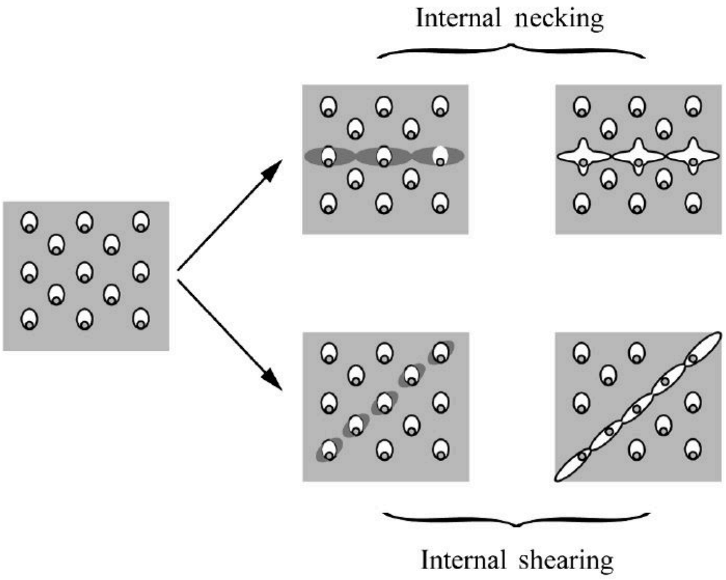

Figure 2.2: Schematic of the three stages of ductile fracture. Void nucleation and growth (on the left) followed by strain localization and void coalescence (on the right) (Zhu et al., 2019).

cracks, it cannot effectively model crack initiation and propagation from notches, and its applicability is strongly dependent on specimen geometry rather than being an intrinsic material property (Besson, 2010; Sumpter, 1993).

In response to these limitations, more physically based descriptions of fracture have been developed, collectively referred to as the "local approach to fracture" (Besson et al., 2006; Pineau, 2006). This approach is called "local" because it involves a detailed, physically based description of damage phenomena within the fracture process zone. Within the local approach, two primary types of models have emerged: phenomenological and micromechanical models.

Among the phenomenological models, Lemaître's model (Lemaître, 1985) stands out for its macroscopic description of damage. In contrast, micromechanical models focus on the analysis of damage mechanisms based on the microstructure of the material. The early development of micromechanical models for ductile fracture was pioneered by Rice and Tracey (Rice and Tracey, 1969). Later, Gurson (Gurson, 1977) introduced the first model to account for material softening. A detailed discussion of these models is presented in the following section.

The Rice & Tracey model

The Rice & Tracey model (Rice and Tracey, 1969) contains most of the essential elements needed to describe ductile fracture. In its simplest form, the model describes the growth of an isolated spherical cavity in an infinite, perfectly rigid and plastic material following von Mises plasticity. In this scenario, the growth rate of a cavity with radius R is expressed as:

$$\frac{\dot{R}}{R} = \alpha \exp\left(\beta \frac{\sigma_m^\infty}{\sigma_{eq}^\infty}\right) \dot{\kappa}^\infty \tag{2.1}$$

where α and β are constants that can be adjusted, σ_{eq}^{∞} is the von Mises equivalent stress at infinity, $\dot{\kappa}^{\infty}$ is the plastic strain rate at infinity and σ_{m}^{∞} is the average stress, given by:

$$\sigma_m^{\infty} = \frac{1}{3}\mathrm{trace}(\boldsymbol{\sigma}^{\infty}) \tag{2.2}$$

The ratio σ_m/σ_{eq} in Equation 2.1 corresponds to the stress triaxiality. The model can be applied to establish a failure criterion by integrating along the loading path:

$$\log\left(\frac{R}{R_0}\right) = \int_{\kappa_c}^{\kappa} \alpha \left(\beta \frac{\sigma_m}{\sigma_{eq}}\right) d\kappa \tag{2.3}$$

where κ^c is the critical strain at which damage initiates. The Rice & Tracey has led to the definition of a simple rupture criterion stating that fracture occurs when the normalized void radius has reached a critical value:

$$(R/R_0) = (R/R_0)_c \tag{2.4}$$

where R_0 represents the initial void radius, and the ratio R/R_0 can be determined by integrating Equation 2.1. The term $(R/R_0)_c$ is a material-specific parameter that indicates the critical value for void growth, as described by Marini et al., 1985. The model encompasses all the key aspects necessary to describe ductile fracture, including damage growth that depends non-linearly on stress triaxiality, the requirement for increasing plastic deformation to fracture the material, void nucleation (characterized by the parameter κ_c), void coalescence, and eventual fracture (represented by the parameter $(R/R_0)_c$). This model can be effectively applied in the post-processing of elasto-plastic structures to determine the precise locations and moments where fracture initiation occurs. Furthermore, the approach can be extended by introducing a damage indicator, D, whose evolution can be generally expressed as a function of the stress state and strain level, as follows:

$$\dot{D} = f(\boldsymbol{\sigma}, \kappa)\dot{\kappa} \tag{2.5}$$

Considering this model, failure takes place when $D = 1$. Even though this model is still used today for computations of ductile damage, its application should be limited to preliminary studies or to modeling the initiation of failure (ideally in structures without pre-existing cracks). This limitation arises because the model cannot account for the interactions between voids or the impact of void growth (i.e., softening) on the material's mechanical behavior.

The Gurson model

The previous model does not account for the interaction between voids and the effect of void growth on material behavior, such as softening. This problem was first addressed by Gurson, 1977 in an analysis of a finite sphere containing a spherical void in the case of a rigid, perfectly plastic matrix. In this analysis, damage is represented by the void volume fraction (porosity) f, which is the ratio of the volume of the void to the volume of the sphere. This results in a plastic yield surface that accounts for the porosity and its evolution:

$$\Phi = \frac{\sigma_{eq}^2}{\sigma_0^2} + 2f\cosh\left(\frac{1}{2}\frac{\sigma_{ii}}{\sigma_0}\right) - 1 - f^2 \tag{2.6}$$

where σ_{eq} represents the von Mises equivalent stress, σ_0 denotes the yield stress, and σ_{ii} is the trace of the stress tensor. When considering an undamaged material ($f = 0$), the von Mises criterion is retrieved.

Material failure is characterized by the stress tensor being null; considering the previous equation, this condition leads to $f = 1$ which implies the material consists entirely of voids, which does not accurately reflect real failure scenarios. Gurson's micromechanical approach ensures that the normality rule applies to the homogenized porosity/matrix assembly, so that the plastic strain increment tensor is written as:

$$\dot{\boldsymbol{\varepsilon}}_p = \lambda \frac{\partial \Phi}{\partial \boldsymbol{\sigma}} \tag{2.7}$$

where λ is the plastic multiplier. The evolution of porosity can be derived from the principle of mass conservation, so that:

$$\dot{f} = (1 - f)\mathrm{trace}(\dot{\boldsymbol{\varepsilon}}_p) \tag{2.8}$$

It follows from the definition of the yield surface (as outlined in Equation 2.6) that the elastic domain contracts with the progression of porosity, as illustrated in Figure 2.3.

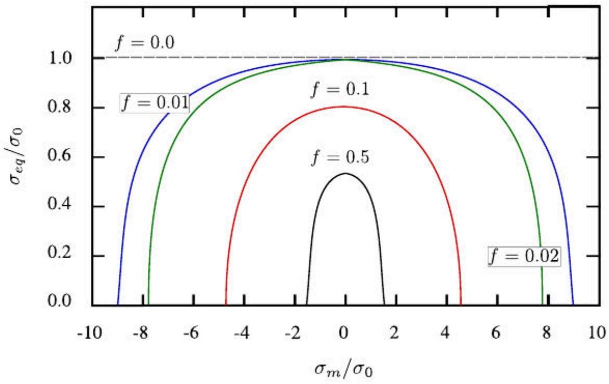

Figure 2.3: Evolution of the Gurson elastic domain for increasing porosities values.

The Gurson-Tvergaard-Needleman (GTN) model

Several models derived from the Gurson model (Gurson, 1977) have been used to develop semi-empirical extensions based on phenomenological descriptions of various damage mechanisms, including void nucleation, growth, and coalescence. A porosity variable related to the void nucleation (f_n) was introduced by Chu and Needleman, 1980. Additionally, Tvergaard and Needleman, 1984 introduced a modified version of the Gurson model that can account for void coalescence and represent failure. This new modified model is referred to as the "Gurson-Tvegaard-Needleman" (GTN) model.

To incorporate void nucleation into the GTN model, porosity is divided into two components: void growth ($\dot{f}_g$), which is derived from mass conservation (Equation 2.8), and a new term representing void nucleation ($\dot{f}_n$), which depends on the accumulated plastic strain rate ($\dot{\kappa}$) as follows:

$$\dot{f} = \dot{f}_g + \dot{f}_n = (1 - f)\mathrm{trace}(\dot{\boldsymbol{\varepsilon}}_p) + A_n \dot{\kappa} \tag{2.9}$$

A gaussian form for the nucleation rate (A_n) was introduced by Chu and Needleman, 1980 and is expressed as:

$$A_n = \frac{f_N}{s_N\sqrt{2\pi}} \exp\left[-\frac{1}{2}\left(\frac{\kappa - \varepsilon_N}{s_N}\right)^2\right] \tag{2.10}$$

Equation 2.10 introduces three additional material parameters: f_N, ε_N, and s_N. The parameter f_N

indicates the volume fraction of inclusions at which damage nucleation initiates. ε_N is the strain at which 50% of the inclusions are broken. s_N is the standard deviation associated with the nucleation strain. The values assigned to these parameters depend on several factors, including material type, chemical composition, and thermal treatments, as discussed in Besson, 2010. It is noteworthy that alternative forms for A_n are also suitable (Prat et al., 1998; Z. Zhang et al., 2000).

To include the effect of coalescence in the model, Tvergaard and Needleman, 1984 proposed the following modified yield surface as:

$$\Phi = \frac{\sigma_{eq}^2}{\sigma_0^2} + 2q_1 f_* \cosh\left(\frac{q_2}{2}\frac{\sigma_{ii}}{\sigma_0}\right) - 1 - q_1^2 f_*^2 \tag{2.11}$$

The novel parameters q_1 and q_2 serve as material coefficients that allow the representation of porosity growth kinetics observed in unit cell calculations. These parameters were first introduced by Tvergaard, 1981 to bring the shear band bifurcation predictions of the Gurson constitutive relation into closer agreement with the corresponding results of full numerical analyses of a periodic array of voids. Based on the calculations of Koplik and Needleman, 1988, common values for these coefficients are often given as $q_1 = 1.5$ or 1.25 and $q_2 = 1.0$, although they are subject to variation depending on the material under study. Subsequent research (Faleskog et al., 1998) has shown that these parameters depend on the plastic strain hardening exponent and the ratio of yield stress to Young's modulus.

Another key parameter introduced by the GTN model is the effective porosity (f^*), proposed by Tvergaard and Needleman, 1984 to account for the effects of rapid void coalesce at failure. Initially, $f^* = f$, as originally proposed by Gurson, 1977, but at a critical void fraction (f_c), the dependence of f^* on f is increased in order to simulate a faster decrease in strength as the voids coalesce. To represent this mechanism, f^* can be expressed as (see Figure 2.4):

$$f^* = \begin{cases} f, & f \leq f_c \\ f_c + \frac{f_R^* - f_c}{f_R - f_c}(f - f_c), & f > f_c \end{cases} \tag{2.12}$$

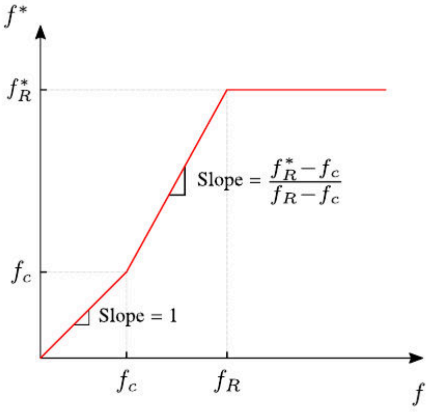

Figure 2.4: Schematic of the effective posority (f^*) evolution to account for void coalescence.

The constant f_R^* is the value of f^* at zero stress in the Equation 2.11, *e.g.* $f_R^* = 1/q_1$. Since $f \rightarrow f_R$, $f^* \rightarrow f_R^*$ and the material loses its stress carrying capacity. Tvergaard and Needleman, 1984 suggested in their work that the values of f_c and f_R can be taken as 0.15 and 0.25, respectively. However, the fracture porosity (f_R) remains a flexible parameter, allowing freedom in its selection. The determination of f_c can be achieved by unit cell calculations, as presented by Z. Zhang et al., 2000. While the given expression for f_* is commonly used, alternative forms may also be appropriate. It should be noted that employing low values for both f_c and f_R can cause convergence problems when using the finite element (FE) method.

GTN model extensions

The classical GTN model is limited in its ability to accurately predict damage under low triaxiality or shear-dominated loading conditions, as noted by H. Li et al., 2011. To address these limitations, several extensions have been proposed, focusing on incorporating the effects of cavity rotation, shape evolution, and shear damage mechanisms. A key feature of these models is the inclusion of the third stress invariant or Lode parameter in the porosity evolution equations. The extensions that enhance the GTN model's capability under shear-dominated conditions are summarized bellow.

- *Nahshon & Hutchison extension:* This extension was proposed by Nahshon and Hutchinson, 2008, where they introduced a shear porosity term in addition to the conventional porosity growth within the GTN model. Its evolution is governed by the Lode parameter, deviatoric stress, and a material constant. This extension was successful in modeling ductile failure under low triaxiality, but produced non-negligible effects under high triaxiality loading. Nielsen and Tvergaard, 2009 later refined the model by introducing a function to limit the influence of shear porosity based on stress triaxiality.
- *Xue Extension:* Xue, 2008 proposed a similar approach, introducing a shear damage variable that evolves based on total porosity, shear loading, and a Lode angle-dependent function. The model provides parameters for 2D and 3D applications and offers two implementation strategies: treating the shear damage variable as an internal variable affecting material behavior or calculating it post-integration from stress and porosity.
- *Shape and Rotation Extensions:* Kailasam and Castañeda, 1998 highlighted the importance of cavity shape and orientation in macroscopic material behavior. Their model, later extended by Danas and Castañeda, 2009 and applied to the GTN framework by Cao et al., 2015, incorporates anisotropy through an *ad hoc* modification of the GTN yield function. By introducing a tensor to describe ellipsoidal voids and their orientations, this model implicitly accounts for shear effects. While it delivers realistic results for hydrostatic and shear loading, its complexity and computational cost remain significant compared to simpler shear-focused extensions.

These advancements expand the GTN model's applicability to low triaxiality loading, but come with trade-offs in complexity and computational demands. Further comparison of their numerical efficiency and predictive accuracy is necessary for practical implementation.

Phenomenological constitutive models

The constitutive models presented here build on the works of Lemaître, 1985 and Kachanov, 1958 within the framework of Continuum Damage Mechanics (CDM). These phenomenological models, based on macroscopic considerations, describe damage evolution using scalar or tensorial variables. Unlike micromechanically models, these formulations incorporate features such as kinematic hardening and damage closure under compression, facilitating their application to cyclic loading scenarios. The models are built in a consistent thermodynamic approach (Germain et al., 1983) to ensure positive dissipation, with variations addressing brittle fracture, creep, and fatigue (Lemaitre and Desmorat, 2005). While micromechanics-based approaches also employ continuous damage descriptions, these phenomenological models prioritize ease of implementation and flexibility across diverse material behaviors.

Key elements of these models include internal variables, such as plastic strain, hardening parameters, and a scalar damage variable. Damage evolution begins with plastic deformation and may incorporate thresholds based on plastic strain or stored energy. Advanced modifications enable anisotropic damage descriptions, cyclic closure effects, and applications to complex stress states, as demonstrated in extensions by Lemaitre et al., 2000. Models like Rousselier's (Rousselier, 1987; Rousselier, 2001) integrate porosity as a damage variable within a thermodynamic framework, differing notably from Gurson-type models by allowing damage evolution under pure shear or hydrostatic stress states. These frameworks provide versatile tools for modeling ductile failure, fatigue, and damage in various engineering materials. For a detailed analysis and comparison of the various cited phenomenological damage models, please refer to Besson, 2010.

2.2 Regularized damage models

The use of local damage models can result in strain and damage localization, leading to spurious mesh dependency issues. To address these problems, various strategies have been proposed in the literature. This section provides an overview of strain and damage localization phenomena and discusses nonlocal damage models developed to mitigate these issues.

2.2.1 Strain and damage localization

During the ductile failure process, a pronounced softening effect is observed. This softening, induced by increasing damage, leads to instability in the macroscopic behavior of the material and results in significant strain localization in a thin zone near the failure region. The size of this zone, often referred to as the "localization band", depends on the material properties, the structure's geometry, and the nature of the loading.

Finite elements simulations of this process show a strong dependence on mesh size: damage tends to localize in a band formed by a single layer of elements, regardless of the mesh size. In addition, the orientation of the damage band is affected by the mesh orientation. For these models, reducing the mesh size does not lead to a converged solution. If an infinitely refined mesh is used, the thickness of the localization band tends to zero, resulting in zero dissipated energy, which is an unrealistic result.

Localization is assumed to occur in an infinite planar band characterized by its normal $\boldsymbol{n}$ and displacement is assumed to be discontinuous across this band. The direction of the displacement jump is referred to as $\boldsymbol{g}$, as shown in Figure 2.5. According to Rice, 1976; Rice, 1980, it was shown that the jump of the strain rate tensor across the localization bands can be expressed as:

$$\Delta\dot{\varepsilon} = \frac{1}{2}(\boldsymbol{n} \otimes \boldsymbol{g} + \boldsymbol{g} \otimes \boldsymbol{n}) \tag{2.13}$$

where $\boldsymbol{n}$ is the vector normal to the band and $\boldsymbol{g}$ the velocity jump. The normal vector $\boldsymbol{n}$ can be obtained as the vector that minimizes the Rice criterion for band localization. In the case of infinitesimal strain theory, it can be expressed as:

$$\det(\boldsymbol{n} \cdot \mathbb{D} \cdot \boldsymbol{n}) = 0 \tag{2.14}$$

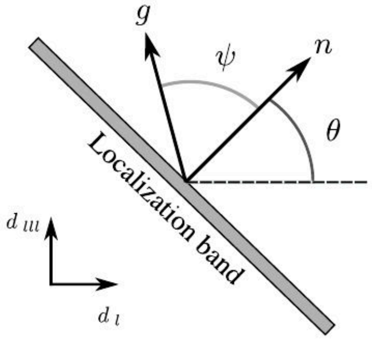

Figure 2.5: Schematic of the localization band (Besson, 2010).

where, for elasto-plastic materials, $\mathbb{D}$ is the elasto-plastic tangent matrix, ($\dot{\boldsymbol{\sigma}} = \mathbb{D} : \dot{\boldsymbol{\varepsilon}}$). Additional terms are needed for the finite strain case (Besson et al., 2001; Huespe et al., 2012).

2.2.2 Mesh size sensitivity

As previously discussed, strain and damage localization occurs when the constitutive law includes softening induced by damage evolution. When such constitutive laws are used in finite element analysis, spurious mesh dependence and unrealistic predictions can occur. This section illustrates the effect of mesh dependence using a study case proposed by Besson, 2010.

The simulations in the following used Compact Tension (CT) specimens. The simulations were performed using a GTN model under plane-strain conditions. The sample is loaded by applying a uniaxial (vertical) displacement on the center of a wedge (red area in Figure 2.6). Several simulations were performed using different mesh sizes in the crack propagation zone. Figure 2.6 shows the force versus Crack Mouth Opening Displacement (CMOD) for each of the considered mesh sizes. The results clearly show that for a given CMOD, decreasing the mesh size correlates with an increase in the equivalent strain at the crack tip, resulting in earlier crack initiation and the absence of convergence when mesh size is decreased. The influence of mesh size on crack initiation can be attributed to the high stress and

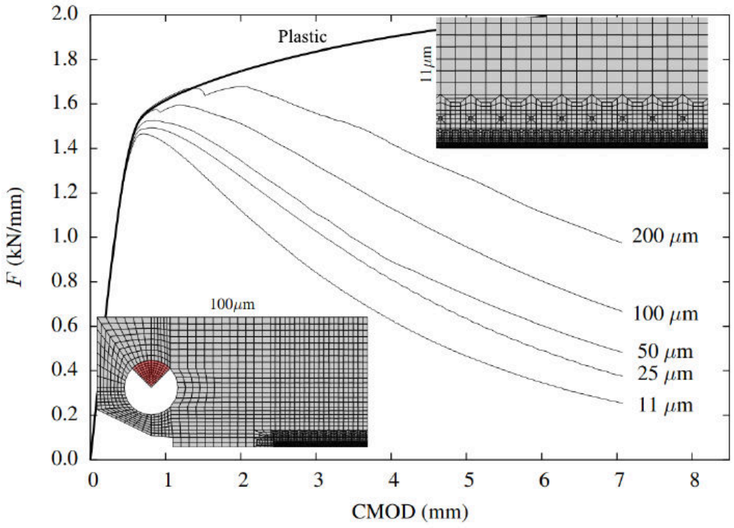

Figure 2.6: Simulations of Compact Tension (CT) specimens suing different mesh-sizes. Adapted from (Besson, 2021).

strain gradients present at the crack tip. For a given applied displacement, the strain calculated at the Gauss points near the crack tip is greater in finer meshes, leading to earlier crack initiation. The effect of mesh size on crack propagation can be understood as follows: the mechanical work dissipated per crack increment due to inelastic deformation in a finite element model with the dimensions width (w), thickness (b), and height (h) is:

$$U_d = \int_{\Omega_e} \int_0^{t_R} (\boldsymbol{\sigma} : d\boldsymbol{\varepsilon}_p)\, d\Omega_e \tag{2.15}$$

where Ω_e is the volume of the element and t_R is the time at which the element is considered broken. Given that the volume of the element remains nearly constant, Equation 2.15 can be expressed as follows:

$$U_d = u_d \Omega_e = u_d \times (wbh) \tag{2.16}$$

where u_d is a rupture energy per unit volume. At t_R, the element is considered broken; this corresponds to a crack extension area of $\Delta a = wb$, so that the energy dissipated per crack extension increment is equal to:

$$\Gamma_0 = \frac{U_d}{\Delta a} = \frac{u_d wbh}{wb} = u_d h \propto h \tag{2.17}$$

where Γ_0 can be interpreted as a specific "separation work" (Steglich et al., 1999). Increasing the element height results in greater dissipation of mechanical work, which affects the overall behavior of the structure. In this study, the relationship between Γ_0 and the structural response is complex due to the prevalence of large-scale yielding conditions. The fracture energy u_d is highly dependent on the local load history, especially the local constraint: u_d tends to be high for low local stress triaxiality ratios and low for high triaxialities. The dependence of u_d, and hence Γ_0, on the local history, complicates the establishment of a direct correspondence between continuum damage models and cohesive zone models, as discussed in Steglich et al., 1999.

Mesh-size as a material parameter

The mesh size dependence discussed in the previous section results from material softening induced by damage progression. It has been observed that refining the mesh does not necessarily lead to converged results. A practical approach to this problem is to treat the mesh size as an additional material parameter (Rousselier, 1987; Ruggieri and Dodds, 1996). In such cases, the mesh size in the crack propagation zone is often assumed to represent the mean distance between inclusions (ℓ_c). This approach views the material as an assembly of cells of size ℓ_c, each containing a single inclusion or void.

This simplified representation overlooks cell deformation and the influence of secondary inclusions, which are typically smaller and more closely spaced. Experimental observations on aluminum alloys support this view (Hahn and Rosenfield, 1975; Steglich and Brocks, 1997). However, it is evident that simulation results still depend on mesh orientation and element type (shape, interpolation degree, etc.), thereby limiting the predictability of the model (Besson et al., 2006).

2.2.3 Nonlocal damage models

Several strategies have been proposed in the literature to address the issue of mesh dependence. These strategies, known as "nonlocal" damage models, were first introduced in the context of elasticity (Eringen and Edelen, 1972) and were quickly extended to plasticity and damage contexts. These approaches involve the introduction of a material internal length scale. They maintain the constitutive equations with minor modifications, which is particularly advantageous for constitutive models that rely on a detailed micro-mechanical description of damage processes. This section introduces several nonlocal models, such the integral, the implicit gradient, the micromorphic, the gradient-enhanced energy (GEE), and the phase field model.

Integral method

The integral nonlocal approach is proposed to describe microstructural behavior in an averaged manner. This model assumes that the material behavior at a given point depends not only on the local values of various state variables but also on the values of these variables in the surrounding region. According to this approach, a nonlocal variable $\bar{D}$ in a material point x is considered as a weighted average of the local values D in all material points of the body Ω (Bažant and Pijaudier-Cabot, 1988; Pijaudier-Cabot and Bažant, 1987):

$$\bar{D}(x) = \frac{1}{\Psi(x)} \int_{\Omega} \psi(x, y) z(y) \, d\Omega \tag{2.18}$$

where y is the position vector of the infinitesimally small volume $d\Omega$ and $\psi(x, y)$ is the weight function, e.g. of the Gaussian form (Engelen et al., 2003):

$$\psi(x, y) = \frac{1}{(2\pi)^{3/2} \ell_c^3} \exp\left(-\frac{|x - y|^2}{2\ell_c^2} \right) \tag{2.19}$$

The length parameter ℓ_c determines the size of the volume that effectively contributes to the nonlocal quantity and is related to the scale of the microstructure. The integral nonlocal kernel described above has the property that the local continuum is retrieved if $\ell_c \to 0$. It is important to note that $\bar{D}$ naturally equals D for homogeneous strain states due to the use of the normalization factor $\Psi(x)$ in Equation 2.18, which is given by:

$$\Psi(x) = \int_{\Omega} \psi(x, y) \, d\Omega \tag{2.20}$$

Explicit/implicit gradient method

To avoid the complex implementation of the integral method, a Taylor expansion of D (Bažant et al., 1984) can be used to derive the gradient-enhanced models:

$$\begin{aligned} D(y) = D(x) &+ \frac{\partial D}{\partial x_i}(y_i - x_i) \\ &+ \frac{1}{2!} \frac{\partial^2 D}{\partial x_i \partial x_j}(y_i - x_i)(y_j - x_j) \\ &+ \frac{1}{3!} \frac{\partial^3 D}{\partial x_i \partial x_j \partial x_k}(y_i - x_i)(y_j - x_j)(y_k - x_k) \\ &+ \frac{1}{4!} \frac{\partial^4 D}{\partial x_i \partial x_j \partial x_k \partial x_l}(y_i - x_i)(y_j - x_j)(y_k - x_k)(y_l - x_l) + ... \end{aligned} \tag{2.21}$$

where Einstein's summation convention applies to the indices i, j, k, l. Substituting Equation 2.21 into Equation 2.18 and evaluating the integral on $\mathbb{R}^3$ yields:

$$\bar{D}(x) = D(x) + c_2 \nabla^2 D(x) + c_4 \nabla^4 D(x) + \ldots \tag{2.22}$$

The Laplacian operator ∇^n is defined as $\nabla^2 = \sum_i \frac{\partial^2}{\partial x_i^2}$ and $\nabla^{2n} = (\nabla^2)^n$. It is important to note that the gradient parameters c_2 and c_4 both have the dimensions of a length raised to an even power and that odd-order derivatives vanish due to the isotropy of the Gaussian weight function (Equation 2.19). To approximate the nonlocal kernel, one can disregard terms of order four and higher, resulting in the following explicit gradient approximation:

$$\bar{D}(x) = D(x) + c_2 \nabla^2 D(x) = D(x) + \ell_c^2 \Delta D(x) \tag{2.23}$$

The parameter c_2 in Equation 2.23 represents a squared length, which introduces an internal length ℓ_c in the explicit formulation of the gradient, similar to the approach used in the integral method. However, this explicit formulation is not suitable for the finite element method for two main reasons: (i) it requires extrapolating to the nodes, which introduces potential errors, and (ii) it involves computing the Laplacian of the extrapolated variable, which may not be continuously differentiable. A viable solution to this limitation is to adopt an implicit formulation, as suggested by Peerlings et al., 1996. For this formulation, the Laplacian operator must be applied to Equation 2.23:

$$\Delta D(x) = \Delta \bar{D}(x) - c_2 \nabla^4 D(x) \tag{2.24}$$

Substituting Equation 2.24 into 2.22 leads to:

$$\bar{D}(x) = D(x) + c_2 \nabla^2 D(x) + (c_4 - c_2^2) \nabla^4 D(x) + \dots \tag{2.25}$$

Finally, the implicit gradient formulation is obtained after neglecting higher order terms:

$$\bar{D}(x) = D(x) + c_2 \nabla^2 \bar{D}(x) = D(x) + \ell_c^2 \Delta(x) \tag{2.26}$$

In the context of ductile failure, Mediavilla et al., 2006 and Feld-Payet et al., 2011 proposed replacing the local accumulated plastic strain κ with its nonlocal counterpart $\bar{\kappa}$ in the damage evolution variables. Specifically, for the GTN model, the nonlocal accumulated plastic strain was employed to regularize both void growth (f_g) and nucleated (f_n). Additionally, the nonlocal plastic strain can be used to regularize hardening, as outlined by Peerlings et al., 2012. However, the implicit gradient formulation does not provide clear guidelines for expressing the constitutive equations in terms of nonlocal variables. By using $\bar{\kappa}$, it becomes possible to regularize three local variables (κ, f_g and f_n) at the computational cost of only one additional unknown field ($\bar{\kappa}$), as shown by Linse et al., 2012. A local tensor variable can also be employed, as demonstrated by Hütter et al., 2013. In their work, a nonlocal counterpart $\bar{\boldsymbol{\varepsilon}}_p$ based on the plastic strain tensor $\boldsymbol{\varepsilon}_p$ is computed and used to calculate the evolution of void growth and nucleation.

The concept of using multiple internal length scales for ductile failure was introduced by V. Nguyen et al., 2020. In their model, an internal length scale was associated with each damage mechanism: (i) void growth based on the classical GTN model, (ii) void coalescence by internal necking governed by a heuristic extension of the Thomason yield surface based on the maximum principal stress, and (iii) shear-dominated coalescence mechanisms driven by the maximum shear stress. While the model proposes different internal length scales, the same characteristic length was assigned to the three nonlocal variables in the simulations presented.

Micromorphic model

The micromorphic approach enhances the kinematics of material points by introducing additional degrees of freedom associated with plastic strain, damage, or phase field variables. A key feature of these theories is the inclusion of the gradient of the micromorphic variable in the constitutive functions, in particular the Helmholtz energy, thereby introducing an internal length parameter (Forest, 2018). The local internal variables have micromorphic counterparts that account for interactions at the microscopic level. For an elasto-plastic material, the accumulated plastic strain κ and its micromorphic counterpart κ_χ are expressed in terms of the Helmholtz energy as follows (Mazière and Forest, 2015):

$$\psi = \frac{1}{2}(\boldsymbol{\varepsilon} - \boldsymbol{\varepsilon}_p) : \mathbb{E} : (\boldsymbol{\varepsilon} - \boldsymbol{\varepsilon}_p) + \psi_p(\kappa) + \frac{1}{2}H_\chi(\kappa - \kappa_\chi)^2 + \frac{1}{2}A_\chi \nabla\kappa_\chi \cdot \nabla\kappa_\chi \tag{2.27}$$

where A_χ and H_χ are additional parameters introduced by the model, $\mathbb{E}$ is the elasticity tensor, $\boldsymbol{\varepsilon}_e$ is the elastic strain tensor, ψ_p is the contribution to the Helmholtz energy governing the hardening of the material. Thus, the thermodynamical associated forces are:

$$\boldsymbol{\sigma} = \frac{\partial\psi}{\partial\boldsymbol{\varepsilon}} = \mathbb{E} : (\boldsymbol{\varepsilon} - \boldsymbol{\varepsilon}_p) \tag{2.28}$$

$$R_\chi = \frac{\partial\psi}{\partial\kappa} = R + H_\chi(\kappa - \kappa_\chi) \tag{2.29}$$

$$a_\chi = \frac{\partial\psi}{\partial\kappa_\chi} = -H_\chi(\kappa - \kappa_\chi) \tag{2.30}$$

$$\boldsymbol{b}_\chi = \frac{\partial\psi}{\partial\nabla\kappa_\chi} = A_\chi\nabla\kappa_\chi \tag{2.31}$$

where a_χ and $\boldsymbol{b}_\chi$ are driving forces associated with the state variables. The yield surface can be expressed as:

$$\phi = \sigma_{eq} - (\sigma_0 + R_\chi) = \sigma_{eq} - (\sigma_0 + R + H_\chi(\kappa - \kappa_\chi)) \tag{2.32}$$

Different from gradient methods, which are not based on the theory of generalized standard materials, the micromorphic model naturally defines the coupling between the micromorphic variable κ_χ and the constitutive equation through the thermodynamic force representing the hardening, R_χ.

The dissipated energy can be expressed as:

$$\mathcal{D} = \int_\Omega (\boldsymbol{\sigma} : \dot{\boldsymbol{\varepsilon}}_p - R_\chi\dot{\kappa} - a_\chi\dot{\kappa}_\chi - \boldsymbol{b}_\chi \cdot \nabla\dot{\kappa}_\chi)\, d\Omega \tag{2.33}$$

Using divergence theorem on Equation 2.33, the dissipation potential can be written as:

$$\mathcal{D} = \int_\Omega (\boldsymbol{\sigma} : \dot{\boldsymbol{\varepsilon}}_p - R_\chi\dot{\kappa} - (A_\chi\Delta\kappa_\chi + H_\chi(\kappa - \kappa_\chi))\dot{\kappa}_\chi)\, d\Omega - \int_{\partial\Omega} A_\chi\nabla\kappa_\chi \cdot \boldsymbol{n}\dot{\kappa}_\chi\, dS \tag{2.34}$$

Based on the hypothesis that the dissipation potential related to the micromorphic variable κ_χ is null, the following is obtained:

$$A_\chi\Delta\kappa_\chi + H_\chi(\kappa - \kappa_\chi) = 0 \Rightarrow \kappa_\chi = \kappa + \frac{A_\chi}{H_\chi}\Delta\kappa_\chi \tag{2.35}$$

where Δ is the Laplacian operator. This equation shows an equivalence between the micromorphic model and the implicit gradient approach, where the characteristic length scale is defined as:

$$\ell_c^2 = \frac{A_\chi}{H_\chi} \tag{2.36}$$

The material parameters and H_χ and A_χ are assumed to be positive to ensure stability.

Localization and damage leading to fracture represent key applications of the micromorphic approach. Internal lengths are essential for accurately predicting crack initiation, propagation, and branching. Successful applications include ductile fracture studies in metals and alloys, as evidenced by examples such as those presented in Dillard et al., 2006; Feld-Payet et al., 2015; Lorentz et al., 2008.

Gradient-enhanced energy model

The gradient-enhanced energy (GEE) approach, as proposed in Lorentz, 2005; Lorentz and Andrieux, 1999; Lorentz and Godard, 2011; Y. Zhang et al., 2017, involves incorporating a positive function of the gradient of a local variable into the Helmholtz energy. Specifically, the gradient of the hardening variable, $\nabla\kappa$, is introduced into the Helmholtz free energy density, leading to the following:

$$\psi = \frac{1}{2}(\boldsymbol{\varepsilon} - \boldsymbol{\varepsilon}_p) : \mathbb{E} : (\boldsymbol{\varepsilon} - \boldsymbol{\varepsilon}_p) + \psi_p(\kappa) + \frac{c}{2}\nabla\kappa \cdot \nabla\kappa \tag{2.37}$$

where c is a strictly positive parameter with the dimension of force, which weights the nonlocal interactions between neighboring material points. A larger value of c results in a smoother spatial distribution of the hardening variable.

This approach has been applied to the GTN model as described in Y. Zhang et al., 2017. To regularize the nucleation porosity f_n and the growth porosity f_g, the gradient of the accumulated plastic strain κ must be calculated. However, since κ is defined at the integration points, its gradient cannot be directly computed without extrapolation to the nodes. To address this, a "relaxed" formulation was proposed in Y. Zhang et al., 2017, which introduces a nodal variable a and ensures the equality of κ and a in a weak sense. This weak equality is enforced using a Lagrangian multiplier l, and is expressed as follows:

$$\begin{aligned} \mathcal{L}(\boldsymbol{\varepsilon}, \boldsymbol{\varepsilon}, \kappa, a, l) &= \int_\Omega \psi(\boldsymbol{\varepsilon}, \boldsymbol{\varepsilon}_p, \kappa, a, l)\, d\Omega \\ &= \int_\Omega \psi_{loc}(\boldsymbol{\varepsilon}, \boldsymbol{\varepsilon}_p, \kappa)\, d\Omega + \int_\Omega \psi_{gdt}(a)\, d\Omega + \int_\Omega \psi_{rlx}(\kappa, a, l)\, d\Omega \end{aligned} \tag{2.38}$$

where,

$$\psi_{loc}(\boldsymbol{\varepsilon}, \boldsymbol{\varepsilon}_p, \kappa) = \frac{1}{2}(\boldsymbol{\varepsilon} - \boldsymbol{\varepsilon}_p) : \mathbb{E} : (\boldsymbol{\varepsilon} - \boldsymbol{\varepsilon}_p) + \psi_p(\kappa) \tag{2.39}$$

$$\psi_{gdt}(a) = \frac{c}{2}\nabla a \cdot \nabla a \tag{2.40}$$

$$\psi_{rlx}(\kappa, a, l) = l(a - \kappa) \tag{2.41}$$

The associated forces to the state variables are then expressed as:

$$\boldsymbol{\sigma} = \frac{\partial \psi}{\partial \boldsymbol{\varepsilon}} = \mathbb{E} : (\boldsymbol{\varepsilon} - \boldsymbol{\varepsilon}_p) \tag{2.42}$$

$$R_{nl} = \frac{\partial \psi}{\partial p} = R(\kappa) - l \tag{2.43}$$

$$R_a = \frac{\partial \psi}{\partial a} = l \tag{2.44}$$

$$R_l = \frac{\partial \psi}{\partial l} = a - \kappa \tag{2.45}$$

$$R_{\nabla a} = \frac{\partial \psi}{\partial \nabla a} = c \nabla a \tag{2.46}$$

The yield surface is then expressed as:

$$\Phi = \sigma_{eq} - (\sigma_0 + R_{nl}) = \sigma_{eq} - (\sigma_0 + R - l) \tag{2.47}$$

The nodal forces obtained are similar to those derived from micromorphic approach, except for the Lagrangian term (R_l). It is important to note that a is introduced only to facilitate the numerical solution and should not be considered as the micromorphic counterpart of κ. The equality between κ and a is weakly enforced. In the micromorphic model, as previously mentioned, the near equality between κ and κ_χ is achieved by using a very high value for H_χ, which acts as a penalty factor.

The dissipation energy is written as follows:

$$\begin{aligned}\mathcal{D} &= \int_\Omega (\boldsymbol{\sigma} : \dot{\boldsymbol{\varepsilon}})\, d\Omega - \dot{\mathcal{L}} \\ &= \int_\Omega \Big(\boldsymbol{\sigma} : \dot{\varepsilon}_p - (R - l)\dot{\kappa} - l\dot{a} - c\nabla a \cdot \nabla \dot{a} - (a - \kappa)\dot{l}\Big)\ d\Omega\end{aligned} \tag{2.48}$$

Using the divergence theorem, Equation 2.48 can be rewritten as follows:

$$\mathcal{D} = \int_\Omega (\boldsymbol{\sigma} : \dot{\boldsymbol{\varepsilon}} - (R - l)\dot{\kappa} - (a - \kappa)\dot{l} - (l - c\Delta a)\dot{a})\, d\Omega - \int_{\partial\Omega} c\nabla a \cdot \boldsymbol{n}\dot{a}\, dS \tag{2.49}$$

The new variables (a and l) do not contribute to the dissipation and as in the case of the micromorphic model, the strong form is obtained as:

$$\begin{aligned} a &= \kappa \\ l - c\Delta a &= 0 \\ \Delta a \cdot \boldsymbol{n} &= 0 \quad \text{on} \quad \partial\Omega \end{aligned} \tag{2.50}$$

To account for the nonlocal effect, the yield surface can be rewritten as follows:

$$\phi = \sigma_{eq} - (\sigma_0 + R - l) = \sigma_{eq} - (\sigma_0 + R - c\Delta a) \tag{2.51}$$

Phase-field model

The phase-field method is a mathematical and computational approach used to model and simulate the evolution of interfaces and phase boundaries within materials. It gained significant attention since the work of Francfort and Marigo, 1998 and is particularly useful for solving complex problems involving fractures, phase transitions, and microstructural evolution in various materials. This method is built upon Griffith's thermodynamic framework and has demonstrated effectiveness in modeling brittle fractures as well as analyzing ductile damage (Martínez-Pañeda et al., 2018).

This model introduces an order parameter, typically denoted as ϕ, which varies continuously across the interface between different phases or regions of a material: $\phi = 0$ represents an intact material while $\phi = 1$ indicates a fully broken material.

The phase-field method minimizes energy by defining a free energy functional that incorporates all relevant contributions (bulk, interfacial, and external energies). The evolution of the system is governed by equations derived from this functional, ensuring that the system progresses towards states of lower energy. The free energy function of a system can be expressed as:

$$\mathcal{E}(\boldsymbol{u}, \Gamma) = \int_\Omega \psi_e(\varepsilon(\boldsymbol{u}))\, d\Omega + G_c \int_\Gamma dS \tag{2.52}$$

where ψ_e is the elastic density function, G_c is the material fracture toughness and Γ is the admissible crack set. Based on the work of Bourdin et al., 2000, another variational formulation based on regularizing the energy functional is expressed as:

$$\mathcal{E}_l(\boldsymbol{u}, \phi) = \int_\Omega ((1-\phi)^2 + k)\psi_e(\varepsilon(\boldsymbol{u}))\, d\Omega + G_c \int_\Omega \left(\frac{\phi^2}{2\ell_c} + \frac{\ell_c}{2} |\nabla \phi|^2 \right) d\Omega \tag{2.53}$$

where ℓ_c is the characteristic length that controls the width of the transition zone and k is a dimensionless parameter needed to prevent numerical difficulties that occur at total failure.

2.3 Locking-free finite element models

This section discusses volumetric locking, a numerical problem commonly encountered in finite element simulations involving nearly incompressible materials or constrained deformation scenarios. Volumetric locking leads to excessive stiffening in the numerical model, resulting in inaccurate predictions of material behavior, especially in cases of plasticity or when simulating materials with high Poisson's ratio.

To mitigate this problem, this section presents several numerical solutions aimed at overcoming volumetric locking. These include the use of higher order elements, reduced or selective integration techniques, and mixed formulation methods.

2.3.1 Volumetric locking

Volumetric locking is a well-known numerical issue in finite element analysis (FEA), particularly observed in simulations involving quasi-incompressible materials or scenarios where the Poisson's ratio approaches 0.5, as is the case in many elastoplastic materials (in that case, the tangent elastoplastic ratio tends to 0.5). This problem arises from the finite element model's inability to accurately represent incompressible behavior, leading to an artificial increase in stiffness and imposing excessive constraints on the material's volume change.

Quasi-incompressibility is mathematically characterized by:

$$J = \det(\boldsymbol{F}) \approx 1 \quad \text{or} \quad \text{trace}(\boldsymbol{\varepsilon}) \approx 0 \tag{2.54}$$

where J is the Jacobian of the deformation gradient $\boldsymbol{F}$, $\text{trace}(\boldsymbol{\varepsilon})$ denotes the trace of the strain tensor. For materials with a Poisson's ratio $\nu \approx 0.5$, the bulk modulus $K \to \infty$, as described by the relation:

$$K = \frac{E}{3(1-2\nu)} \tag{2.55}$$

where E is the Young's modulus. Consequently, according to Hooke's law, the volumetric strain approaches zero:

$$\text{trace}(\boldsymbol{\varepsilon}) = \frac{\text{trace}(\boldsymbol{\sigma})}{K} \to 0 \tag{2.56}$$

This leads to minimal volume change, imposing restrictions on the model's displacement field.

Lower-order elements, such as linear quadrilateral or hexahedral elements, are particularly prone to volumetric locking because they lack the ability to accurately capture the complex deformation patterns of nearly incompressible materials. Volumetric locking typically manifests itself as an overly stiff numerical response, resulting in incorrect stress and displacement fields. In this scenario, the material artificially resists changes in volume, leading to errors in strain distribution and ultimately inaccurate results.

If $\text{trace}(\boldsymbol{\varepsilon}) = \nabla \cdot \boldsymbol{u} \approx 0$, the effective degrees of freedom in the displacement field are significantly reduced. As a result, certain material points become "locked", and spurious pressure oscillations appear. These oscillations are particularly pronounced near areas of high plastic strain, such as in the case of a blunted crack. Figure 2.7 illustrates the occurrence of volumetric locking ahead of a blunted crack, where the standard displacement-based finite element formulation leads to strong pressure oscillations.

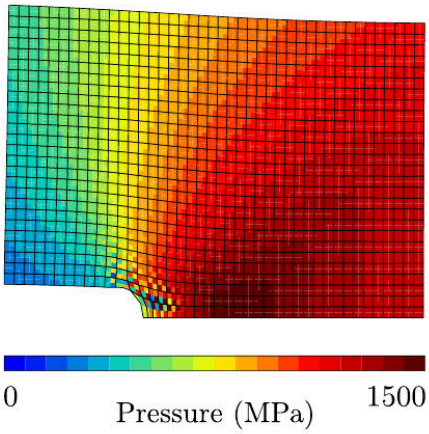

Figure 2.7: Volumetric locking observed ahead of a blunted crack.

Over the years, several strategies have been developed to address the problem of volumetric locking in finite element analysis. The following section presents some of the approaches used to overcome this problem.

2.3.2 Locking-free strategies

This section provides a brief overview on the numerical approaches used to mitigate volumetric locking. For more information about each formulation, please refer to the cited references.

Reduced integration

The reduced integration technique was first introduced by Zienkiewicz et al., 1971 to mitigate volumetric locking in finite element analysis. This method uses lower-order quadrature formulas to estimate the stiffness matrix, thereby reducing the number of integration points within each finite element. As a result, the constraints on the divergence of the displacement field, $\nabla \cdot \boldsymbol{u} \approx 0$, are less strict, allowing for the recovery of some lost degrees of freedom.

However, this technique can lead to a singular stiffness matrix and introduce zero-energy modes, which are non-physical deformations that result from insufficient integration points. These problems can affect the stability and accuracy of the numerical solution. Despite these challenges, the reduced integration technique remains a valuable tool, especially for the analysis of soft materials or conditions prone to volumetric locking.

Selective integration

The selective integration technique was first proposed by Doherty et al., 1969. This approach involves applying different integration orders to various components of the stiffness matrix. Typically, full integration is employed for certain components, such as deviatoric stresses, while reduced integration is used for others, like volumetric stresses. By selectively integrating the volumetric portion of the stiffness matrix, this technique effectively reduces the artificial stiffness associated with nearly incompressible materials. As a result, it eases volumetric locking without compromising the accuracy of the deviatoric response.

$\boldsymbol{B}$-bar and $\boldsymbol{F}$-bar formulations

This approach, introduced by Hughes, 2012; Hughes, 1980, employs the strain-displacement matrix $\boldsymbol{B}$, which relates the nodal displacements of a finite element to the strain field within the element. In this formulation, the strain operator $\boldsymbol{B}$ is first decomposed into deviatoric ($\boldsymbol{B}_d$) and hydrostatic ($\boldsymbol{B}_h$) components. The hydrostatic component is then modified into $\bar{\boldsymbol{B}}_h$, typically by averaging $\boldsymbol{B}_h$ over the element. This ensures that the trace of the strain tensor, trace($\boldsymbol{\varepsilon}$), is constant across the element. Since pressure is related to volume changes, this modification helps mitigate pressure fluctuations within the element. As a result, the new strain operator $\bar{\boldsymbol{B}}$ is expressed as follows:

$$\bar{\boldsymbol{B}} = \boldsymbol{B}_d + \bar{\boldsymbol{B}}_h \tag{2.57}$$

The $\bar{\boldsymbol{B}}$-bar formulation enhances the stability of the numerical solution, effectively mitigating locking issues that often observed in standard formulations, particularly when using lower-order elements.

A similar approach is employed within the $\boldsymbol{F}$-bar framework, which relies on the multiplicative decomposition of the deformation gradient $\boldsymbol{F}$ into deviatoric (shape-changing) and hydrostatic (volume-changing) components. This decomposition has been widely used in several studies (de Souza Neto et al., 1996; Moran et al., 1990; Simo and Taylor, 1991; Simo et al., 1985) to handle the incompressibility constraint in finite deformation problems. The deformation gradient is split as follows:

$$\boldsymbol{F} = \boldsymbol{F}_d \boldsymbol{F}_h \tag{2.58}$$

where $\boldsymbol{F}_d$ and $\boldsymbol{F}_h$ represent the deviatoric and hydrostatic components of $\boldsymbol{F}$, respectively. By construction, these components satisfy the following relations:

$$\det(\boldsymbol{F}_d) = 1, \quad \det(\boldsymbol{F}_h) = \det(\boldsymbol{F}) = J \tag{2.59}$$

where J is the Jacobian of the deformation gradient $\boldsymbol{F}$. The deviatoric and hydrostatic components can then be defined as:

$$\boldsymbol{F}_d = J^{-1/3}\boldsymbol{F}, \quad \boldsymbol{F}_h = J^{1/3}\mathbb{1} \tag{2.60}$$

where $\mathbb{1}$ denotes the identity tensor. The deformation gradient $\boldsymbol{F}_0$ results from the conventional displacement interpolation at the centroid if the element (de Souza Neto et al., 1996). Similarly to Equation 2.58, it can be split into deviatoric and hydrostatic components as follows:

$$\boldsymbol{F}_0 = (\boldsymbol{F}_0)_d (\boldsymbol{F}_0)_h \tag{2.61}$$

Finally, the modified deformation gradient $\bar{\boldsymbol{F}}$ can be defined as the composition of the deviatoric component of $\boldsymbol{F}$ with the hydrostatic component of $\boldsymbol{F}_0$, resulting in the following expression:

$$\bar{\boldsymbol{F}} \coloneqq \boldsymbol{F}_d (\boldsymbol{F}_0)_h = \left(\frac{\det(\boldsymbol{F}_0)}{J} \right)^{1/3} \boldsymbol{F} \tag{2.62}$$

Mixed formulation

The mixed formulation approach, initially introduced by Herrmann, 2012, has been adopted by several studies (Al Akhrass et al., 2014; Cervera et al., 2010; Taylor, 2000; Y. Zhang et al., 2017). Unlike the standard formulation, this method introduces additional nodal unknowns, such as stress, pressure, strain gradient, and volume variation.

When pressure (p) and volume variation (θ) are treated as additional unknowns, the strain tensor is enhanced as follows:

$$\tilde{\boldsymbol{\varepsilon}} = \boldsymbol{\varepsilon} + \boldsymbol{\varepsilon}' \tag{2.63}$$

where,

$$\boldsymbol{\varepsilon}' \approx \theta - \operatorname{trace}(\boldsymbol{\varepsilon}) \tag{2.64}$$

This modified strain tensor is then used in the constitutive law. The weak equality between θ and trace($\boldsymbol{\varepsilon}$) is enforced through the introduction of a Lagrange multiplier, p, which corresponds to the pressure.

By incorporating these additional variables, mixed formulations improve the stability and accuracy of numerical solutions, offering advantages in cases where standard formulations may struggle with issues such as volumetric locking or spurious oscillations. However, it is important to consider that the increasing the number of degrees of freedom can lead to higher computational costs.

Hybrid higher-order method

The Hybrid High-Order (HHO) method, introduced by Di Pietro and Ern, 2015 for linear elasticity and by Pietro et al., 2014 for diffusion problems, divides each element into two distinct components: the faces (the element boundaries, represented as line segments in 2D and surfaces in 3D) and the cell (the volume of the element excluding the faces). In contrast to traditional methods that rely on nodal unknowns (displacements $\{\boldsymbol{u}\}$), the HHO method employs face-based unknowns $\{\boldsymbol{u}\}_1$ and cell-based unknowns $\{\boldsymbol{u}\}_2$, facilitating a discontinuous displacement field.

This method enhances the strain operator $\boldsymbol{B}$ by incorporating an additional term $\boldsymbol{B}'$ as follows:

$$\boldsymbol{B}' : \tilde{\boldsymbol{B}}(\boldsymbol{u}_1, \boldsymbol{u}_2) = \boldsymbol{B}(\boldsymbol{u}_1) + \boldsymbol{B}'(\boldsymbol{u}_1 - \boldsymbol{u}_2) \tag{2.65}$$

where $\boldsymbol{B}$ concerns the unit cell and $\boldsymbol{B}'$ the faces. The weak enforcement of consistency between unknowns is achieved through a penalty term. The cell unknowns can be locally eliminated through a static condensation technique, significantly reducing the computational size by involving only the face unknowns in the formulation.

The HHO method effectively mitigates volumetric locking, enhancing stability. It supports general meshes, including non-conforming ones, and is dimension-independent. However, implementing the HHO method within existing finite element software presents challenges, as traditional formulations may not be applicable. Although it demonstrates potential in elastic-plastic and hyper-elastic contexts (Abbas et al., 2018; Abbas et al., 2019a; Abbas et al., 2019b), further investigations are required to assess its robustness in more complex scenarios.

2.4 Hydrogen embrittlement on steels

Hydrogen exhibits high solubility in a wide range of metals and alloys. It can diffuse over significant distances due to its high jump frequency between interstitial sites. Hydrogen can enter metals through cathodic charging or exposure to gaseous environments, and its presence, regardless of the method of entry, can lead to hydrogen embrittlement (HE).

This section examines the effects of hydrogen on pipeline steels. It then reviews the mechanisms of hydrogen embrittlement discussed in the literature and examines the numerical models used to represent this phenomenon.

2.4.1 Hydrogen effects on pipeline steels

The phenomenon of hydrogen embrittlement (HE) was first identified by Johnson and Thomson, 1875. Since then, it has been extensively studied using both experimental methods (Briottet et al., 2012; Depover and Verbeken, 2016; Feaugas and Delafosse, 2019; Madi et al., 2024; Robertson et al., 2015) and numerical simulations (Ahn et al., 2007; Depraetere et al., 2021; Lin et al., 2022; Lopes Pinto et al., 2023; Martínez-Pañeda et al., 2018) to gain a deeper understanding of how hydrogen affects the mechanical properties of steels.

On a macroscopic scale, HE in pipeline steels primarily results in substantial reductions in ductility and fracture toughness (Madi et al., 2024; Nanninga et al., 2012; T. T. Nguyen et al., 2020). In contrast, the impact of hydrogen on the yield stress and tensile strength of these steels is relatively minor (Briottet et al., 2012; Martin et al., 2020). The extent of embrittlement varies significantly across different steel grades and is highly dependent on testing conditions (Depover et al., 2014). Therefore, the reduction in ductility and fracture toughness due to hydrogen is not an inherent material property but is influenced by multiple test parameters (Gallon, 2021), including strain rate, hydrogen concentration, and other factors.

Studies have shown that slower strain rates result in increased levels of embrittlement (Briottet et al., 2012; Laureys et al., 2022; Trasatti et al., 2005). This effect is due to diffusion kinetics, as slower testing allows more time for hydrogen to penetrate and diffuse throughout the material, leading to greater embrittlement. Similarly, higher hydrogen concentrations, such as those achieved under elevated pressures in gaseous environments, cause greater degradation of ductility and toughness. However, the deterioration of mechanical properties increases with pressure only up to a certain threshold, beyond which further hydrogen embrittlement does not occur. Experimental evidence supporting this phenomenon is provided in studies by Briottet et al., 2012; Madi et al., 2024; Martin et al., 2020. Additionally, different microstructures can exhibit varying levels of hydrogen embrittlement, as they may affect the kinetics of hydrogen diffusion and trapping within the material.

2.4.2 Hydrogen embrittlement mechanisms

Hydrogen embrittlement refers to a variety of mechanisms that degrade material properties by introducing hydrogen atoms into its structure. Over the past few decades, numerous models elucidating different hydrogen embrittlement mechanisms have emerged. These models primarily revolve around the interactions between hydrogen and metallurgical heterogeneities. According to these models, hydrogen, along with possibly other solutes, tends to segregate within defects, consequently reducing their formation energies. Therefore, trapped hydrogen can decrease the energies for emission and mobility of dislocations, vacancies formation, and cohesion of interfaces, which may result in fracture modes with a strong contribution of plasticity and/or interface decohesion.

This section summarizes the main HE mechanisms presented in the literature: Hydrogen Enhanced Localized Plasticity (HELP) (Barnoush and Vehoff, 2010; Beachem, 1972; Ferreira et al., 1999), Hydrogen Enhanced Decohesion (HEDE) (Gerberich et al., 2013; Troiano, 2016), Adsorption-induced dislocation emission (AIDE) and Hydrogen Enhanced Strain-Induced Vacancy (HESIV) (Nagumo et al., 2001).

It is important to mention that these mechanisms may act simultaneously or independently, resulting in a deterioration of the mechanical properties of metals subjected to hydrogen embrittlement. Extensive research is required to fully understand the interaction between these mechanisms and to develop effective strategies to prevent hydrogen embrittlement.

Hydrogen Enhanced Localized Plasticity (HELP)

The concept of the Hydrogen Enhanced Localized Plasticity (HELP) mechanism was initially proposed by Beachem, 1972, based on fractographic observations. Subsequently, this theory gained further support from studies by Ferreira et al., 1999; Sofronis and McMeeking, 1989. This idea suggests that hydrogen-assisted cracking (HAC) is facilitated by solute hydrogen's ability to increase dislocation movement. Since hydrogen tends to accumulate near crack tips, due to hydrostatic stresses or hydrogen ingress, it enhances dislocation activity, leading to localized deformation near the crack tips.

In certain cases, reduced flow stresses have been observed in tensile tests conducted on specimens

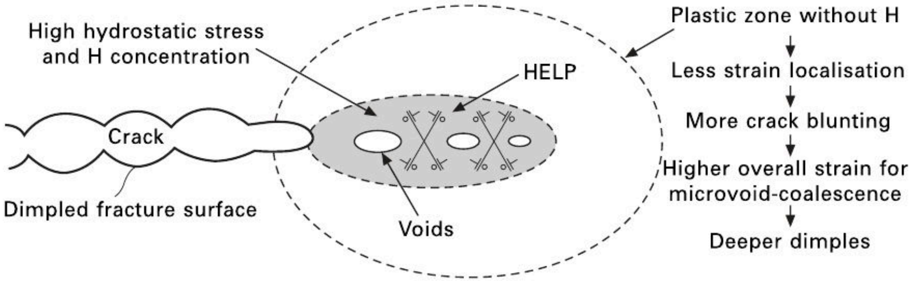

Figure 2.8: Schematic of the Hydrogen Enhanced Localized Plasticity (HELP) mechanism, involving a microvoid-coalescence process, with plasticity localized and facilitated in regions of high hydrogen concentrations (Lynch, 2011).

charged with hydrogen or subjected to very slow strain rates in hydrogen gas, compared to hydrogen-free specimens tested under atmospheric conditions (Beachem, 1972). However, the impact of hydrogen on stress-strain curves varies depending on numerous factors including material composition, purity, strain rate, temperature, and other environmental variables. It should be noted that in some scenarios, a hardening effect can be observed. The degree of softening, when present, tends to be minor (approximately 10% in hydrogen-charged aluminum and nickel specimens). Nonetheless, there are cases where significant softening is observed, particularly in hydrogen-charged pure iron single crystals subjected to low temperatures and low strain rates (Birnbaum and Sofronis, 1994; Ferreira et al., 1999; Hirth, 1980).

Hydrogen Enhanced Decohesion (HEDE)

The Hydrogen Enhanced Decohesion (HEDE) theory was originally proposed by Pfeil, 1926, who suggested that hydrogen reduces cohesion across cleavage planes and grain boundaries. Conventionally, decohesion is viewed as the sequential tensile separation of atoms when a critical Crack Tip Opening Displacement (CTOD) is reached. This critical distance is generally about half the interatomic spacing. However, the separation of atoms at crack tips is constrained by surrounding atoms, so the separation process could be more complex and involve incipient shear movement of atoms to reach the critical CTOD (Knott, 1994).

High hydrogen concentrations have been observed at grain boundaries and particle-matrix interfaces using a variety of techniques. Quantum mechanical calculations support the concept of weakening of interatomic bonds by hydrogen, leading to HEDE, especially when slip planes around crack tips are unfavorably aligned (Daw and Baskes, 1987; Hoagland and Heinisch, 1992). However, despite the theoretical support and indirect experimental evidence, obtaining direct evidence of HEDE remains challenging due to the lack of techniques capable of directly observing atomic-scale events at crack tips in bulk materials.

Adsorption-Induced Dislocation Emission (AIDE)

In the mechanism known as Adsorption-Induced Dislocation Emission (AIDE), the term “dislocation emission” refers to both the initiation and the subsequent movement of dislocations away from the crack tip. It is important to emphasize that the adsorption-driven nucleation phase is of particular importance. Once nucleated, dislocations can move away from the crack tip in response to applied stress. The nucleation phase involves the simultaneous development of a dislocation core and a surface

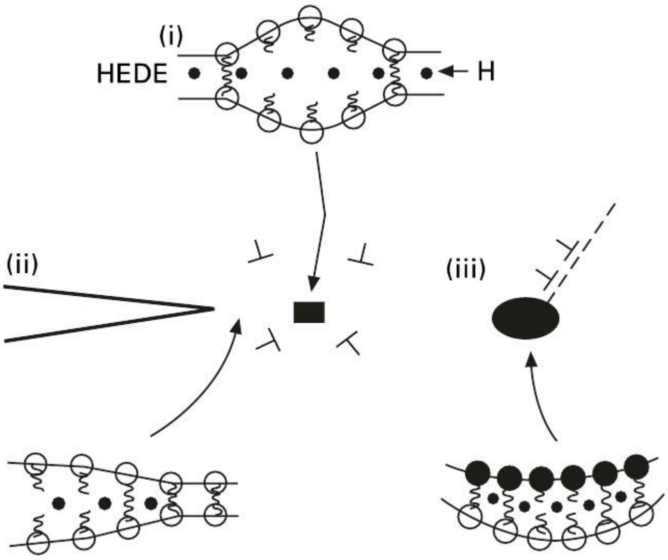

Figure 2.9: Illustration of the Hydrogen Enhanced Decohesion (HEDE) mechanism involves the tensile separation of atoms, attributed to the reduced interatomic bonds caused by (i) hydrogen within the lattice, (ii) absorbed hydrogen, and (iii) hydrogen present at particle-matrix interfaces (Lynch, 2011).

step through cooperative atomic shearing, involving the breaking and reforming of interatomic bonds over multiple atomic distances. The presence of "adsorbed" hydrogen thus weakens interatomic bonds and facilitates this process (Lynch, 1979).

In this model, crack growth under monotonically increasing stresses occurs not only by dislocation emission from crack tips but also from void nucleation and growth ahead of crack tips. Void nucleation and growth at slip-band intersections of second-phase particles, or other locations within the plastic zone ahead of cracks, occur because the stresses required for dislocation emission are sufficiently high, leading to significant dislocation activity in those regions. Void formation contributes to crack growth and also serves to re-sharpen crack tips, resulting in small crack-tip-opening angles. However, crack growth primarily occurs by dislocation emission from crack tips, as represented in Figure 2.10.

In this model, crack growth under monotonically increasing stresses is driven not only by dislocation emission from crack tips but also by void nucleation and growth ahead of the crack tips. Void nucleation and growth can occur at second-phase particles, slip band interfaces, or other locations within the plastic zone ahead of cracks. This happens because the stresses required for dislocation emission are high enough to induce general dislocation activity in these regions. Void formation contributes to crack growth and sharpens the crack tips, resulting in smaller crack tip opening angles. However, as illustrated in Figure 2.10, the primary mechanism of crack growth is still dislocation emission from the crack tips.

Hydrogen Enhanced Strain-Induced Vacancy (HESIV)

The Hydrogen Enhanced Strain-Induced Vacancy (HESIV) mechanism, a recent proposal based on experimental observations, still lacks theoretical support (Nagumo et al., 2001). It is based on the assumption that hydrogen in the material induces vacancy formation during plastic deformation. Consequently, the embrittlement of the metal results from an excessive accumulation of vacancies in the material rather than directly from the presence of hydrogen. This mechanism, illustrated in Figure 2.11, suggests that the damage associated with the presence of hydrogen is irreversible.

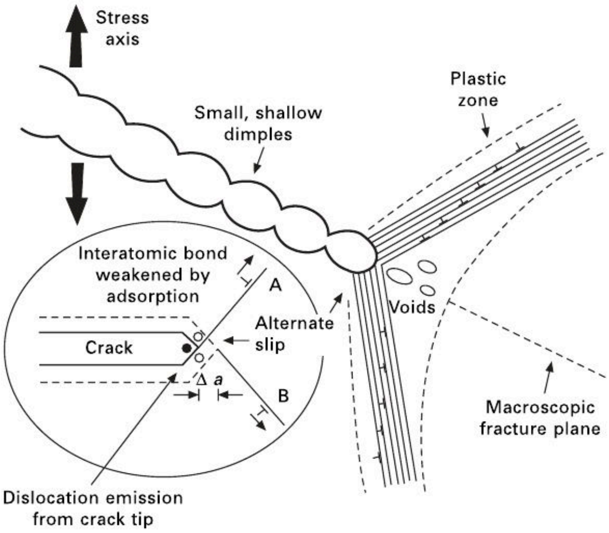

Figure 2.10: Representation of the Adsorption-Induced Dislocation Emission (AIDE) mechanism, which involves crack growth by alternate-slip (for transgranular paths) from crack tips, facilitating coalescence of cracks with voids formed in the plastic zone ahead of cracks (Lynch, 2011).

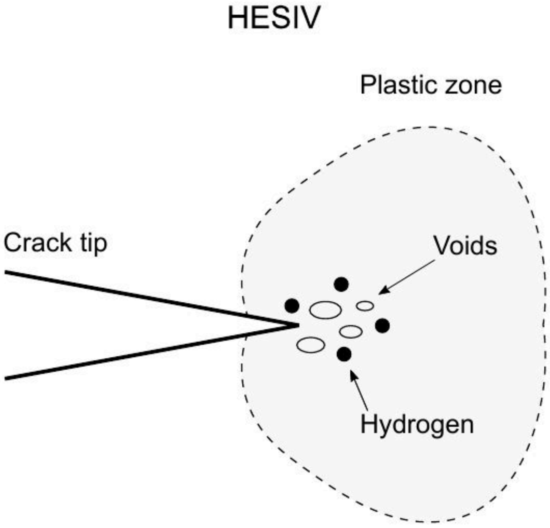

Figure 2.11: Schematic of the Hydrogen Enhanced Strain-Induced Vacancy (HESIV) mechanism: hydrogen induces vacancy formation during plastic deformation.

This model was recently utilized in the work of Yu et al., 2025, where a void-based hydrogen embrittlement (CVHE) predictive framework was developed to effectively capture ductile failure, hydrogen-induced loss of ductility, and, most importantly, the ductile-to-brittle transition. Consistently grounded in the void-mediated failure process, this model can be easily linked to the HESIV mechanism.

2.4.3 Hydrogen adsorption and absorption

The initial stage of hydrogen penetration into a material is adsorption, which occurs through physical and chemical interactions between hydrogen and the surface of the metal. Following adsorption, the absorbed hydrogen is then incorporated into the crystal lattice and diffuses throughout the material. These processes are primarily dependent on the charging mode, whether it is in an aqueous or gaseous form.

Gaseous environment

In a gaseous environment, hydrogen penetration into a material begins with physisorption of hydrogen molecules on the surface of the metal. This enables the formation of bonds with low activation energy values between the hydrogen molecules and the surface atoms. The next step is the dissociation of the hydrogen molecules, followed by chemisorption, which results in the formation of strong bonds between hydrogen atoms and metal atoms. The adsorption of hydrogen can be described by the following Equation 2.66 (Brass et al., 2000):

$$2M + H_2 \rightarrow 2MH_{\text{ads}} + Q \tag{2.66}$$

where H_{ads} is the adsorbed hydrogen on the surface of the metal M and Q is a quantity of heat, whose sign determines the exothermic or endothermic character of the reaction. Absorption corresponds to the reversible reaction where it occurs the transfer from the surface hydrogen atoms to the volume of the material, as shown by Equation 2.67.

$$MH_{\text{ads}} \rightleftharpoons MH_{\text{abs}} \tag{2.67}$$

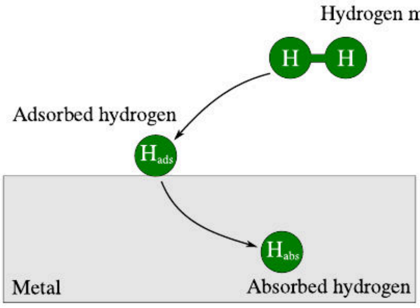

Figure 2.12: Schematic of the adsorption and absorption phenomenon for a gaseous environment.

Aqueous environments: cathodic charging

The penetration of hydrogen from an aqueous medium is characterized by anodic and cathodic reactions, which require the presence of electrolytes and electrodes. In a cathodic loading process, the material is immersed in a solution that generates hydrogen ions. The efficacy of these reactions is dependent on a variety of factors, including the nature of the medium, whether it is an acidic or basic environment.

- In an acidic environment:

$$H_3O^+ + e^- + M \rightarrow H_2O + MH_{\text{ads}} \tag{2.68}$$

- In a basic environment:

$$H_2O + e^- + M \rightarrow MH_{\text{ads}} + OH^- \tag{2.69}$$

The main distinction between adsorption in gas and liquid phases is that in the latter, the H_2 molecule does not dissociate on the metal surface as hydrogen exists in the solution as protons.

Hydrogen adsorption can be followed by two recombination mechanisms: a Heyrovsky reaction, in which an adsorbed hydrogen atom and a proton combine electrochemically to form H_2; or a Tafel reaction, in which two hydrogen atoms chemically combine to release a H_2 molecule (Laveissiere et al., 1991). The specific mechanisms occurring at the surface are influenced by various factors, such as the type and surface state of the metal, the solution's pH, the applied overvoltage, and the electrolyte's characteristics (Bockris et al., 1965; Liu et al., 2014; Newman and Shreir, 1969).

2.4.4 Hydrogen transport equations

The hydrogen transport model was initially proposed by Sofronis and McMeeking, 1989 and subsequently corrected by Krom et al., 1999, building upon the equilibrium theory proposed by Oriani, 1970. This model states that hydrogen can localize at either normal interstitial lattice sites (NILS), denoted by concentration C_L (Figure 2.13a), or trapping sites. Traps are considered isolated entities, forming no extended network. Consequently, hydrogen transport between trap sites results through the diffusion of lattice hydrogen. The model is capable of considering several trapping mechanisms ($i = 1, 2, \ldots, N$). The trapped hydrogen concentration for each mechanism is referred to as C_T^i (Figure 2.13b), where the total trapped concentration is: $C_T = \sum_i^N C_T^i$. Only the lattice concentration is able to diffuse and the total hydrogen concentration is expressed as $C = C_L + C_T$.

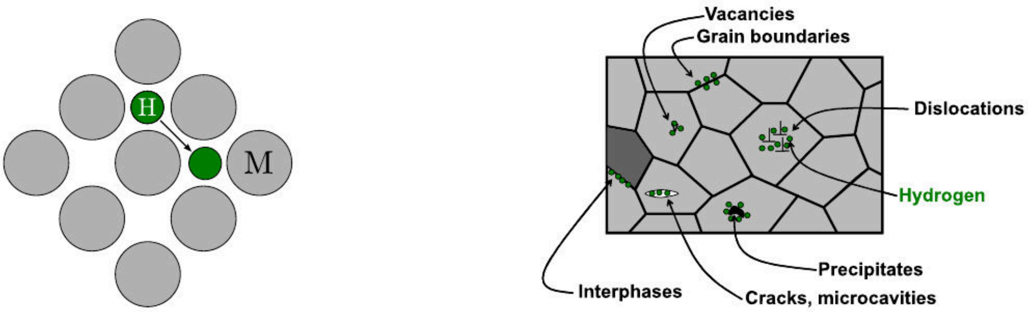

(a) Lattice hydrogen concentration (C_L).

(b) Trapped hydrogen concentration (C_T) (Moro, 2009).

Figure 2.13: Representation of the two possible hydrogen concentration types.

Following the principle of mass conservation, the rate of change of the total hydrogen concentration within a volume Ω is equal to the flux through a surface $\partial\Omega$:

$$\frac{d}{dt}\int_{\Omega}(C_L + C_T)\ d\Omega + \int_{\partial\Omega} \boldsymbol{J} \cdot \boldsymbol{n}\, dS = 0 \tag{2.70}$$

with $\boldsymbol{J}$ being the hydrogen flux and $\boldsymbol{n}$ the outward-pointing normal vector. The hydrogen flux can be defined as:

$$\boldsymbol{J} = -D_L \nabla C_L + \frac{D_L C_L V_H}{RT} \nabla p \tag{2.71}$$

where D_L is the diffusion coefficient, V_H is the partial molar volume of hydrogen, R is molar gas constant, p is the hydrostatic pressure and is calculated as $p = \frac{1}{3}\text{trace}(\boldsymbol{\sigma})$, and T is the absolute temperature. In regions subjected to tensile hydrostatic stress, the chemical potential of hydrogen decreases, leading to the generation of a hydrogen flux towards these areas to minimize the chemical potential gradient. Conversely, regions experiencing compressive hydrostatic stresses exhibit the opposite effect. The diffusion coefficient in solids at different temperatures is generally found to be well predicted by the Arrhenius equation:

$$D_L = D_0 \exp\left(-\frac{E_A}{RT}\right) \tag{2.72}$$

where D_0 (in m^2/s) is a constant and E_A (in kJ/mol) is the activation energy for diffusion. The hydrogen concentration at lattice sites, measured in hydrogen atoms per unit volume (H atoms/m^3), can be expressed as a function of the occupancy of the lattice (θ_L):

$$C_L = \beta N_L \theta_L \tag{2.73}$$

where β represents the number of lattice sites per host atom and N_L is the number of lattice atoms per unit volume, expressed as:

$$N_L = \frac{N_A}{V_M} \tag{2.74}$$

where N_A is Avogadro's number and V_M is the molar volume of the host lattice measured in units of volume per lattice mole. Similarly, the hydrogen concentration at trapping sites can be expressed as a function of the occupancy of trapping sites θ_T^i and the trap density N_T^i:

$$C_T^i = N_T^i \theta_T^i \tag{2.75}$$

The trap density for each trap type (N_T^i), expressed in m^{-3}, depends on the particular trapping site under consideration. In the case of traps such as grain boundaries or carbides, it is commonly assumed that the trap densities remain uniform through the material (Jemblie et al., 2017). However, when dislocations are regarded as trapping sites, the trap density varies and depends on the local accumulated plastic strain (κ), as dislocations increase with plastic strain (Sofronis and McMeeking, 1989).

The equilibrium between lattice and trapped hydrogen atoms can be expressed as (Oriani, 1970):

$$\frac{1-\theta_L}{\theta_L} \frac{\theta_T^i}{1-\theta_T^i} = K^i \quad \forall\, i \tag{2.76}$$

where K^i denotes the trap equilibrium constant, given by Equation 2.77:

$$K^i = \exp\left(\frac{W_B^i}{RT}\right) \tag{2.77}$$

where W_B^i represents the trap binding energy for each trap type. According to the literature, W_B^i exhibits a range of values from 15 to 110 kJ/mol (Drexler et al., 2019). The specific values of W_B^i are contingent upon the type of trap. Shallow traps, such as those found at dislocations or martensitic lath boundaries, typically exhibit low binding energies. Conversely, deep traps, often categorized as "quasi-irreversible" or "irreversible" traps, such as carbide interfaces or defects introduced into the microstructure during thermal processing (Drexler, Depover, et al., 2020) or severe plastic deformation (Drexler, Bergmann, et al., 2021; Drexler, Siegl, et al., 2020; Kholtobina et al., 2020), typically possess higher binding energies. Notably, these trapping sites retain hydrogen even following prolonged vacuum treatments at room temperature (Drexler, Vandewalle, et al., 2021). Figure 2.14 contains a representation of shallow and deep trapping sites.

It is assumed that $\theta_L \ll 1$, so that the Equation 2.76 can be rewritten as follows:

$$\theta_T^i = \frac{K^i \theta_L}{1 + K^i \theta_L} \tag{2.78}$$

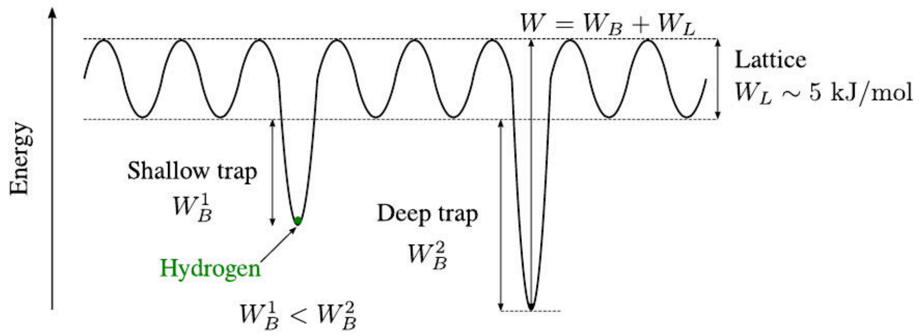

Figure 2.14: Schematic of shallow and deep hydrogen trapping sites. Deep traps have higher trap binding energies (W_B^i) than shallow traps.

Substituting Equation 2.78 into Equation 2.75, C_T^i can be expressed as:

$$C_T^i = N_T^i \frac{K^i \frac{C_L}{\beta N_L}}{1 + K^i \frac{C_L}{\beta N_L}} = N_T^i \frac{\mu^i C_L}{1 + \mu^i C_L} \qquad \text{with} \qquad \mu^i = \exp\left(\frac{W_B^i}{RT}\right)\frac{1}{N_L \beta} \tag{2.79}$$

Taking the temporal derivative of C_T^i, one gets:

$$\dot{C}_T^i = \frac{1}{N_T^i}\frac{dN_T^i}{d\kappa} C_T^i \dot{\kappa} + \frac{C_L N_T^i}{(1+\mu^i C_L)^2}\mu^{i\prime}\dot{T} + \frac{\mu^i N_T^i}{(1+\mu^i C_L)^2}\dot{C}_L \equiv \dot{h}_\kappa^i + \dot{h}_T^i + H_{C_L}^i \dot{C}_L \tag{2.80}$$

where,

$$\mu^{i\prime} = \frac{d\mu^i}{dT} = -\frac{W_B^i}{RT^2}\mu^i \tag{2.81}$$

For an isothermal case, $\dot{h}_T^i = 0$. Considering temperature variation is important in cases where temperature changes affect hydrogen trapping/detrapping kinetics, as well as hydrogen diffusion. The rate of trapped hydrogen concentration is then:

$$\dot{C}_T = \sum_i^N \dot{C}_T^i = \sum_i^N \dot{h}_\kappa^i + \sum_i^N \dot{h}_T^i + h^i \dot{C}_L \equiv \dot{h}_\kappa + \dot{h}_T + H_{C_L}\dot{C}_L \equiv \dot{h} + H_{C_L}\dot{C}_L \tag{2.82}$$

Following Sofronis and McMeeking, 1989, this allows defining an effective diffusion coefficient D_{eff}, expressed as:

$$D_{\text{eff}} = \frac{D_L}{1 + \sum_i^N \frac{C_T^i / C_L}{1 + \mu^i C_L}} \tag{2.83}$$

2.4.5 Modeling of hydrogen embrittlement

To simulate hydrogen embrittlement (HE), it is crucial to account for its detrimental effect on the mechanical properties of materials. The literature offers several models based on different approaches. One of these models proposes that hydrogen causes material softening, while other models that incorporate damage mechanisms suggest that hydrogen accelerates or increases the damage evolution of the material. The following section provides a comprehensive overview of the models that have been developed to represent HE and its deleterious effects.

Hydrogen induced softening

In the work of Birnbaum and Sofronis, 1994, they have argued that at the temperatures and strain rates at which hydrogen embrittlement is experimentally observed, hydrogen induces microscale material softening by enhancing dislocation mobility, which corresponds to the Hydrogen-Enhanced Localized Plasticity (HELP) mechanism. From a continuum perspective, this softening can be described by a local yield stress that decreases with increasing hydrogen concentration. It is important to note that "local flow stress" in this context refers to the intrinsic flow properties of a small volume of material at the microscale where hydrogen has accumulated due to stress and strain localization (Sofronis et al., 2001).

Based on microscopic studies of the effect of hydrogen on dislocation behavior in iron, Tabata and Birnbaum, 1983 determined the local flow stress of the material as a decreasing function of the hydrogen content in the material. The effect of hydrogen on the local flow stress σ_Y can be represented as follows (Sofronis et al., 2001):

$$\sigma_Y = \sigma_0^H H(\kappa) \tag{2.84}$$

where σ_0^H is the initial yield stress in the presence of hydrogen, which decreases with increasing hydrogen concentration, and $H(\kappa)$ is a hardening function dependent on the accumulated plastic strain κ. The equation 2.84 indicates that the effect of hydrogen on the local continuum yield stress is influenced by the initial yield stress, so it can be expressed as:

$$\sigma_0^H = \phi(C)\sigma_0 \tag{2.85}$$

where $\phi(C)$ is a decreasing function of the local total hydrogen concentration C (atH/atFe) and σ_0 is the initial yield stress in the absence of hydrogen. It is assumed that the local hydrogen concentration is sufficiently low that $C \ll 1$. Sofronis et al., 2001 proposed the following linear form for $\phi(C)$:

$$\phi(C) = 1 - (1 - \xi)C \tag{2.86}$$

where $\xi < 1$ is a material parameter. If $C = 1$, $\phi = \xi$ and $\sigma_0^H = \xi\sigma_0$ denote the ratio of the yield stress in the presence of hydrogen (σ_0^H) to that in the absence of hydrogen (σ_0), at the maximum hydrogen concentration of 1. Later, Ahn et al., 2007 proposed a modified version of the softening function:

$$\phi(C) = \begin{cases} 1 - (1 - \xi)\frac{C}{C_L^0}, & \phi(C) > \mu \\ \mu, & \phi(C) \leq \mu \end{cases} \tag{2.87}$$

where μ is the maximum reduction of the yield stress by hydrogen with $0 \leq \mu \leq 1$. This means that the hydrogen softening effect saturates at a certain hydrogen concentration level. C_L^0 is the hydrogen concentration in the unstressed lattice in equilibrium with hydrogen gas at 1 atm. However, Yu et al., 2018 argued that a linear softening could not lead to a shearing failure and for this reason, a sigmoidal softening law was proposed:

$$\phi(C) = 1 + \frac{\mu - 1}{1 + \exp[-k(C_H - C_{H,0})]} \tag{2.88}$$

where the total hydrogen concentration has been normalized $C_H = C_L + C_T/C_0^S$, with C_0^S being the concentration level at which hydrogen softening begins. For the simulations, Yu et al., 2018 considered $C_{H,0} = 1.15$ and $\mu = 0.5$ and evaluated the influence of k, which plays a role in the slope of the transition of the sigmoidal curve. Figure 2.15 contains a comparison between the linear and sigmoidal functions proposed in the literature.

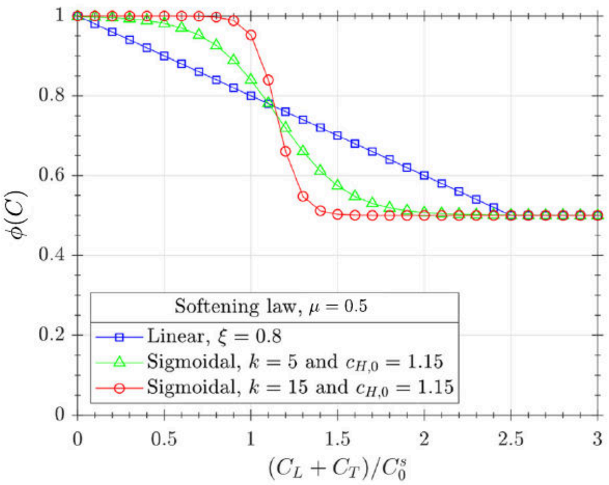

Figure 2.15: Comparison between a linear softening function and a sigmoidal function (Díaz et al., 2019).

Hydrogen-sensitive phase-field damage

Recently, the phase-field model has been used to simulate the degrading effects of hydrogen on metals. In the study by Martínez-Pañeda et al., 2018, hydrogen transport toward the fracture process zone and the resulting cracking are investigated using a coupled mechanical-diffusion-phase-field finite element model. To represent hydrogen embrittlement, the fracture surface energy is modeled as a function of the hydrogen content in the material. As previously mentioned in Section 2.2.3, in the phase field model, a fracture energy due to the formation of a crack can be expressed as:

$$\int_\Gamma G_c(\theta)\, dS \approx \int_\Omega G_c(\theta) \left(\frac{1}{2\ell}\phi^2 + \frac{\ell}{2}|\nabla\phi|^2 \right) dV \tag{2.89}$$

where G_c is the critical Griffith-type energy release rate, which is dependent on the hydrogen coverage θ.

To numerically capture the reduction in toughness caused by hydrogen, a degradation law can be formulated. G_c is assumed to decrease with increasing hydrogen content, consistent with the HEDE mechanism. In its most general form, the evolution of the critical fracture energy can be expressed as follows:

$$G_c(\theta) = f(\theta) G_c(0) \tag{2.90}$$

where $f(\theta)$ is a hydrogen degradation function. Martínez-Pañeda et al., 2018 defined this function linearly as:

$$\frac{G_c(\theta)}{G_c(0)} = 1 - \chi\theta \tag{2.91}$$

where χ is a damage coefficient that quantifies the reduction in fracture energy due to the presence of hydrogen. In the study of Lin et al., 2022, the hydrogen degrading function was defined as:

$$\frac{G_c(\theta)}{G_c(0)} = 1 - 1.04670\theta + 0.1687\theta^2 \tag{2.92}$$

Hydrogen-informed GTN model

In the study by Yu et al., 2019, a hydrogen-informed Gurson model was developed to account for the Hydrogen-Enhanced Localized Plasticity (HELP) mechanism. The parameters of the model were calibrated using a single void unit cell approach. Later, Depraetere et al., 2021 introduced an empirical hydrogen acceleration function that affects either void nucleation or growth. This model captures the hydrogen-induced loss of ductility by increasing the rate of void nucleation or growth, consistent with the HELP or HESIV mechanisms.

$$\dot{f}_{\text{nucleation}}(C) = \dot{f}_{\text{nucleation0}}(1 + k_n C) \tag{2.93}$$

$$\dot{f}_{\text{growth}}(C) = \dot{f}_{\text{growth0}}(1 + k_g C) \tag{2.94}$$

where $\dot{f}_{\text{nucleation0}}$ and $\dot{f}_{\text{growth0}}$ represent the void nucleation and growth rates in the absence of hydrogen, respectively. C denotes the total hydrogen concentration, while k_n and k_g are factors representing hydrogen-assisted degradation for void nucleation and growth, respectively. Lin et al., 2022 introduced a stress-controlled decohesion criterion based on the maximum principal stress, which serves as a threshold for decohesion and is incorporated into the Complete Gurson Model (CGM). This modification allows both void coalescence and decohesion criteria to coexist within the model, now referred to as CGM+. The actual failure mode in CGM+ is determined by the competition between void coalescence and decohesion.

Depraetere et al., 2023 proposed a new relation to account for hydrogen-assisted degradation, based on experimental observations of failure mechanisms. They found that void nucleation in hydrogen-charged samples occurred at significantly lower plastic strains. Consequently, the mean void nucleation parameter, ε_N, which serves as the scale parameter in the Weibull distribution, was adjusted to reflect the presence of hydrogen. Studies indicate that the degradation of mechanical properties increases rapidly with rising hydrogen concentration until reaching a saturation level (Laureys et al., 2022; Xu, 2012). Therefore, an exponentially decreasing degradation function depending on the total hydrogen concentration was proposed:

$$\boldsymbol{\varepsilon}_N = \boldsymbol{\varepsilon}_{N,0} - \zeta_1(1 - \exp(-\zeta_2 \times C_L)) \tag{2.95}$$

where $\varepsilon_{N,0}$ is the scale parameter in the absence of hydrogen and ζ_1 and ζ_2 are degradation parameters. The value $\varepsilon_{N,0} - \zeta_1$ defines the minimum possible value for ε_N, with ζ_2 governing the rate of degradation. Notably, the equation only accounts for the lattice hydrogen concentration C_L, excluding the effects of trapped hydrogen concentration C_T. This exclusion is due to the lack of consensus about whether degradation models should be based on only C_L or C (Depraetere et al., 2021).

2.5 Mechanical tests on sub-size specimens

To ensure the safety and reliability of hydrogen transportation systems, it is essential to perform mechanical tests to monitor the material's properties and maintain its integrity. Due to the limitations of thin-walled tubes used in gas transport, extracting standard-sized specimens is not feasible. Therefore, using sub-size specimens machined from extracted coupons directly from the transport installations offers a possible solution (Kumar et al., 2017; Madi et al., 2024).

The use of mini-toughness specimens has been developed in the nuclear industry to study the ductile-to-brittle transition in irradiated pressure vessels. This approach involves machining fracture toughness specimens, such as Compact Tension (CT) specimens, from the undeformed sections of broken standard Charpy specimens. Studies comparing sub-size and standard-size specimens have shown that sub-size specimens are suitable for measuring mechanical fracture properties, provided that scale effects are appropriately accounted for (M. Li et al., 2023; Miura and Soneda, 2012; Scibetta et al., 2002).

To be considered valid, a toughness test must be conducted on sufficiently large specimens. ASTM E1820 (*Standard Test Method for Measurement of Fracture Toughness*, 2023) imposes several requirements to ensure that the plastic zone is much smaller than the specimen's thickness and ligament size, indicating that the process zone is also considerably smaller than these dimensions. However, since hydrogen embrittlement reduces material toughness and results in a smaller plastic zone, meeting the standard size requirements becomes more achievable.

This section provides an overview of fracture toughness testing, including the standard requirements for validating these tests. Additionally, it addresses the impact of specimen size and thickness on toughness measurements. Understanding these factors is crucial, as they will be necessary to the numerical simulations of fracture toughness tests conducted in this study.

2.5.1 Fracture toughness tests

The toughness of materials is a fundamental mechanical property in the design and evaluation of structures, as it determines a material's ability to resist crack initiation and propagation under mechanical loadings. Unlike some other material properties, toughness is not intrinsic; it varies depending on factors such as specimen geometry, size, and thickness (M. Li et al., 2023; Ono et al., 2004). To ensure consistency and reliability in measuring fracture toughness, organizations like the American Society for Testing and Materials (ASTM) have established standardized testing procedures. This section introduces the two standards employed in this study to estimate fracture toughness:

- ASTM E399 – Standard Test Method for Linear-Elastic Plane-Strain Fracture Toughness of Metallic Materials
- ASTM E1820 – Standard Test Method for Measurement of Fracture Toughness

Other organizations, such as the British Standards Institution (BSI), the International Organization for Standardization (ISO), and the Japan Society of Mechanical Engineers (JSME), have also published standardized procedures for measuring fracture toughness. However, these methodologies will not be covered in this study. The following section provides a brief overview of the relevant ASTM standards for fracture toughness; for comprehensive information, please refer to the full guidelines.

ASTM E399 – Linear-Elastic Fracture Toughness

When a material exhibits linear elastic behavior prior to failure, with the plastic zone remaining small relative to the specimen dimensions, the critical value of the Mode I stress intensity factor, K_{IC}, can serve as an appropriate fracture parameter.

Small specimens or thin sections tend to fail under plane stress conditions, while thicker sections typically exhibit plane strain fracture (Anderson, 2017). This view is embedded in the ASTM E399 test method (*Standard Test Method for Linear-Elastic Plane-Strain Fracture Toughness K_{IC} of Metallic*

Materials, 2022). Over time, it has become widely accepted that toughness decreases with increasing specimen size until it stabilizes at a plateau. The specimen size requirements in ASTM E399 are designed to ensure that K_{IC} measurements accurately reflect this assumed plane-strain plateau.

The current version of ASTM E399 allows four specimen configurations: Compact Tension (CT), Bend Specimen (SEB), arc-shaped (Tension (AT) and Bend (AB)), and Disk-Shaped Compact Tension (DCT). For K_{IC} testing, specimens are typically machined with a width W that is twice the thickness B. These specimens are fatigue pre-cracked to achieve a crack length to width ratio a/W between 0.45 and 0.55. This design ensures that the critical dimensions a, B, and $W - a$ are approximately equal, optimizing material usage. The standard requires that each of these dimensions be significantly larger than the plastic zone to ensure accurate fracture toughness measurements. If the plastic zone at fracture is too large, it is not possible to obtain a valid K_{IC}.

Due to the strict size requirements, ASTM E399 recommends that a preliminary validity check should be performed to determine the correct sample dimensions. The criteria for valid K_{IC} measurements are as follows:

$$2.5\left(\frac{K_{IC}}{\sigma_{YS}}\right)^2 < W - a \tag{2.96}$$

where σ_{YS} corresponds to the 0.2% offset yield stress in tension and $W - a$ is the uncracked ligament size. To determine the necessary specimen dimensions, the user should first make an approximate estimate of the expected K_{IC} for the material. Since K_{IC} and σ_{YS} do not have the same dimensions, a length is necessary to link both, thus: $K_{IC} = \sqrt{\ell} \times \sigma_{YS}$. However, according to Anderson, 2017, even tough there is a tendency for toughness to decrease with increasing strength, there is not a unique relationship between K_{IC} and σ_{YS} in metals. For plane-strain conditions, the plastic zone size is defined as:

$$R_p = \frac{1}{3\pi}\left(\frac{K_I}{\sigma_{YS}}\right)^2 \tag{2.97}$$

thus, Equation 2.96 can be rewritten as:

$$R_p < \frac{1}{24}(W - a) \tag{2.98}$$

Thus, the plastic zone is much smaller than the ligament size. K_I is related to the applied force as follows:

$$K_I = \frac{F}{B\sqrt{W}} f(a/W) \tag{2.99}$$

where $f(a/W)$ is a dimensionless function of a/W. This function is given in a polynomial form in the E399 standard for the four specimen types. For instance, in the case of a compact tension (CT) specimen, $f(a/W)$ is defined as:

$$f(a/W) = \frac{2 + a/W}{(1 - a/W)^{3/2}}\left(0.886 + 4.64\frac{a}{W} - 13.32\left(\frac{a}{W}\right)^2 + 14.72\left(\frac{a}{W}\right)^3 - 5.6\left(\frac{a}{W}\right)^4\right) \tag{2.100}$$

The K_I value calculated from Equation 2.99 is considered a valid K_{IC} result only if all the validity criteria specified in the standard are satisfied. ASTM E399 is primarily designed for materials exhibiting brittle behavior or limited plasticity, requiring strict plane-strain conditions, achievable only for sufficiently thick specimens. For materials exhibiting ductile behavior and significant plastic deformation, a more recent standard, the ASTM E1820 (*Standard Test Method for Measurement of Fracture Toughness*, 2023), offers an alternative testing methodology.

ASTM E1820 – Nonlinear elasto-plastic fracture

The ASTM E1820 standard determines the J-integral, which characterizes the energy release rate. The E1820 applies the same test specimens as those specified in the E399 standard, but also for side-grooved specimens. This standard is designed for plane strain conditions, but is versatile enough to be applied to fully brittle, fully ductile, and transition regimes where some ductile crack growth may occur prior to brittle fracture.

The standard assumes that J-integral can be split into an elastic and plastic terms, as follows:

$$J = J_e + J_p \tag{2.101}$$

The elastic part of J is computed the elastic stress intensity:

$$J_e = K_I^2 \frac{(1-\nu^2)}{E} \tag{2.102}$$

where K_I was defined by Equation 2.99. If the specimen is side-grooved, K_I is modified as follows:

$$K_I = \frac{F}{\sqrt{BB_N W}} f(a/W) \tag{2.103}$$

where B_N corresponds to the net specimen thickness. J_p can be determined from the plastic area under the load-displacement curve:

$$J_p = \frac{\eta_p A_p}{B_N(W-a)} \tag{2.104}$$

For non side-grooved specimens, $B_N = B$. η_p is a dimensionless function of a/W that depends on the specimen geometry. A_p is the plastic area under the load-displacement curve (see Figure 2.16).

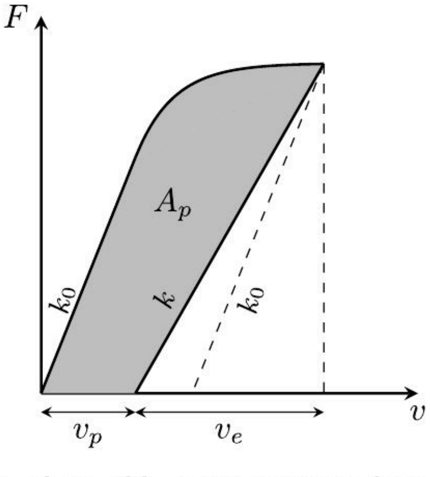

Figure 2.16: Plastic energy energy absorbed by a test specimen during a J_I test (Besson et al., 2023).

Equation 2.104 is valid only for a case where the crack does not propagate. The case of a propagating crack has an incremental procedure to compute J_p, based on the the work of Ernst et al., 1981:

$$J_p^i = \left[J_p^{i-1} + \frac{\eta_p^{i-1}}{b^{i-1} B_N} \left(A_p^i - A_p^{i-1} \right) \right] \times \left[1 + \frac{\gamma_p^{i-1}}{b^{i-1}} \left(a^i - a^{i-1} \right) \right] \tag{2.105}$$

where i is the loading step, b is the remaining ligament length, defined as $b = W - a$, and γ_p is dimensionless factor. For a CT specimen, the standard provides the following for η_p and γ_p:

$$\eta_p^{i-1} = 2 + 0.522\frac{b^{i-1}}{W} \tag{2.106}$$

$$\gamma_p^{i-1} = 1 + 0.76\frac{b^{i-1}}{W} \tag{2.107}$$

Thus, the J-integral can be computed if the crack length, a, is known. There are several methods for determining the crack advance, one of which is the "unloading compliance" method. In this technique, the specimen is partially unloaded to measure its compliance, as shown in Figure 2.17.

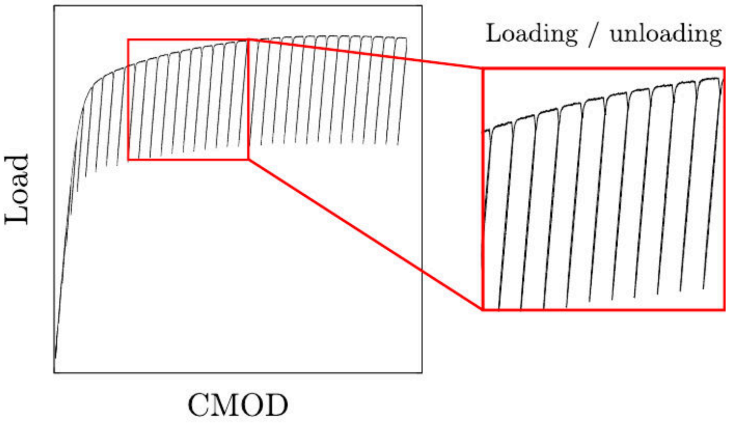

Figure 2.17: Experiment on a CT specimen from a pipeline steel with the unloading compliance method.

The change in compliance is difficult to detect, requiring highly accurate extensometers to measure the Crack Mouth Opening Displacement (CMOD). Since compliance is dependent on crack length, any variation in compliance can be linked to crack propagation. The compliance measured during partial discharge is calculated according to:

$$C_m = \frac{\Delta CMOD}{\Delta F} \tag{2.108}$$

Throughout the test, the specimen geometry changes, and the standard accounts for the rotation of specimens. The corrected compliance in the unrotated configuration is then evaluated as:

$$C_c = C_m \times c \tag{2.109}$$

where c is a correction factor that depends on the geometry of the specimen and the opening displacement. For a single-specimen test method using an elastic compliance technique on a Compact Tension (CT) specimen, with crack opening displacements measured along the load line, the crack size is determined as follows:

$$\frac{a_i}{W} = 1.000196 - 4.06319u + 11.242u^2 - 106.043u^3 + 464.335u^4 - 650.677u^5 \tag{2.110}$$

where

$$u = \frac{1}{1 + \sqrt{B_e E C_c^i}} \tag{2.111}$$

For specimens without side-grooves, $B_e = B_N = B$, otherwise it is defined as:

$$B_e = B - \frac{(B - B_N)^2}{B} \tag{2.112}$$

Calculating the J integral and the crack extension ($\Delta a = a - a_0$) gives the $J - \Delta a$ curve. An example of this curve is shown in Figure 2.18, which illustrates the importance of the rotation correction.

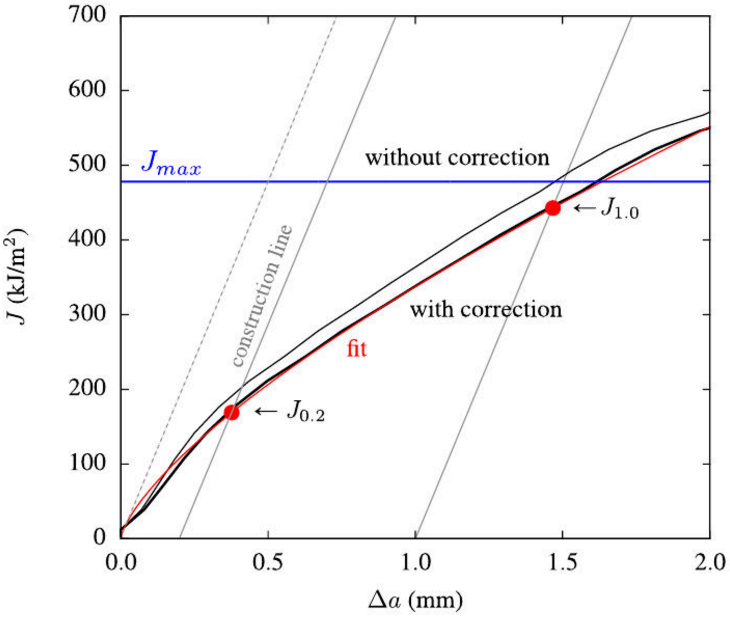

Figure 2.18: $J - \Delta a$ curve for a vintage X52 pipeline steel using a CT specimen with $B = 10$ mm and $b = 13$ mm (Adapted from Besson et al., 2023).

The standard provides the following expression to compute the blunting (offset) line:

$$J = 2\sigma_Y \Delta a \tag{2.113}$$

where σ_Y is the flow stress, defined as the average of the yield stress, σ_{YS}, and the ultimate tensile strength (UTS). The toughness of the material is characterized by $J_{0.2}$, which corresponds to a crack propagation of 0.2 mm. This value is determined by the intersection of the $J - \Delta a$ curve with the blunting line offset by 0.2 mm, as shown in Figure 2.18.

The experimental data for the $J - \Delta a$ curve can be fitted with a power law, as shown by the red curve in Figure 2.18. For the results to be considered valid, toughness tests must be performed on sufficiently large specimens. According to ASTM E1820, the maximum J-integral capacity that a specimen can achieve is determined as follows:

$$J_{max} \leq \frac{1}{10} \min\,(B, W - a_0)\sigma_Y \tag{2.114}$$

This is represented by the blue horizontal line in Figure 2.18. This criterion ensures that the fracture process zone is significantly smaller than both the specimen thickness and the ligament size. The size of the process zone can be approximated as J/σ_Y.

2.5.2 Thickness effects on toughness

Experimental observations reported by Barsom and Rolfe, 1987 indicate that the measured K_I values decrease with specimen thickness until they reach a plateau, where toughness becomes relatively insensitive to further increases in thickness (see Figure 2.19). This plateau in the toughness versus thickness trend is denoted by K_{Ic} and is referred to as "plane strain fracture toughness" (Steigerwald, 1969). The K_{Ic} value is considered a material property that is independent of specimen size.

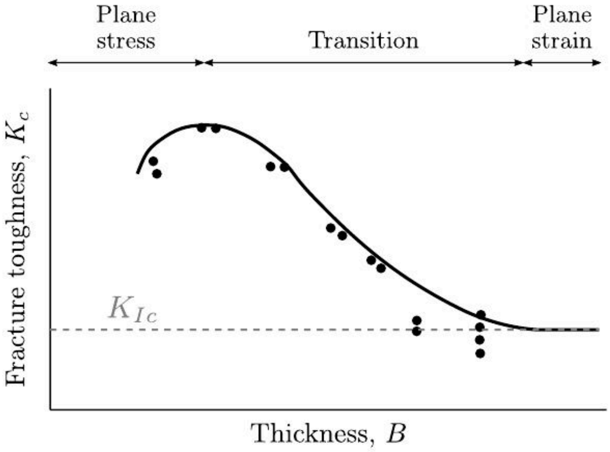

Figure 2.19: Variation of measured fracture toughness with specimen thickness. Adapted from Barsom and Rolfe, 1987.

This trend is attributed to the stress state of the specimen during testing. As the specimen thickness decreases, the stress state shifts to plane stress, causing the plastic zone at the crack tip to increase towards the specimen's side surfaces. This results in failure due to generalized plasticity, with increased energy consumption during plastic deformation, leading to higher toughness. Conversely, as specimen thickness increases, the stress state transitions to plane strain. In this regime, toughness initially decreases with increasing thickness until it levels off and reaches a plateau.

The decrease in apparent toughness with increasing specimen thickness, as shown in Figure 2.19, is typical of materials where crack propagation is ductile and characterized by microvoid coalescence (Anderson, 2017). In such materials, cracks tend to propagate preferentially in regions of high triaxiality, while growth in the outer regions of the specimen lags and occurs at a 45° angle to the applied load. This results in a fracture surface with a central flat region and 45° shear lips at the edges. Figure 2.20 depicts the fracture surfaces for different specimen thicknesses. For very thin plates or sheets, fractures generally exhibit a 45° shear mode. As the specimen thickness increases, a combination of shear and flat fracture modes is typically observed. The effect of thickness on apparent fracture toughness is attributed to the balance between flat and shear fracture regions. In very thick specimens, the flat fracture mode predominates, and further increases in thickness have minimal impact on the measured toughness.

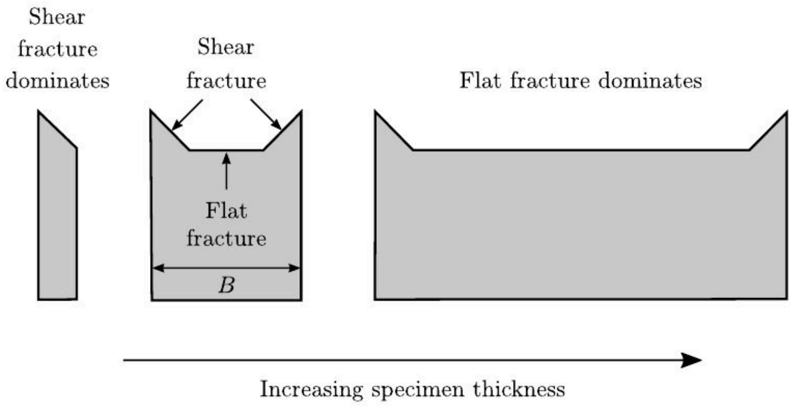

Figure 2.20: Effect of specimen thickness on fracture surface morphology for materials that exhibit ductile crack growth. Adapted from Anderson, 2017.

2.6 Conclusions

This chapter introduced the fundamentals of ductile failure, hydrogen embrittlement (HE) and fracture toughness testing, in order to address the study of *“Finite element models for the study of hydrogen embrittlement of steel structures”*. The focus was made on the modeling methods, necessary for the simulation of ductile failure and the coupling with hydrogen diffusion/trapping.

First, a description of damage models was given, focusing on void-driven ductile fracture, which is typically divided into three stages: void nucleation, void growth, and void coalescence. These models represent material degradation as a spatial field, commonly referred to as “damage field”. Damage models can be classified as either coupled or uncoupled. In coupled models, such as the Gurson-Tvergaard-Needleman (GTN) model, the damage field directly affects the material behavior, resulting in softening. However, the use of coupled models can cause damage to localize within narrow bands when critical damage levels are reached. This localization often results in pathological mesh dependency, where the solution fails to converge as the mesh is refined. To overcome this problem, regularized damage models are required.

Next, a literature review of various regularized damage models was presented. These models address the issue of mesh dependence by incorporating an internal length scale, which is a material property, into the formulation. In this study, the implicit gradient formulation was used to simulate ductile failure. It is important to note, however, that other regularized damage models could have been incorporated into the framework developed.

Subsequently, a literature review on hydrogen embrittlement (HE) in steels and its underlying mechanisms was conducted, focusing on the modeling methods available in the literature. The hydrogen transport equations were introduced to capture the coupling between diffusion and plasticity. Then, an overview of the models used to represent the degrading effects of hydrogen on the mechanical properties of steels was provided. These models are based on different approaches, including hydrogen-induced softening and hydrogen-enhanced damage.

Finally, the fundamentals of fracture toughness testing were discussed, including the specific requirements outlined in the ASTM E399 and E1820 standards. The impact of specimen thickness on fracture toughness was also addressed. These concepts are essential for simulating fracture toughness using sub-size specimens extracted from hydrogen transportation pipelines.

3

Study of hydrogen embrittlement in steels using pressurized disks

This chapter is based on a paper published in the International Journal of Hydrogen Energy (Santana et al., 2024).

Abstract Integrating hydrogen into natural gas pipelines introduces challenges related to Hydrogen Embrittlement (HE), demanding careful material selection and specialized testing methods. The Disk Pressure Test (DPT) is one such method, where a clamped disk is pressurized until failure. However, failures frequently occur at the clamping zone, complicating analysis. This study aims to develop new disk geometries that control the failure location while preserving the original test setup. Testing was conducted with two steel grades – a vintage X52 pipeline steel and a modern E355 modified steel suitable for pipeline applications – under helium and hydrogen at different pressure rise rates. Results indicate that the new geometries successfully shifted the failure location away from the clamping zones, proving their effectiveness. Hydrogen embrittlement was observed by comparing failure pressures under helium and hydrogen at varying pressure rise rates. Combining experimental testing with simulation, this study offers valuable insights into hydrogen embrittlement mechanisms.

Résumé L'intégration de l'hydrogène dans les gazoducs de gaz naturel présente des défis liés à la fragilisation par l'hydrogène (FPH), nécessitant une sélection minutieuse des matériaux et des méthodes d'essai spécialisées. Le test de pression sur disque (DPT) est l'une de ces méthodes, consistant à pressuriser un disque jusqu'à la rupture. Cependant, les ruptures surviennent fréquemment dans la zone de serrage, rendant l'analyse difficile. Cette étude vise à développer de nouvelles géométries de disque pour contrôler l'emplacement de la rupture tout en conservant le montage d'essai initial. Les essais ont été réalisés avec deux types d'acier – un acier de pipeline vintage X52 et un acier moderne E355 modifié, adapté aux applications de gazoducs – sous hélium et hydrogène à différents vitesses de pressurisation. Les résultats montrent que les nouvelles géométries permettent de déplacer efficacement la rupture en dehors des zones de serrage, prouvant leur efficacité. La fragilisation par l'hydrogène a été observée en comparant les pressions de rupture sous hélium et hydrogène à diverses vitesses de pressurisation. En combinant essais expérimentaux et simulations, cette étude offre des perspectives significatives sur les mécanismes de fragilisation par l'hydrogène.

Contents

3.1 Introduction

Transporting hydrogen gas through pipeline systems presents significant challenges. Hydrogen requires high pressures for storage and transportation, requiring materials that can withstand harsh conditions. In addition, the highly flammable nature of hydrogen poses risks related to potential pipeline leaks (Lu et al., 2024; W. Zhang and Zhao, 2024). Furthermore, due to hydrogen embrittlement (HE), it is essential to monitor the degradation of pipelines exposed to hydrogen throughout their service life to prevent catastrophic failures.

The need to monitor the mechanical properties of materials exposed to hydrogen has led to the development of various experimental methods (Madi et al., 2024). These methods facilitate the measurement of hydrogen embrittlement levels in materials such as steels and other metallic alloys. One such method is outlined in the ISO/FDIS 11114-4 standard (method A): the Disk Pressure Test (DPT) (International Organization for Standardization, 2023). The DPT involves pressurizing a clamped disk until it fails. This test is conducted under both hydrogen and helium (an inert gas), and the Hydrogen Embrittlement Index (HEI) is determined as the ratio of the rupture pressure in helium, $P_r(\mathrm{He})$, to that in hydrogen, $P_r(\mathrm{H_2})$, according to the following equation:

$$\mathrm{HEI} = \frac{P_r(\mathrm{He})}{P_r(\mathrm{H_2})} \tag{3.1}$$

The HEI estimated by the standard depends depends on the pressurization rate, so the test is conducted under several rates and the worst value is adopted.

The DPT was first implemented by Fidelle et al., 1974, who emphasized its advantages, including high sensitivity to hydrogen effects, rapid execution, and simplicity and relatively low cost in apparatus construction. Over the years, it has been successfully employed as an industrial qualification test for metallic alloys in hydrogen storage (Ardon et al., 2013; Briottet et al., 2012; Murali et al., 1980). However, the test has one notable limitation: the disk often fails in the clamping zone. This tendency of the disk to fail in the clamping zone is comparable to a tensile test in which the specimen fails either in the clamping area or at the fillets, which can invalidate the results because such failures occur outside the gauge length. In addition, failures in the standard disk specimen can sometimes initiate in the center, making the exact location of the failure unpredictable.

Simulating the DPT presents several numerical challenges, particularly due to the high plastic strain fields that develop in the fracture zone (Charles et al., 2019). The complex stress field in this region, combined with inherent experimental variations, can lead to significant scatter in the results, as reported in Briottet et al., 2012; Charles et al., 2019. Additionally, simulating HE is inherently challenging because it requires capturing the intricate coupling between mechanical deformation and hydrogen diffusion. The plastic behavior of materials strongly influences hydrogen diffusion, as hydrogen atoms tend to migrate towards regions of high hydrostatic stress. Conversely, hydrogen diffusion can significantly alter the mechanical properties of the material. These two mechanisms are deeply interdependent, and for accurate results, simulation models must account for both. Several authors have attempted to simulate the DPT and explore these complexities (Beghini et al., 1996; Charles et al., 2012; Charles et al., 2019; Looney et al., 2020; Lopes Pinto et al., 2023).

This chapter is organized as follows: Section 3.2 describes the materials analyzed in this study, including their mechanical characterization and the determination of the coefficients for the elasto-plastic constitutive law. Section 3.3 discusses the motivation for modifying the disk geometry and presents the new geometries developed for testing. Section 3.4 describes the DPT and examines factors such as specimen geometry, hydrogen effects, and pressurization rates. This section also includes an analysis of the fracture surfaces of broken specimens, which provides important insights for numerical modeling. Finally, section 3.5 outlines the numerical model developed to simulate hydrogen embrittlement and presents simulation results that evaluate various hydrogen trapping models to accurately reproduce experimental results. The chapter concludes by proposing a relationship between maximum principal stress and total hydrogen concentration in the fracture zone to characterize hydrogen-induced quasi-brittle failure.

This work was conducted in close collaboration with Luciano Meirelles Santana, a PhD student also involved in this project. Luciano was responsible for conducting all the mechanical tests and provided the experimental data used for the numerical simulations. This chapter focuses on the numerical aspect of the DPT. For details about the mechanical characterization and the tests, please refer to Santana et al., 2024.

3.2 Materials

In this study, two grades of steel were investigated: an X52 normalized steel (referred to as X52 steel), obtained from a vintage pipeline with a thickness of 7.92 mm, and a modern E355 modified steel (referred to as E355 mod. steel), supplied in the form of a hot-rolled tube with a thickness of 12.7 mm. Both materials are seamless, and their chemical compositions are detailed in Table 3.1.

Figures 3.1a and 3.1b show the microstructures of the X52 and E355 mod. steels, respectively. It reveals a ferritic matrix with elongated pearlite bands in the longitudinal and transverse directions. The

Wt.%	C	Mn	Si	Cr	Ni	Mo	S	P	Fe
X52	0.16	0.64	0.08	<0.03	0.05	<0.03	0.024	0.015	Bal.
E355 mod.	0.15	1.38	0.19	0.04	0.02	0.01	0.002	0.015	Bal.

Table 3.1: Chemical compositions of the X52 and E355 mod. steels.

X52 steel shows elongated inclusions aligned in both the L and T directions with a volume fraction of 0.27%. In contrast, the modified E355 mod. steel presents globular inclusions and has a lower volume fraction of 0.06%. The inclusions of both steels are also shown in Figure 3.1.

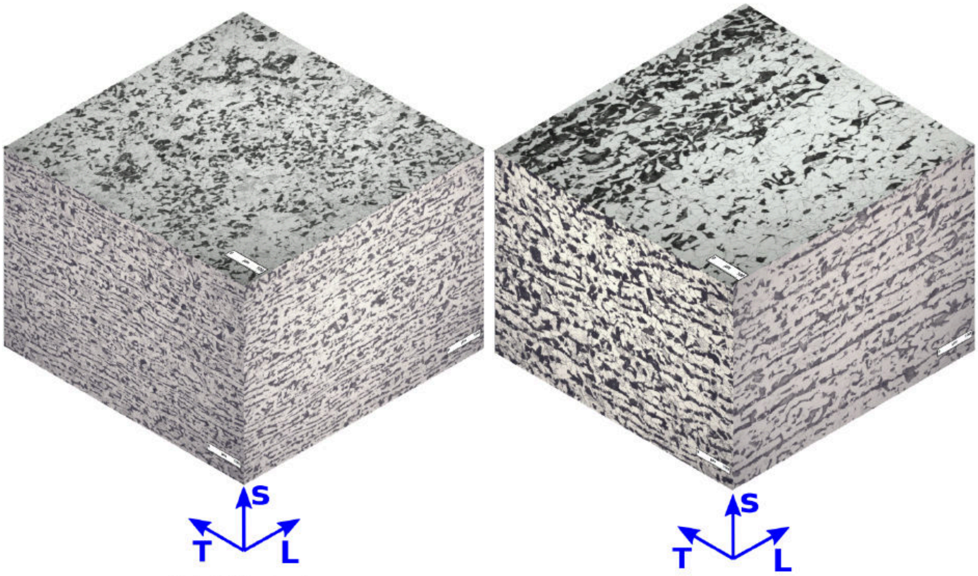

(a) X52 steel.

(b) E355 mod. steel.

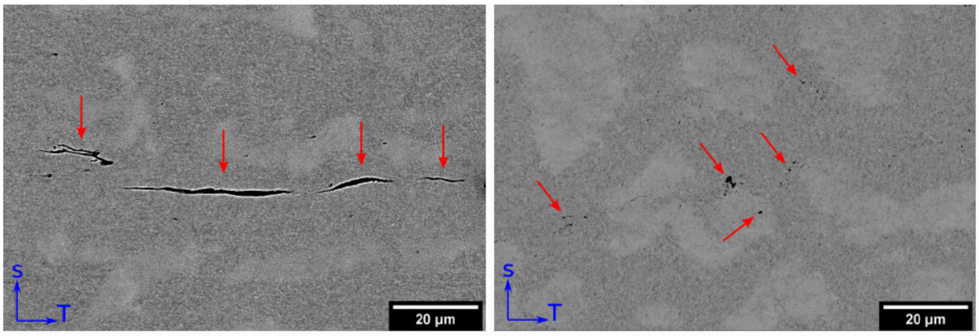

(c) X52 steel.

(d) E355 mod. steel.

Figure 3.1: Microstructure of (a) the X52 steel and (b) the E355 mod. steel, both consisting of ferrite and pearlite. Inclusions in the X52 steel are shown in (c), featuring globular inclusions. Inclusions in the E355 mod. steel are depicted in (d), featuring elongated inclusions.

3.2.1 Mechanical characterization

Tensile tests were conducted using smooth axisymmetric specimens with a diameter, Φ_0, of 4 mm and gauge length, L_0, of 20 mm. These specimens were extracted from the longitudinal direction of the tubes. The specimen's geometry is illustrated in Figure 3.2.

The tests were conducted at different strain rates: 5×10^{-4}, 1×10^{-5}, and 1×10^{-6} s^{-1} to evaluate the

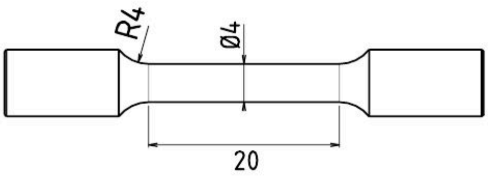

Figure 3.2: Geometry of the tensile specimen (in mm).

strain rate dependence of the material properties. During the experiments, two digital cameras captured images, enabling the calculation of radial strain ($\Delta\Phi/\Phi_0$) throughout the tests, both in the thickness direction of the tube (S-direction – $\Delta\Phi_S/\Phi_0$) and in the transverse direction (T-direction – $\Delta\Phi_\perp/\Phi_0$). This technique was applied to characterize the anisotropic elastoplastic behavior of the two steel grades. For more details on the methodology, refer to previous studies Madi et al., 2024; Shokeir et al., 2022.

The results of the tensile tests are shown in Figure 3.3, which presents the $F/S_0 - \Delta\Phi/\Phi_0$ curves for both the X52 and E355 mod. steels. Here, F represents the applied force, and S_0 is the initial cross-sectional area. The X52 steel exhibited different radial deformations in the thickness and transverse directions. Thus, the equivalent radial deformation, $\Delta\Phi_{\text{eq}}/\Phi_0$, is also plotted. $\Delta\Phi_{\text{eq}}$ can be calculated using the following equation:

$$\Delta\Phi_{\text{eq}} = \Phi_0 - \sqrt{(\Phi_0 - \Delta\Phi_\perp)(\Phi_0 - \Delta\Phi_S)} \tag{3.2}$$

3.2.2 Elasto-plastic behavior

The coefficients of the constitutive law for X52 and E355 mod. steels were determined using optimization algorithms implemented in Z-set[1], a finite element software developed by Mines Paris and Onera, the French aerospace laboratory. The materials are modeled within the framework of von Mises plasticity with isotropic hardening. Thus, the yield surface is defined as:

$$\Phi = \sigma_{\text{eq}} - \sigma_F(\kappa) \tag{3.3}$$

where σ_{eq} is the von Mises equivalent stress and $\sigma_F(\kappa)$ is the flow stress, which depends on the accumulated plastic strain, κ. The flow stress is expressed as:

$$\sigma_F(\kappa) = \max(\sigma_L, \sigma_0 + Q_1(1 - \exp(-b_1\kappa)) + Q_2(1 - \exp(-b_2\kappa)) + H\kappa) \tag{3.4}$$

where σ_L represents the Lüders stress, which can be experimentally identified from the tensile curves as the plateau that appears at the onset of yielding. σ_L is fixed at 395 MPa for the X52 steel and at 325 MPa for the E355 mod. steel. The yield stress in the absence of a plateau is denoted by σ_0. The parameters Q_1, b_1, Q_2, b_2, and H characterize the evolution of plastic hardening. Based on experimental observations, the materials exhibit slight rate dependency. In such cases, the plastic strain rate is expressed as:

$$\dot{\kappa} = \dot{\kappa}_0 \left\langle \frac{\sigma_{\text{eq}} - \sigma_F(\kappa)}{K} \right\rangle^n \tag{3.5}$$

In this expression, $\dot{\kappa}_0$, K, and n are coefficients that describe the viscoplastic properties of the material. These coefficients were initially calibrated for E355 mod. steel. However, due to the considerable variability and scatter in the experimental data for X52 steel, and for the sake of simplicity, the same

---

[1] http://www.zset-software.com/

coefficients were applied to both steels.

The various model parameters were optimized by minimizing the difference between the experimental and numerical $F/S_0 - \Delta\Phi/\Phi_0$ curves. This approach allowed for the successful fitting of the hardening law beyond the necking point and up to just before crack initiation. However, accurately capturing the development of necking requires finite element simulations of the tensile specimen with a finite strain formulation, as detailed in Shokeir et al., 2022. The simulations employed axisymmetric elements, and for the anisotropic X52 steel, $\Delta\Phi_{\mathrm{eq}}/\Phi_0$ was utilized.

The coefficients determined for both steels are listed in Table 3.2 and were applied to simulations across multiple strain rates ($5{\times}10^{-4}$, $1{\times}10^{-5}$, and $1{\times}10^{-6}$ s^{-1}). Figure 3.3 shows a comparison of the numerical and experimental results. For clarity, the curve for the $1{\times}10^{-5}$ s^{-1} strain rate was omitted, as it closely matched the results at $1{\times}10^{-6}$ s^{-1}. For both steels, Poisson's ratio and Young's modulus were set to 0.3 and 200 GPa, respectively.

	σ_0 (MPa)	Q_1 (MPa)	b_1 (–)	Q_2 (MPa)	b_2 (–)	H (MPa)	$\dot{\kappa}_0$ (s^{-1})	K (MPa)	n (–)
X52	269	191	41.45	358	3.15	10.23	1	213	4.43
E355 mod.	273	214	19.29	141	2.75	148			

Table 3.2: Coefficients of the elasto-visco-plastic constitutive law for the X52 and E355 mod. steels.

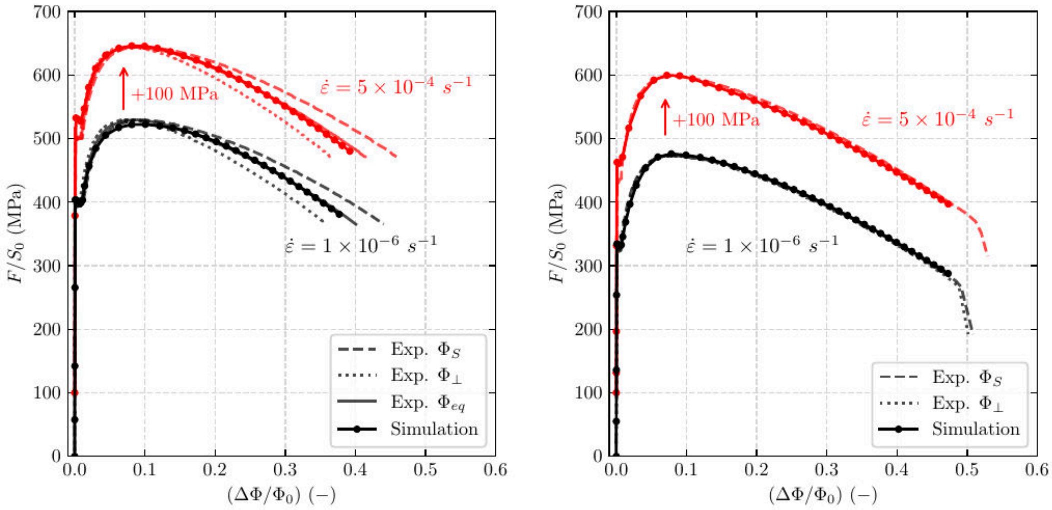

(a) X52 steel.

(b) E355 mod. steel.

Figure 3.3: Tensile tests performed for both steels using specimens extracted along the longitudinal direction. The curves display the nominal stress (F/S_0) against the radial deformation in the thickness direction (Φ_S) and in the perpendicular direction ($\Phi_\perp$) for the experimental data and the numerical results. Tests conducted under strain rates of $1{\times}10^{-6}$ and $5{\times}10^{-4}$ s^{-1}. The curves of the strain rate of $5{\times}10^{-4}$ s^{-1} where shifted by 100 MPa for clarity.

Table 3.3 compares the experimental and simulated Ultimate Tensile Stress (UTS) values for the X52 and E355 mod. steels across various strain rates. As previously mentioned, both steels show a slight rate dependence, with higher stress values observed at increased strain rates. The simulations align well with the experimental data in all cases.

	5×10^{-4} (s^{-1})		1×10^{-5} (s^{-1})		1×10^{-6} (s^{-1})	
	Experiment	Simulation	Experiment	Simulation	Experiment	Simulation
X52	544	546	527	528	530	523
E355 mod.	498	500	482	481	475	476

Table 3.3: Experimental and simulated Ultimate Tensile Stresses (in MPa) for the X52 and E355 mod. steels for three different strain rates.

3.3 Geometry optimization

As specified in the ISO 11114 standard International Organization for Standardization, 2023, the Disk Pressure Test (DPT) requires a disk specimen with a diameter of 58mm and a thickness of 0.75mm, as shown in Figure 3.4. However, this standard geometry often experiences failure in the clamping zone, complicating the analysis of the test results. To evaluate plastic localization, finite element (FE) simulations were performed using an elasto-plastic material model. The simulations used axisymmetric meshes and assumed frictionless contact between the disk specimens and the indentor. Pressure was applied to the lower part of the specimen at a constant linear rate ($\dot{P}_a$). The boundary conditions used in the model are shown in Figure 3.5. The simulation results, shown in Figure 3.6, show that the accumulated plastic strain, κ, is highest in the center and in the clamping zone, precisely the two areas where failure occurs.

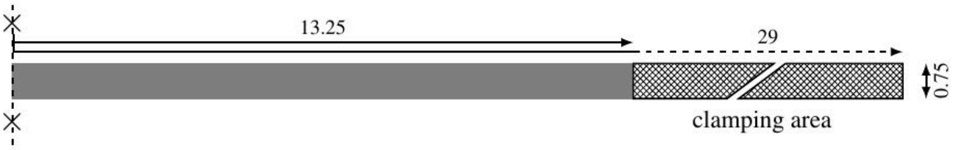

Figure 3.4: Geometry of standard disk specimen (in mm).

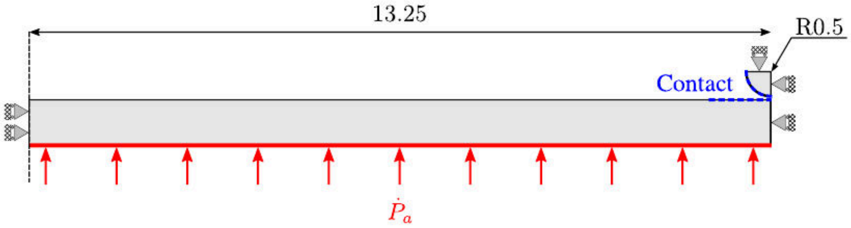

Figure 3.5: Boundary conditions applied to the standard specimen for the simulations.

To ensure that fracture occurs away from the clamping zone, two alternative geometries were introduced in this study: a cup-shaped specimen and a notched disk. The cup geometry consists of a 3 mm thick disk with a truncated spherical cup machined in the center. As shown in Figure 3.7, the central region reaches a minimum thickness of 0.75 mm. The dimensions of R and ℓ were optimized using elasto-plastic finite element simulations to ensure that failure occurs at the center of the specimen. Considering $R = 15$ mm and $\ell = 4$ mm yields the numerical results shown in Figure 3.8, which successfully predicts failure at the center of the specimen.

The notched disk specimen has a thicker disk (2 mm) with an axisymmetric semicircular notch with a radius of 1.25 mm, ensuring a minimum thickness of 0.75mm at the root of the notch, as required by the standard. This geometry is shown in Figure 3.9. Similar to the cup-shaped specimen, the notch

Figure 3.6: Accumulated plastic strain (κ) field in the standard disk specimen. Its maximum values correspond to the failure location, which generally takes place at the clamping zone.

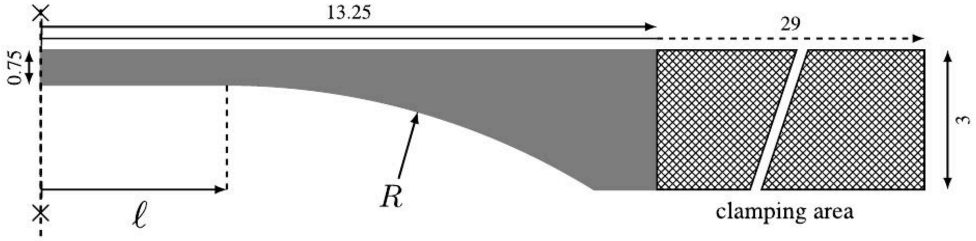

Figure 3.7: Geometry of cup disk specimen (in mm).

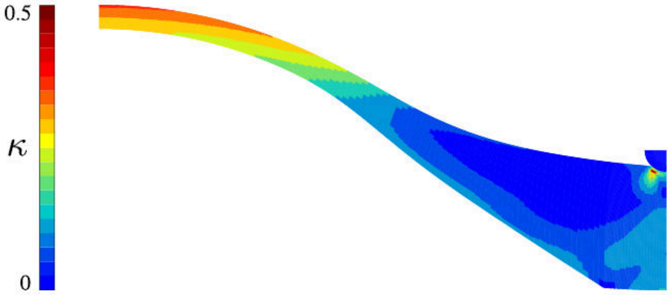

Figure 3.8: Accumulated plastic strain (κ) field in the standard disk specimen. The failure zone is displaced to the center of the disk.

geometry was optimized by adjusting the distance from the center of the disk to the center of the notch (R'). The goal for this specimen was to concentrate the plastic deformation at the notch root, which was achieved with $R' = 10.25$ mm. The numerical simulation results for this geometry are shown in Figure 3.10.

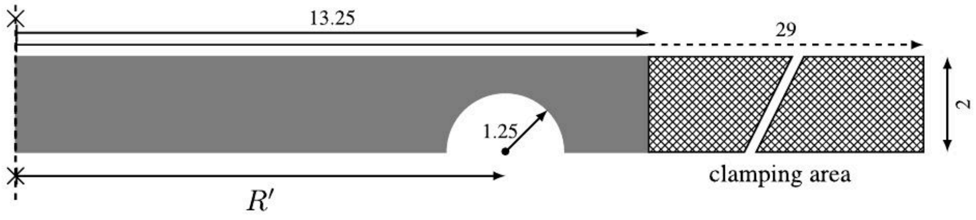

Figure 3.9: Geometry of notched disk specimen (in mm).

All the specimens have a nominal minimum thickness of 0.75 mm. The three disk geometries (Figure 3.11) were later employed for Disk Pressure Test (DPT).

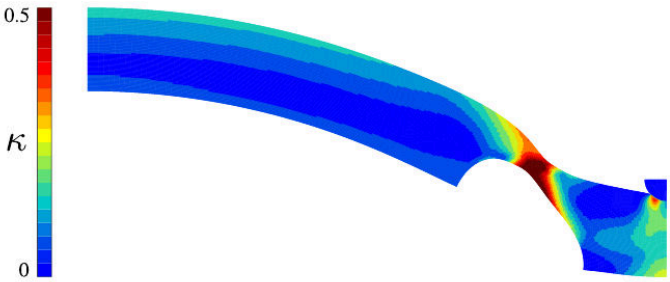

Figure 3.10: Accumulated plastic strain (κ) field in the notched disk specimen. The failure zone is displaced to the root of the notch.

Figure 3.11: Standard, cup and notched disk specimens, respectively.

3.4 Tests on pressurized disks

After machining and treating the new geometries, they were selected based on standard specifications for roughness and flatness. The specimens were then tested using a dedicated setup, as shown in Figure 3.12. A Linear Variable Differential Transformer (LVDT) was positioned at the discharge port to measure displacement at the center of the specimen during testing. The gas flow was manually regulated to achieve the desired pressure rise rate ($\dot{P}_a$).

The tests were performed using either helium or hydrogen, until the specimen either failed or began leaking. A total of 46 tests were conducted, applying four nominal Pressure Rise Rates ($\dot{P}_a$): 0.025, 0.250, 2.500, and 25.00 MPa/min. However, precise control of the pressurization rate proved difficult due to manual adjustment via a valve. As a result, the actual pressure rise rates during testing ranged from 0.025 MPa/min to 35 MPa/min. The full set of test parameters is detailed in Appendix A.

The rupture pressure was measured for both helium (P_r(He)) and hydrogen ($P_r(\mathrm{H}_2)$). In compliance with the ISO 11114 standard, the rupture pressure must be adjusted to account for deviations from the "ideal value", which may arise due to thickness variations. Consequently, the corrected rupture pressure (P_r') is determined using the following equation:

$$P_r' = P_r \frac{0.75}{e_m} \tag{3.6}$$

where P_r' represents the rupture-corrected pressure, while P_r denotes the measured rupture pressure. The value 0.75 mm corresponds to the minimum thickness specified by the standard. The term e_m refers to the average measured thickness of the sample, also in millimeters. For cup specimens, e_m is measured at the center, whereas for notched specimens, it is measured at the root of the notch.

Table 3.5 provides a summary of the experimental results from this study. It details the average, minimum and maximum P_r' values for both helium and hydrogen gases for the three specimen geometries and two materials. The average P_r' for helium is slightly higher in E355 mod. steel compared to X52

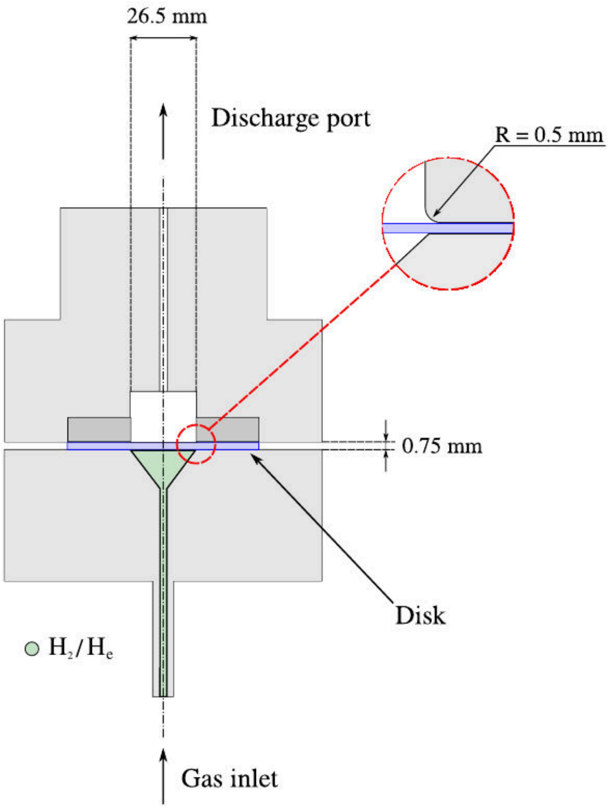

Figure 3.12: Illustration of the machine set-up used for the Disk Pressure Test (DPT).

steel. The range between the minimum and maximum P_r' values reflects the typical dispersion observed in the DPT. For a comprehensive view of all P_r' values obtained, see Appendix A.

3.4.1 Effect of specimen geometry (under helium)

Figure 3.13 shows the numerical and experimental results for the three specimen geometries subjected to helium charging at a nominal rate of 0.25 MPa/min for both steels. The tests were simulated using the elasto-plastic model described in Section 3.2.2. Details on the displacement and pressure boundary conditions are provided in Section 3.3. The purpose of the simulation is the validation of the test results and their interpretation.

A comparison of the displacement-pressure curves shows that thicker specimens – specifically, notched specimens with a 2 mm thickness and cup disks with a 3 mm thickness – exhibit a longer linear displacement-pressure behavior compared to standard specimens. This linear section of the curve represents a phase during testing where the failure zone of the specimens remains elastic, as confirmed by the simulations. Additionally, it is noted that P_r' values for both standard and notched disks fall within the same range (40–50 MPa) for both materials. In contrast, P_r' values for cup disks are consistently higher, around 70 MPa, for both materials.

The displacement at failure is also noticeable across the different specimen types. The standard disk, having lower stiffness compared to the thicker specimens, shows a greater displacement at rupture, typically between 6 and 8 mm. In contrast, the notched disk displays a smaller displacement at rupture, ranging from 3 to 4 mm. The cup disk exhibits an intermediate displacement at rupture, falling between 4 and 6 mm.

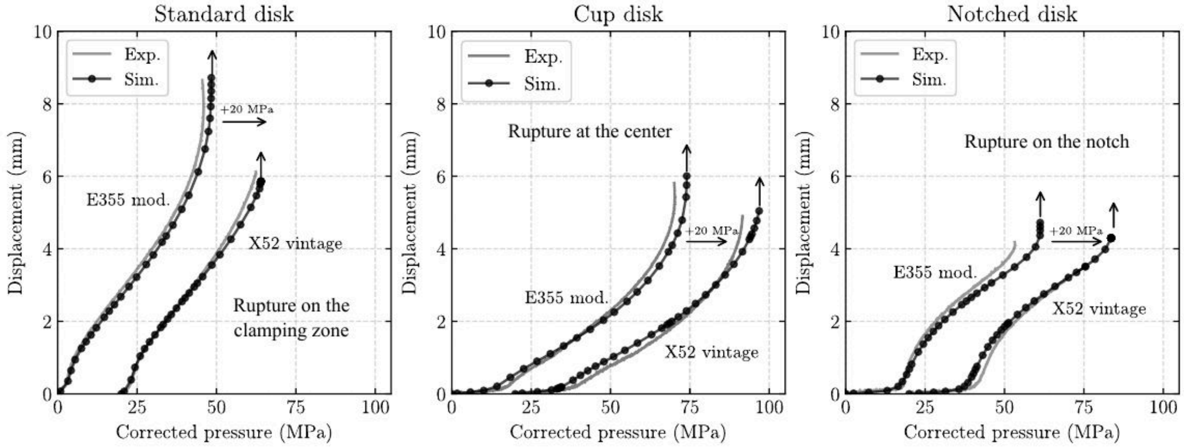

Figure 3.13: Simulation and experimental results for the deflection at the center of the disk against the corrected gas pressure for the three geometries (standard, cup, and notched) for the two steel alloys (E355 mod. and X52) tested under helium for a pressure rate of 0.25 MPa/min. The pressure in the case of the X52 steel is shifted by 20 MPa for clarity.

The P_r' values for each type of disk were found to be within a similar range for both steels. Notably, the displacement at rupture was higher for E355 mod. steel, which is consistent with the mechanical characterization from tensile tests, where E355 mod. steel exhibited greater ductility compared to X52 steel. Although the simulations do not account for damage evolution, they can accurately predict the failure point – defined as the point where pressure can no longer be increased due to the reduction in disk thickness, which represents a limit load condition. The predicted failure points, marked by vertical arrows in Figure 3.13, closely align with the experimental results. This agreement suggests that disk failure is primarily driven by plasticity and occurs under a limit load scenario.

It is also noteworthy that fractures consistently occurred at the center of the cup disks. In the notched specimens, fractures always occurred at the notch, confirming that failure took place at the area with the smallest cross-section, as intended. By contrast, in standard disk specimens, fractures primarily occurred in the clamping zone, though in some cases involving the highly ductile E355 mod. steel, fractures were also observed at the center of the disk. Figure 3.14 shows the disks after failure, where the fracture location can be observed.

Figure 3.14: Standard, cup and notched disk specimens after failure, respectively.

Simulations were conducted on both cup and notched specimens, with pressure applied to the flat side. The results indicated that, in both cases, the highest plastic strain occurred on the side opposite to where pressure was applied (Figure 3.15). It was then reasoned that to obtain an optimal HE sensitivity, the most effective approach is to induce the maximum plastic strain in a region exposed to H_2.

To investigate how the surface of pressure application affects the pressure-displacement response, an experimental test was performed under helium on X52 steel, using a notched disk with pressure

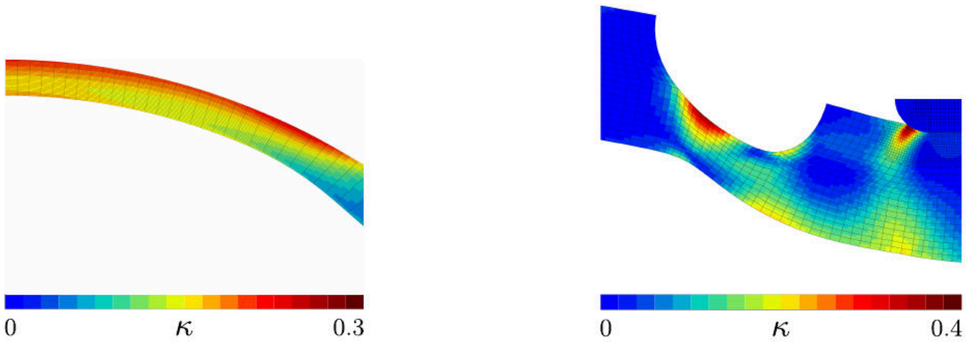

(a) Cup specimen.

(b) Notched specimen.

Figure 3.15: Simulation of cup and notched disks with pressure applied to the flat side of the specimen. The zoomed-in views highlight the failure zones, located at the center for the cup specimen and at the notch for the notched specimen. The results show that, in both cases, the highest plastic strain (κ) occurred on the side opposite to the gas exposure.

applied to the flat side. No test applying pressure to the flat side of the cup specimen was performed. Figure 3.16 compares the numerical and experimental pressure-displacement curves for two notched disk configurations (with pressure applied to either the notched or flat side). The results reveal similar overall behavior for both configurations, although the displacement at the disk's center is greater when pressure is applied to the notched side.

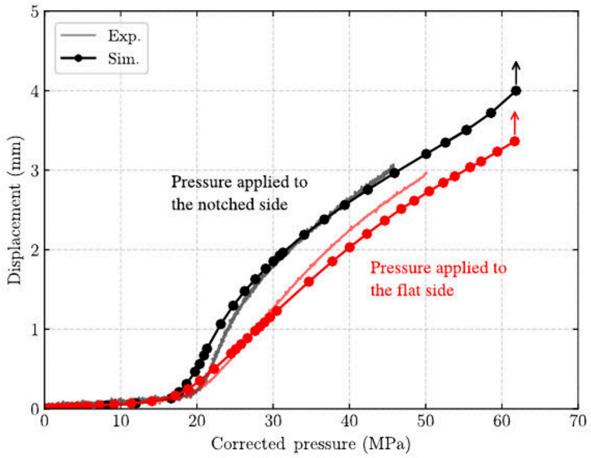

Figure 3.16: Comparison of numerical and experimental pressure-displacement curves for two notched disk configurations in X52 steel, with pressure applied to either the notched or flat side. Both cases are at a pressurization rate of $\dot{P} = 0.25$ MPa/min.

Figure 3.17 presents a Scanning Electron Microscopy (SEM) image of the fracture surface of an inverted notched disk. In Figure 3.17a, the flat side, which was exposed to H_2, displays a brittle appearance, while the outer side, exposed to air, exhibits a ductile tearing pattern. The region highlighted by the red square in Figure 3.17a is shown at higher magnification in Figure 3.17b, where detailed features of quasi-cleavage can be observed.

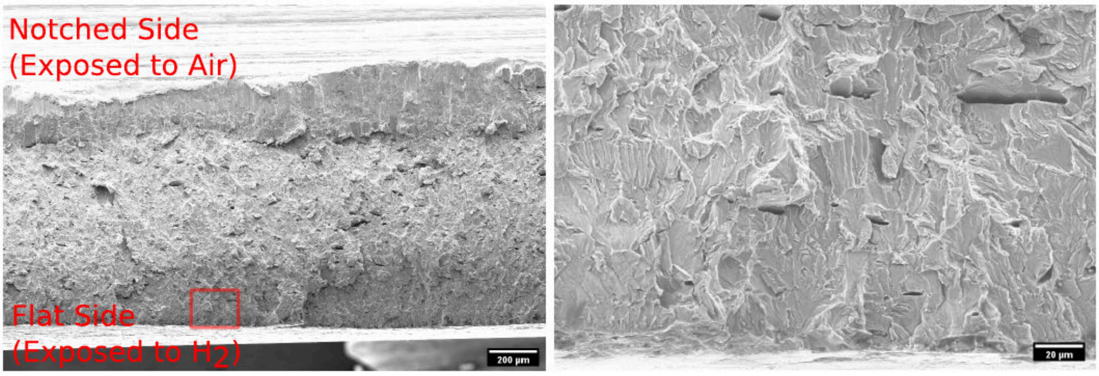

(a) (b)

Figure 3.17: Scanning Electron Microscopy (SEM) image of the fracture surface of an inverted notched disk. In (a), the flat side exposed to H_2 shows a brittle appearance. The region highlighted by the red square in (a) is magnified in (b), revealing detailed quasi-cleavage features.

3.4.2 Effect of hydrogen

This section analyzes the effect of hydrogen on displacement-pressure curves for the three disk geometries for both steel alloys. Figure 3.18a illustrates the results for the E355 mod. steel at a nominal pressurization rate $\dot{P}_a = 0.25$ MPa/min. The curves clearly show the embrittlement effect of H_2, as evidenced by a significant decrease in P_r' and displacement at fracture for standard specimens. Specifically, $P_r'(H_2)$ decreases by about 50% compared to $P_r'(\mathrm{He})$. For the cup disk, the difference between $P_r'(H_2)$ and $P_r'(\mathrm{He})$ is less pronounced, although significant differences remain in the displacements at failure. This effect is attributed to the rapid increase in displacement as the applied pressure approaches the limit pressure. In the case of the notched disk, the hydrogen effect is much more pronounced, causing an approximately 50% reduction in the pressure at failure and also significantly affecting the displacement at failure.

The pressure-displacement curves for all geometries show no changes due to hydrogen up to the point of failure. This suggests that hydrogen does not affect the elasto-plastic behavior of the material, allowing the previously derived hardening law to be used in simulations involving hydrogen. Rupture occurs very quickly, indicating that crack initiation leads almost immediately to catastrophic failure of the disk. This behavior aligns with a load-controlled test, where crack propagation is so rapid that hydrogen cannot diffuse into the material during failure. As a result, the crack propagates in a field of constant hydrogen concentration.

Figure 3.18b illustrates the effect of hydrogen on X52 steel across the three different disk specimen geometries. The findings are similar to those observed with E355 mod. steel.

3.4.3 Effect of the pressurization rate

This section analyzes the effect of the pressurization rate ($\dot{P}_a$) on the rupture failure (P_r') of the different disk geometries and steel alloys under helium and hydrogen gases. The disks were tested at various $\dot{P}_a$ values ranging from 0.025 to 35 MPa/min. Figure 3.19 presents the results, with $P_r'(\mathrm{He})$ represented by black triangles and $P_r'(H_2)$ by red circles. Under helium, there is a minimal dependence on the pressurization rate due to the material's limited strain rate sensitivity. This trend is consistently observed across all specimens and materials.

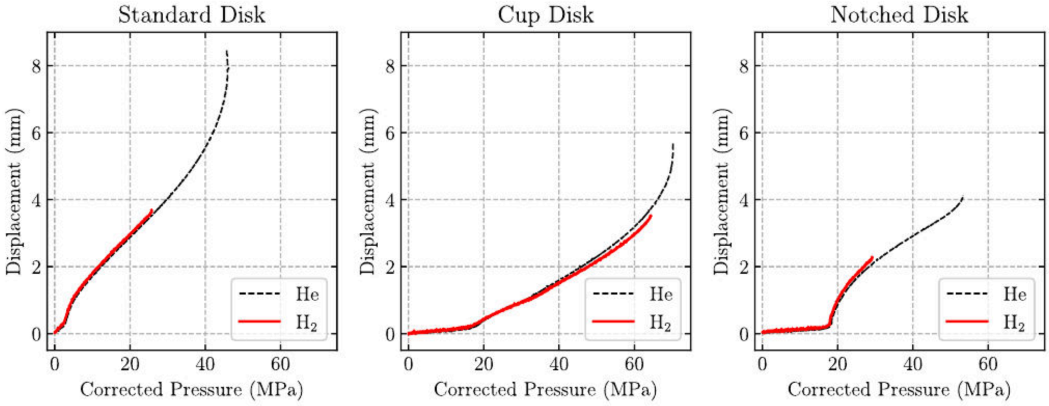

(a) E355 mod. steel.

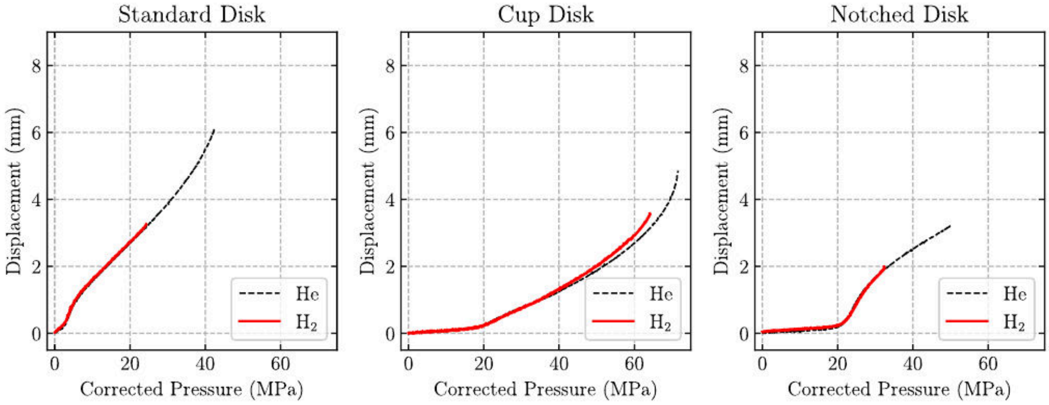

(b) X52 steel.

Figure 3.18: Hydrogen effect on both steel alloys for the three different specimen geometries at a pressure rate of 0.25 MPa/min.

Surprisingly, the effect of $\dot{P}_a$ on hydrogen behavior is also very limited, showing a scatter similar to that seen under helium. This result is unexpected when compared to other studies. For example, Fidelle et al., 1975 showed that $\dot{P}_a$ significantly affects hydrogen embrittlement (HE) in materials that are particularly susceptible to this phenomenon. They identified four distinct zones based on the relationship between $P'_r(\mathrm{H_2})$ and $\log t$ (where t is inversely proportional to $\dot{P}_a$):

- Zone I: For high $\dot{P}_a$, where $P'_r(\mathrm{H_2})$ increases significantly.
- Zone II: At moderate $\dot{P}_a$, where $P'_r(\mathrm{H_2})$ levels off, showing maximum HE over a range of $\dot{P}_a$.
- Zone III: At low $\dot{P}_a$, where $P'_r(\mathrm{H_2})$ increases compared to Zone II, due to slower dislocation motion allowing hydrogen to escape and redistribute by regular diffusion.
- Zone IV: At very low $\dot{P}_a$, where $P'_r(\mathrm{H_2})$ reaches a higher plateau than in Zone II, as hydrogen entry is primarily controlled by regular diffusion.

Recent studies by Charles et al., 2012 for commercial pure iron and Briottet et al., 2012 for X80 grade steel have also investigated the effect of $\dot{P}_a$ on $P'_r(\mathrm{H_2})$. Despite some variability, both studies observed a

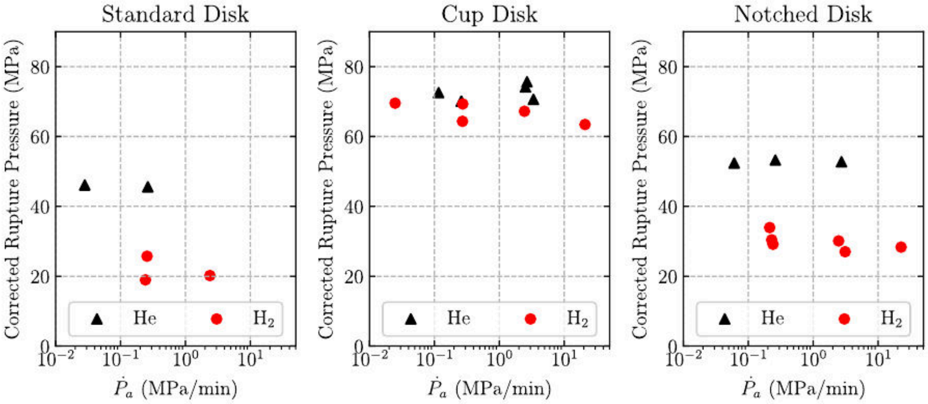

(a) E355 mod. steel.

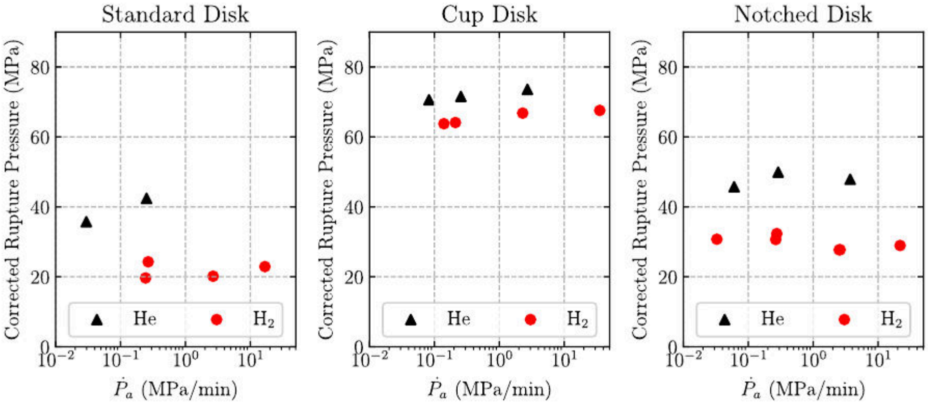

(b) X52 steel.

Figure 3.19: Effect of the pressurization rate on both steel alloys for the three different specimen geometries.

plateau in P_r' at moderate $\dot{P}_a$ and an increase at higher $\dot{P}_a$, consistent with zones I and II described by Fidelle et al., 1975. The observed lack of dependence on pressurization rate is further explored through fracture surface observations in Section 3.4.5 and discussed in Section 3.5.4.

3.4.4 Hydrogen Embrittlement Index

The Hydrogen Embrittlement Index (HEI) is calculated for the three disk specimens following the ISO 11114 standard (see Equation 3.1), which considers the worst ratio $P_r(\text{He})/P_r(\text{H}_2)$ obtained for several tests under distinct Pressure Rise Rates ($\dot{P}_a$). The tests were carried out at three nominal pressure rate values for $\dot{P}_a$ of 2.5, 25 and 2.5 MPa/min for the X52 steel and of 0.25, 25 and 2.5 MPa/min for the E355 mod. steel. Average failure pressures across all loading rates are used for this calculation. The results are presented in Table 3.4.

The HEI values for standard disks are similar, with the E355 mod. steel at 2.41 and X52 steel at 2.47, both exceeding the acceptable threshold of 2 according the standard. In contrast, the HEI for notched disks is closer to that of standard disks, with values of 1.96 for the E355 mod. and 1.77 for the X52. The

	Standard	Cup	Notched
X52	2.47	1.12	1.77
E355 mod.	2.41	1.21	1.96

Table 3.4: Hydrogen Embrittlement Index (HEI) values calculated for the three disk geometries for both E355 mod. and X52 steels.

lowest HEI values were observed for cup disks, with 1.2 for the E355 mod. and 1.12 for the X52 steels.

These results clearly demonstrate that the HEI is significantly influenced by the specimen type. Different geometries create distinct stress states at the fracture zone, a topic that will be further explored in Section 3.5.4. Consequently, the interaction between hydrogen and the fracture zone varies, leading to differences in the HEI. For example, a slightly sharper notch radius in the notched disk could yield an HEI similar to that of the standard disk.

3.4.5 Fractography

This section examines the fracture surfaces of specimens tested under both helium and hydrogen. The fracture surfaces of all specimens tested under helium displayed almost identical features, characterized by ductile fractures with voids elongated in the thickness direction. Figure 3.20 shows the fracture surfaces of disk specimens for both E355 mod. and X52 steels. In Figure 3.20b, the red arrows highlight the elongated voids initiated from MnS inclusions, a feature observed exclusively in X52 steel.

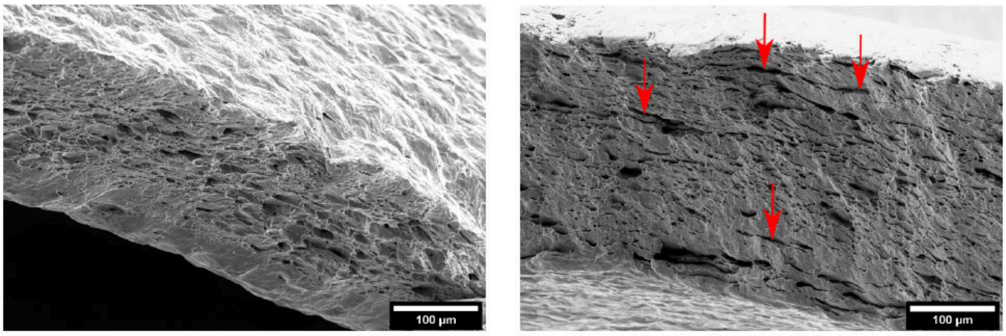

(a) E355 mod. steel.

(b) X52 steel.

Figure 3.20: Fracture surface of cup disks tested under helium. Red arrows highlight elongated voids initiated on MnS inclusions.

Figure 3.21 shows the fracture surfaces of specimens taken from the E355 mod. material tested in the presence of hydrogen. The left column presents the overall appearance of the fractures. In all specimens, two distinct zones are evident: the side exposed to the gas, which corresponds to the crack initiation site, shows a zone embrittled by hydrogen. The crack then propagates into a second zone, where the fracture is ductile. The hydrogen-embrittled zone is shown in greater detail in the right column, where a characteristic quasi-cleavage fracture pattern is visible.

A similar analysis was performed for the X52 steel. Figure 3.22 displays the fracture surfaces of the X52 steel specimens tested in a hydrogen environment. The findings for X52 steel are consistent with those observed for E355 mod. steel, with a distinct separation between the embrittled and ductile zones in most cases. However, the standard disk specimen (Figure 3.22a) shows extensive shearing, making it more challenging to clearly identify the fracture mechanisms.

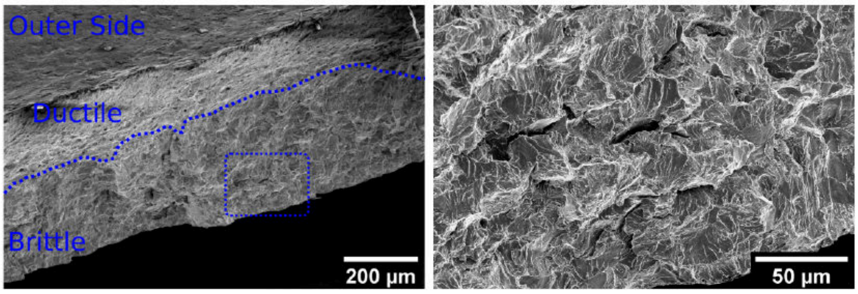

(a) Standard disk. (b) Detail on standard disk.

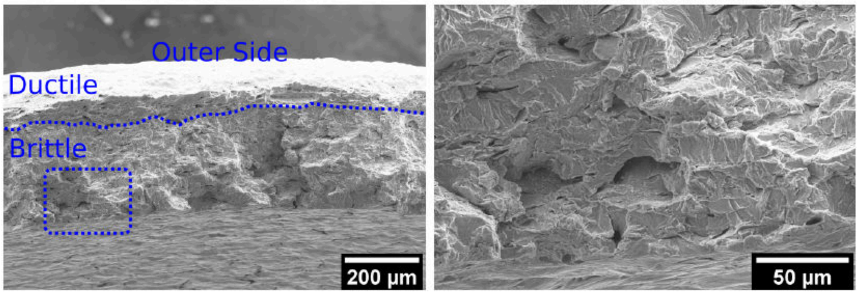

(c) Cup disk. (d) Detail on cup disk.

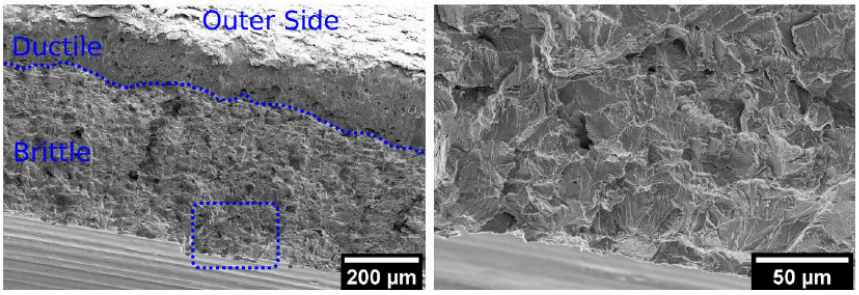

(e) Notched disk. (f) Detail on notched disk.

Figure 3.21: Surface fractures of E355 mod. steel disk specimens tested under hydrogen.

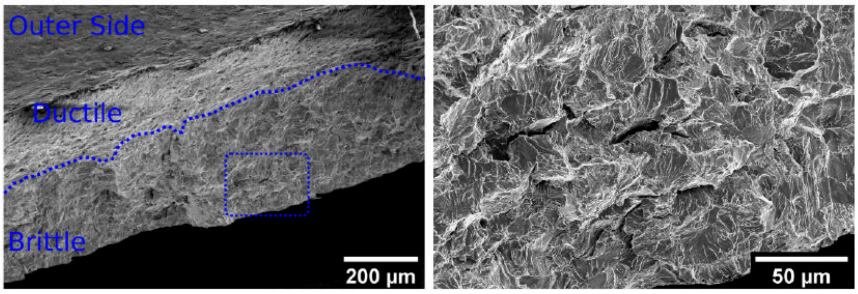

(a) Standard disk. (b) Detail on standard disk.

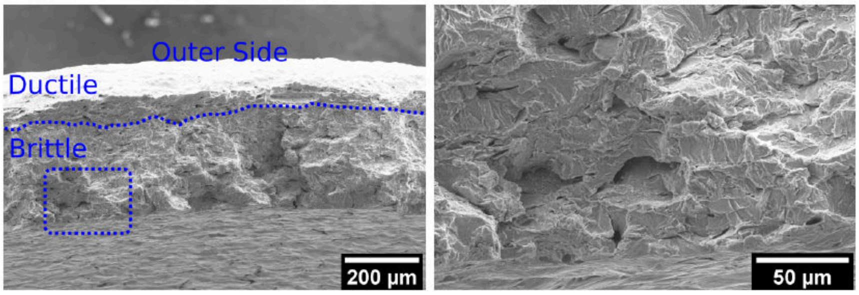

(c) Cup disk. (d) Detail on cup disk.

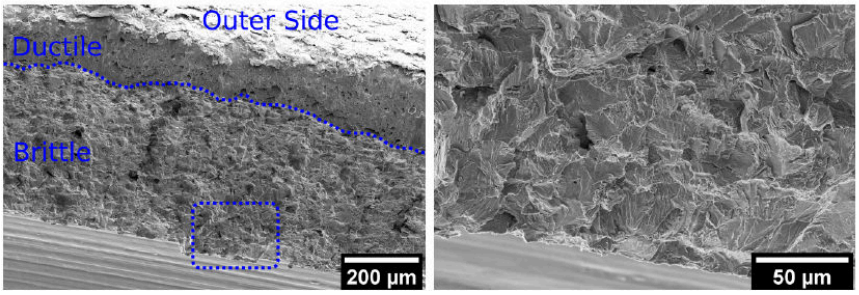

(e) Notched disk. (f) Detail on notched disk.

Figure 3.22: Surface fractures of X52 steel disk specimens tested under hydrogen.

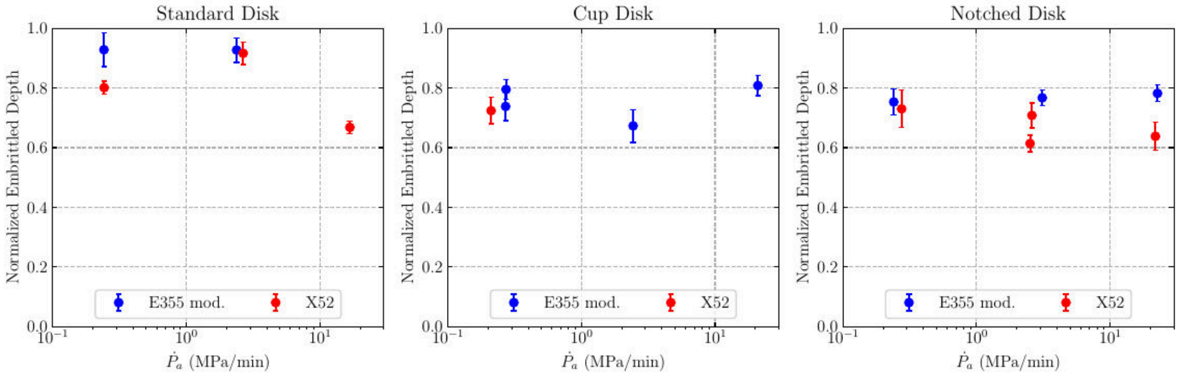

Figure 3.23: Maximum normalized embrittled depth according to pressurization rate ($\dot{P}_a$).

	Standard				Cup				Notched			
	P_r' (He)		P_r' (H_2)		P_r' (He)		P_r' (H_2)		P_r' (He)		P_r' (H_2)	
X52	Avg.	Min.	Avg.	Min.	Avg.	Min.	Avg.	Min.	Avg.	Min.	Avg.	Min.
		35.8		19.7		70.6		63.8		45.8		27.7
	39.1	Max.	21.8	Max.	71.9	Max.	65.6	Max.	48.4	Max.	29.8	Max.
		42.4		24.3		73.6		67.6		50.1		32.3
E355 mod.	Avg.	Min.	Avg.	Min.	Avg.	Min.	Avg.	Min.	Avg.	Min.	Avg.	Min.
		45.6		19.0		70.1		63.4		52.4		27.0
	45.9	Max.	21.6	Max.	73.1	Max.	66.8	Max.	52.8	Max.	29.8	Max.
		46.1		25.7		75.7		69.6		53.3		33.9

Table 3.5: Summary of the results obtained in DPT with X52 and E355 mod. steels (in MPa). The values reported encompass the full range of tests conducted, with Pressure Rise Rates ($\dot{P}_a$) varying from 0.025 to 35 MPa/min.

The disk specimens were then sectioned and examined by Scanning Electron Microscopy (SEM) to determine the depth of the embrittled zone around the entire fracture perimeter. Figure 3.23 shows the maximum observed embrittlement depth, normalized to the local final thickness of the specimens, as a function of pressurization rate ($\dot{P}_a$) for the three disk geometries. The purpose of this analysis was to determine if the pressurization rate affected the size of the embrittled zone. The maximum embrittlement depth was calculated as the average of nine measurements taken from the most embrittled areas. Blue circles represent values for E355 mod. steel, while red circles represent those for X52 steel, with error bars indicating the standard deviation of the measurements. Some data points are missing due to leakage in disks that experienced through-wall cracking rather than fracture, making fracture analysis impossible.

The normalized embrittlement depth ranges from 0.67 to 0.93 for the standard disk specimens, from 0.67 to 0.81 for the cup specimens, and from 0.61 to 0.78 for the notched specimens. The pressurization rate ($\dot{P}_a$) does not appear to have a significant effect on the extent of the embrittlement zone, which is consistent with the observation that $P_r'(H_2)$ is not affected by $\dot{P}_a$ for any specimen or material type. This finding is crucial for the selection of an appropriate numerical model for hydrogen diffusion and trapping. The effect of the pressurization rate is further investigated and discussed in Section 3.5.4, based on the numerical simulations performed for this study.

3.5 Simulation of pressurized disks

This section introduces the numerical model used for the finite element simulation of the Disk Pressure Test (DPT). The model integrates both plasticity and hydrogen diffusion/trapping mechanisms, providing a framework for interpreting the experimental results.

3.5.1 Modeling of hydrogen transport

The hydrogen transport model employed in this study was previously introduced in Section 2.4.4. In the case of the DPT, the temperature is held constant, making the time-dependent temperature term ($\dot{T}$) in Equation 2.80 equal to zero.

3.5.2 Finite elements discretization and model parameters

To accurately model the plastic behavior of materials in the presence of hydrogen, it is crucial to account for the strong coupling between mechanics and diffusion, as hydrogen diffusion can significantly affect the material's mechanical properties. Additionally, finite strains must be considered to accurately represent disk deformation. The algorithm used to manage this coupling is described in Lopes Pinto et al., 2023 and will be further elaborated in Chapter 5. Only a brief overview is provided here. The proposed model has been implemented in the Z-set software.

This study presents an alternative approach to addressing the coupled diffusion/mechanics problem by employing mixed finite elements. This technique has also proven effective in addressing problems affected by volumetric locking at high plastic strains, as documented in previous studies (Al Akhrass et al., 2014; Bellet, 1999; Taylor, 2000; Y. Zhang et al., 2017). The primary nodal unknowns in this formulation are displacement $\{\boldsymbol{u}\}$, pressure $\{p\}$, and volume variation $\{\theta\}$. Displacements are interpolated using quadratic shape functions, while both pressure and volume variation are interpolated using linear shape functions. Because pressure is defined at the nodes, its gradient can be directly computed, eliminating the need for extrapolation from integration points. Figure 3.24 presents a comparison of the pressure fields obtained using the standard and mixed formulations. In the first case, volumetric locking causes discontinuities in the pressure field. In contrast, the mixed formulation employed in the second case effectively mitigates these instabilities.

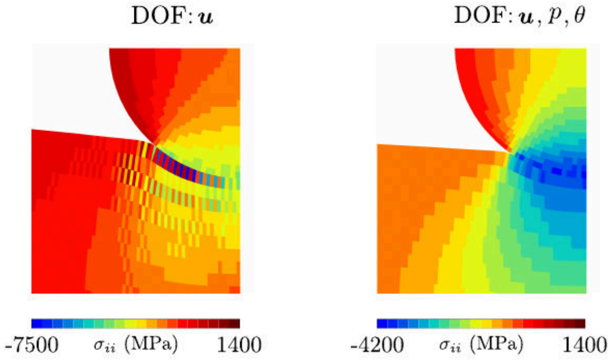

Figure 3.24: Comparison of the contact zone in the disk simulation using standard and mixed formulations. At high strain levels, the standard formulation exhibits pressure field instabilities caused by volumetric locking.

Additionally, a nodal field representing the lattice hydrogen concentration $\{C_L\}$ is introduced, which is also interpolated using linear shape functions. Figure 3.25 illustrates the degrees of freedom for an element, using reduced integration in this mixed formulation.

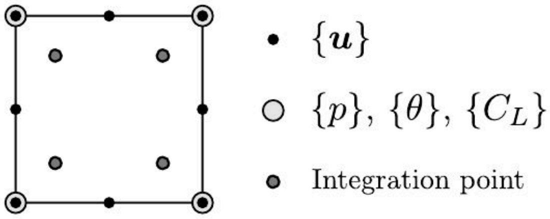

Figure 3.25: Representation of a square element with the mixed formulation with 4 degrees of freedom and reduced integration.

Table 3.6 presents the coefficients used in the simulations. These parameters are taken from the literature (Lopes Pinto et al., 2023). Different values for the binding energy (W_B) and the trap density (N_T) are used in the simulations.

Property	Value	Unit
β	6	—
R	8.31	J/mol K
T	295	K
C_S	0.0129	appm
P_s	0.1013	MPa
D_L	1.27×10^{-8}	m^2/s
N_A	6.022×10^{23}	mol^{-1}
V_M	7.09×10^{-6}	m^3/mol
N_L	8.47×10^{28}	m^{-3}
V_H	2.0×10^{-6}	m^3/mol

Table 3.6: Material parameters.

3.5.3 Boundary conditions for the hydrogen diffusion problem

Axisymmetric elements with reduced integration were employed to model the disks. While this approach could be extended to 3D cases, it would result in significantly increased computational time. Figure 3.26 depicts the boundary conditions (hydrogen and mechanical) for the standard disk case.

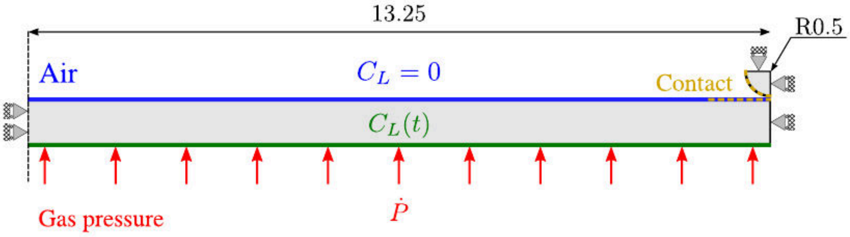

Figure 3.26: Representation of the boundary conditions (hydrogen and mechanical) applied to the standard specimen for the simulation.

Sieverts' law is applied to determine the lattice hydrogen concentration at boundaries exposed to the gas environment (Sofronis and McMeeking, 1989). For simplicity, hydrogen is assumed to behave as an ideal gas. Consequently, the lattice hydrogen concentration, C_L, is expressed as a function of hydrogen pressure, as shown below (Marchi et al., 2007):

$$C_L = C_S \sqrt{\frac{P_a}{P_s}} \tag{3.7}$$

where C_S represents a thermally activated term, P_a is the applied hydrogen gas pressure, and P_s is a reference pressure. This condition is imposed on the lower part of the specimen (green line in Figure 3.26), resulting in an increase in the applied concentration as the pressure rises. Additionally, based on the experimental findings of Kasuya et al., 2021, it is reasonable to assume that hydrogen rapidly escapes from the top surface of the sample (blue contour in Figure 3.26), so the lattice hydrogen concentration, C_L, is set to zero at this boundary. The hydrogen flux through all other boundaries is assumed to be zero. The mechanical boundary conditions are identical to those described in Section 3.3. Simulations of the tests conducted under helium, as mentioned above, utilize the same methodology, but without considering hydrogen diffusion.

3.5.4 Simulations of hydrogen embrittlement and discussions

In this study, damage development due to hydrogen embrittlement (HE) is not considered in the simulations, which were carried out up to the experimentally observed rupture pressure (P_r') for each respective material and geometry. The subsequent analyses focus on hydrogen concentration and the stress state. For example, Figure 3.27 shows a comparison between the cross-section of a fractured notched disk and the plastic strain field obtained from the numerical simulation for the E355 mod. steel. The simulation accurately predicts the fracture location, as highlighted by the regions of high plastic strain. The primary fracture zone, along with smaller secondary cracks indicated by red arrows, aligns with areas of maximum plastic strain. However, the greater deformation observed experimentally, shown on the left side of the figure, is attributed to the actual failure of the specimen, whereas the simulation only accounts for the material's elastoplastic behavior.

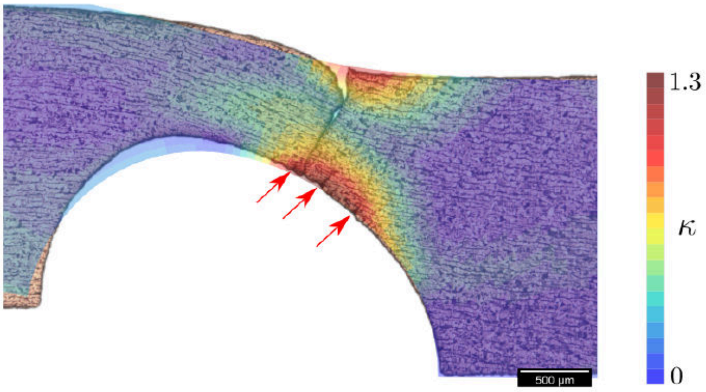

Figure 3.27: Superposition of the fractography of the ruptured cross section of the notched disk with the plastic strain field obtained from the finite element modeling for E355 mod. steel.

Several models in the literature describe the evolution of trap density as a function of plastic strain and trap binding energies, W_B, which range from 15 to 110 kJ/mol (Drexler et al., 2019). This study focuses on two commonly used models for hydrogen trapping in pipeline steels. The first model, proposed by Moro et al., 2010, applies to high-strength API X80 steel and assumes a trap binding energy of $W_B = 40$ kJ/mol. The trap density in this model is given by the expression $\log_{10} N_T = 24.73 - 3.74 \exp(-60.17\kappa)$, where κ represents the accumulated plastic strain. The second model, introduced by Kumnick and Johnson, 1980 and further employed by Depraetere et al., 2021, represents a X70 pipeline steel. This model assumes a trap binding energy of $W_B = 60$ kJ/mol with $\log_{10} N_T = 23.26 - 2.33 \exp(-5.5\kappa)$ governing the evolution of trap density relative to accumulated plastic strain.

Even tough both models analyze similar materials, they exhibit significant differences in the evolution of trap density with plastic strain, as shown in Figure 3.28. In particular, the model proposed by Moro et al., 2010 reaches its maximum value at remarkably low strains and has a much higher maximum value than the model proposed by Kumnick and Johnson, 1980. Consequently, the use of the former model results in a significantly higher number of traps than the latter.

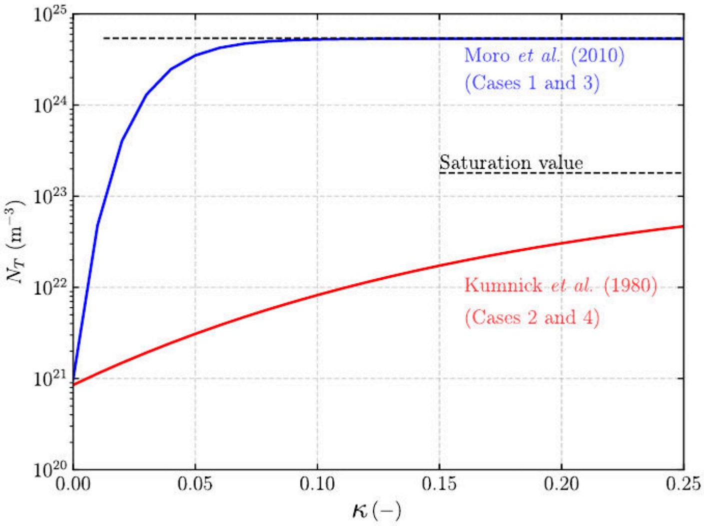

Figure 3.28: Evolution of the trap density according to the accumulated plastic strain, following the evolution laws proposed by Moro et al., 2010 and Kumnick and Johnson, 1980.

Based on the values of binding energies and the expressions for trap density, four distinct cases can be identified:

- **Case 1:** $W_B = 40$ kJ/mol, $\log_{10} N_T = 24.73 - 3.74 \exp(-60.17\kappa)$
- **Case 2:** $W_B = 40$ kJ/mol, $\log_{10} N_T = 23.26 - 2.33 \exp(-5.5\kappa)$
- **Case 3:** $W_B = 60$ kJ/mol, $\log_{10} N_T = 24.73 - 3.74 \exp(-60.17\kappa)$
- **Case 4:** $W_B = 60$ kJ/mol, $\log_{10} N_T = 23.26 - 2.33 \exp(-5.5\kappa)$

Figure 3.29 summarizes the results for each of the four notched disk cases at pressure rise rates of $\dot{P}_a = 0.25$ and $\dot{P}_a = 25$ MPa/min for the E355 mod. steel. It compares the total hydrogen concentration fields for each model under slow and fast test conditions, as well as the maximum concentration values achieved. Notably, for the cases using the N_T function proposed by Moro et al., 2010 (cases 1 and 3), significant differences are observed in the penetration profiles between the two pressurization rates. The maximum concentration reaches much higher values due to the rapid increase in trap density with accumulated plastic strain.

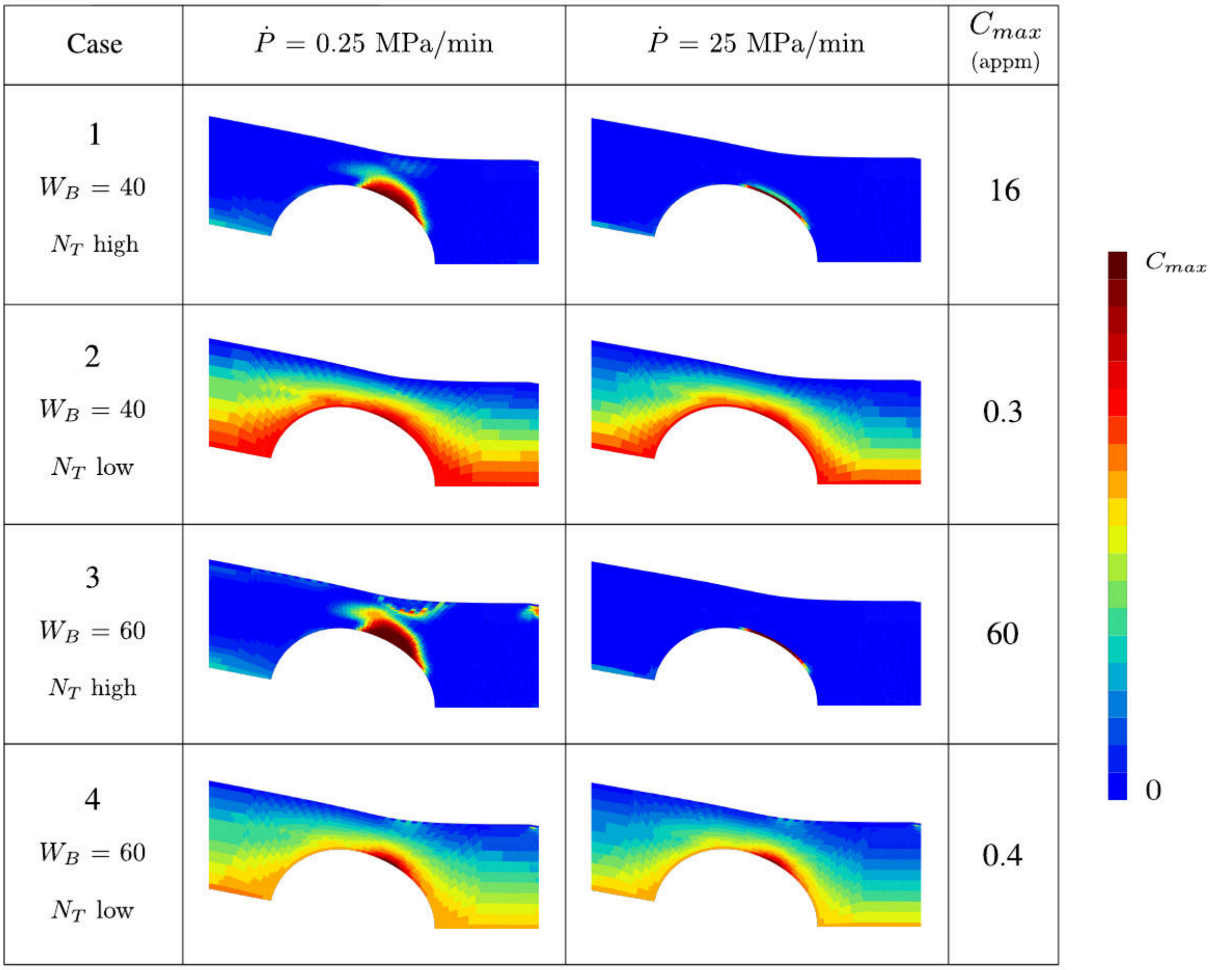

Figure 3.29: Total hydrogen concentration field in the rupture zone of the notched disk at rupture (P'_r = 29 MPa for all cases). Simulations are performed using all four possible models based on the binding energies W_B and the trap density expressions N_T for the E355 mod. steel.

In contrast, the models using the N_T function proposed by Kumnick and Johnson, 1980 (cases 2 and 4) show very similar concentration profiles across both pressurization rates, but with lower maximum concentration values. Experimental observations, as illustrated in Figure 3.23, reveal that the embrittled depth in notched specimens is about 80% of the total thickness is independent of the pressurization rate. This suggests that hydrogen diffuses deeply into the material before failure occurs, with crack propagation happening so rapidly that it can be assumed to occur within a nearly static hydrogen concentration field, as previously discussed in Section 3.4.3.

Therefore, the model that aligns most closely with experimental observations is the one proposed by Kumnick and Johnson, 1980, where N_T increases moderately with plastic strain κ. Since this model represents dislocations as traps, considered to be shallow, a lower binding energy value is more consistent, as supported by literature references (Drexler, Depover, et al., 2020; Drexler et al., 2019). Consequently, case 2 has been chosen for all subsequent simulations.

Figure 3.30 presents the total hydrogen concentration fields for both standard and cup specimens, highlighting the fracture zones in the clamping area and at the center, respectively. Notably, the hydrogen fields appear similar across both pressurization rates. Although the slower test might show slightly higher concentration values due to the longer diffusion time, the results indicate that the concentration fields at both rates are comparable.

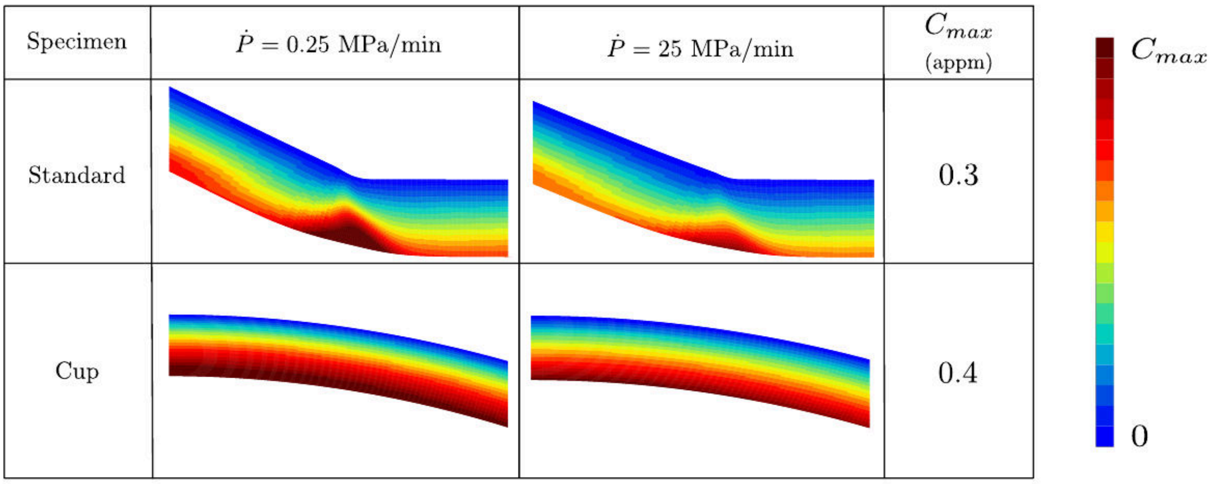

Figure 3.30: Total hydrogen concentration fields in the rupture zones for both standard and cup specimens. Failure occurs at the clamping zone in the standard disk and at the center in the cup specimen. Simulations use the W_B and N_T coefficients from case 2 for E355 mod. steel.

An additional analysis was performed for the three disk geometries and both X52 and E355 mod. steels to examine how the maximum principal stress (σ_I) in the fracture zone evolves with hydrogen gas pressure. Figure 3.31 displays the results for each geometry, revealing distinct behaviors. For the standard and notched specimens, a noticeable change in slope at around 300 MPa indicates the onset of plasticity. In contrast, for the cup specimen, bending during loading causes the surface in contact with air to be in tension, while the surface in contact with hydrogen is in compression, as illustrated in Figure 3.31. As deformation progresses, tensile stresses develop in the membrane, but the stress difference between the air side and the hydrogen side persists, leading to higher stress levels on the air side. According to Equation 2.71, hydrogen migrates towards regions of high tensile stress. Therefore, despite higher tensile stresses on the outer surface, failure typically initiates on the hydrogen-exposed side, suggesting potential hydrogen leakage on the air-exposed surface. This supports the use of the boundary condition ($C_L = 0$) for this surface. The stress response behavior is similar for both steels.

Further analysis was conducted to explore the potential correlation between principal stress and hydrogen concentration within the fracture zone. This analysis was performed at two pressurization rates ($\dot{P}_a = 0.25$ and 25 MPa/min) for both X52 and E355 mod. steels. The results, illustrated in Figure 3.32 for the three disk geometries, demonstrate that as hydrogen concentration increases, the critical principal stress required to initiate fracture decreases. Specifically, for hydrogen concentrations below 0.25 appm, no hydrogen embrittlement is observed in these steels under the conditions of this test. Given that hydrogen embrittlement typically manifests through quasi-cleavage, the observed relationship suggests a viable dependence law.

The X52 steel exhibits higher stress values compared to the E355 mod. steel, which aligns with the mechanical properties derived from tensile tests, as depicted in Table 3.3. Additionally, for the cup specimen, the E355 mod. steel exhibits a higher hydrogen concentration. This can be attributed to its greater ductility, i.e. higher strains, which generates more trapping sites and thus increase hydrogen concentration. This effect is particularly pronounced for the cup specimen, as it undergoes higher strains compared to the standard and notched specimens.

To accurately describe hydrogen-induced quasi-brittle failure (HEDE) using a GTN model, Lopes

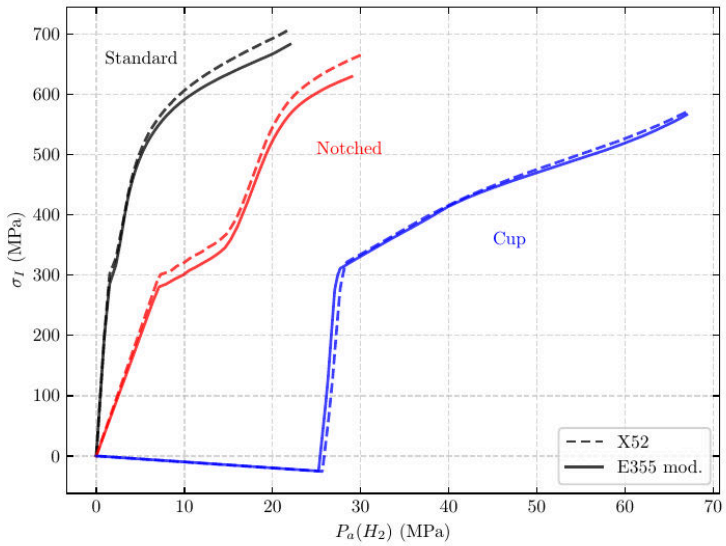

Figure 3.31: Evolution of the maximum principal stress in the fracture zone with respect to the gaseous hydrogen pressure for $\dot{P}_a = 0.25$ MPa/min.

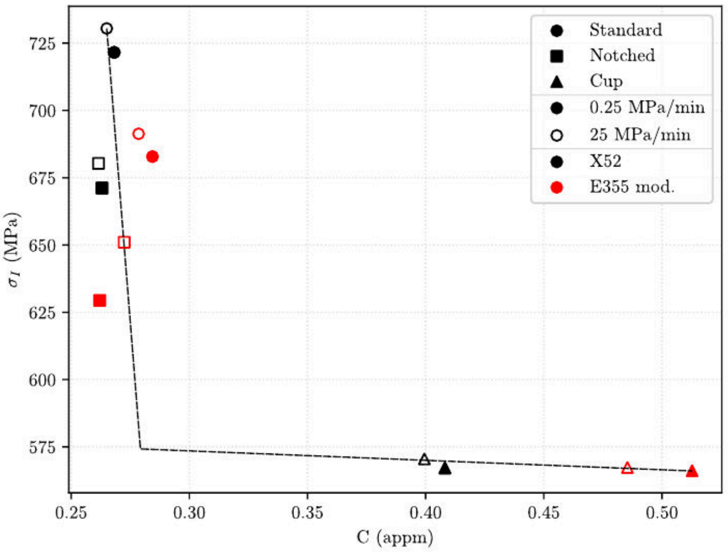

Figure 3.32: Reduction in critical principal stress to initiate fracture with increasing hydrogen concentration for pressurization rates equal to 0.25 and 25 MPa/min for both the X52 and the E355 mod. steels.

Pinto et al., 2023 proposed that the critical stress required for fracture decreases with increasing hydrogen concentration. As illustrated in Figure 3.32, specimens with geometries that generate higher principal stress in the fracture zone tend to fail at lower hydrogen concentrations. This finding supports Lopes Pinto et al., 2023 proposal and indicates that the failure criterion for the Disk Pressure Test (DPT) is related to the interplay between maximum principal stress and hydrogen concentration in the fracture zone, consistent with the HEDE theory.

3.6 Conclusions

This study successfully met its primary objectives by integrating numerical simulations with experimental analysis. Luciano Meirelles Santana conducted all experimental tests and mechanical characterizations in close collaboration with the numerical simulations. Two innovative disk specimen geometries were designed to control failure locations while maintaining the DPT testing configuration specified by the ISO 11114 standard. Additionally, a computational framework was developed to accurately simulate plasticity and its interaction with hydrogen. The combined experimental and numerical approaches provided valuable insights into several key aspects of the study, leading to the following conclusions:

- The development and validation of a constitutive law derived from an innovative tensile test setup, which facilitated the simulation of the DPT for three distinct disk specimen geometries across two different materials.
- The design of novel disk specimen geometries effectively redirected rupture locations away from the clamping zones, with ruptures specifically occurring in areas of reduced thickness-namely, the central zone for the cup disk and near the bottom of the notch for the notched disk.
- The experimental observation that, despite a wide range of $\dot{P}_a$ values tested, there was no evident correlation between the severity of hydrogen embrittlement and $\dot{P}_a$. This is attributed to the consistent maximum embrittled depth across varying $\dot{P}_a$ values within the same specimen geometry.
- Numerical simulations using the Kumnick and Johnson, 1980 model for the evolution of hydrogen trap density with accumulated plastic strain corroborated experimental findings, showing similar hydrogen concentration profiles for significantly different pressurization rates. This supported the experimental evidence of $P'_r(\mathrm{H}_2)$ independence from $\dot{P}_a$.
- Detailed analyses connecting the evolution of maximum principal stress (σ_I) in the fracture zone with hydrogen pressure and concentration levels demonstrated that increasing hydrogen concentrations decrease the σ_I necessary to initiate fractures, providing insights into the mechanical vulnerability caused by hydrogen embrittlement.

In summary, this study demonstrates that the Disk Pressure Test (DPT) offers a simpler and more cost-effective alternative to traditional mechanical tests conducted under gaseous hydrogen. By using both modified and standard specimen geometries, distinct stress and strain states can be achieved, facilitating a more detailed examination of hydrogen's effects on fracture behavior. Additionally, the development of a numerical framework for simulating hydrogen embrittlement serves as a valuable tool for interpreting experimental results.

4

Simulation of hydrogen uptake during a tensile test

Abstract Hydrogen offers significant potential for the decarbonization of industry, but its interaction with metals, in particular the phenomenon of hydrogen embrittlement (HE), requires careful investigation. This study investigates how different loading conditions affect hydrogen absorption in structural materials. Thermal desorption spectroscopy (TDS) was used to measure hydrogen concentration. Tensile tests were performed on flat samples exposed to a gaseous hydrogen environment to evaluate hydrogen uptake under different conditions, including different strain levels, strain rates and dwell times. In this context, dwell time refers to the time a specimen is exposed to hydrogen without further deformation until it reaches the same exposure time as the most deformed specimen. A numerical model coupling hydrogen diffusion and plasticity was employed for the simulations. The results show that lower strain rates and longer exposure times increased the hydrogen concentration. The numerical model is capable of predicting hydrogen behavior and provides valuable insights into hydrogen-metal interactions.

Résumé L'hydrogène offre un potentiel important pour la décarbonisation de l'industrie, mais son interaction avec les métaux, en particulier le phénomène de fragilisation par l'hydrogène (FPH), doit être étudiée avec soin. Cette étude examine comment différentes conditions de chargement affectent l'absorption d'hydrogène dans les matériaux structurels. La spectroscopie de désorption thermique (TDS) a été utilisée pour mesurer la concentration d'hydrogène. Des essais de traction ont été réalisés sur des éprouvettes plates exposées à un environnement d'hydrogène gazeux afin d'évaluer l'absorption d'hydrogène dans différentes conditions, notamment différents niveaux de déformation, taux de déformation et temps de maintien. Dans ce contexte, le temps de maintien fait référence à la durée d'exposition d'une éprouvette à l'hydrogène sans déformation supplémentaire jusqu'à ce qu'il atteigne la même durée d'exposition que l'éprouvette la plus déformée. Un modèle numérique couplant la diffusion de l'hydrogène et la plasticité a été utilisé pour les simulations. Les résultats montrent que des vitesses de déformation plus faibles et des temps d'exposition plus longs augmentent la concentration d'hydrogène. Le modèle numérique est capable de prédire le comportement de l'hydrogène et fournit des informations précieuses sur les interactions hydrogène-métal.

Contents

4.1 Introduction

Hydrogen presents considerable advantages as an energy vector. It is naturally abundant, causes minimal projected environmental impact, and holds significant potential for decarbonizing several industrial sectors (Guo et al., 2024; Pleshivtseva et al., 2023). However hydrogen embrittlement (HE) necessitates careful consideration, as it can severely degrade the mechanical properties of structural metals (Gangloff, 2008). While several factors influence a material's susceptibility to HE, the interactions between hydrogen and metals – such as hydrogen uptake, diffusion, and trapping – have a particularly strong effect. For instance, the extent of degradation in the toughness or ductility of metals is closely correlated with the hydrogen concentration present (Gangloff, 2008; Wang et al., 2022).

To study hydrogen embrittlement, several experimental methods and techniques have been developed to assess hydrogen-metal interactions (X. Li et al., 2020; Madi et al., 2024; Verbeken, 2012). For example, the total hydrogen content can be determined using techniques such as inert gas fusion, vacuum fusion, silicone oil, and laser thermal desorption (Brun and Allison, 2022; García-Macías et al., 2024). However, the two most widely adopted methods for evaluating hydrogen interactions with metallic microstructures are hydrogen permeation and Thermal Desorption Spectroscopy (TDS) (Depover and Verbeken, 2021; Zafra et al., 2022).

Permeation tests involve the uptake of hydrogen on one side of a thin membrane, either through exposure to gaseous hydrogen or electrochemical hydrogen charging, followed by measurement of the hydrogen flux on the opposite side of the membrane. This flux can be measured using methods such as mass spectrometry, changes in vacuum pressure, or oxidation current density (Van den Eeckhout et al., 2023). The permeation test generates a curve of hydrogen flux versus time, which can be analyzed using theoretical models to determine the effective diffusion coefficient. While permeation tests are relatively straightforward to implement and analyze, they are prone to significant variability between tests (Turnbull, 1995; Zafra et al., 2022).

In contrast, the TDS test employs a hydrogen pre-charged specimen and applies a temperature ramp to measure the hydrogen desorption through a high-resolution mass spectrometer. The resulting data provides a curve of hydrogen desorption flux versus temperature. By analyzing this curve, key hydrogen-metal interaction parameters – such as binding energies, trap densities, and total hydrogen concentration – can be determined (Verbeken, 2012). The main advantage of TDS is its ability to calculate most primary hydrogen-metal interaction parameters. However, the method requires an ultra-high vacuum environment and the use of uniformly pre-charged specimens, which can be challenging to prepare.

One key area of interest is the relationship between loading conditions and the amount of hydrogen absorbed during loading. In the study by Moro, 2009, tensile specimens were exposed to varying strain levels at a same strain rate and charged under a hydrogen pressure of 300 bar. The resulting hydrogen content was measured to investigate the relationship between charging conditions and hydrogen concentration.

The strain level significantly influences the number of hydrogen traps, which directly affects the hydrogen concentration within the material. Moreover, the exposure time to hydrogen also impacts the amount of hydrogen absorbed during charging. Building on this, the present study aims to examine and interpret the effects of strain level, strain rate, and the exposure time on hydrogen absorption in the specimens. Hydrogen concentration measurements are performed using Thermal Desorption Spectroscopy (TDS).

The mechanical loading of the specimens in a gaseous hydrogen chamber was conducted at FenHYx (Future Energy Networks for Hydrogen and miX), a research laboratory of GRTgaz[1], dedicated to studying the effects of hydrogen on structural materials. Subsequently, the TDS tests were carried out by Luciano Meirelles Santana at the Ecole des Mines de Saint-Etienne.

This chapter is organized as follows: Section 4.2 provides the chemical composition of the steel analyzed in this study and the coefficients of the elasto-plastic constitutive law. Section 4.3 outlines the experimental procedures used during hydrogen charging in the tensile tests, detailing the various conditions applied, followed by the Thermal Desorption Spectroscopy (TDS) procedure and the method used to measure the hydrogen content for each test. Section 4.4 presents the experimental results of the TDS tests. Section 4.5 introduces the hydrogen diffusion model, the corresponding hydrogen boundary conditions and the finite element model employed for the numerical simulations. Finally, Section 4.6 compares the experimental and numerical results, analyzes the effect of each test condition on the hydrogen content, and discusses the model's capability to predict the hydrogen concentration in the material.

4.2 Material

This work examined a X52 API grade steel, produced in 1968 and previously analyzed in detail by Shokeir et al., 2022. The chemical composition of this "vintage" steel is provided in Table 4.1. Notably, this steel has a sulfur concentration approximately ten times higher than that of modern steels.

---

[1] https://www.grtgaz.com/

C	Mn	S	Al	Si	Cr	Cu	Mo	V	Ti	Fe
0.17	1.22	0.054	0.036	0.27	≤ 0.01	0.06	≤ 0.01	≤ 0.01	≤ 0.01	bal.

Table 4.1: Chemical composition of the studied X52 API grade steel in %wt.

This steel exhibits anisotropic plastic behavior due to the crystallographic texture developed during its fabrication. However, for simplicity, and because the studied case does not reach high strain levels, the simulation model will use a von Mises plasticity framework with isotropic hardening. In this model, the yield surface is defined as:

$$\Phi = \sigma_{\text{eq}} - \sigma_F(\kappa) \tag{4.1}$$

where the flow stress σ_F depends on the accumulated plastic strain κ and is defined by a Voce law as follows:

$$\sigma_F(\kappa) = \max(\sigma_L, \sigma_0 + Q_1(1 - \exp(-b_1\kappa)) + Q_2(1 - \exp(-b_2\kappa)) + H\kappa) \tag{4.2}$$

where σ_L is the Lüders stress and can be experimentally determined. The hardening function presents a linear term along with two nonlinear terms, allowing it to capture hardening behavior over a large strain range ($\kappa \geq 1.2$). The Young's modulus is 219 GPa, and the Poisson's ratio is 0.3. The simulated length of the Lüders plateau is approximately 1%.

The material is assumed to exhibit slight rate dependence, where the plastic strain rate is defined as:

$$\dot{\kappa} = \dot{\kappa}_0 \left\langle \frac{\sigma_{\text{eq}} - \sigma_F(\kappa)}{K} \right\rangle^n \tag{4.3}$$

where $\dot{\kappa}_0$, K and n are coefficients describing the viscoplastic properties of the material. Table 4.2 provides the hardening law coefficients identified through optimization, following the same procedure detailed in Section 3.2.2. A comparison between the experimental and numerical results employing the coefficients of Table 4.2 will be provided in Section 4.6.1.

σ_L (MPa)	σ_0 (MPa)	Q_1 (MPa)	b_1 (-)	Q_2 (MPa)	b_2 (-)	H (MPa)	$\dot{\kappa}_0$ (s^{-1})	K (MPa)	n (-)
380	344	288	7.9	82	26.7	65.7	1	176	5

Table 4.2: Model parameters used to define the X52 hardening law.

4.3 Experimental procedure

This section provides an overview of the experimental procedure used for mechanical testing in a gaseous hydrogen atmosphere under various conditions. The primary focus of the present chapter is on the numerical simulation of these tests. Therefore, only a summary of the experimental setup and procedure is presented here.

4.3.1 Tensile tests in gaseous atmosphere

The experimental setup used in this study consists of a MTS-engineered servo-hydraulic tensile machine, modified with a custom high-pressure chamber. A schematic of the setup is shown in Figure 4.1. This equipment enables the execution of tests, particularly tensile tests, in a gaseous environment at pressures up to 100 bar. The setup can also accommodate a hydrogen-resistant force sensor and an extensometer placed directly inside the autoclave.

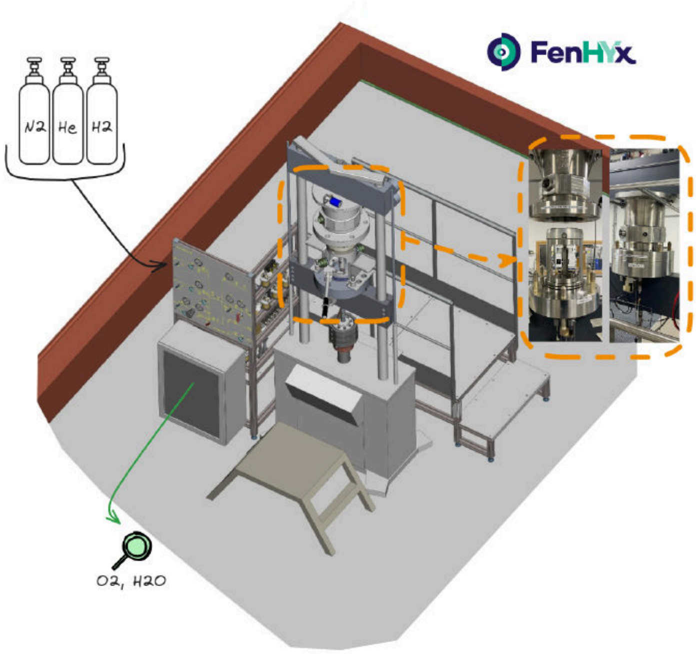

Figure 4.1: Description of the test setup at FenHYx.

Significant attention was devoted to ensuring the stability and reliability of the various sensors used in the hydrogen atmosphere. Achieving stable sensor performance is essential, as it can be affected by factors such as temperature, pressure, and hydrogen concentration.

The purity of hydrogen gas in test conditions is a critical factor that significantly influences the experimental results. This involves not only the selection of high-quality source gas but also meticulous purging processes to maintain purity levels. It is crucial to recognize that the purity of the test gas should not be presumed to be equivalent to that of the source gas. For these experiments, hydrogen gas of 6.0 quality (99.9999% purity, with oxygen levels capped at 0.5 wppm) was utilized. To secure optimal testing conditions, various preparatory procedures were evaluated prior to the start of the test campaign. The initial inertization process comprised several stages: (i) three nitrogen purges (up to 10 bars); (ii) vacuum application; (iii) leak testing with helium (up to test pressure); (iv) a second vacuum; and (v) hydrogen filling.

Figure 4.2 shows the dimensions of the tensile specimen used in this study. It consists of a flat tensile specimen with width of 9.5 mm, thickness of 4 mm and gage length of 20 mm. The particular geometry of the specimen comes from the need to fit it into the quartz tube of the TDS test, represented in Figure 4.4. and the tension machine while maximizing the effective volume of the specimen. The aim is to achieve a high amount of hydrogen within the material, thereby facilitating measurement by Thermal Desorption Spectroscopy (TDS). The sample has been polished to achieve an average roughness (Ra) of less than 1 µm.

Table 4.3 summarizes the parameters varied in this study, which include strain level, strain rate, and dwell time under gaseous hydrogen exposure. In this context, “dwell time” refers to the duration for which the specimens are exposed to the hydrogen environment without undergoing further deformation.

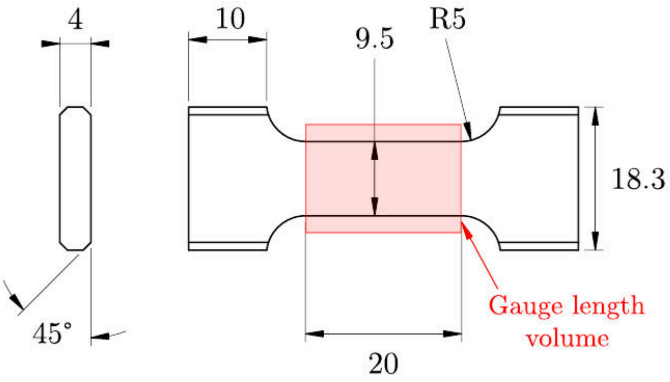

Figure 4.2: Specimen's dimensions.

Figure 4.3: TDS specimen.

This period ensures that all specimens achieve the same total exposure time as the most deformed specimen, which corresponds to 12% elongation, corresponding to the onset of necking. The purpose of this test condition is to compare the amount of hydrogen absorbed by specimens exposed to hydrogen for the same total time but at different strain levels. The experiments were conducted in two environments: air at atmospheric pressure and 85 bar of H_2.

Environment	Air, 85 bar H_2
Strain	0%, 30%Rp02, 90%Rp02, 3%, 6%, 12%
Strain Rate (s^{-1})	1×10^{-5}, 1×10^{-4}, 1×10^{-3}
Dwell	No dwell, Dwell

Table 4.3: Test parameters.

Six strain levels were investigated. Specimens marked as 30%Rp02 and 90%Rp02 were loaded to 30% and 90% of the yield strength (Rp02), meaning they were exposed to H_2 under elastic deformation. Specimens at 0% deformation were not subjected to either elastic or plastic deformation. Strains values of 3%, 6%, and 12% indicate specimens loaded until reaching 3%, 6%, and 12% strain, respectively.

Strain rate levels of 1×10^{-5}, 1×10^{-4}, and 1×10^{-3} s^{-1} were tested. Additionally, some specimens were maintained under H_2 exposure during a dwelling period. The total exposure time (loading and dwelling) for specimens loaded at a strain rate of 1×10^{-5} s^{-1} was 12,000 s, while for those loaded at 1×10^{-3} s^{-1}, it lasted 120 s. Following H_2 charging, all specimens were preserved in liquid nitrogen to prevent unwanted desorption of hydrogen atoms before TDS analysis.

Environment	Strain rate (s^{-1})	Dwell	Strain (%)
85 bar H_2	1×10^{-3}	No dwell	12
85 bar H_2	1×10^{-5}	No dwell	12
85 bar H_2	1×10^{-4}	No dwell	12
85 bar H_2	1×10^{-4}	Dwell	6
85 bar H_2	1×10^{-4}	Dwell	3
85 bar H_2	1×10^{-4}	No dwell	3
85 bar H_2	1×10^{-4}	No dwell	6
85 bar H_2	5 s	Dwell	30% Rp02
85 bar H_2	17 s	Dwell	90%Rp02
85 bar H_2	0	Dwell	0
85 bar H_2	17 s	No dwell	90%Rp02
Air	0	No dwell	0
85 bar H_2	1×10^{-5}	Dwell	6
85 bar H_2	1×10^{-5}	Dwell	3
Air	0	No dwell	0
85 bar H_2	1×10^{-5}	No dwell	3
Air	0	No dwell	0
Air	0	No dwell	0

Table 4.4: Summary of the test matrix.

4.3.2 Thermal Desorption Spectroscopy (TDS)

Figure 4.4 presents a schematic of the TDS equipment used in this study. The setup includes a resistance furnace that accommodates a quartz tube holding the specimen for analysis. Two vacuum systems are connected to this tube, each equipped with a rotary vane pump and a turbomolecular pump. The vacuum system on the right side initiates the pre-vacuum process within the tube, while the system on the left maintains a stable vacuum in the spectrometer system. Argon can be introduced into the tube as needed to break the vacuum.

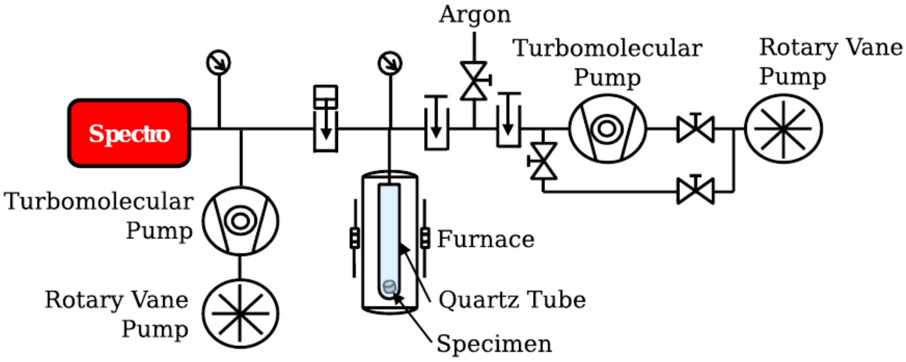

Figure 4.4: Schematic of the TDS (Thermal Desorption Spectroscopy) setup, featuring a resistance furnace, quartz tube, dual vacuum systems, and argon input.

The sample is removed from liquid nitrogen, cleaned, and rewarmed to ambient temperature with ethanol, then dried with optical paper. Argon is introduced to break the vacuum, allowing the specimen to be inserted into the tube. The initial vacuum stage is achieved with a sliding vane pump until a pressure of 3×10^{-2} mbar is reached. Next, the turbomolecular pump is activated, achieving a vacuum of approximately 6×10^{-6} mbar. Once this level is reached, the primary vacuum valve is closed, and the valve linking the spectrometer to the specimen tube is opened, establishing a vacuum near the spectrometer at around 7×10^{-7} mbar. This entire process takes approximately one hour. The relatively long duration, compared to other TDS machines, is due to the high internal volume of this specific machine, which allows it to accommodate large specimens, such as full tensile specimens, without the need for cutting. Once the setup is complete, the heating process begins, and data acquisition by the spectrometer is initiated.

The TDS equipment offers high precision, with a detection limit of 10^{-3} wppm. It was calibrated using a Certified Reference Material (CRM) containing $(1.00 \pm 0.05) \times 10^{-6}$ g of hydrogen, corresponding to a 95% confidence level. Desorption analysis of the CRM was performed twice: first with the hydrogen-loaded CRM and then with the hydrogen expected to be absent (Figure 4.5a). The integration of the difference between the two curves yields a value proportional to the hydrogen content in the CRM (Figure 4.5b). The calibration procedure was performed at the beginning, middle, and end of the test campaign to ensure spectrometer stability. The calibration factor (K) was determined by dividing the area under the curve by the known hydrogen mass of the CRM. For this campaign, K was calculated as 8.2366 g/A·s. This factor will subsequently be used to calculate the hydrogen content in the TDS tests.

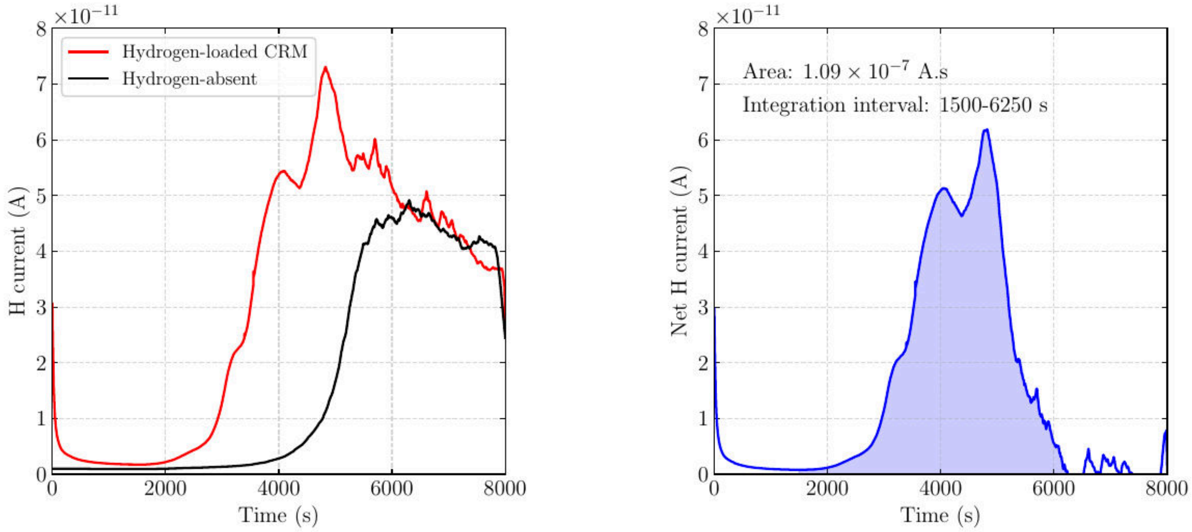

(a) Hydrogen current vs. time.

(b) Net hydrogen current vs. time.

Figure 4.5: Calibration procedure of the TDS test.

The TDS analysis of the tensile specimens was conducted with a temperature ramp of 10°C/min up to 600°C. A baseline curve, corresponding to a hydrogen-free specimen of the same dimensions, was subtracted from the obtained curve (Figure 4.6a). The three additional peaks observed at temperatures above 300°C are attributed to contamination from specimen engraving or other sources not investigated in this study. These peaks will be excluded from the analysis.

The hydrogen quantity was determined by integrating the first peak in the TDS spectra, with the resulting area multiplied by the calibration factor K. The hydrogen concentration for each specimen was then calculated by dividing the TDS-derived hydrogen content by the mass of the gauge length volume (red region in Figure 4.2), measured individually for each specimen. Only the gauge length volume is considered because it corresponds to the region of maximum plastic strain, where hydrogen is expected to be most concentrated. Figure 4.6b contains an example of a desorption curve for a TDS test.

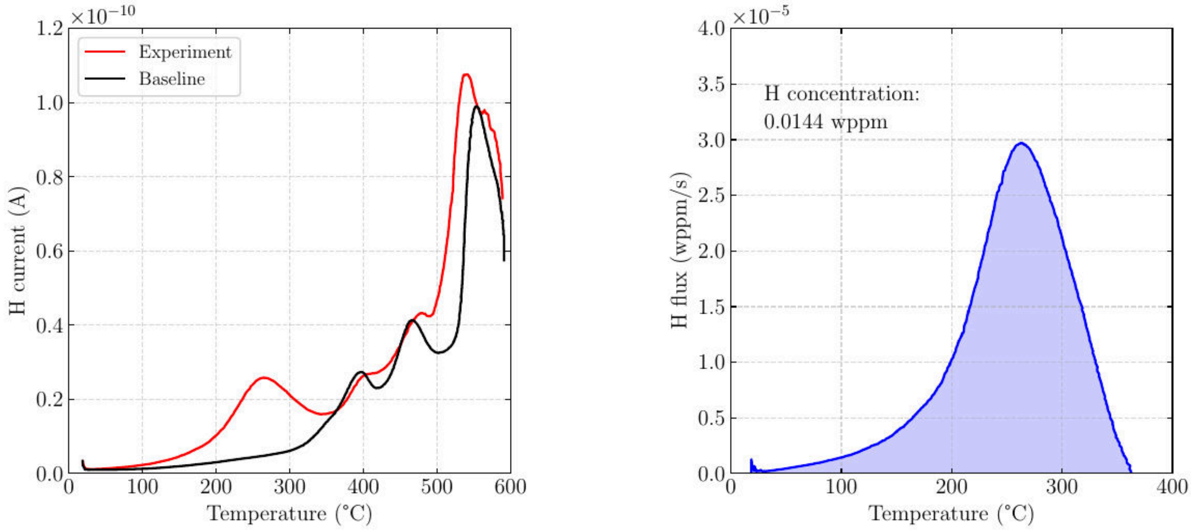

(a) Hydrogen current vs. temperature.

(b) Hydrogen flux vs. temperature.

Figure 4.6: Experimental procedure for calculating the hydrogen concentration. Test conditions: $\dot{\varepsilon} = 1 \times 10^{-5}$ s^{-1}, 3% strain, with dwell.

4.4 Experimental results

This section presents the experimental results from the TDS tests, which will subsequently be simulated and compared to the numerical outcomes predicted by the model.

4.4.1 Strain effect

As previously discussed, the TDS specimens were loaded until reaching different strain levels in order to analyze the relation between strain and the hydrogen content absorbed by the specimen. The specimens were then loaded up to 90%Rp02, 3%, 6% and 12%, at a strain rate equal to 1×10^{-4} s^{-1} under a hydrogen pressure of 85 bar. The longest test, up to 12% strain, lasted 1,200 s, while the shortest, up to 90%Rp02, lasted only 17 s.Figure 4.7 contains the experimental results for the F/S_0 vs. time and $\Delta l/l_0$ vs. time at different strain levels.

Figure 4.8a shows the experimental TDS desorption curves, illustrating that higher strain levels correspond to higher hydrogen peaks. Additionally, the peaks occur at higher temperatures for lower strain levels. Figure 4.8b presents the hydrogen concentrations obtained by integrating the curves of Figure 4.8a, confirming that higher strain levels lead to increased hydrogen concentrations. The results of this test are summarized in Table 4.5.

Strain rate (s^{-1})	Strain (%)	Dwell	H concentration (wppm)
1×10^{-4}	12	No dwell	0.0306
1×10^{-4}	6	No dwell	0.0068
1×10^{-4}	3	No dwell	0.0013
17s	90%Rp02	No dwell	0.0009

Table 4.5: Experimental results for the TDS test under different strain levels.

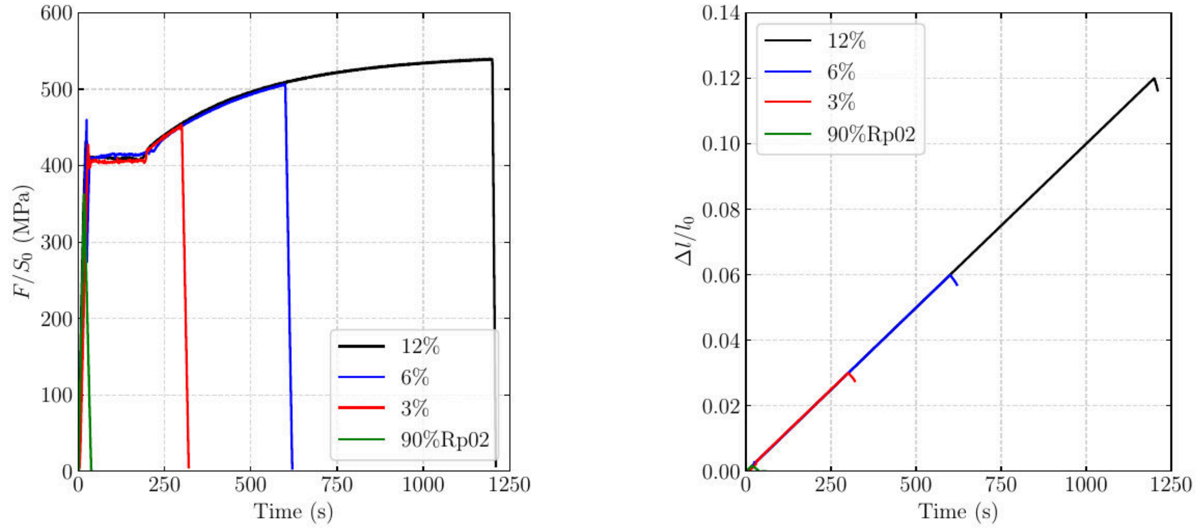

(a) Stress vs. time.

(b) Strain vs. time

Figure 4.7: Experimental tensile curves at different strain levels at $\dot{\varepsilon} = 1 \times 10^{-4}$ s^{-1}.

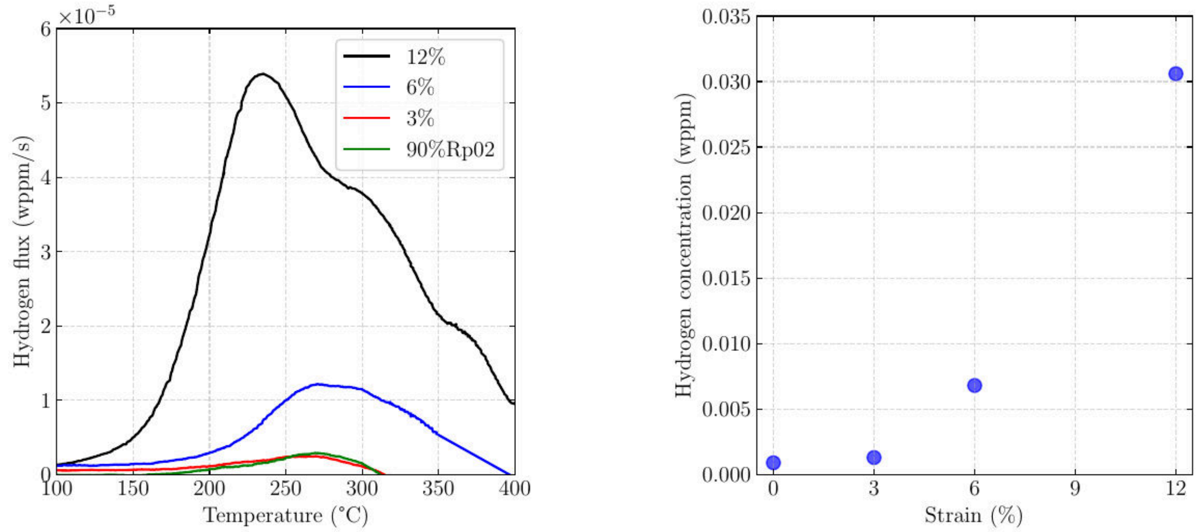

(a) Hydrogen flux vs. temperature.

(b) Hydrogen concentration vs. strain

Figure 4.8: Experimental results of the TDS test under different strain levels.

4.4.2 Strain rate effect

This study also analyzed the influence of strain rate on the hydrogen content absorbed by the specimen. Three strain rates were considered: 1×10^{-3}, 1×10^{-4} and 1×10^{-5} s^{-1}, corresponding to test durations of 120, 1,200 and 12,000 s, respectively. In each test, specimens were loaded to a strain of 12% without any dwell time, meaning they were immediately removed from the hydrogen atmosphere upon reaching the desired strain. Figure 4.9 presents the F/S_0 vs. time and $\Delta l/l_0$ vs. time curves for these tests.

Figure 4.10a presents the desorption curve from the TDS test, illustrating that for a same strain level (12% in this case), lower strain rates result in a higher hydrogen peak. For all cases, the first peak occurs at approximately the same temperature, around 240°C. Two additional peaks appear at temperatures above 250°C, particularly in the case at 1×10^{-4} s^{-1}. These peaks may originate from

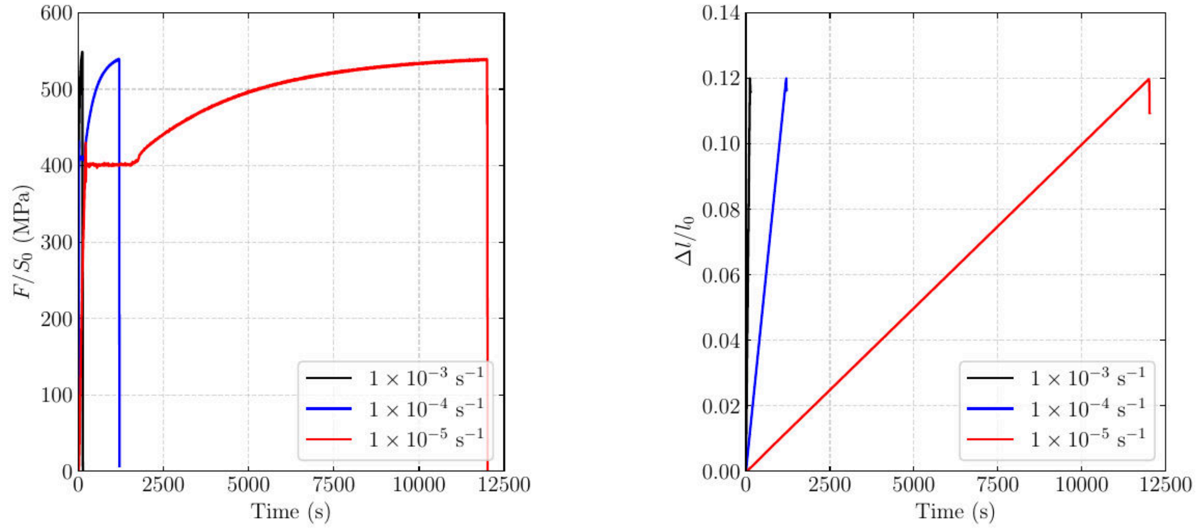

(a) Stress vs. time.

(b) Strain vs. time

Figure 4.9: Experimental tensile curves at different strain rates.

other trap sites with higher binding energies than the first peak. However, the analysis of these deeper traps is beyond the scope of this study. Figure 4.10b demonstrates that lower strain rates lead to higher hydrogen concentrations. Table 4.6 provides a summary of the results for this test condition.

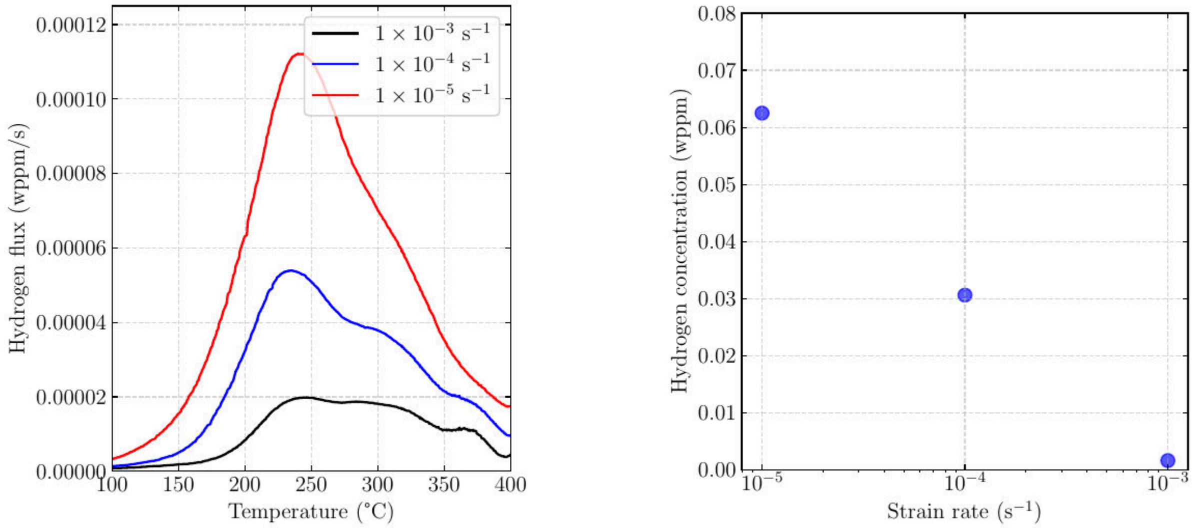

(a) Hydrogen flux vs. temperature

(b) Hydrogen concentration vs. strain rate

Figure 4.10: Experimental results of the TDS test under different strain rates.

Strain rate (s^{-1})	Strain (%)	Dwell	H concentration (wppm)
1×10^{-3}	12	No dwell	0.0116
1×10^{-4}	12	No dwell	0.0306
1×10^{-5}	12	No dwell	0.0625

Table 4.6: Experimental results for the TDS test under different strain rates.

4.4.3 Dwell effect

To investigate the dwell effect, specimens were deformed at a strain rate of 1×10^{-4} s^{-1} to a specific strain level and then either held in a hydrogen environment for a total test duration of 1,200 s or removed immediately after deformation. The experimental conditions for the test are illustrated in Figure 4.11.

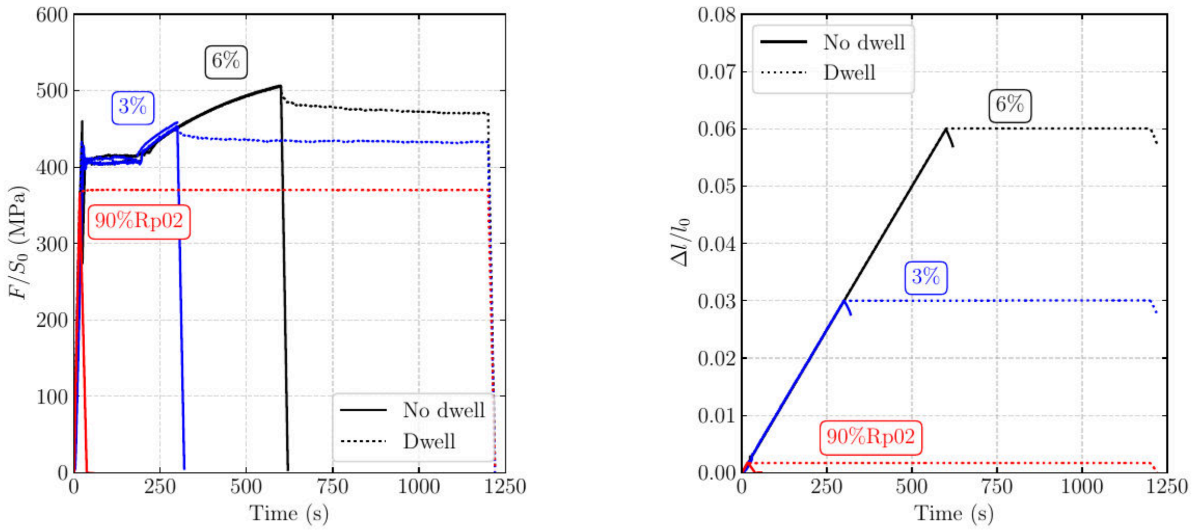

(a) Stress vs. time.

(b) Strain vs. time

Figure 4.11: Experimental tensile curves with and without dwell times at $\dot{\varepsilon} = 1 \times 10^{-4}$ s^{-1}.

Figure 4.12a presents the TDS results, demonstrating that specimens exposed to a hydrogen environment after deformation exhibit a higher hydrogen peak and, consequently, a greater hydrogen concentration at the same strain level. Furthermore, the data reveals that as the desorption peak height increases, the associated temperature decreases. Two key trends emerge from these results: (i) higher strain leads to increased hydrogen concentration, as previously observed; (ii) longer dwell times increase the hydrogen concentration. However, the tests conducted up to 90%Rp02 did not show a significant influence of dwell time on the hydrogen concentration. This effect becomes more pronounced at higher strain levels. The results are summarized in Table 4.7.

Strain rate (s^{-1})	Strain (%)	Dwell	H concentration (wppm)
17 s	90%Rp02	No dwell	0.0009
17 s	90%Rp02	Dwell	0.0016
1×10^{-4}	3%	No dwell	0.0013
1×10^{-4}	3%	Dwell	0.0131
1×10^{-4}	6%	No dwell	0.0068
1×10^{-4}	6%	Dwell	0.0175

Table 4.7: Experimental results for the TDS test with and without dwell times.

Additionally, a comparison was performed for tests conducted up to 3% strain at strain rates of 1×10^{-5} and 1×10^{-4} s^{-1}, with and without dwell periods. For the tests with dwell, the complete test duration was equal to 12,000 s at 1×10^{-5} s^{-1} and 1,200 s at 1×10^{-4} s^{-1}. Without dwell, the total test duration was 3,000 s at 1×10^{-5} s^{-1} and 300 s at 1×10^{-4} s^{-1}. The experimental conditions for these tests are shown in Figure 4.13.

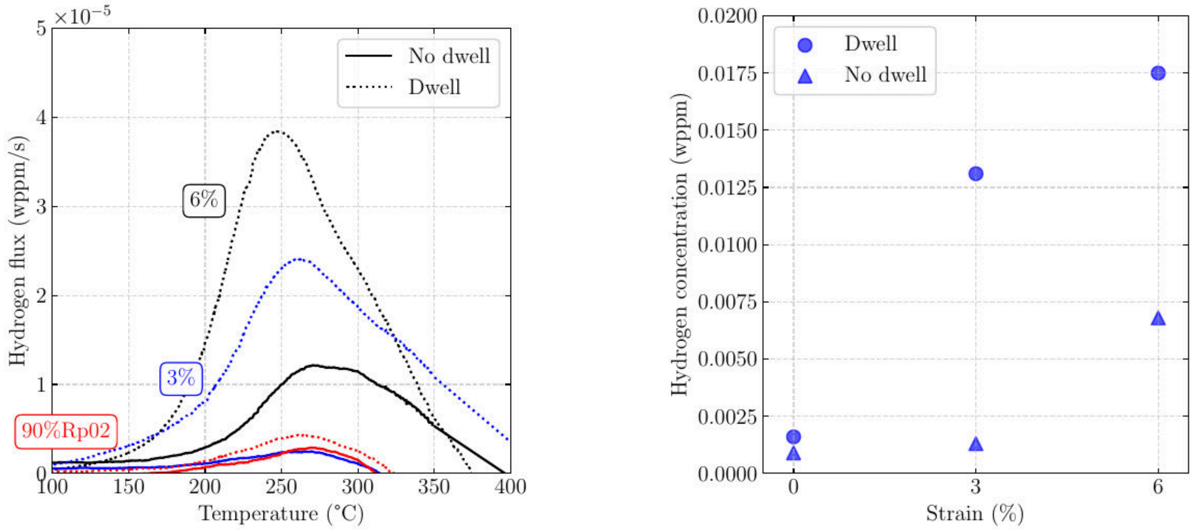

(a) Hydrogen flux vs. temperature

(b) Hydrogen concentration vs. strain rate

Figure 4.12: Experimental results of the TDS test with and without dwell times at $\dot{\varepsilon} = 1 \times 10^{-4}$ s^{-1}.

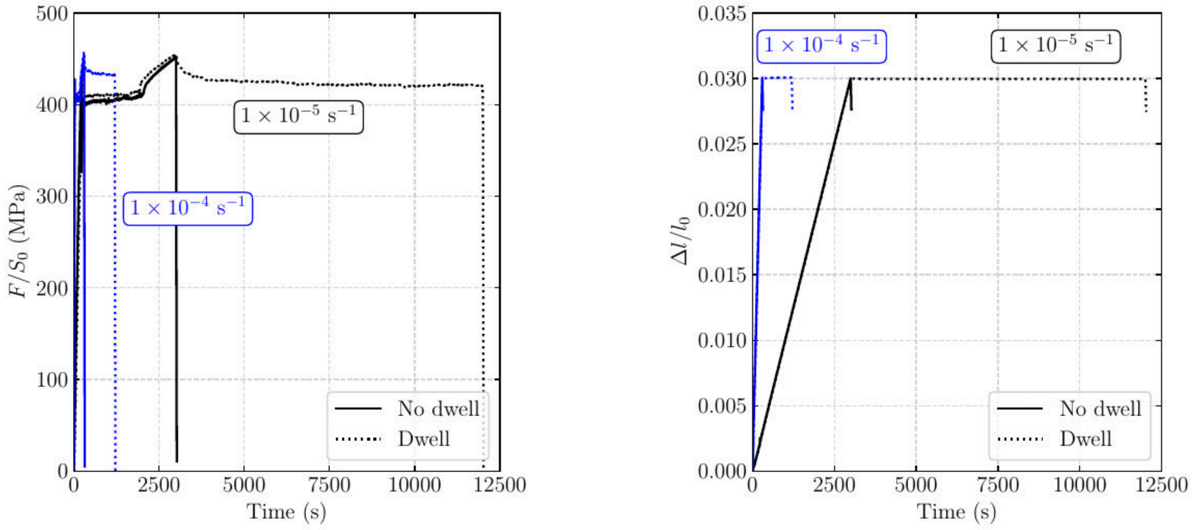

(a) Stress vs. time.

(b) Strain vs. time

Figure 4.13: Experimental tensile curves with and without dwell times at $\dot{\varepsilon} = 1 \times 10^{-5}$ and 1×10^{-4} s^{-1} for 3% strain.

Figure 4.14a shows the TDS spectra for the tests described above. In all cases, the hydrogen desorption peak occurs at approximately the same temperature of 260°C. From these curves, the hydrogen concentration was estimated and is presented in Figure 4.14. A summary of the results from this analysis is provided in Table 4.8.

From Figure 4.14b, it can be observed that, for the same strain of 3%, the tests conducted at a slower strain rate (1×10^{-5} s^{-1}) exhibit a higher hydrogen concentration, as previously noted. Tests incorporating a dwell time show a greater hydrogen concentration due to the increased hydrogen exposure time. Furthermore, the results indicate that tests performed at the higher strain rate (1×10^{-4} s^{-1}) display a more significant difference in hydrogen concentration between conditions with and without dwell times.

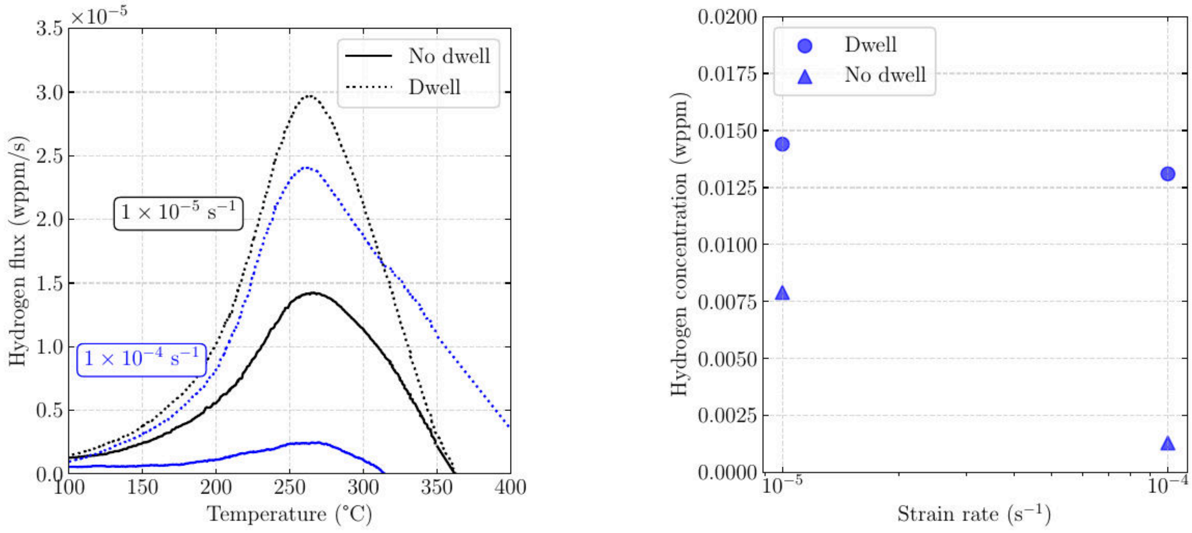

(a) Hydrogen flux vs. temperature

(b) Hydrogen concentration vs. strain rate

Figure 4.14: Experimental results of the TDS test with and without dwell times at $\dot{\varepsilon} = 1 \times 10^{-5}$ and 1×10^{-4} s^{-1} for 3% strain.

Strain rate (s^{-1})	Strain (%)	Dwell	H concentration (wppm)
1×10^{-5}	3%	No dwell	0.0079
1×10^{-5}	3%	Dwell	0.0144
1×10^{-4}	3%	No dwell	0.0013
1×10^{-4}	3%	Dwell	0.0131

Table 4.8: Experimental results for the TDS test with and without dwell times at $\dot{\varepsilon} = 1 \times 10^{-5}$ and 1×10^{-4} s^{-1} at 3% strain.

4.5 Simulation model

The hydrogen diffusion model used in this study was previously presented in Section 2.4.4. Please refer to this section for all the details. This model is able to consider one or several trapping sites at once, differing by its trapping binding energy and the trap density, which can be constant or evolve with plastic strain, such as dislocations.

The simulations in this study employed linear elements with full integration, significantly reducing the degrees of freedom compared to quadratic elements. To avoid extrapolating integrated pressure values to the nodes for computing pressure gradients, necessary for hydrogen flux calculations, pressure is treated as a linear degree of freedom within the model. Similarly, the lattice hydrogen concentration was also treated as a linear degree of freedom. Therefore, the unknowns in this problem are displacement $\{\boldsymbol{u}\}$, pressure $\{p\}$, and lattice hydrogen concentration $\{C_L\}$.

To mitigate volumetric locking, the B-bar formulation was employed, effectively addressing pressure oscillations associated with this numerical issue. An analysis of the effectiveness of this element formulation is presented in Section 6.4.1.

In cases of high binding energies ($W_B \geq 60$ kJ/mol), integrated concentration values may oscillate and become unstable, potentially leading to negative concentrations and convergence difficulties. To mitigate this, a “lumped” diffusivity matrix is used (Fried and Malkus, 1975; Zienkiewicz, 1977). This approach involves performing Gauss integration of the diffusivity matrix using shape functions evaluated at the node nearest to the integration point, as illustrated in Figure 4.15. This approach requires an equal number of integration points and nodes, thus full integration is considered. Positioning element nodes at integration points results in a diagonal diffusivity matrix, effectively preventing concentration oscillations.

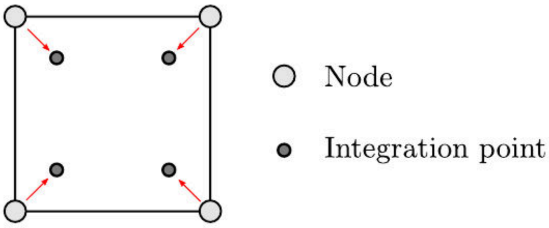

Figure 4.15: Representation of a linear square element with full integration where the lumping procedure is applied.

4.5.1 Hydrogen boundary conditions

Dirichlet and Neumann boundary conditions are applied to define the lattice hydrogen concentration (C_L) and the hydrogen flux ($\boldsymbol{J}$) on specific boundaries of the body. When hydrogen pressure (P_a) is applied, the hydrogen concentration can be determined using Sieverts’ law, which states (Sofronis and McMeeking, 1989):

$$C_L = C_S \sqrt{\frac{P_a}{P_S}} \tag{4.4}$$

where C_S is a thermally activated term and P_S is a reference pressure. This coefficients were identified and are listed in Table 4.9.

4.6 Numerical results and discussions

This section presents the numerical results of the TDS test simulations and provides a comparison with the experimental findings. Each test condition is analyzed, highlighting the differences and correlations between the simulated and experimental data, and discussing the implications of these observations on model accuracy. This analysis aims to assess the model’s effectiveness in capturing hydrogen diffusion behavior under varying conditions.

4.6.1 Simulation model

The numerical simulations employed a 3D mesh representing one-eighth of the specimen’s geometry, as shown in Figure 4.17a. Mechanical boundary conditions were applied to maintain the specimen’s symmetry, with displacements constrained as illustrated in Figure 4.17c. A displacement was imposed at the top of the specimen (green arrows) to match the strain rate specific to each case. Figure 4.16 shows a comparison between experimental and numerical results of the TDS test. The simulations employed the constitutive law detailed in Table 4.2, demonstrating that the model effectively captures the elasto(visco)-plastic behavior of the material.

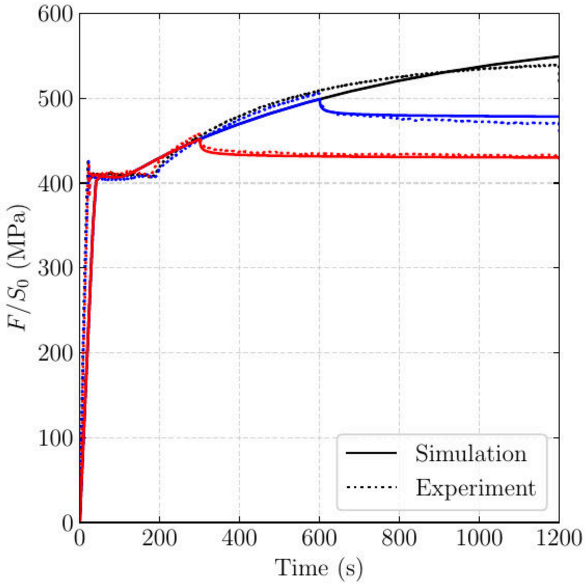

Figure 4.16: Comparison between experimental and numerical results for F/S_0 vs. time for tests deformed up to 3, 6 and 12% strain at 1×10^{-4} s^{-1}.

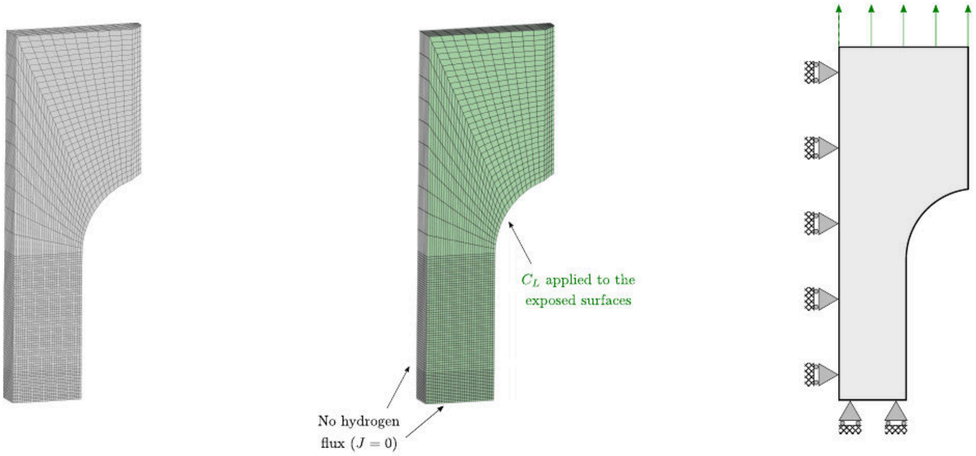

(a) 3D finite element mesh. (b) Hydrogen boundary conditions. (c) Mechanical boundary conditions.

Figure 4.17: Mesh and boundary conditions of the problem.

The specimens were exposed to a hydrogen pressure of 85 bar. The lattice hydrogen concentration (C_L) corresponding to this pressure can be estimated using Sieverts' law (Equation 4.4), yielding a value of 0.0021wppm (or 0.1182appm). This concentration was assigned to all surfaces in contact with hydrogen, as indicated by the green surfaces in Figure 4.17b. The lattice hydrogen concentration was applied exclusively to the specimen surfaces during loading.

The preparations required before the TDS test take approximately one hour, during which hydrogen can freely desorb from the specimen. Therefore, a one-hour resting period is considered in the model, assuming a zero lattice hydrogen concentration at the specimen's surfaces, allowing hydrogen to exit. At the end of the simulation, the total hydrogen concentration (C) within the specimen was determined through post-processing by integrating the hydrogen content over the entire specimen volume. The hydrogen-related coefficients used in the model are listed in Table 4.9.

Property	Value	Unit
β	6	–
R	8.31	J/mol K
T	295	K
C_S	0.0129	appm
P_S	0.1013	MPa
D_L	1.27×10^{-8}	m^2/s
N_A	6.022×10^{23}	mol^{-1}
V_M	7.09×10^{-6}	m^3/mol
W_B	40	kJ/mol
N_L	8.47×10^{28}	m^{-3}
V_H	2.0×10^{-6}	m^3/mol

Table 4.9: Coefficients of the hydrogen diffusion model.

The trapping model considered only a single type of trap, corresponding to dislocations. These traps have relatively low binding energies (W_B), set to 40 kJ/mol in this model. Since dislocation density increases with plastic strain, the trap density (N_T) is expressed as a function of the accumulated plastic strain (κ). Various models for representing trap density as a function of plastic strain are available in the literature, as previously discussed in Section 3.5.4.

The first model, proposed by Moro et al., 2010, estimates the trap density for high-strength API X80 steel as $\log_{10} N_T = 24.73 - 3.74 \exp(-60.17\kappa)$. To fit this trap density function, Moro, 2009 tested a tensile specimen in a gaseous atmosphere at 300 bar of H_2 under different strain levels. The hydrogen concentration for each case was measured, with only the trapped hydrogen concentration considered, since $C_L \ll C_T$. The model assumes a trap binding energy (W_B) of 40 kJ/mol, corresponding to a dislocation core. This energy value results in an occupancy of trap sites of 78%. Using Equation 2.75, the trap density for each case can be estimated, and the N_T equation as a function of accumulated plastic strain κ is determined.

The second model, introduced by Kumnick and Johnson, 1980 and also employed by Depraetere et al., 2021, represents a X70 pipeline steel, with $\log_{10} N_T = 23.26 - 2.33 \exp(-5.5\kappa)$. Both models yield similar trap density values when plastic strain is zero. However, as plastic strain develops, the model from Moro et al., 2010 increases sharply, saturating around 8% strain. In contrast, the model by Kumnick and Johnson, 1980 increases more gradually, yielding lower trap densities throughout, as illustrated in Figure 4.18a.

The two models were used for simulating the experimental tests under various conditions, while accounting for the loading phase (depending on the test conditions) and one-hour resting time for all cases. The results indicated that the model from Moro et al., 2010 overestimates the hydrogen content due to its assumption of a very high trap density. In contrast, the model from Kumnick and Johnson, 1980 allows all hydrogen to desorb from the specimen within the one-hour resting time. Consequently, a new trap density function was required to more accurately estimate the hydrogen content for the analyzed material.

Based on the results obtained from the two previous models, a suitable trap density relation for accurately predicting the hydrogen content in the X52 steel examined in this chapter should yield intermediate values between those models. Various functions were tested, and the one that provided the most accurate results is described below:

$$\log_{10} N_T = 24.67 - 3.74\exp(-60.17\kappa) \tag{4.5}$$

Only a minor modification was made to the model proposed by Moro et al., 2010. The proposed equation was calibrated by simulating the experimental tests detailed in Section 4.4.1 and comparing the hydrogen concentrations predicted by the simulation with the experimental results for each strain level. Equation 4.5 starts at the same initial value as the model from Moro et al., 2010 when plastic strain is zero ($\kappa = 0$). Like this model, it increases rapidly and saturates at a relatively low strain level (approximately 8%), but with a lower saturation value, corresponding to 87% of the maximum trap density predicted in Moro et al., 2010. The saturation value of the function proposed in Moro et al., 2010 is equal to 5.36×10^{24} m^{-3} while it is equal to 4.67×10^{24} m^{-3} for the new N_T model. A comparison of the models is shown in Figure 4.18.

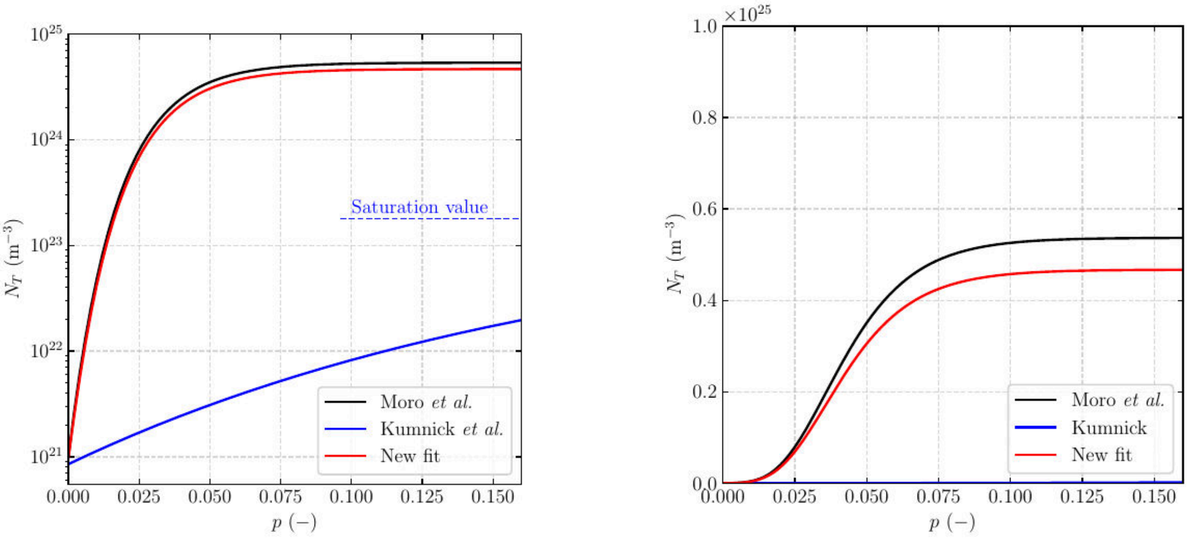

(a) Logarithmic scale.

(b) Normal scale.

Figure 4.18: Models for trap density evolution as a function of the accumulate plastic strain.

The model is then used to simulate the experimental conditions of the TDS tests. The following section presents a detailed comparison between the experimentally measured hydrogen content and the simulated results for each test condition.

4.6.2 Strain effect

This simulation model was designed to replicate the experimental conditions outlined in Section 4.4.1, using the same strain levels: 90%Rp02, 3%, 6%, and 12%, all applied at a strain rate of 1×10^{-4} s^{-1}. The loading phase durations for these tests were equal to 17, 300, 600, and 1,200 s, respectively. During the loading phase, a lattice hydrogen concentration (C_L) of 0.0021 wppm was applied to the specimen surfaces, corresponding to a hydrogen pressure of 85 bar.

As already mentioned, after the loading phase, a one-hour resting time was applied, during which the lattice hydrogen concentration was set to zero on the specimen's free surfaces to allow hydrogen desorption. Figure 4.19 compares the measured hydrogen concentrations from each test with the hydrogen content estimated by the simulation model. A summary of the test conditions and results is provided in Table 4.10.

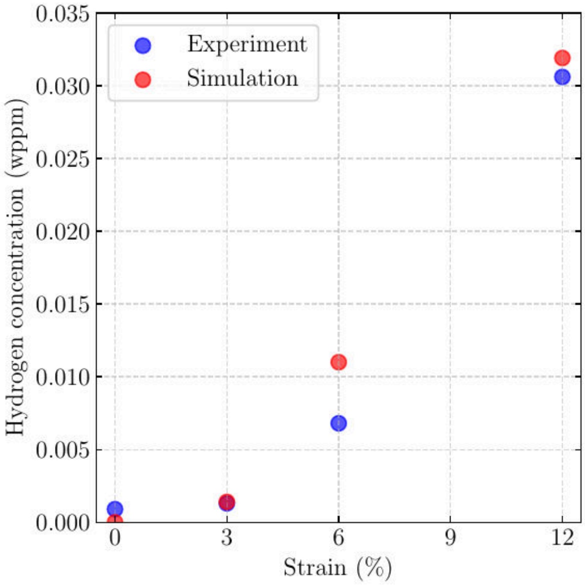

Figure 4.19: Comparison between experimental and numerical hydrogen concentrations measured for different strain levels.

Strain rate (s^{-1})	Strain (%)	Dwell	H concentration (wppm)	
			Experiment	Simulation
1×10^{-4}	12	No dwell	0.0306	0.0319
1×10^{-4}	6	No dwell	0.0068	0.0110
1×10^{-4}	3	No dwell	0.0013	0.0014
17 s	90%Rp02	No dwell	0.0009	0.0000

Table 4.10: Tests conditions and results at different strain levels.

The numerical results align well with experimental data, revealing a clear trend: higher plastic strain levels correspond to increased hydrogen content. High strain levels generate more dislocations, where hydrogen atoms get trapped, reducing diffusion. Figure 4.20 illustrates the total hydrogen concentration field (C) immediately after loading and before the one-hour resting period at the surface and the mid-section of the specimen. The specimen's center, where the maximum plastic strain occurs, also displayed the highest hydrogen concentrations. Additionally, in all tests, hydrogen diffusion did not reach the center of the specimen, with most hydrogen being located near the surface. Please note that for all cases, $C_L \ll C_T$, thus most of the total hydrogen concentration (C) corresponds to the trapped concentration.

The amount of hydrogen released from the specimen during the resting time can also be estimated from the numerical simulations. Table 4.11 summarizes these results across all cases. A clear trend emerges: as the strain level increases, the relative amount of hydrogen leaving the specimen during the resting time decreases. In cases without plastic strain, the trap density is minimal, so most of the hydrogen concentration corresponds to the lattice concentration, which can diffuse freely and exit the specimen during the resting time. Conversely, at higher plastic strain levels, additional traps form,

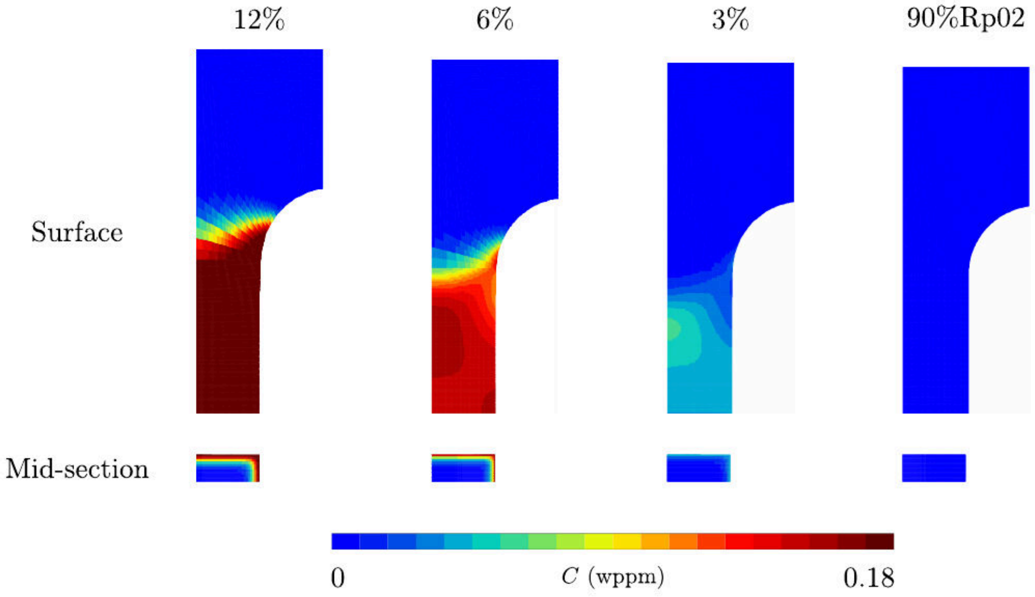

Figure 4.20: Surface front and cut bottom views of total hydrogen concentration (C) immediately after loading and before the resting time for different strain levels.

capturing hydrogen that cannot desorb under the same conditions; releasing this trapped hydrogen would require high temperatures, as in the TDS test. However, for the analyzed cases and considering this numerical model, at least 80% of hydrogen is released during the resting time.

Strain (%)	H concentration before 1h resting (wppm)	H concentration after 1h resting (wppm)	H remaining (%)
12	0.1562	0.0319	20.46
6	0.0797	0.0110	13.80
3	0.0307	0.0014	4.56
90%Rp02	0.0051	0.0000	0.00

Table 4.11: Comparison between the hydrogen content before and after one-hour resting across tests.

Figure 4.21 shows the total hydrogen concentration field immediately after loading and before the one-hour resting time and after one-hour resting time for the test deformed up to 12% strain. Before the resting time, most hydrogen is concentrated near the surface, as previously noted. After resting, part of the hydrogen content of the specimen was able to desorb. Meanwhile, the remaining hydrogen within the specimen continued to diffuse inward until reaching the specimen's center.

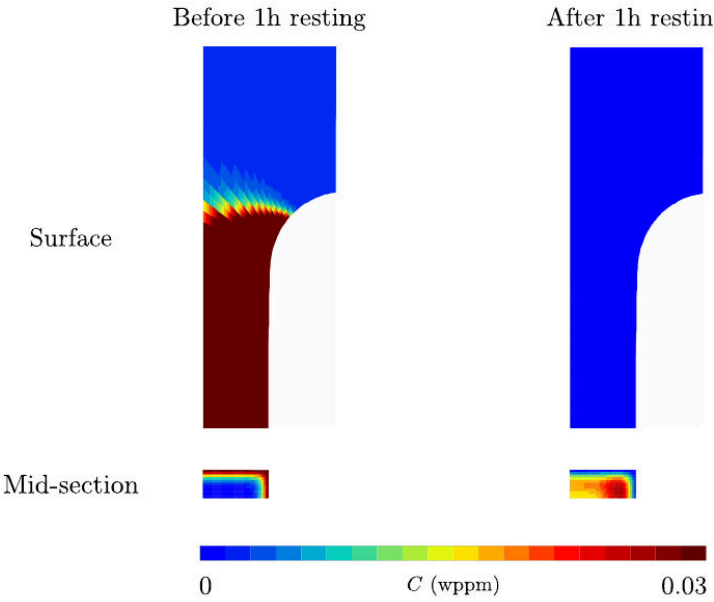

Figure 4.21: Surface front and cut bottom views of the total total hydrogen concentration before and after the one-hour resting time at 12% strain.

4.6.3 Strain rate effect

As in the previous case, a comparison between the experimental and numerical results was conducted at three strain rates: 1×10^{-3}, 1×10^{-4}, and 1×10^{-5} s^{-1} with loading durations of 120, 1,200 and 12,000 s, respectively. No dwell time was applied in all cases, but a one-hour resting time was considered after loading. The results are summarized in Figure 4.22 and Table 4.12.

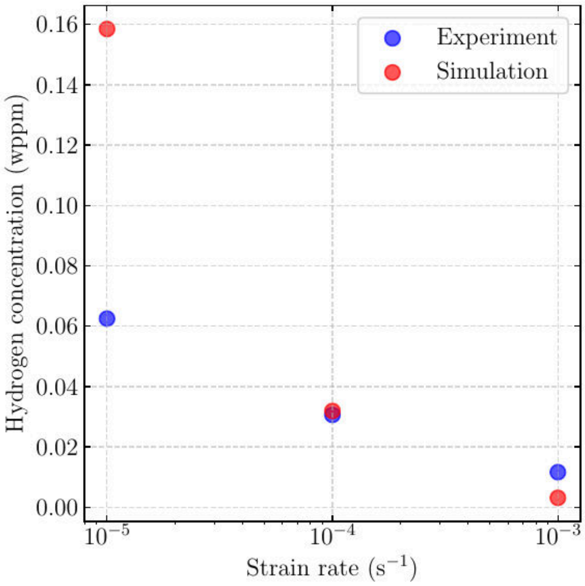

Figure 4.22: Comparison between experimental and numerical hydrogen concentrations measured at different strain rates.

The results indicate that the model accurately predicts hydrogen content for the two higher strain rates (1×10^{-4} and 1×10^{-3} s^{-1}). However, for the slowest strain rate (1×10^{-5} s^{-1}), the model

Strain rate (s^{-1})	Strain (%)	Dwell	H concentration (wppm)	
			Experiment	Simulation
1×10^{-3}	12	No dwell	0.0116	0.0031
1×10^{-4}	12	No dwell	0.0306	0.0319
1×10^{-5}	12	No dwell	0.0625	0.1585

Table 4.12: Tests conditions and results at different strain rates.

overestimates the hydrogen content by a factor of 2.5. Despite this discrepancy, the model successfully captures the experimental trend: lower strain rates lead to higher hydrogen content, as hydrogen has more time to diffuse throughout the material.

Figure 4.23 illustrates the hydrogen distribution across the specimen immediately after loading and before resting for each of the three tested strain rates. In the the fastest test, hydrogen diffusion was limited by the fast loading, resulting in hydrogen being located near the specimen's surface. Conversely, in slowest test, hydrogen had sufficient time to diffuse throughout the specimen, reaching the center.

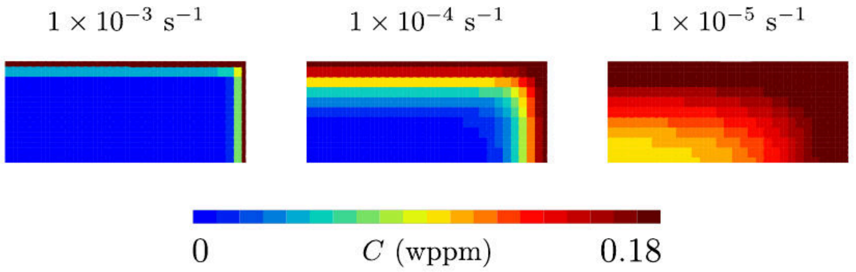

Figure 4.23: Mid-section view of the total hydrogen concentration immediately after loading and before resting at different strain rates. All tests were conducted until 12% strain and without dwell times (see Table 4.12.)

Figure 4.24 presents the hydrogen content in each specimen after the one-hour resting period, during which most of the hydrogen was able to desorb. The remaining hydrogen continued to diffuse towards the specimen's center. As expected, test at the slowest strain rate (1×10^{-5} s^{-1}) exhibited the highest hydrogen concentration.

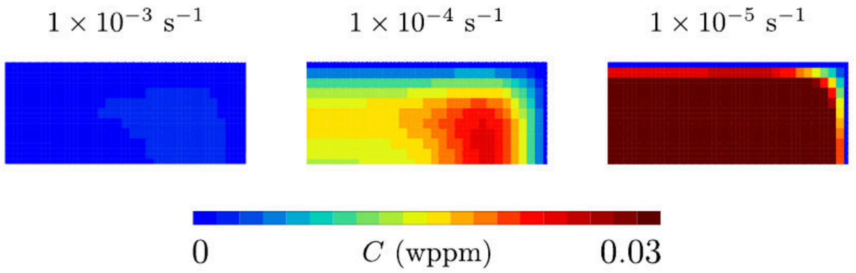

Figure 4.24: Mid-section view of the total hydrogen concentration after one-hour resting at different strain rates.

4.6.4 Dwell time effect

Figure 4.25 compares experimental and numerical results for TDS tests conducted at strain levels of 3% and 6% with and without dwell times, at a strain rate of 1×10^{-4} s^{-1}. For tests without dwell times, loading durations were equal to 17, 300 and 600 s, respectively. For tests considering dwell times, the loading duration was extended to 1,200 s to allow for increased hydrogen exposure. Following loading, all samples were held for one-hour resting period, which resulted in hydrogen desorption before hydrogen measurement.

The numerical results align with the experimental data, showing two trends: (i) introducing a dwell time leads to higher hydrogen concentrations, as the prolonged exposure allows more hydrogen to diffuse into the material; (ii) higher strain levels also result in increased hydrogen concentrations due to the generation of additional trapping sites, as described by Equation 4.5. These findings illustrate the impact of both strain rate and dwell time on hydrogen uptake and diffusion. However, the current model tends to underestimate the hydrogen concentration in the specimen loaded to 90%Rp02. In this case, the model predicts that the hydrogen content after loading and a one-hour resting period is zero. Table 4.13 summarizes the results.

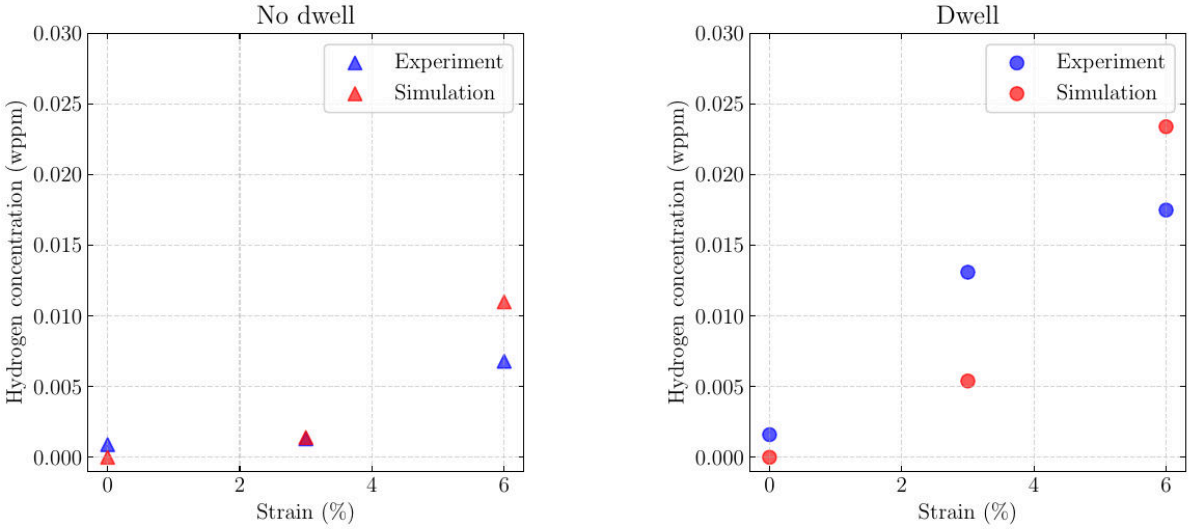

Figure 4.25: Comparison between experimental and numerical hydrogen concentrations measured without and with dwell times at 1×10^{-4} s^{-1}.

Strain rate (s^{-1})	Strain (%)	Dwell	H concentration (wppm)	
			Experiment	Simulation
17 s	90%Rp02	No dwell	0.0009	0.0000
17 s	90%Rp02	Dwell	0.0016	0.0000
1×10^{-4}	3	No dwell	0.0013	0.0014
1×10^{-4}	3	Dwell	0.0131	0.0054
1×10^{-4}	6	No dwell	0.0068	0.0110
1×10^{-4}	6	Dwell	0.0175	0.0234

Table 4.13: Tests conditions and results without and with dwell times at 1×10^{-4} s^{-1}.

Similar to the experimental test, an analysis was conducted for specimens deformed up to 3% with and without dwell times, at strain rates of 1×10^{-5} and 1×10^{-4} s^{-1}. The results presented in Figure 4.26 indicate that while the model tends to underestimate the hydrogen content for the analyzed cases, it effectively captures the relationship between strain, strain rate, and hydrogen uptake. The simulated values remain close to the experimental data, preserving consistency with the experimental order of magnitude for hydrogen concentration. Table 4.14 summarizes these results.

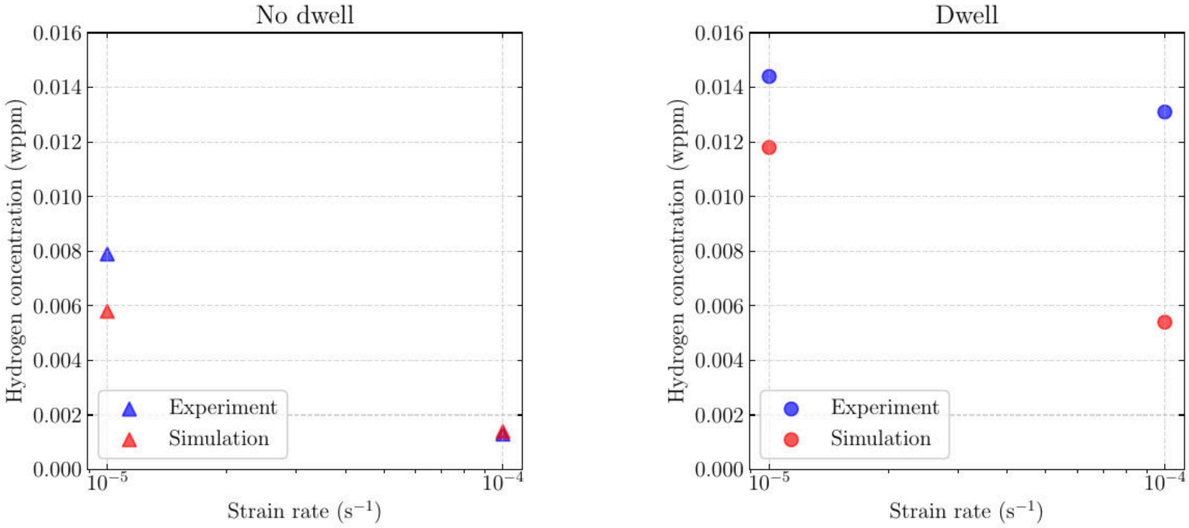

Figure 4.26: Comparison between experimental and numerical hydrogen concentrations measured at 3% strain without and with dwell times at 1×10^{-5} and 1×10^{-4} s^{-1}.

Strain rate (s^{-1})	Strain (%)	Dwell	H concentration (wppm)	
			Experiment	Simulation
1×10^{-5}	3	No dwell	0.0079	0.0058
1×10^{-5}	3	Dwell	0.0144	0.0118
1×10^{-4}	3	No dwell	0.0013	0.0014
1×10^{-4}	3	Dwell	0.0131	0.0054

Table 4.14: Tests conditions and results for tests at 3% strain without and with dwell times at 1×10^{-5} and 1×10^{-4} s^{-1}.

Figure 4.27 compares the total hydrogen concentration profiles after loading and one-hour resting for the tests of Table 4.14. The results demonstrate that, at the same strain level, the specimen maintained in a hydrogen environment exhibited a higher hydrogen concentration due to its prolonged exposure time, allowing for greater hydrogen uptake.

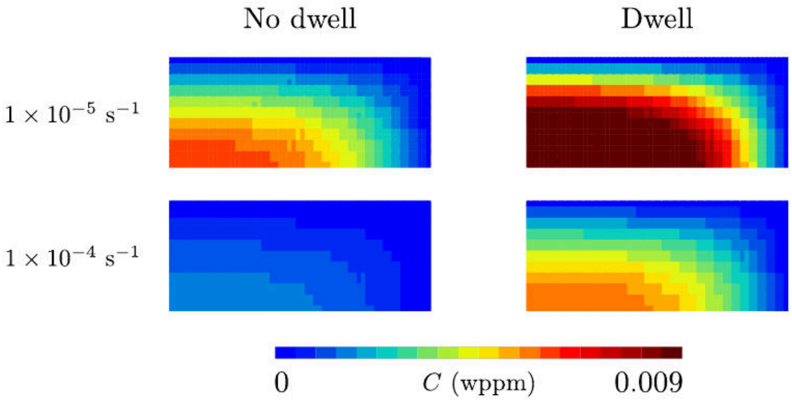

Figure 4.27: Mid-section view of the total hydrogen concentration profiles at 3% strain with and without dwell. after loading and one-hour resting.

4.7 Conclusions

This chapter presented a comprehensive analysis of experimental results and numerical simulations related to Thermal Desorption Spectroscopy (TDS). Prior to the TDS, tensile tests were conducted using flat specimens under a gaseous hydrogen environment to examine the influence of various test conditions, including strain level, strain rate, and dwell time, on the hydrogen absorption of the specimens. The TDS tests were then carried out, and from its results, the total hydrogen concentration for each test condition was estimated.

The numerical model used in this study couples hydrogen diffusion and plasticity and it focuses on a single type of hydrogen trap, specifically dislocations, which evolve with increasing plastic strain. While this approach simplifies the analysis, models incorporating multiple types of traps could also be used, although at the cost of higher complexity and a greater number of material coefficients. The trap density employed in this study was derived using functions from the literature. The model was adjusted for the studied material in order to provide the desired results and trends, but remains very close to that proposed by Moro et al., 2010. Hydrogen boundary conditions were defined using Sieverts' law, based on the hydrogen pressure in the gas phase.

The results reveal several key trends: higher strain levels lead to increased hydrogen concentrations due to a greater number of available traps. Moreover, as strain levels rise, less hydrogen desorbs during the resting phase. Tests at lower strain rates showed greater hydrogen uptake, as hydrogen had more time to diffuse into the material. Introducing a dwell time further increased hydrogen concentration, as prolonged exposure allowed for more diffusion. However, in two tests where specimens were kept in a hydrogen environment for the same interval, the specimen with a higher strain also showed the highest hydrogen concentration, emphasizing the impact of strain on hydrogen absorption.

The numerical simulations showed good agreement with the experimental data, successfully reproducing the relationships between strain, strain rate, dwell time, and hydrogen concentration. These results demonstrate the model's capability to predict hydrogen behavior under varying test conditions and provide valuable insights into the interactions between hydrogen and structural materials.

5

Simulation of hydrogen embrittlement of steel

This chapter is based on a paper published in the European Journal of Mechanics / A Solids (Lopes Pinto et al., 2023).

Abstract This study proposes a new simulation approach for hydrogen embrittlement using a multi-field finite element method with displacements, pressure, volume variation, nonlocal damage variables, and lattice hydrogen concentration as key unknowns. The material behavior is described by a modified Gurson–Tvergaard–Needleman (GTN) model that incorporates hydrogen-enhanced decohesion (HEDE), with a fully implicit finite element formulation. A mixed pressure/volume variation formulation addresses volumetric locking, facilitating pressure gradient calculations that drive hydrogen diffusion, while an implicit gradient nonlocal formulation manages mesh-size dependence. Damage is controlled by plastic volume variation and accumulated plastic strain, guiding void nucleation. The model is applied to an experimental database, accurately replicating key findings on tensile failure rates, fracture transitions, toughness reductions, fracture locations, and pressurization rate effects in disk tests.

Résumé Cette étude propose une nouvelle approche de simulation de la fragilisation par l'hydrogène à l'aide d'une méthode d'éléments finis multi-champs avec les déplacements, la pression, la variation de volume, les variables d'endommagement non locales et la concentration d'hydrogène dans le réseau en tant qu'inconnues du problème. Le comportement du matériau est décrit par un modèle Gurson-Tvergaard-Needleman (GTN) modifié qui incorpore la décohésion dû l'hydrogène (HEDE), avec une formulation d'éléments finis entièrement implicite. Une formulation mixte de variation de pression/volume prend en compte le verrouillage volumétrique, facilitant les calculs de gradient de pression qui entraînent la diffusion de l'hydrogène, tandis qu'une formulation nonlocale de gradient implicite gère la dépendance de la taille des mailles. L'endommagement est contrôlé par la variation du volume plastique et la déformation plastique accumulée, guidant la nucléation des vides. Le modèle est appliqué à une base de données expérimentale, reproduisant les principaux résultats: l'impact du taux de déformation sur la rupture des éprouvettes de traction, la transition de rupture de surface à interne avec l'augmentation du taux de déformation, la forte diminution de la ténacité en présence d'hydrogène, la localisation de la fracture et l'effet du taux de pressurisation dans les tests sur disque

Contents

5.1 Introduction

As global power demand continues to rise and the urgency to address climate change increases, there is a growing need for alternative energy sources that can contribute to decarbonization efforts. Hydrogen, produced from water via renewable or nuclear energy, is emerging as a promising solution due to its potential as a clean, renewable energy vector (Abbasi and Abbasi, 2011; Meibom and Karlsson, 2010). It holds significant promise for helping to decarbonize the energy sector and achieve climate targets.

However, one critical challenge in using hydrogen as an energy vector is its tendency to diffuse through metals and accumulate at high-stress areas, leading to premature failures characterized by decreased ductility and toughness. This phenomenon, known as hydrogen embrittlement (HE) (Hirth, 1980; Robertson et al., 2015; Sofronis and McMeeking, 1989), involves a complex combination of mechanical and chemical factors. Understanding hydrogen embrittlement and the long-term behavior of metals in power generation and transmission infrastructure is therefore essential to ensure their safety and reliability.

Hydrogen embrittlement has been widely studied, with several mechanisms proposed to explain its effects. These include Hydrogen Enhanced Localized Plasticity (HELP) (Barnoush and Vehoff, 2010; Beachem, 1972; Ferreira et al., 1999), Hydrogen Enhanced Decohesion (HEDE) (Gerberich et al., 2013; Troiano, 2016), and Hydrogen Enhanced Strain-Induced Vacancy (HESIV) (Nagumo et al., 2001). The HELP mechanism suggests that hydrogen increases dislocation mobility near crack tips, locally enhancing plasticity, which reduces fracture toughness and increases susceptibility to brittle fracture. The HEDE mechanism supposes that hydrogen weakens the atomic bonds in the material lattice, leading to atom separation. In the HESIV mechanism, hydrogen enhances vacancy formation in the metal lattice, weakening the material and making it more prone to fracture (Depraetere et al., 2021; Nagumo, 2004). These mechanisms can act independently or concurrently, leading to a deterioration of mechanical properties in hydrogen-exposed metals. However, further research is still necessary to fully understand these interactions and develop strategies to prevent hydrogen embrittlement.

Accurately modeling hydrogen embrittlement requires accounting for its degradation of material properties, specifically through damage mechanisms influenced by hydrogen concentration. One approach is the Cohesive Zone Modeling (CZM), which has been widely used in hydrogen embrittlement simulations at the continuum level (Ahn et al., 2007; Jemblie et al., 2017; Xia et al., 2019). In the CZM method, cohesive elements are introduced along a predefined crack path, with the cohesive strength decreasing as hydrogen concentration increases. An alternative approach is the phase-field method, which has been explored in recent studies (Martínez-Pañeda et al., 2018). This method represents the material as a continuous field governed by partial differential equations that describe hydrogen diffusion and the mechanical response. Both the phase-field and CZM approaches are commonly used to describe the HEDE mechanism. The Gurson–Tvergaard–Needleman (GTN) model, a widely used micromechanical framework for ductile fracture, has also been adapted to include hydrogen embrittlement effects (Depraetere et al., 2021; Lin et al., 2022; Yu et al., 2019). In some studies, the GTN model has been coupled with CZM to describe both ductile and hydrogen-induced quasi-brittle fractures (Lin et al., 2022).

In this study, a finite element strategy is proposed to simulate hydrogen embrittlement using the GTN model, modified to account for hydrogen's effects. The simulation approach integrates plasticity and damage while considering hydrogen diffusion. To avoid volumetric locking, a mixed formulation in displacement, pressure, and volume variation is employed (Bellet, 1999; Taylor, 2000; Y. Zhang et al., 2017), allowing for better evaluation of hydrostatic pressure, which plays a key role in both damage growth and hydrogen diffusion. To address mesh dependency in damage models, an implicit gradient nonlocal formulation with two internal lengths is used (Peerlings et al., 1996; Seupel et al., 2020; Tuhami et al., 2022), providing regularization for void growth and strain-controlled nucleation, thereby improving the reliability of hydrogen embrittlement simulations.

This chapter is structured as follows: Section 5.2 introduces the formulation of the nonlocal Gurson–Tvergaard–Needleman (GTN) model. Section 5.3 presents the hydrogen transport equations, the coupling of these equations with the GTN model, and a review of various hypotheses from the literature. Section 5.4 details the finite element implementation of the proposed framework. Section 5.5 specifically addresses the boundary conditions of hydrogen diffusion. Finally, Sections 5.6 and 5.7 present the simulations used to validate the proposed model and compare the results to existing experimental data, with particular emphasis on the impact of loading methods and boundary conditions.

5.2 Nonlocal GTN model

The GTN model, like other continuum damage models, introduces material softening leading up to failure. This softening behavior results in pathological mesh dependence when implemented in standard displacement-based finite element formulations. The issue arises from the formation of localized strain and damage bands with an indeterminate width (Rice, 1976; Rudnicki and Rice, 1975; Tvergaard, 1982). To address this problem, nonlocal models are often employed, as they incorporate material internal length scales that are absent in conventional damage models. Several approaches have been proposed in the literature to address this issue, particularly in the context of ductile fracture, and a brief review of these solutions is provided below.

The first solution involves local enrichment by embedding a finite thickness band, as proposed by Huespe et al., 2009. This band is introduced when localization is detected, following the bifurcation analysis outlined by Rice, 1976, which also determines the orientation of the newly formed band.

Another effective approach is the implicit gradient model (Hütter et al., 2013; Javani et al., 2016; Leclerc et al., 2020; Linse et al., 2012; Mediavilla et al., 2006; Seupel et al., 2020), which provides a straightforward means of incorporating material length scales. Peerlings et al., 1996 interpret this model as an approximation of the integral methods originally proposed by Pijaudier-Cabot and Bažant, 1987 for quasi-brittle materials, although it is also applicable to ductile fracture (Enakoutsa et al., 2007; Tvergaard and Needleman, 1995).

Micromorphic models (Forest, 2009) represent another approach for modeling ductile failure, as demonstrated by Brepols et al., 2017 and Diamantopoulou et al., 2017. Additionally, a gradient-enhanced energy (GEE) model has been proposed for ductile failure (Chen et al., 2020; Y. Zhang et al., 2017). This model employs the accumulated plastic strain, defined both locally (at the Gauss point) and globally. To weakly enforce the equivalence between these two representations of the same physical quantity, Lagrange multipliers are employed. The free energy is formulated to penalize steep gradients, leading to regularization. Scherer et al., 2020 demonstrated that this model can be viewed as a limit case of the micromorphic model, where the micromorphic variable and its counterpart are constrained to be equal.

Finally, phase-field models have also been adopted, initially designed to describe brittle failure (Tanné et al., 2018) and later extended to ductile failure (Ambati et al., 2015; Eldahshan et al., 2021; Miehe et al., 2016). Furthermore, this same framework has been utilized for modeling hydrogen embrittlement in metals, as discussed in Martínez-Pañeda et al., 2018.

In this study, a nonlocal GTN model based on the implicit gradient formulation integrating two material lengths, as proposed by Tuhami et al., 2022, is employed. This model features two nonlocal variables related to the plastic volume change and the accumulated plastic strain. Based on the formulation of the GTN model proposed by Besson et al., 2001, an effective scalar stress σ_* is implicitly defined as follows:

$$\Phi = \frac{\sigma_{\text{eq}}^2}{\sigma_*^2} + 2q_1 f_* \cosh\left(\frac{q_2}{2}\frac{\sigma_{ii}}{\sigma_*}\right) - 1 - q_1^2 f_*^2 \overset{\text{def. } \sigma_*}{=} 0 \tag{5.1}$$

where σ_{eq} is the von Mises stress, σ_{ii} is the trace of the stress tensor $\boldsymbol{\sigma}$, f_* is the effective porosity and q_1 and q_2 are model parameters. The yield surface is the given by:

$$\Phi = \sigma_* - \sigma_F(\kappa) \tag{5.2}$$

where σ_F is the flow stress, defined as a function of the accumulated plastic strain κ. The plastic flow is derived by applying the normality rule, and the plastic strain rate tensor is expressed as:

$$\dot{\boldsymbol{\varepsilon}}_p = (1 - f_g)\dot{\kappa}\frac{\partial \Phi}{\partial \boldsymbol{\sigma}} = (1 - f_g)\dot{\kappa}\frac{\partial \sigma_*}{\partial \boldsymbol{\sigma}} \tag{5.3}$$

where f_g represents the porosity resulting from void growth. Noting that σ_* is a homogeneous function of degree 1 with respect to $\boldsymbol{\sigma}$, it follows from Euler's Lemma that:

$$\dot{\boldsymbol{\varepsilon}}_p : \boldsymbol{\sigma} = (1 - f_g)\dot{\kappa}\sigma_* \tag{5.4}$$

In this study, the material is considered to exhibit slight rate dependence, leading to the expression for

$\dot{\kappa}$ as:

$$\dot{\kappa} = \mathcal{F}(\Phi) = \dot{\kappa_0} \left\langle \frac{\sigma_* - \sigma_F(\kappa)}{K} \right\rangle^n \tag{5.5}$$

where $\dot{\kappa_0}, K$ and n are material parameters. An additive strain decomposition is used so that the strain tensor is expressed as:

$$\boldsymbol{\varepsilon} = \boldsymbol{\varepsilon}_e + \boldsymbol{\varepsilon}_p \tag{5.6}$$

where $\boldsymbol{\varepsilon}_e$ and $\boldsymbol{\varepsilon}_p$ are respectively the elastic and the plastic strain tensors. The stress tensor is given by:

$$\boldsymbol{\sigma} = \mathbb{E} : \boldsymbol{\varepsilon}_e \tag{5.7}$$

where $\mathbb{E}$ is the fourth order elasticity tensor. A fully implicit finite strain framework is considered.

To address damage localization, a nonlocal formulation incorporating two internal length scales is used to regularize two key state variables: the plastic volume variation ($\omega = \text{trace}(\boldsymbol{\varepsilon}_p)$) and the accumulated plastic strain (κ), as proposed by Tuhami et al., 2022. The nonlocal counterparts of these variables are denoted as $\bar{\omega}$ and $\bar{\kappa}$. Their evolution within the material body Ω is governed by the following Helmholtz-type equations:

$$\bar{\omega} - \ell_\omega^2 \Delta\bar{\omega} = \omega \quad \text{in} \quad \Omega \tag{5.8}$$

$$\bar{\kappa} - \ell_\kappa^2 \Delta\bar{\kappa} = \kappa \quad \text{in} \quad \Omega \tag{5.9}$$

where ℓ_ω and ℓ_κ are two characteristic lengths, respectively associated to void growth and nucleation mechanisms. The following natural boundary conditions are used:

$$\boldsymbol{\nabla}\bar{\omega} \cdot \boldsymbol{n} = 0 \quad \text{on} \quad \partial\Omega \tag{5.10}$$

$$\boldsymbol{\nabla}\bar{\kappa} \cdot \boldsymbol{n} = 0 \quad \text{on} \quad \partial\Omega \tag{5.11}$$

where $\partial\Omega$ corresponds to the boundary of the body Ω and $\boldsymbol{n}$ is the normal vector to the surface of the considered body. The nonlocal variables $\bar{\omega}$ and $\bar{\kappa}$ are then used to formulate the evolution of the damage variables for void growth ($\dot{f}_g$) and nucleation ($\dot{f}_n$), as follows:

$$\dot{f}_g = (1 - f_g)\dot{\bar{\omega}} \tag{5.12}$$

$$\dot{f}_n = A_n(\bar{\kappa})\dot{\bar{\kappa}} \tag{5.13}$$

where A_n represents the damage nucleation rate. Several nucleation models have been proposed in the literature. Chu and Needleman, 1980 assumed that nucleation strain follows a normal distribution. Dalloz et al., 2009 suggested a nucleation rate dependent on stress triaxiality, while Petit et al., 2019 introduced a model based on the maximum principal stress. Other forms of nucleation rates also exist. As discussed in Tuhami et al., 2022, Equation 5.12 slightly differs from the original formulation, where $\dot{f}_g$ is expressed as $\dot{f}_g = (1 - f_g - f_n)\dot{\bar{\omega}}$. This modification reflects the fact that nucleation on primary inclusions (such as MnS, TiN, and oxides in steel) occurs in the early stages of deformation, with their volume fraction typically incorporated as the initial porosity f_0. In this study, the damage nucleation rate is assumed as follows:

$$A_n(\bar{\kappa}) = \begin{cases} A_n^0, & \text{if } \bar{\kappa} \geq \bar{\kappa}_c \\ 0, & \text{otherwise} \end{cases} \tag{5.14}$$

where $\bar{\kappa}_c$ represents the critical (nonlocal) plastic strain that triggers secondary void nucleation. The total damage within the material is then given by:

$$f_t = f_g + f_n \tag{5.15}$$

The effective porosity f_* from Equation 5.1 is defined as:

$$f^* = \begin{cases} f_t, & f_t \leq f_c \\ f_c + \frac{f_R^* - f_c}{f_R - f_c}(f - f_c), & f_t > f_c \end{cases} \tag{5.16}$$

where f_c is the porosity on the onset of void coalescence and f_R is the porosity at failure. Failure occurs when $f_* = 1/q_1$.

It is important to highlight that employing the implicit gradient model to represent both damage and strain gradient plasticity can result in inconsistencies, as noted by Forest, 2009 and Peerlings et al., 2012. Within the current framework, this inconsistency would manifest as expressing σ_F as a function of $\bar{\kappa}$ rather than as a function of κ in Equation 5.2. If strain gradient plasticity effects are to be considered as in Martínez-Pañeda et al., 2016, micromorphic models or gradient enhanced models could be used to simultaneously deal with damage. They, however, offer less flexibility if several nonlocal variables are used. Using the present model, possible hardening due to plasticity gradients close to notches or cracks is not represented.

5.3 Hydrogen embrittlement modeling

Hydrogen embrittlement (HE) is a complex, multidisciplinary phenomenon involving multiple processes, such as plastic deformation, hydrogen diffusion, and material damage. To accurately and effectively simulate HE in steels, any model must account for all these factors. A comprehensive HE model not only predicts hydrogen-assisted failure but also estimates the hydrogen distribution within the material, aiding in the interpretation and understanding of experimental results. This section introduces the model used to simulate HE, incorporating all the previously mentioned aspects.

5.3.1 Hydrogen transport

The model employed in this study was previously introduced in Section 2.4.4. For a detailed explanation, please refer to that section.

5.3.2 Coupling with the GTN model

The Hydrogen-Enhanced Localized Plasticity (HELP) mechanism is often associated to material softening due to its influence on dislocation motion and interactions within the material. Hydrogen atoms reduce the energy barriers for dislocation movement by weakening atomic bonds in the metal lattice. This facilitates dislocation mobility, leading to plastic deformation at lower applied stresses than in hydrogen-free conditions. In this way, hydrogen effectively softens the material, making it more prone to plastic flow.

To model the HELP mechanism, Ahn et al., 2007 proposed that the flow stress of the material should be a decreasing function of hydrogen concentration. Accordingly, the flow stress can be expressed as:

$$\sigma_F(\kappa, C) = \sigma_F^0(\kappa) \times \lambda(C) \tag{5.17}$$

where $\sigma_F^0(\kappa)$ represents the flow stress in the absence of hydrogen, and ξ is an *ad hoc* function introduced to capture the effects of hydrogen. The yield surface, as defined in Equation 5.2, for the voided solid is now expressed as:

$$\Phi = \sigma_* - \sigma_F(\kappa, C) \tag{5.18}$$

In the work of Faleskog et al., 1998, unit cell simulations demonstrated that the GTN model's coefficients q_1 and q_2 depend on the material hardening, which is influenced by the hydrogen concentration C. Variations in q_1 and q_2 directly impact void growth kinetics. Additionally, hydrogen diffusion at the microscale around voids can further modify these kinetics, potentially leading to earlier failure (Ahn et al., 2007; Yu et al., 2019). Depraetere et al., 2021 proposed modifying the void growth rate as:

$$\dot{f}_g = \dot{f}_g^0(1 + k_g^L C_L + k_g^T C_T) \tag{5.19}$$

where $\dot{f}_g^0$ represents the kinetics in the absence of hydrogen, while k_g^L and k_g^T are coefficients to be determined. This approach assumes that q_1 and q_2 remain constant and can be fitted using hydrogen-free materials. Similarly, Lin et al., 2022 adopted this formulation but without distinguishing between C_L and C_T, leading to:

$$\dot{f}_g = \dot{f}_g^0(1 + k_g C) \tag{5.20}$$

where k_g is another coefficient to be fitted. Using these modified expressions, the original void growth rate equation, $\dot{f}_g = (1 - f_g)\mathrm{trace}(\dot{\varepsilon}_p)$, no longer applies. As this equation represents mass conservation, modifying it could be undesirable. Therefore, it is proposed in this study to express q_1 and q_2 as functions of C (or possibly C_L and C_T), to more accurately represent the accelerated void growth in the presence of hydrogen.

Building on the work of Depraetere et al., 2021, the nucleation rate can also be modified. Following similar principles applied to growth, it is proposed that the nucleation rate in the presence of hydrogen be expressed as:

$$\dot{f}_n = \dot{f}_n^0(1 + k_n^L C_L + k_n^T C_T). \tag{5.21}$$

Alternatively, as presented by Lin et al., 2022, this can be simplified to:

$$\dot{f}_n = \dot{f}_n^0(1 + k_n C) \tag{5.22}$$

where $\dot{f}_n^0$ represents the nucleation rate in the absence of hydrogen, and k_n^L, k_n^T, and k_n are parameters that need to be calibrated.

In steels, nucleation is associated with the cracking or debonding of iron carbides, as coarse inclusions (such as MnS, CaS, TiN, etc.) are expected to debond or crack at the onset of plasticity, corresponding to the initial porosity of the material. Hydrogen may facilitate these processes, which is why the approach proposed by Depraetere et al., 2021 will also be employed in this study. Furthermore, hydrogen Enhanced Dechohesion (HEDE) is proposed to be characterized by the nucleation of damage. Since this mechanism is not present in hydrogen-free materials, a specific term must be incorporated. Therefore, the following nucleation kinetics is proposed:

$$\dot{f}_n = A_n(\bar{\kappa}) \times \xi(C)\dot{\bar{\kappa}} + B_n(\sigma_I, C)\dot{\bar{\kappa}} \tag{5.23}$$

where A_n represents the nucleation of carbides and is assumed to be strain-controlled. The term λ denotes the acceleration of nucleation induced by hydrogen, while B_n corresponds to hydrogen Enhanced Decohesion (HEDE) and is assumed to be dependent on the maximum principal stress σ_I, which accounts for the quasi-brittle nature associated with this damage mechanism, and on the total hydrogen concentration C. The trap density (N_T) is expressed as a function of the nonlocal accumulated plastic strain $\bar{\kappa}$, which mitigates strong localization of C_T and allows for consistent control of damage nucleation.

This section presents a comprehensive framework that enables the coupling of the GTN model with hydrogen embrittlement. However, it is important to note that not all options need to be utilized simultaneously. For instance, in scenarios where quasi-brittle failure is the primary failure mechanism, the model can be simplified by setting $q_2 = 0$ (no void growth), neglecting ductile damage nucleation ($A_n = 0$), and employing an *ad hoc* B_n function to represent damage evolution. This coupling also enables the description of the transition from pure ductile failure to pure quasi-brittle failure within a single model, which is crucial for accurately representing the effects of loading rate on the failure mode.

5.4 Finite element formulation

Since hydrogen diffusion depends on the pressure gradient and the material's plastic behavior can be affected by hydrogen content, it is essential to model the interaction between mechanics and diffusion. This coupling is commonly achieved using a staggered scheme. First, the incremental mechanical problem is solved for fixed values of lattice (C_L) and trapped (C_T) hydrogen concentrations at each time step, which allows the calculation of the pressure ($p = \frac{1}{3}\text{trace}(\boldsymbol{\sigma})$). However, since pressure is evaluated at integration points, it must be extrapolated to the nodes to compute the pressure gradient using the shape function derivatives, as in Krom et al., 1999. This gradient is then used as input for solving the incremental diffusion problem. The resulting hydrogen concentration field is subsequently used in the next mechanical loading step. This process is repeated iteratively.

This work adopts an alternative approach to solving the coupled diffusion/mechanics problem, utilizing mixed finite elements typically employed in cases where volumetric locking occurs (Al Akhrass et al., 2014; Bellet, 1999; Kasper and Taylor, 2000; Y. Zhang et al., 2017). All the implementations were carried out in the Z-set software. In this method, the nodal unknowns are displacement $\{\boldsymbol{u}\}$, pressure $\{p\}$, volume variation $\{\theta\}$, lattice hydrogen concentration $\{C_L\}$ and the nonlocal variables $\{\bar{\omega}\}$ (nonlocal plastic volume variation) and $\{\bar{\kappa}\}$ (nonlocal accumulated plastic strain). Displacements are interpolated using quadratic shape functions, $\{\boldsymbol{N}_q\}$, while all the other unkowns are interpolated with linear shape functions, $\{\boldsymbol{N}_l\}$. Since pressure is directly known at the nodes, its gradient can be computed without needing to interpolate from integration points. Figure 5.1 contains a schematic of a square element of the mesh with the degrees of freedom related to each node.

5.4.1 Constitutive equations implementation

Following the generic representation of constitutive equations proposed by Foerch et al., 1997, the implementation within the finite element code involves a time integration process that takes a set of

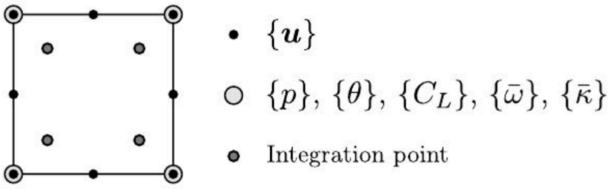

Figure 5.1: Degrees of freedom of the mixed formulation.

input variables ($\boldsymbol{V}_{IN}$) to derive the output variables ($\boldsymbol{V}_{OUT}$). Simultaneously, the variables representing the material's state ($\boldsymbol{V}_{int}$) are integrated. For the material model presented in this study, these data sets are defined as follows:

$$\boldsymbol{V}_{IN} = (\boldsymbol{\varepsilon}, \bar{\omega}, \bar{\kappa}, C_L, \boldsymbol{\nabla} C_L, \boldsymbol{\nabla} p) \tag{5.24}$$

$$\boldsymbol{V}_{OUT} = (\boldsymbol{\sigma}, \omega, \kappa, \boldsymbol{J}, h, H_{C_L}) \tag{5.25}$$

$$\boldsymbol{V}_{int} = (\boldsymbol{\varepsilon}_e, f_g, f_n, \omega, \kappa) \tag{5.26}$$

The evolution laws of the state variables can be expressed as functions of the rates of input variables:

$$\begin{cases} \dot{\boldsymbol{\varepsilon}}_e = \dot{\boldsymbol{\varepsilon}} - (1 - f_g)\dot{\kappa}\boldsymbol{n} \\ \dot{f}_g = \dot{\boldsymbol{\varepsilon}} - (1 - f_g)\dot{\bar{\kappa}} \\ \dot{f}_n = A_n(\bar{\kappa})\dot{\bar{\kappa}} \\ \dot{\omega} = (1 - f)\dot{\kappa}\mathrm{tr}(\boldsymbol{n}) \\ \dot{\kappa} = \mathcal{F}(\Phi) \end{cases} \tag{5.27}$$

The integration of the system of equations over a finite time step Δt using a fully implicit scheme requires solving the following set of nonlinear equations with respect to the increments of the state variables $\Delta \boldsymbol{V}_{int}$ for a given increment of the input variables $\Delta \boldsymbol{V}_{IN}$. For the differential equations under consideration, the residual equations are as follows:

$$\begin{cases} \boldsymbol{R}_e = \Delta\boldsymbol{\varepsilon}_e + (1 - f_g)\Delta\kappa\boldsymbol{n} - \Delta\boldsymbol{\varepsilon} \\ R_{f_g} = \Delta f_g - (1 - f_g)\Delta\bar{\omega} \\ R_{f_n} = \Delta f_n - A_n \Delta\bar{\kappa} \\ R_{\omega} = \Delta\omega - (1 - f_g)\Delta\kappa\mathrm{tr}(\boldsymbol{n}) \\ R_{\kappa} = \Delta\kappa - \mathcal{F}(\Phi)\Delta t \end{cases} \tag{5.28}$$

Solving the previous system with the Newton-Raphson method requires the evaluation of its Jacobian matrix, which is formally expressed as:

$$\boldsymbol{J} = \frac{\partial \boldsymbol{R}}{\partial \Delta \boldsymbol{V}_{int}} \tag{5.29}$$

where $\boldsymbol{R} = (\boldsymbol{R}_e, R_{f_g}, R_{f_n}, R_{\omega}, R_{\kappa})$. The Jacobian matrix, $\boldsymbol{J}$, can be efficiently computed in a block-wise manner. Further details on this computation are provided in Appendix C.

Solving the system of equations 5.28 yields the increments of the output variables, $\Delta \boldsymbol{V}_{OUT}$. This solution enables the numerical computation of the consistent tangent matrix, based on the principle that any small variation in the input variables induces corresponding changes in the state variables, ensuring that the residual equations remain satisfied. The consistent tangent matrix takes the form of a block matrix, expressed as:

$$\boldsymbol{M} = \frac{\partial \Delta \boldsymbol{V}_{OUT}}{\partial \Delta \boldsymbol{V}_{IN}} = \begin{pmatrix} \frac{\partial \Delta \sigma}{\partial \Delta \varepsilon} & \frac{\partial \Delta \sigma}{\partial \Delta \bar{\omega}} & \frac{\partial \Delta \sigma}{\partial \Delta \bar{\kappa}} & \cdots \\ \frac{\partial \Delta \omega}{\partial \Delta \varepsilon} & \frac{\partial \Delta \omega}{\partial \Delta \bar{\omega}} & \frac{\partial \Delta \omega}{\partial \Delta \bar{\kappa}} & \cdots \\ \frac{\partial \Delta \kappa}{\partial \Delta \varepsilon} & \frac{\partial \Delta \kappa}{\partial \Delta \bar{\omega}} & \frac{\partial \Delta \kappa}{\partial \Delta \bar{\kappa}} & \cdots \\ \cdots & \cdots & \cdots & \ddots \end{pmatrix} \tag{5.30}$$

The matrix $\boldsymbol{M}$ is used exclusively to compute the elementary stiffness matrix $\boldsymbol{K}$, which plays a key role in the iterative solution of the system. The constitutive equations are integrated using a fully implicit scheme. Further details on the methodology are provided in Appendix C.

5.4.2 Mixed formulation

Following Taylor, 2000, the virtual power principle for a mixed formulation can be expressed as:

$$\int_{\Omega} \left[\left(\mathbb{K} : \dot{\boldsymbol{\varepsilon}} + \frac{1}{3}\dot{\theta}\mathbb{1} \right) : \boldsymbol{\sigma}^{\star} + \dot{p}(\mathrm{trace}(\boldsymbol{\varepsilon}) - \theta) + (\mathrm{trace}(\dot{\boldsymbol{\varepsilon}}) - \dot{\theta})p \right] d\Omega + \dot{\Pi}_e = 0 \tag{5.31}$$

where $\mathbb{K}$ is the fourth-order tensor that associates a second-order tensor to its deviator. $\mathbb{1}$ is the unit second-order tensor. $\dot{\boldsymbol{\varepsilon}}$ is the symmetric part of the velocity gradient. $\dot{\Pi}_e$ represents the power of external forces and Ω is the volume of the body. The stress tensor $\boldsymbol{\sigma}^{\star}$ is obtained by integrating the constitutive equations using:

$$\dot{\boldsymbol{\varepsilon}}^{\star} = \mathbb{K} : \dot{\boldsymbol{\varepsilon}} + \frac{1}{3}\dot{\theta}\mathbb{1} \tag{5.32}$$

and,

$$\boldsymbol{\sigma}^{\star} = \mathbb{K} : \dot{\boldsymbol{\varepsilon}} + p\mathbb{1} \tag{5.33}$$

After rearranging Equation 5.31, it can be expressed as:

$$\int_{\Omega} \left[\dot{\boldsymbol{\varepsilon}} : \boldsymbol{\sigma} + \dot{\theta} \left(\frac{1}{3}\mathrm{trace}(\boldsymbol{\sigma}^{\star}) - p \right) + \dot{\kappa}(\mathrm{trace}(\boldsymbol{\varepsilon}) - \theta) \right] d\Omega + \dot{\Pi}_e = 0 \tag{5.34}$$

The solution is obtained using an incremental-iterative Newton method where the load steps are defined for time increments $[t_n, t_{n+1}]$, $\Delta t = t_{n+1} - t_n$. The values at the beginning and at the end of the increment are given with indexes n and $n+1$. A mid-increment scheme is adopted in which deformation rates are evaluated on the intermediate configuration $n + 1/2$, which is conditionally stable and second-order accurate. A finite strain formulation is used and the transformation gradient is computed as follows:

$$\boldsymbol{F} = \frac{\partial \boldsymbol{x}}{\partial \boldsymbol{X}} = \mathbb{1} + \boldsymbol{B}_F \cdot \{\boldsymbol{u}\} \tag{5.35}$$

with $\boldsymbol{x} = \boldsymbol{X} + \boldsymbol{u}$, where $\boldsymbol{X}$ and $\boldsymbol{x}$ are respectively the positions in the initial and final configurations and $\boldsymbol{u}$ is the displacement. The matrix $\boldsymbol{B}_F$ is constructed using the derivatives of the quadratic shape functions ($\boldsymbol{N}_q$) with respect to the initial configuration. $\boldsymbol{B}_F$ depends only on the initial element coordinates, and is therefore constant. Then, $\boldsymbol{F}$ can be expressed at mid-increments and end of increments, as follows:

$$\boldsymbol{F}_{n+1/2} = \mathbb{1} + \boldsymbol{B}_F \cdot \{\boldsymbol{u}\}_{n+1/2}, \quad \boldsymbol{F}_{n+1} = \mathbb{1} + \boldsymbol{B}_F \cdot \{\boldsymbol{u}\}_{n+1} \tag{5.36}$$

A polar decomposition is used to express the transformation gradients as follows:

$$\boldsymbol{F}_{n+1/2} = \boldsymbol{R}_{n+1/2} \cdot \boldsymbol{U}_{n+1/2}, \quad \boldsymbol{F}_{n+1} = \boldsymbol{R}_{n+1} \cdot \boldsymbol{U}_{n+1} \tag{5.37}$$

The deformation rate $\dot{\boldsymbol{\varepsilon}}$ (the symmetric part of the velocity gradient $\boldsymbol{L} = \partial\dot{\boldsymbol{u}}/\partial\boldsymbol{x}$) is expressed as:

$$\dot{\boldsymbol{\varepsilon}} = \boldsymbol{B} \cdot \{\dot{\boldsymbol{u}}\} \tag{5.38}$$

where $\boldsymbol{B}$ is computed using the derivatives of the quadratic shape functions with respect to the final configuration. The strain increment is then computed as:

$$\Delta\boldsymbol{\varepsilon} = \boldsymbol{B}_{n+1/2} \cdot (\{\boldsymbol{u}\}_{n+1} - \{\boldsymbol{u}\}_n) = \boldsymbol{B}_{n+1/2} \cdot \Delta\{\boldsymbol{u}\} \approx \dot{\boldsymbol{\varepsilon}}_{n+1/2}\Delta t \tag{5.39}$$

The matrix $\boldsymbol{B}_{n+1/2}$ is computed using the derivatives of the quadratic shape functions and the positions of the nodes at mid-increment. The volume variation is computed from θ using the linear shape functions as:

$$\theta = \boldsymbol{N}_l \cdot \{\theta\}, \quad \Delta\theta = \boldsymbol{N}_l \cdot (\{\theta\}_{n+1} - \{\theta\}_n) \tag{5.40}$$

where $\boldsymbol{N}_l$ is the vector of linear shape functions. The strain increment (Equation 5.39) can then be modified as follows:

$$\Delta\boldsymbol{\varepsilon}^\star = \mathbb{K} : \Delta\boldsymbol{\varepsilon} + \frac{1}{3}\Delta\theta\mathbb{1} \tag{5.41}$$

The modified strain increment is then rotated in the material unrotated configuration:

$$\Delta\boldsymbol{\varepsilon}^{\star\star} = \boldsymbol{R}^T_{\frac{1}{2}} \cdot \Delta\boldsymbol{\varepsilon}^\star \cdot \boldsymbol{R}_{\frac{1}{2}} \tag{5.42}$$

$\boldsymbol{\varepsilon}^{\star\star}$ is then used as the input strain for the constitutive equations, which provide the corresponding stress tensor $\boldsymbol{\sigma}^{\star\star}$, which is rotated to the end of the increment as follows:

$$\boldsymbol{\sigma}^\star = \boldsymbol{R} \cdot \boldsymbol{\sigma}^{\star\star} \cdot \boldsymbol{R}^T \tag{5.43}$$

Finally, a modified stress tensor corrected for pressure is computed:

$$\boldsymbol{\sigma} = \mathbb{K} : \boldsymbol{\sigma}^\star + p\mathbb{1} \quad \text{with} \quad p = \boldsymbol{N}_l \cdot \{p\} \tag{5.44}$$

The elementary forces for the degrees of freedom $\{\boldsymbol{u}\}$, $\{p\}$ and $\{\theta\}$ can then be defined from Equation 5.34 as follows:

$$\{\boldsymbol{F}\}_u = \int_{\Omega_e} \boldsymbol{B}^T \cdot \sigma \, d\Omega \tag{5.45}$$

$$\{\boldsymbol{F}\}_p = \int_{\Omega_e} (\text{trace}(\Delta\boldsymbol{\varepsilon}) - \Delta\theta)\boldsymbol{N}_l \, d\Omega \tag{5.46}$$

$$\{\boldsymbol{F}\}_\theta = \int_{\Omega_e} \left(\frac{1}{3}\text{trace}(\boldsymbol{\sigma}^\star) - p\right) \boldsymbol{N}_l \, d\Omega \tag{5.47}$$

$$\tag{5.48}$$

where Ω_e represents the volume of the element at the end of the increment. The volume integration is performed using a standard Gauss method.

Since in this formulation the pressure is a degree of freedom and is thus defined at the nodes, its gradient can be directly computed as:

$$\nabla p = \boldsymbol{G} \cdot \{p\} \tag{5.49}$$

where $\boldsymbol{G}$ is computed using the derivative of the linear shape functions and the nodal positions at the end of the increment. As previously discussed, ∇p is used as an input variable for the constitutive equations.

5.4.3 Nonlocal variables

Based on the boundary condition given by Equation 5.10, the weak form of Equation 5.8 is expressed as:

$$\int_{\Omega} [(\bar{\omega} - \omega)\bar{\omega}^* + \ell_\omega^2 \nabla\bar{\omega} \cdot \nabla\bar{\omega}^*] \, d\Omega = 0 \quad \forall \bar{\omega}^* \tag{5.50}$$

where $\bar{\omega}^*$ is an arbitrary test function. The corresponding elementary force for $\bar{\omega}$ is then:

$$\{\boldsymbol{F}\}_{\bar{\omega}} = \int_{\Omega_e} ((\bar{\omega} - \omega)\boldsymbol{N}_l + \ell_\omega^2 \boldsymbol{G}^T \cdot \boldsymbol{G} \cdot \{\bar{\omega}\}) \, d\Omega \tag{5.51}$$

where $\bar{\omega} = \boldsymbol{N}_l \cdot \{\bar{\omega}\}$. The exact same procedure is applied for $\bar{\kappa}$, then its elementary force is defined as:

$$\{\boldsymbol{F}\}_{\bar{\kappa}} = \int_{\Omega_e} ((\bar{\kappa} - \kappa)\boldsymbol{N}_l + \ell_\kappa^2 \boldsymbol{G}^T \cdot \boldsymbol{G} \cdot \{\bar{\kappa}\}) \, d\Omega \tag{5.52}$$

5.4.4 Hydrogen diffusion

From the principle of mass conservation, the rate of change of the total hydrogen concentration within a volume Ω is equal to the flux through a surface $\partial\Omega$. It can be expressed as follows:

$$\frac{d}{dt} \int_{\Omega} (C_L + C_T) \, d\Omega + \int_{\partial\Omega} \boldsymbol{J} \cdot \boldsymbol{n} \, dS = 0 \tag{5.53}$$

where $\boldsymbol{n}$ is the outward normal vector to Ω. Following the approach proposed in Sofronis and McMeeking, 1989, it is assumed that the solid body's deformation has a negligible impact on hydrogen diffusion. Using the divergence theorem, Equation 5.53 can rewritten in a local strong form as follows:

$$(1 + H_{C_L})\dot{C}_L + h + \text{div}(\boldsymbol{J}) = 0 \tag{5.54}$$

Multiplying Equation 5.54 by an arbitrary test function C_L^* and integrating over the volume of the body leads to the weak form of the problem:

$$\int_{\Omega} \left[(1 + H_{C_L}) \frac{dC_L}{dt} C_L^* + hC_L^* + \text{div}(\boldsymbol{J}) C_L^* \right] d\Omega = 0 \quad \forall C_L^* \tag{5.55}$$

Noting that

$$\text{div}(C_L^* \boldsymbol{J}) = \nabla C_L^* \boldsymbol{J} + C_L^* \text{div}(\boldsymbol{J}) \tag{5.56}$$

Equation 5.55 can be rewritten as:

$$\int_{\Omega} \left[(1 + H_{C_L}) \frac{dC_L}{dt} C_L^* + hC_L^* + \text{div}(C_L^* \boldsymbol{J}) - \nabla C_L^* \boldsymbol{J} \right] d\Omega = 0 \quad \forall C_L^* \tag{5.57}$$

or, using the divergence theorem:

$$\int_{\Omega} \left[(1 + H_{C_L}) \frac{dC_L}{dt} C_L^* + hC_L^* - \nabla C_L^* \boldsymbol{J} \right] d\Omega + \int_{\partial\Omega} C_L^* \boldsymbol{J} \cdot \boldsymbol{n} \;\, \partial\Omega = 0 \quad \forall C_L^* \tag{5.58}$$

This form can then be used to derive the finite element formulation of the problem. The lattice concentration is computed as:

$$C_L = \boldsymbol{N}_l \cdot \{C_L\}, \quad \text{with} \quad \nabla C_L = \boldsymbol{G} \cdot \{C_L\} \tag{5.59}$$

The term dC_L/dt in Equation 5.58 can be approximated as:

$$\frac{dC_L}{dt} = \frac{1}{\Delta t}\boldsymbol{N}_l \cdot (\{C_L\}_{n+1} - \{C_L\}_n) = \frac{1}{\Delta t}\boldsymbol{N}_l \cdot \{\Delta C_L\} \equiv \frac{\Delta C_L}{\Delta t} \tag{5.60}$$

Finally, the elementary forces associated to $\{C_L\}$ are expressed as:

$$\{\boldsymbol{F}\}_{C_L} = \int_{\Omega_e} \left[\left((1 + H_{C_L})\frac{\Delta C_L}{\Delta t} + h \right) \boldsymbol{N}_l - \boldsymbol{G}^T \cdot \boldsymbol{J} \right] d\Omega \tag{5.61}$$

This general form can also be applied to other diffusion scenarios, such as hydrogen diffusion in zirconium alloys with hydride precipitation and dissolution. In that specific case, $H_{C_L} = 0$, and h depends on the kinetics of the precipitation and dissolution process.

At this stage, the finite element formulation is fully established. For efficient convergence of the incremental resolution scheme, it is crucial to evaluate the element stiffness matrix, formally given by:

$$\boldsymbol{K} = \begin{pmatrix} \boldsymbol{K}_{uu} & \boldsymbol{K}_{up} & \boldsymbol{K}_{u\theta} & \dots \\ \boldsymbol{K}_{pu} & \boldsymbol{K}_{pp} & \boldsymbol{K}_{p\theta} & \dots \\ \boldsymbol{K}_{\theta u} & \boldsymbol{K}_{\theta p} & \boldsymbol{K}_{\theta\theta} & \dots \\ \dots & \dots & \dots & \ddots \end{pmatrix} \tag{5.62}$$

where each term is a sub-matrix with can be individually computed as the derivative of the elementary forces with respect to the nodal unknowns, as follows:

$$\boldsymbol{K}_{uu} = \frac{\partial\{\boldsymbol{F}\}_u}{\partial\{\boldsymbol{u}^e\}} \tag{5.63}$$

The details about the computation of the elementary stiffness matrix can be found on Appendix C.

5.5 Hydrogen boundary conditions

Dirichlet and Neumann boundary conditions are employed to prescribe either the lattice hydrogen concentration, C_L, or the flux, $\boldsymbol{J}$, on specific parts of the body's boundaries. When a hydrogen pressure (P_a) is applied, the hydrogen concentration at the boundary is determined using Sieverts' law, as outlined by Sofronis and McMeeking, 1989:

$$C_L = C_S\sqrt{\frac{P_a}{P_S}} \tag{5.64}$$

where P_S is a reference pressure and C_S is a thermally activated term. Before testing, the specimen surfaces are oxidized due to exposure to the atmosphere. Although the oxide layer is thin, it may inhibit or reduce hydrogen penetration into the material. Plastic deformation of the specimen breaks this layer, allowing hydrogen to diffuse into the material. To account for the interfacial resistance to hydrogen penetration, the flux normal to the surface (J_n) can be modeled using a Robin boundary condition:

$$J_n = R_H(C_L^\infty - C_L) \tag{5.65}$$

where C_L^∞ is the equilibrium hydrogen concentration from Equation 5.64, and C_L is the concentration at the free surface (Kasuya et al., 2021). When $R_H \approx 0$, hydrogen penetration is blocked, whereas for large R_H values, $C_L \approx C_L^\infty$. To simulate the cracking of the oxide layer, R_H can be expressed as a function of κ and/or $\dot{\kappa}$.

In the finite element (FE) implementation, it is crucial to account for the dependence of J_n on both C_L and κ to ensure proper convergence. While this boundary condition is not applied in the present study, it could prove valuable for future investigations.

5.6 Simulations of an existing experimental database

5.6.1 Database and material coefficients

This study builds upon the database presented by Briottet et al., 2012 and Moro et al., 2010, which examined the effects of gaseous hydrogen on the mechanical and fracture properties of high-strength steel (API X80 grade) in both hydrogen and neutral gas environments. To achieve this, a series of mechanical tests were conducted, including tensile tests, fracture toughness evaluations using compact tension (CT) specimens, and pressurized disk tests. All experiments were performed at room temperature to accurately simulate typical service conditions. These tests provided a comprehensive characterization of the material's mechanical and fracture properties, allowing for a detailed assessment of the impact of hydrogen on its behavior.

To identify the material parameters for finite element simulations, the stress–strain curve of the smooth specimen was analyzed under nitrogen gas conditions to eliminate any embrittlement effects. The experimental data were then fitted to the following equation:

$$\sigma_F(\kappa) = \sigma_0 + Q_1(1 - \exp(-b_1\kappa)) + Q_2(1 - \exp(-b_2\kappa)) \tag{5.66}$$

where σ_0 is the yield stress, and Q_1, b_1, Q_2, and b_2 characterize the evolution of strain hardening, with κ representing the accumulated plastic strain. Strain-rate sensitivity parameters (Equation 5.5) were also calibrated. The fitted material parameters are summarized in Table 5.1. These coefficients were then employed into an axisymmetric model for a tensile test to compare with experimental data. As shown in Figure 5.2, the fitted parameters provide a good match for the X80 steel.

The initial porosity, representing inclusions such as MnS, CaS, and oxides, was set to 4×10^{-4}, a low value typical of modern pipeline steels. The GTN model coefficient q_1 was set to 1.5, consistent with previous studies, while q_2 was adjusted to reproduce the experimental $J - \Delta a$ curve obtained from air tests. Void nucleation, as modeled by Equation 5.13, was introduced to capture damage initiation on carbides (Tanguy et al., 2008). The effect of hydrogen on carbide nucleation was neglected, meaning $\xi(C) = 1$. The critical porosity for void coalescence was set to $f_c = 0.05$, in agreement with unit cell simulations (Koplik and Needleman, 1988; Shinohara et al., 2016).

The nonlocal model incorporates two internal length scales: ℓ_ω for void growth and ℓ_κ for void nucleation. ℓ_ω was predetermined to be 100 µm, reflecting the typical element size used in pipeline steel

Property	Value	Unit
	Plasticity	
E, ν	209, 0.3	GPa, —
$\sigma_F(\kappa)$	$503 + 360(1 - \exp(-3.15\kappa)) + 130(1 - \exp(-58.5\kappa))$	MPa
$\dot{\kappa}_0$, K, n	1, 57, 5.3	s^{-1}, MPa, —
	Ductile damage	
f_0	4.0×10^{-4}	—
q_1, q_2	1.5, 1.16	—, —
A_n^0, $\bar{k}_c$	0.1, 0.5	—, —
f_c, f_R	0.05, 0.25	—, —
ℓ_ω, ℓ_κ	100, 100 or 30	µm, µm
	Hydrogen diffusion	
β	6	—
N_L	8.47×10^{28}	$\mathrm{at/m^3}$
W_B	40	kJ/mol
R	8.31	J/mol K
T	300	K
N_T	$\log_{10} N_T = 24.73 - 3.74 \exp(-60.17\bar{\kappa})$	$\mathrm{at/m^3}$
D_L	1.27×10^{-8}	$\mathrm{m^2/s}$
V_H	7.09×10^{-6}	$\mathrm{m^3/mol}$
C_S, P_S	0.0129, 0.1013	appm, MPa
	Hydrogen embrittlement	
$\lambda(C)$, $\xi(C)$	1, 1	—, —
σ_c^0, C_0, B_n^0	10,200, 6.1, 300	MPa, appm, —

Table 5.1: Material parameters fitted for the X80 steel.

simulations with local models (Madi et al., 2020). Since the length scale for quasi-cleavage is expected to be smaller, ℓ_κ was set to 30 µm. Based on Tuhami et al., 2022, the mesh size should be less than one-third of the material length, so a mesh size of 10 µm was used in regions where fracture is anticipated. A coarser mesh of 30 µm is applicable if void growth is the dominant failure mechanism.

The experiments conducted by Briottet et al., 2012 showed no noticeable effect of hydrogen on the overall plastic behavior, leading to the choice of $\lambda(C) = 1$ in Equation 5.17. The applied hydrogen pressure was $P_a = 30$ MPa, corresponding to a lattice hydrogen concentration of 4.4×10^{-3} wppm (Moro et al., 2010). Using this, the Sieverts' law parameters at room temperature were determined (see Table 5.1). The diffusion coefficient (D_L), trap density (N_T), and trap binding energy (W_B) were also taken from Moro et al., 2010 and summarized in Table 5.1. All other parameters follow the established values from Sofronis and McMeeking, 1989.

However, different values are reported in the literature; for example, Depraetere et al., 2021 used $W_B = 60$ kJ/mol, $D_L = 1.5 \times 10^{-10}$ $\mathrm{m^2/s}$, and a different expression for the trap density, defined as follows:

$$\log_{10} N_T = 23.26 - 2.33 \exp(-5.5\kappa) \tag{5.67}$$

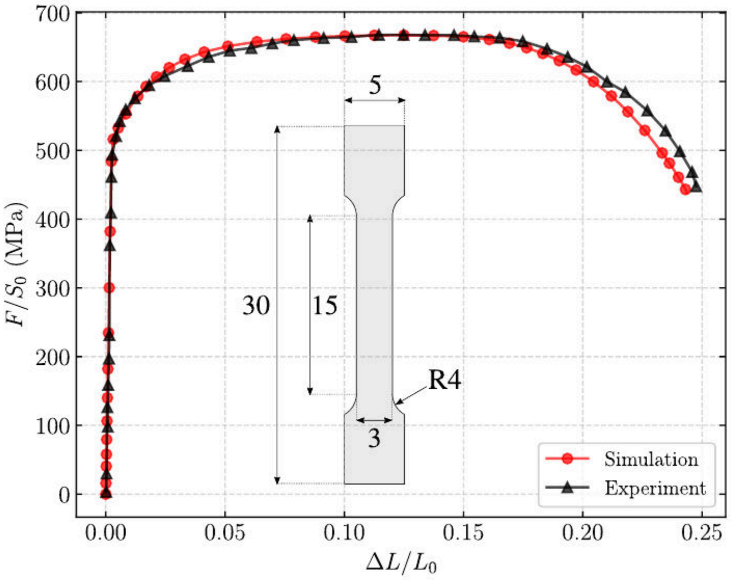

Figure 5.2: Comparison of experimental and numerical results for the tensile test, using the material parameters from Table 5.1. The test was conducted at a strain rate of 5×10^{-5} s^{-1}.

This alternative expression for N_T will be further analyzed and compared with the one used in this study in Section 5.7.

To model hydrogen embrittlement (HE), a nucleation mechanism was incorporated into the GTN model. Since HE is associated with quasi-cleavage, a stress dependence was introduced into the nucleation law. To capture the detrimental effect of hydrogen on fracture resistance, the critical stress required to initiate fracture is formulated as a function of hydrogen concentration as follows:

$$\sigma_c = \sigma_c^0 \exp\left(-\frac{C}{C_0}\right) \tag{5.68}$$

where σ_c^0 and C_0 are material parameters. It is then assumed that the function expressing the nucleation rate due to quasi-cleavage (Equation 5.23) is expressed as:

$$B_n = \frac{B_n^0}{\sigma_c^0} \langle \sigma_I - (1 - q_1 f_*)\sigma_c \rangle \tag{5.69}$$

where $\langle \cdot \rangle$ denotes the positive part, and B_n^0 is a material parameter. The critical stress is scaled by the factor $(1 - q_1 f_*)$ in the previous equation to reflect the decrease in σ_I as damage progresses. Without this term, nucleation would cease prematurely. Figure 5.3 illustrates the relationship between the critical stress and hydrogen concentration. As hydrogen concentration increases, the critical stress required to initiate void nucleation due to hydrogen decreases.

The model requires a significant number of parameters, as it aims to describe ductile failure, hydrogen-induced quasi-brittle failure, and the transition between these mechanisms within a unified framework. In this work, the parameters (see Table 5.1) were identified in distinct groups. First, the elasto-plastic behavior was calibrated using tensile tests conducted under N_2, assuming that damage remains minimal before the onset of a rapid load drop. Next, the parameters governing ductile failure were fitted based on tests conducted without H_2. Finally, the parameters related to hydrogen embrittlement were determined using tests performed in the presence of hydrogen. All hydrogen diffusion-related parameters were taken from the literature.

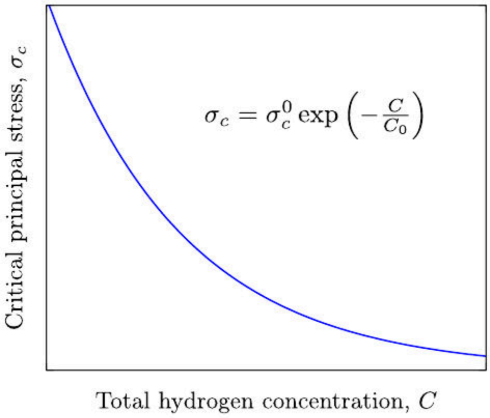

Figure 5.3: Relationship between critical stress for void nucleation and total hydrogen concentration.

5.6.2 Tensile tests

Tensile tests were initially simulated without considering damage to examine the coupling between mechanical loading, hydrogen diffusion, and trapping. The sample had a diameter of $\phi = 6$ mm and a gage length of $L_0 = 30$ mm. Four different simulations were performed: (i) the specimen was subjected to mechanical loading under a hydrogen pressure of 30 MPa; (ii) the specimen was precharged with hydrogen for one hour before loading; (iii) the specimen was precharged and then loaded in air. In cases (i)–(iii), the surface was assumed to allow hydrogen diffusion freely, with the lattice concentration prescribed at the surface (Dirichlet boundary conditions). In case (iii), this assumption led to the surface hydrogen concentration dropping to zero upon loading, allowing hydrogen to escape from the material. (iv) The fourth simulation involved precharging the specimen and then loading it under conditions where hydrogen could not escape (Neumann boundary conditions).

The simulations were stopped when the maximum load was reached, and all were conducted at a strain rate of 5×10^{-5} s^{-1}. To account for symmetry, only half of the axisymmetric specimen was meshed. The material exhibited anisotropic behavior, as the initially circular cross-section deformed into an ellipse, a phenomenon commonly observed in pipeline steels (Shinohara et al., 2012; Tanguy et al., 2008). However, this study assumed isotropic material behavior for simplicity. To account for anisotropy, the von Mises stress in Equation 5.18 could be replaced with an anisotropic stress measure (Bron et al., 2004; Shinohara et al., 2016), which would necessitate a full 3D simulation, significantly increasing the computational cost and simulation time.

The results of the various simulations are presented in Figure 5.4. For each scenario, the lattice (C_L) and trapped (C_T) hydrogen concentrations at the center (black lines) and near the surface (red lines) on the symmetry plane are plotted as a function of time. Additionally, C_T is shown at the stress concentration point (the base of the fillet) for case (iv) (blue lines). The distribution of C_T is provided at the end of the simulation (at = 2700 s), corresponding to a strain level of 13.5%.

Considering the specimen's diameter, the characteristic diffusion time in the absence of trapping is calculated as $t_c = \phi^2/4D_L = 708$ s. Therefore, diffusion occurs relatively quickly compared to the duration of a tensile test. However, the trapping process, particularly the significant increase in the number of trapping sites during plastic deformation, leads to the formation of a hydrogen-rich layer near the outer surface of the specimen (see Figure 5.4). This accumulation of hydrogen is likely to promote crack initiation from the surface, a phenomenon that has been experimentally observed, as shown in

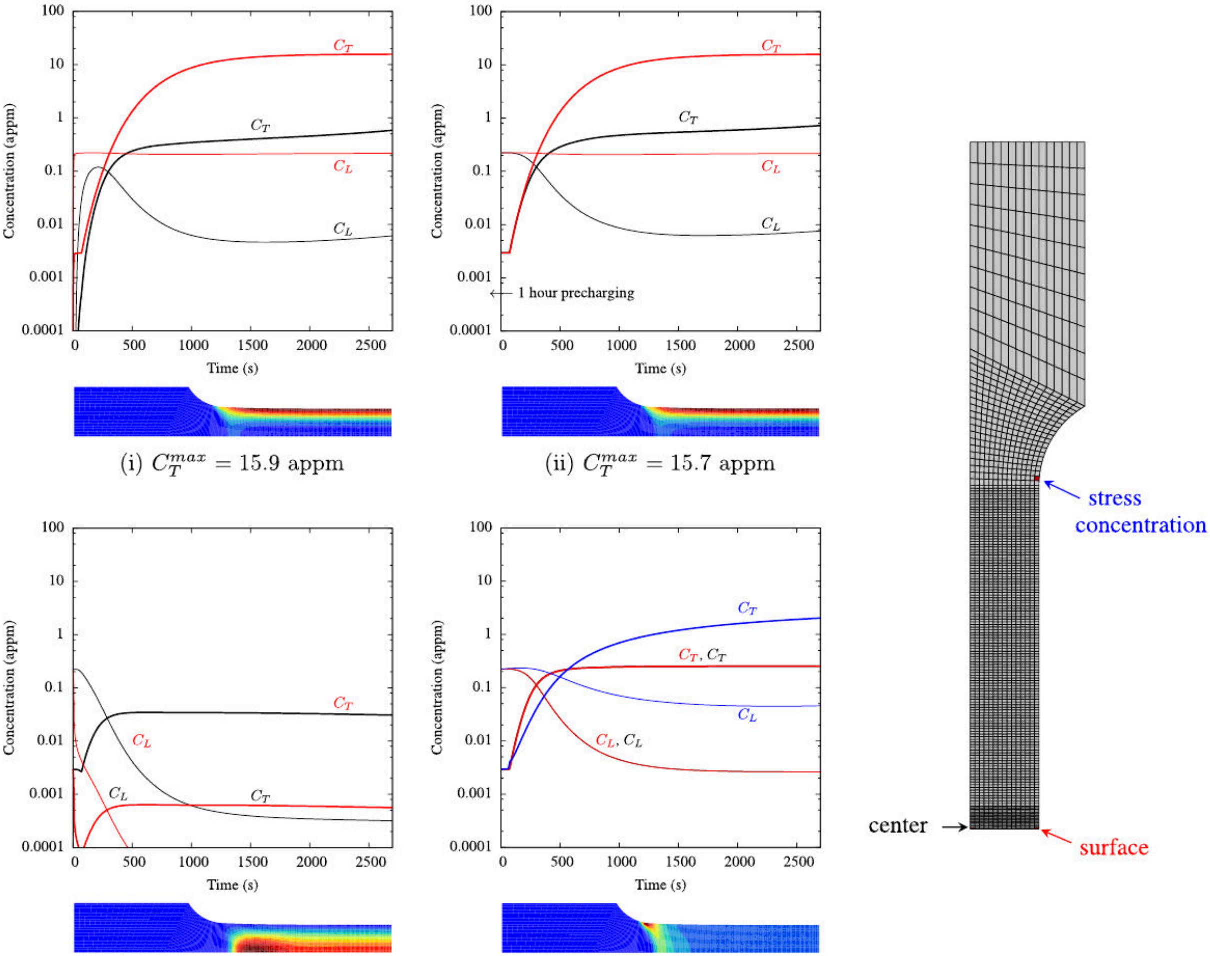

(i) $C_T^{max} = 15.9$ appm

(ii) $C_T^{max} = 15.7$ appm

(iii) $C_T^{max} = 0.04$ appm

(iv) $C_T^{max} = 2.0$ appm

Figure 5.4: Simulation of a tensile test to maximum force under four conditions: (i) loading with hydrogen pressure, (ii) precharging followed by loading under hydrogen, (iii) precharging followed by loading in air, and (iv) precharging and loading with a tight surface assumption. The curves represent hydrogen concentrations C_L (black lines) and C_T (red lines) at the specimen's center and near the outer surface, respectively, along with C_T at the stress concentration area (blue lines). The contour plots display the distribution of C_T at the end of the simulation.

Figure 5.5, taken from Moro et al., 2010.

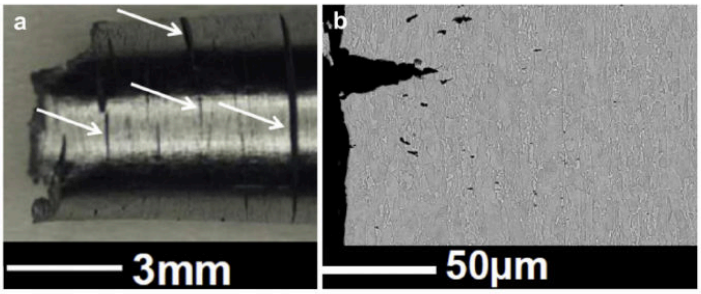

Figure 5.5: Fracture surfaces observed for a test under hydrogen (Moro et al., 2010).

When the specimen is precharged for one hour before testing (Figure 5.4), an initially uniform concentration of hydrogen is achieved throughout the specimen. However, the rapid multiplication of trapping sites soon masks this initial uniformity, resulting in a hydrogen distribution at maximum load that closely resembles that of case (i). In case (iii), hydrogen escapes quickly from the specimen, leading to a very low hydrogen concentration. This suggests that hydrogen embrittlement would be mitigated, assuming the outer surface does not prevent the escape of hydrogen.

In case (iv), the increase in the number of trapping sites results in an increase in C_T and a decrease in C_L along the gauge length of the specimen. The pressure at the root of the fillet is higher, which leads to a slight build-up of hydrogen at this location. Since hydrogen is prevented from escaping, the overall concentration in the material remains low. This indicates that precharging methods, such as electrochemical charging, would need to achieve higher hydrogen concentrations to produce similar levels of embrittlement.

The simulations are now conducted with damage considerations. Figure 5.6a presents the results of tensile tests at various strain rates (5×10^{-7}, 5×10^{-5} and 5×10^{-3} s^{-1}) for case (i), represented by red curves. The results qualitatively illustrate the impact of strain rate on ductility. At the slowest strain rate (5×10^{-7} s^{-1}), hydrogen has sufficient time to diffuse, resulting in significant embrittlement of the material bulk. This leads to increased damage at the specimen's center, where stress levels rise after necking, and a marked loss of ductility.

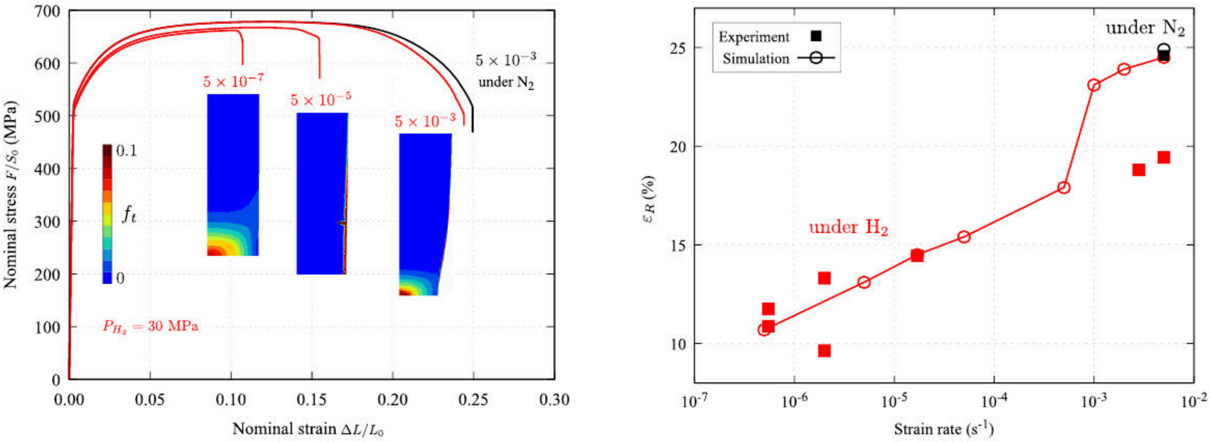

(a) Tensile tests at different strain rates under.

(b) Strain at failure for different strain rates.

Figure 5.6: Analysis of the influence of strain rate on tensile test results conducted under hydrogen conditions.

At an intermediate strain rate (5×10^{-5} s^{-1}) , crack initiation primarily occurs on the surface, aligning with the findings of Briottet et al., 2012. Conversely, the behavior at a strain rate of 5×10^{-3} s^{-1} closely resembles that of specimens tested in nitrogen (shown by the black curve), where failure originates at the center due to ductile damage. However, the overall load-carrying capacity is slightly reduced due to hydrogen-induced surface damage.

Figure 5.6b shows the relationship between failure strain and strain rate for both numerical and experimental tests conducted under hydrogen conditions. The model effectively captures the observed strain rate effect up to 1.0×10^{-3} s^{-1}. Beyond this rate, the model tends to overestimate ductility.

Figure 5.7 provides a detailed analysis of damage progression at a strain rate of 5×10^{-5} s^{-1}. As previously mentioned, crack initiation occurs primarily on the surface of the specimens due to a higher concentration of trapped hydrogen in that region. In Figure 5.7a, the evolution of damage near the surface is shown as nominal strain increases. Initially, damage increases uniformly, but as the simulation advances, multiple surface cracks begin to form. This phenomenon is similar to findings by Sicsic et al., 2014, who employed a gradient damage model to simulate thermal shocks. Despite the differing contexts, the nonlocal model effectively captures this behavior, ultimately leading to the formation of a primary crack that results in final failure, as illustrated in the last image.

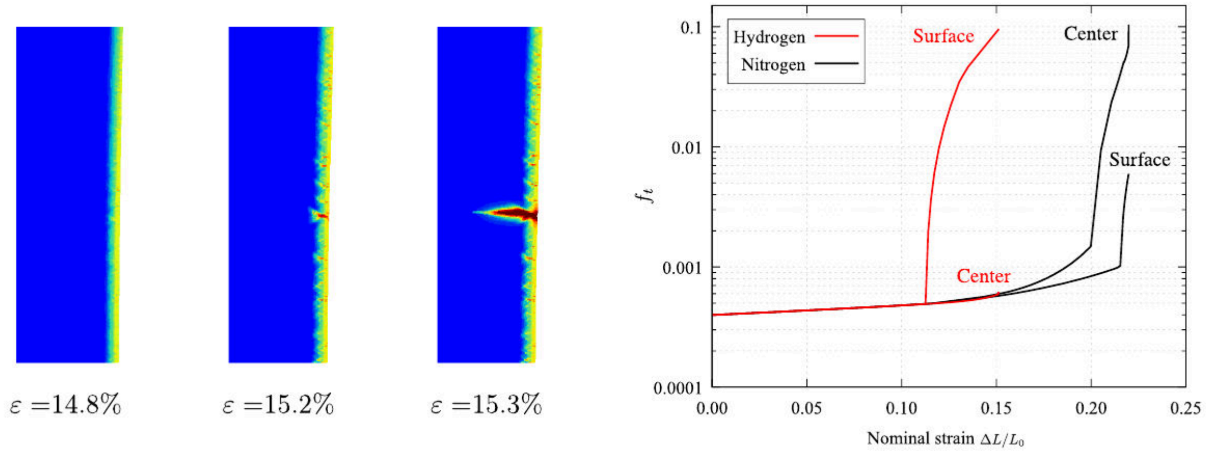

(a) Evolution of surface damage during the tensile test as a function of increasing strain.

(b) Comparison of damage evolution between the center and surface of the specimen under hydrogen and nitrogen charging conditions.

Figure 5.7: Simulation of surface cracking under hydrogen charging conditions.

To assess damage evolution within the specimen, simulations of tensile tests in hydrogen and nitrogen environments are compared at the same strain rate of 5×10^{-5} s^{-1}. Figure 5.7b displays the damage evolution at both the center and surface of the specimen for each condition relative to nominal strain. Significant differences emerge when contrasting the two scenarios. Under hydrogen exposure, damage gradually accumulates at the surface, resulting in surface cracking, while damage at the center remains relatively unchanged. In contrast, during testing under nitrogen, damage is more pronounced in the center of the specimen. Notably, the void volume fraction peaks at a lower strain during the hydrogen test, indicating that hydrogen-induced degradation contributes to premature failure.

5.6.3 Pressurized disk tests

The simulations of the pressurized disk tests in this section follow the ISO standard (International Organization for Standardization, 2023), the same standard referenced in Chapter 3. To summarize, this test provides a reliable method for evaluating materials intended for hydrogen storage, ensuring that only those capable of withstanding the high-pressure conditions associated with hydrogen storage are selected. The testing procedure involves subjecting a clamped disk to progressively increasing pressures of helium or hydrogen gas (see Figure 5.8). The embrittlement ratio I_E is then determined as the ratio of failure pressures in helium and hydrogen at a specified pressure rate. A ratio of less than 2 is considered acceptable for materials used in hydrogen storage.

According to the ISO standard, the pressurized disk test utilizes a disk with a diameter of 58 mm and a thickness of 0.75 mm. The disk is clamped such that pressure is applied to a surface with a diameter of 26.5 mm, while one side is subjected to the pressure. To prevent indentation, the clamping device features a radius of 0.5 mm on the opposite side (see Figure 5.8). A simulation of this test was conducted by Charles et al., 2012, employing a cohesive zone model to analyze the failure zone.

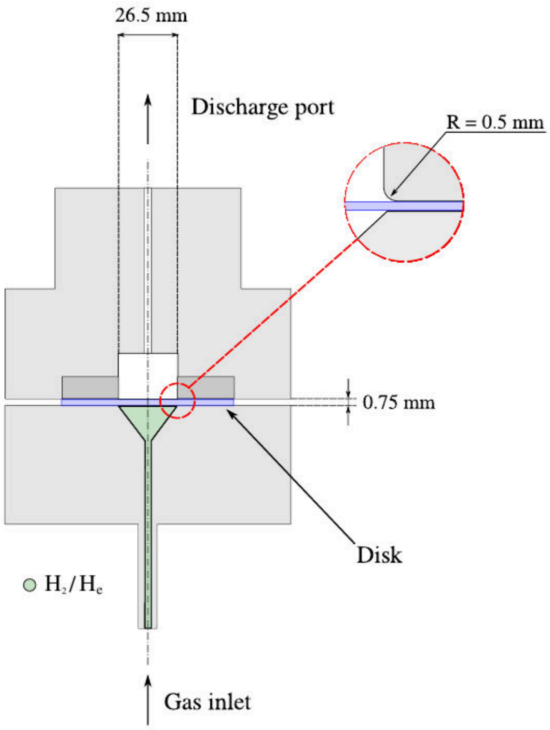

Figure 5.8: Schematic of the machine used for the disk pressure test.

Briottet et al., 2012 investigated the rupture pressure of the disk at various pressurization rates under helium and hydrogen gases. They found that when exposed to helium, the rupture pressure was approximately 60 MPa. In contrast, the rupture pressure for hydrogen ranged from 20 to 50 MPa. This reduction in rupture pressure was attributed to hydrogen embrittlement, where hydrogen diffused into the material, leading to decreased ductility or increased brittleness. Furthermore, the degree of hydrogen embrittlement was found to be dependent on the pressurization rate; lower rates resulted in a more pronounced embrittlement effect due to the extended diffusion time of hydrogen.

For the numerical simulation, an axisymmetric mesh was employed, and contact between the disk and the upper clamping device was modeled with the assumption of no friction. As the simulation progresses with increasing pressure, instability arises, leading to divergence at the rupture point. This divergence corresponds to elevated levels of strain and damage. As the problem is time-dependent (due to the rate dependence of the material and diffusion), it is not possible to use an arc-length method (Riks, 1979).

In simulations involving hydrogen gas, the lattice concentration on the pressurized side is prescribed according to Sieverts' law, while a boundary condition of $C_L = 0$ is applied on the opposite side, allowing hydrogen to escape from the specimen. Notably, using a Neumann boundary condition (with $J_n = 0$) does not affect the results, as failure consistently occurs on the pressurized side within the clamping area.

The results of the simulations are illustrated in Figure 5.9a, which presents the relationship between the displacement at the center of the disk and the gas pressure for a pressurization rate of $\dot{P} = 0.25$ MPa/min. Both tests under helium and hydrogen show rupture pressures closely aligned with the experimental findings of Briottet et al., 2012. The curves exhibit similar trends, as hydrogen is assumed not to influence the material's hardening; however, rupture occurs at a lower pressure under hydrogen.

The simulations indicate that failure under helium primarily results from reaching the limit load of

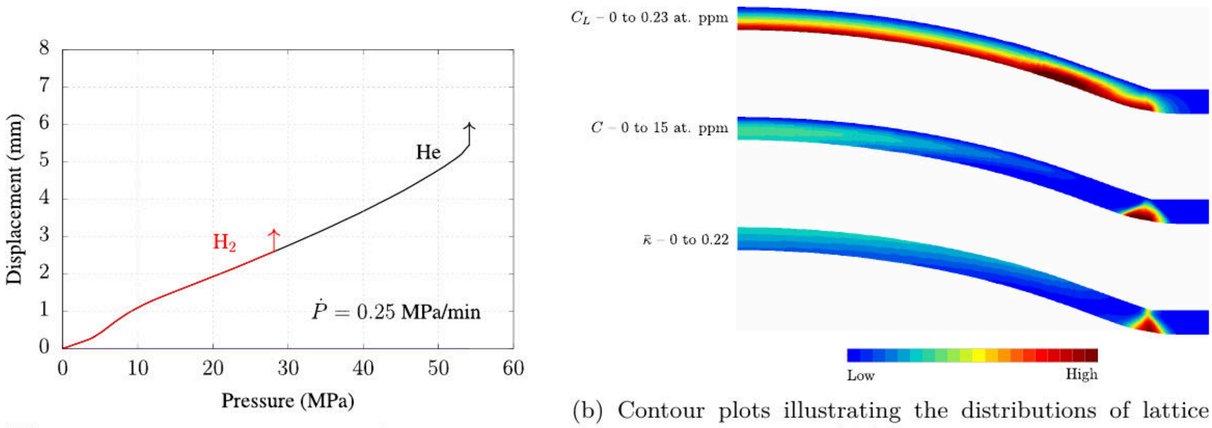

(a) Displacement at the center of the disk as a function of gas pressure for both helium and hydrogen environments.

(b) Contour plots illustrating the distributions of lattice hydrogen concentration (C_L), total hydrogen concentration (C), and accumulated plastic strain ($\bar{\kappa}$) at the moment of failure during testing under hydrogen conditions.

Figure 5.9: Simulation results of the disk pressure test.

the disk, characterized by a significant reduction in thickness near the clamping area. Comparisons of simulations with and without damage yield nearly identical failure pressures. Conversely, under hydrogen pressure, failure arises from damage nucleation due to localized hydrogen uptake, as demonstrated in Figure 5.9b, where the hydrogen concentrations C_L and C are presented for the failure pressure. The accumulated plastic strain $\bar{\kappa}$ is also shown, indicating that failure occurs in the clamping area.

This study also investigates the effect of pressurization rates on disk failure, focusing on their influence on hydrogen diffusion and embrittlement. It was observed that lower pressurization rates ($\dot{P}_a$) result in significant hydrogen-induced embrittlement, as the extended diffusion time allows hydrogen to penetrate the material more effectively. The findings are illustrated in Figure 5.10, demonstrating close alignment with the data presented by Briottet et al., 2012. However, it is important to note that the experimental results show considerable variability. This scattering may arise from failures occurring in the clamping area, where controlling boundary conditions experimentally is challenging. One potential solution could involve machining notches in the disk away from the clamping zone, as suggested by Moro, 2009 and Santana et al., 2024.

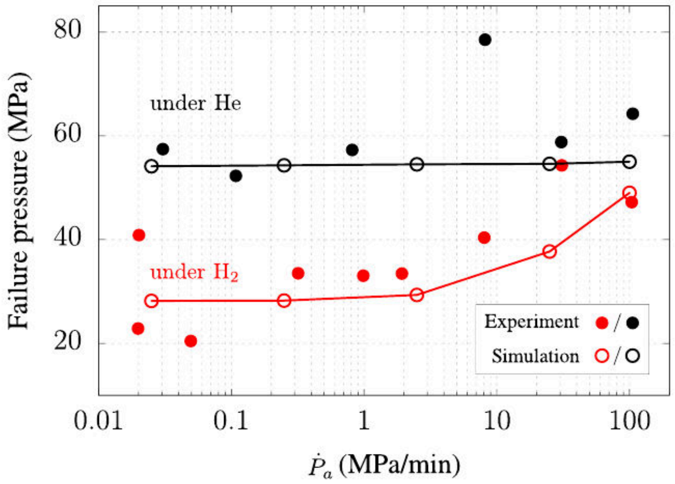

Figure 5.10: Rupture pressure for different pressurization rates under hydrogen and helium.

5.6.4 Fracture toughness tests

Fracture toughness tests using compact tension (CT) specimens were performed by Briottet et al., 2012 at a loading rate of 0.1 mm/min, both in air and hydrogen environments at a pressure of 30 MPa. The sample geometry is illustrated in Figure 5.11a. The tests were conducted without side grooves using the multiple specimen technique of ASTM E1820. The specimens feature a 20 mm deep notch for fatigue pre-cracking. The initial crack length was set at $a_0 = 22$ mm.

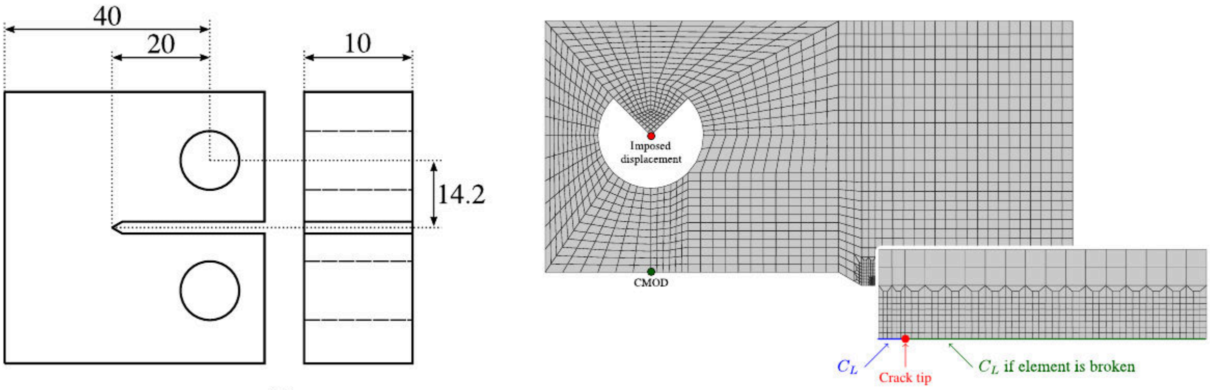

(a) Specimen geometry.

(b) Specific boundary conditions for the lattice hydrogen concentration (C_L) applied to the model.

Figure 5.11: Compact Tension (CT) specimen.

Simulations were conducted under the assumption of plane strain, representing only half of the specimen to account for symmetries. The mesh configuration is displayed in Figure 5.11b. As the crack propagates, it is crucial to apply the lattice hydrogen concentration, as determined by Sieverts' law, to the newly formed crack surfaces. This boundary condition is enforced on a node located on the symmetry plane when one of the elements containing that node is identified as broken.

A similar approach was employed by del Busto et al., 2017, incorporating cohesive elements to model crack advancement. An alternative method could involve significantly increasing the diffusion coefficient in highly damaged areas or implementing a penalty approach, allowing C_L to rapidly reach the prescribed concentration (Martínez-Pañeda et al., 2020).

The crack length was determined through post-processing the simulation, identifying broken elements as those for which all Gauss points have reached $f_* = 0.99/q_1$. Subsequently, the J-integral was calculated according to the ASTM E1820 standard, utilizing the simulated Load–CMOD curve. To account for crack blunting, an effect not captured by considering only broken elements, the crack advance Δa was set to $J/2\sigma_Y$ prior to crack initiation (Chen et al., 2020). Here, $\sigma_Y = 590$ MPa represents the average of the 0.2% yield stress and the Ultimate Tensile Stress (UTS).

The simulated $J - \Delta a$ curves for both air and hydrogen environments are presented in Figure 5.12. The results show good agreement with experimental data obtained in air. However, while the simulation slightly overestimates the J values under hydrogen, it still demonstrates a significant reduction in toughness. Employing a smaller value for ℓ_κ may help address this issue, although it would come at a considerably higher computational cost.

Figure 5.13 illustrates the values of opening stress (σ_{22}) and nonlocal accumulated plastic strain. The results indicate that the stress field remains free of spurious fluctuations, thanks to the implementation of the mixed formulation. Furthermore, the nonlocal formulation prevents strain localization. As

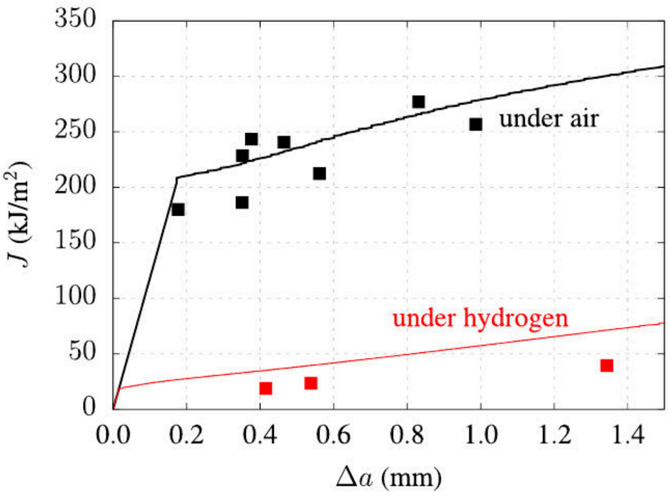

Figure 5.12: Comparison between experimental (symbols) and numerical (lines) results for $J - \Delta a$ curves obtained under air and hydrogen.

anticipated, the damage process zone, characterized by a high-stress region ahead of the crack tip, is larger for the compact tension specimens tested in air.

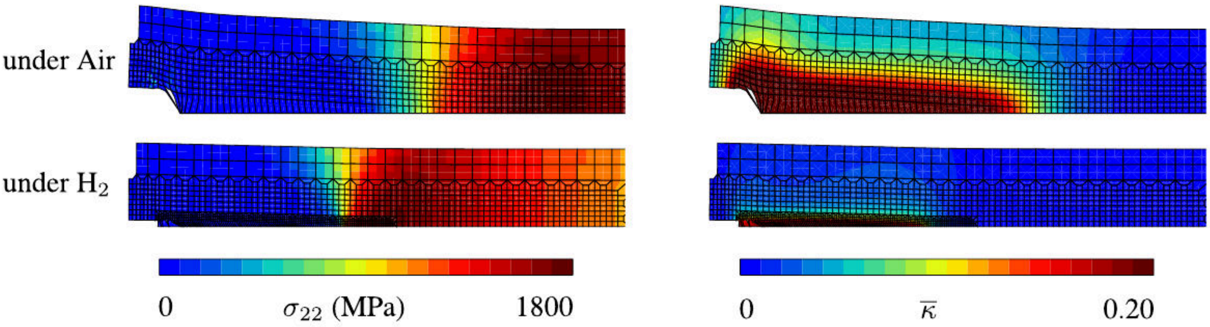

Figure 5.13: Values of opening stress (σ_{22}) and accumulated plastic strain ($\bar{\kappa}$) at Gauss points for compact tension (CT) specimens tested in air and hydrogen environments. A finer mesh with a size of 10 µm is employed for tests under hydrogen to discretize the smaller length scale.

5.7 Discussion: effect of diffusion parameters

As previously discussed, the material parameters W_B, N_T and D_L proposed by Depraetere et al., 2021 and Moro et al., 2010 show significant differences, despite the investigated materials being quite similar (X70 pipeline steel in the former case and X80 in the latter). To assess the impact of these material parameters, the tensile test simulations presented in Figure 5.4 were conducted using the parameter set suggested by Depraetere et al., 2021:

- $W_B = 60$ kJ/mol
- $\log_{10} N_T = 23.26 - 2.33 \exp(-5.5\bar{\kappa})$ m^{-3}
- $D_L = 1.5 \times 10^{-10}$ m^2/s

The values of N_T were already compared in Chapter 3 and are recalled here in Figure 5.14. While the values for $\bar{\kappa} = 0$ are quite similar, they diverge significantly as accumulated plastic strain increases. The values suggested by Moro et al., 2010 rise much more rapidly with plastic strain, quickly approaching a higher limit. Additionally, the characteristic diffusion time is extended because D_L is considerably smaller in Depraetere et al., 2021, resulting in $t_c = 6 \times 10^4$ s, while $t_c = 708$ s using the same diffusion coefficient as in Moro et al., 2010. All other parameters, particularly the boundary conditions, remain constant throughout the simulations.

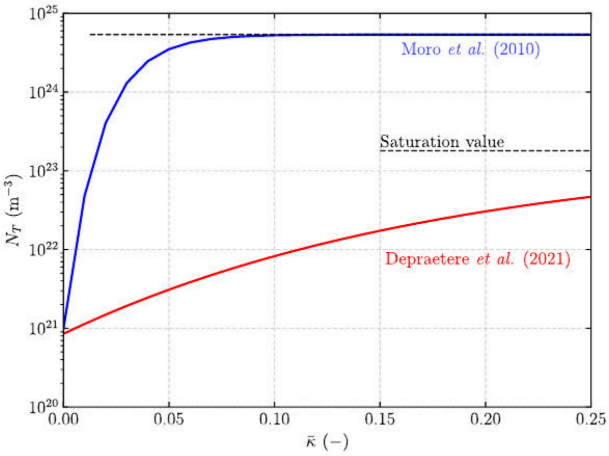

Figure 5.14: Comparison of the N_T function employed by Moro et al., 2010 and Depraetere et al., 2021.

The four cases examined in Section 5.6.2 were simulated using the new set of parameters, and the results are presented in Figure 5.15. For case (i), which involves loading under hydrogen pressure, the hydrogen concentration is notably higher near the specimen's surface, as seen in Figure 5.4. In this case, the high concentration is attributed to slow diffusion into the material, whereas it was primarily due to trapping in previous scenarios. Consequently, the hydrogen concentration is lower in this case (0.39 vs. 16 appm). This indicates that different nucleation parameters (Equations 5.13 and 5.68) should be utilized to accurately describe the reduction in ductility during tensile loading. The one-hour precharging does not significantly alter the results, consistent with the findings in Section 5.6.2.

In case (iii), the low diffusion coefficient limits the escape of hydrogen from the specimen. This aligns with the conclusions drawn by Depraetere et al., 2021, suggesting that hydrogen embrittlement is still expected under these conditions. However, it is likely to diminish when using the parameters proposed by Briottet et al., 2012, providing a potential method to evaluate hypotheses regarding boundary conditions. In case (iv), where the specimen is considered to be insulated, hydrogen redistribution does not occur, contrary to the results discussed in Section 5.6.2. This lack of redistribution is once again attributed to the significantly smaller diffusion coefficient.

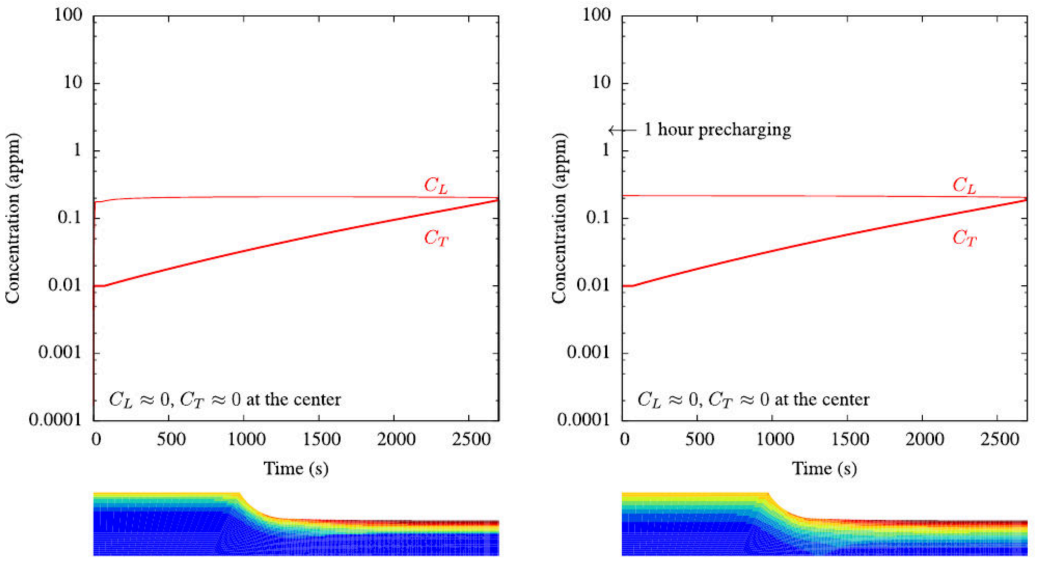

(i) $C^{max} = 0.39$ appm (ii) $C^{max} = 0.39$ appm

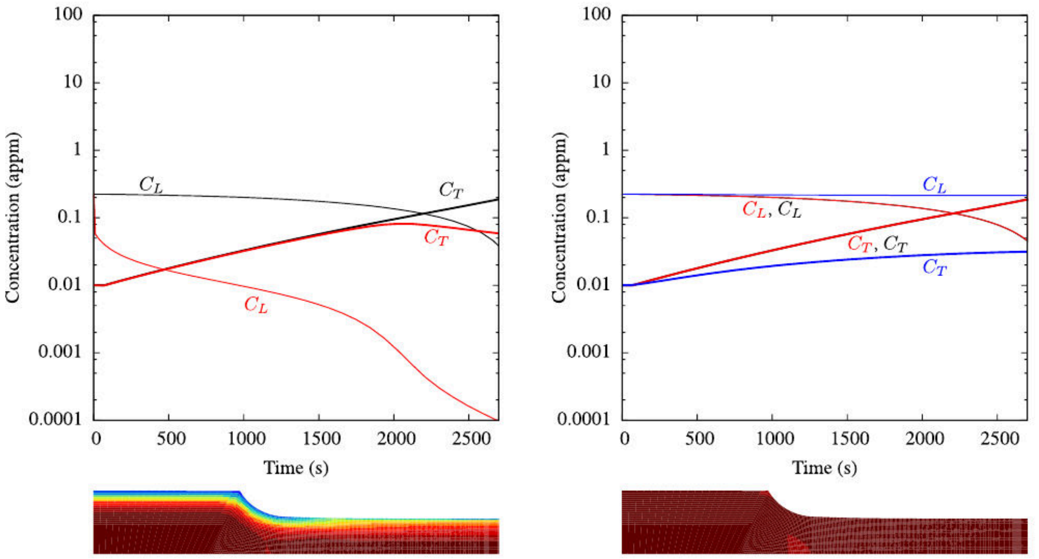

(iii) $C^{max} = 0.23$ appm (vi) $C^{max} = 0.25$ appm

Figure 5.15: Simulation of a tensile test using diffusion parameters from Depraetere et al., 2021, considering: (i) loading under hydrogen pressure, (ii) precharging and loading under hydrogen pressure, (iii) precharging and loading under air, and (iv) precharging with a tight surface. The curves show hydrogen concentrations (C_L and C_T) at the specimen center (black), near the outer surface (red), and in the stress concentration area (blue). Contour plots illustrate the distribution of C at the end of the simulation.

5.8 Conclusions

In this chapter, a numerical framework for simulating hydrogen embrittlement (HE) was introduced using a modified nonlocal Gurson–Tvergaard–Needleman (GTN) model that incorporates hydrogen diffusion. Damage evolution was accelerated by the presence of hydrogen, effectively capturing the hydrogen embrittlement degradation effect (HEDE) and leading to premature failure. To address volumetric locking and maintain continuous pressure fields, a mixed formulation was employed. This formulation incorporates displacement, pressure, and volume variation as nodal unknowns, which offers the additional benefit of simplifying the calculation of pressure gradients that strongly influence hydrogen diffusion. Furthermore, mesh independence was ensured through the use of an implicit gradient model, allowing for the regularization of void growth and strain-controlled nucleation.

To validate the framework, calibration and testing were conducted using experimental data from Moro et al., 2010 and Briottet et al., 2012 on API X80 high-strength steel. The experimental database included tensile, fracture toughness, and pressurized disk tests. Failure initiation was accurately modeled from the specimen surface at low strain rates, with a transition to failure initiation at the specimen's center after necking at high strain rates. Additionally, the model effectively represented the significant toughness reduction in compact tension (CT) specimens under hydrogen. The pressurized disk test results were well captured, particularly reflecting the influence of the loading rate. The use of notched disk specimens is recommended to prevent failure in the clamping area.

The model is designed to simultaneously address ductile fracture and quasi-cleavage induced by hydrogen, ensuring a transition between these mechanisms. This complexity introduces numerous material parameters, making the fitting process challenging. A step-by-step fitting procedure is proposed to assist in parameter identification. Parameters associated with quasi-cleavage (σ_c^0, C_0 and B_n^0) significantly impact the results and are highly sensitive to the selected parameters for hydrogen diffusion and trapping interactions. In this work, the parameters suggested by Moro et al., 2010 were employed, though using those from Depraetere et al., 2021 would result in notably different values for the same parameters.

An *ad hoc* boundary condition was implemented to model the penetration of gaseous hydrogen into newly formed cracks. An improved approach would involve re-meshing to explicitly represent cracks, as demonstrated by Mediavilla et al., 2006 and El Ouazani Tuhami et al., 2023. This would allow boundary conditions to be directly applied to the newly created crack lips, enabling crack propagation over substantial distances while maintaining a manageable problem size by using a finer mesh only in the fracture process zone.

6

Simulation of fracture toughness tests

Abstract This chapter presents a comprehensive study on the simulation of fracture toughness tests, integrating experimental and numerical results. It focuses on two steel grades: a vintage X52 pipeline steel and a modern E355 modified steel, tested using standard and sub-size specimens, including Compact Tension (CT) and mini-Disk Compact Tension (mDCT) geometries, with experimental results serving as benchmarks for numerical simulations. The numerical framework employs a nonlocal Gurson-Tvergaard-Needleman (GTN) damage model combined with the B-bar formulation to mitigate volumetric locking, enabling the modeling of damage evolution and crack propagation. The simulations examine the effects of specimen size and thickness on fracture toughness, utilizing advanced crack propagation techniques such as compliance-based and post-processing methods. The findings highlight the challenges of accurately modeling the ductile response of the E355 steel and reveal the significant impact of ductility and specimen geometry on toughness values, while also exploring the interplay between void nucleation thresholds, damage coefficients, and size effects. This study offers valuable insights into the mechanics of fracture toughness and the application of sub-size specimens, with important implications for material testing and structural integrity evaluations.

Résumé Ce chapitre présente une étude sur la simulation des essais de ténacité, en mettant l'accent sur les aspects expérimentaux et numériques, en se concentrant sur deux matériaux : un acier de pipeline X52 vintage et un acier modifié E355 moderne, testés en utilisant des éprouvettes macros et minis, y compris les géométries Compact Tension (CT) et mini-Disk Compact Tension (mDCT), avec des essais expérimentaux servant de référence pour les simulations numériques. La modélisation utilise un modèle d'endommagement nonlocal Gurson-Tvergaard-Needleman (GTN) intégré à la formulation B-bar pour corriger le verrouillage volumique, permettant la modélisation de l'évolution de l'endommagement et de la propagation des fissures. Les simulations étudient les effets de la taille et de l'épaisseur de l'éprouvette sur la résistance à la rupture, en incorporant des techniques avancées pour le calcul de la propagation des fissures, y compris des méthodes basées sur la complaisance et des méthodes de post-traitement. Les résultats mettent en évidence les difficultés de modélisation de la réponse ductile de l'acier E355 et l'influence significative de la ductilité et de la géométrie de l'éprouvette sur les valeurs de ténacité, tout en explorant également l'interaction entre les seuils de nucléation des porosités, les coefficients d'endommagement et les effets de taille. Cette étude fournit des informations sur la ténacité à la rupture

et l'utilisation d'éprouvettes de taille réduite, avec des implications pour les essais de matériaux et les évaluations de l'intégrité structurelle.

Contents

6.1 Introduction

Fracture toughness testing is commonly used to evaluate and monitor the mechanical properties of materials in industrial structures to ensure their integrity. In the context of hydrogen transport systems, the use of sub-size specimens machined from extracted coupons has been proposed as a way to simplify testing and monitor changes in material properties over time (Kumar et al., 2017; Madi et al., 2021; Madi et al., 2024). Miniature flat tensile specimens are widely accepted for characterizing anisotropy, size effects, and monitoring in-service degradation (Lord et al., 2010; Motarjemi et al., 2002; Scheider et al., 2004; Zvirko et al., 2023). However, the experimental evaluation of fracture toughness using subsize specimens remains less developed.

The use of mini-toughness specimens has been developed in the nuclear industry to study the ductile-to-brittle transition in irradiated steels used in pressure vessels. These specimens are typically Compact Tension (CT) types, machined from the undeformed sections of fractured standard Charpy specimens. This approach, as demonstrated by M. Li et al., 2023; Miura and Soneda, 2012; Scibetta et al., 2002, has shown that, when properly accounting for scale effects, mini-toughness specimens are well-suited for accurately measuring fracture properties. A similar challenge is posed by thin-walled tubes in gas transport systems, where the extraction of standard-sized specimens is impractical. To obtain valid toughness data, tests must be conducted on specimens of sufficient size. As discussed in Section 2.5.1, the maximum capacity of the J-integral that a specimen can achieve is determined by the following criteria:

$$J_{max} \leq \frac{1}{10}\min(B, W - a_0)\sigma_Y \tag{6.1}$$

where B is the specimen's thickness, $W - a_0$ is the initial ligament length, and σ_Y represents the average of the yield stress and ultimate tensile strength. This criterion ensures that the process zone remains significantly smaller than the specimen's thickness and ligament size. Even if the tests do not meet the full validity requirements, such specimens still provide valuable insights for comparing different loading conditions within the same material or for comparing materials extracted from various parts under identical conditions.

This chapter presents both experimental and numerical results for fracture toughness tests conducted on standard and sub-size specimens. The experimental work was performed by Luciano Meirelles Santana, a PhD student involved in the MESSIAH project. His fracture toughness test results, gathered during his thesis, serve as the database for the numerical simulations presented here. The chapter emphasizes the numerical analysis, offering a detailed comparison with the experimental findings. For a comprehensive description of the experimental procedure, please refer to Madi et al., 2024.

6.2 Materials and geometries

6.2.1 Materials

This study examines two steel grades: a X52 vintage normalized steel (referred to as X52 steel), extracted from a pipeline with a thickness of 7.92 mm, and a modern E355 modified steel (referred to as E355 mod. steel), provided as a hot-rolled tube with a thickness of 12.7 mm. Both steels were introduced in Chapter 3. For detailed information on their mechanical characterization and properties, please refer to this chapter.

6.2.2 Geometries

For both steels, standard and sub-size fracture toughness specimens were used in the experimental testing. Compact Tension (CT) specimens were employed for the standard size specimens. The X52 steel tube, with a thickness of 7.92 mm, had its standard specimen machined to a thickness of 7.5 mm. In contrast, the E355 mod. steel tube, with a thickness of 12.7 mm, allowed for a thicker standard specimen, which was machined to a thickness of 10 mm. For the sub-size specimens, mini-Disk Compact Tension (mDCT) specimens were used. Sub-size specimens were machined to two thicknesses – 2 and 5 mm – maintaining the same dimensions for both steel grades. All the specimens were pre-cracked, with a_0 representing the initial crack size. Figure 6.1 shows the geometries for the X52 steel and Figure 6.2 illustrates those for the E355 mod. steel.

Each specimen includes side-grooves on both sides, accounting for 10% of the specimen's thickness (B). Figure 6.3 provides a close-up view of the side-grooves for both macro and sub-size specimens, along with their corresponding dimensions.

The specimens in this chapter will be referred to by their type followed by their thickness, such as "mDCT-2" for a mini-Disk Compact Tension specimen with a thickness of 2 mm.

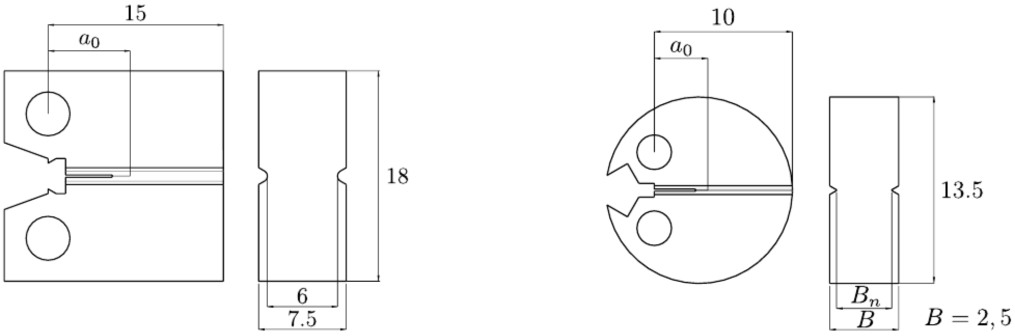

(a) CT.

(b) mDCT.

Figure 6.1: Fracture toughness specimens.

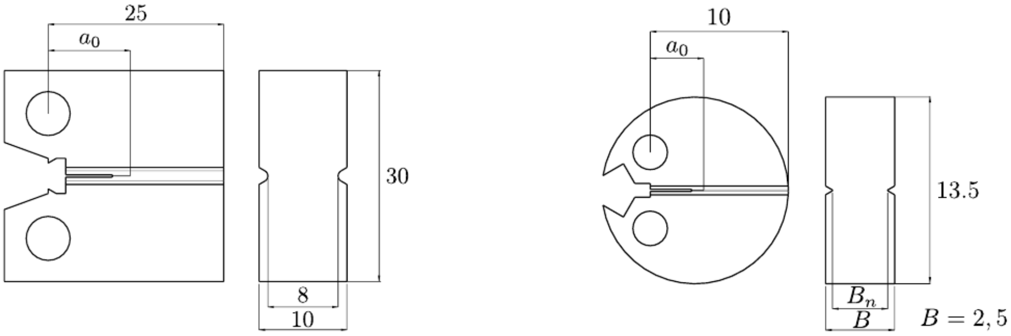

(a) CT.

(b) mDCT.

Figure 6.2: Fracture toughness specimens for the E355 mod. steel.

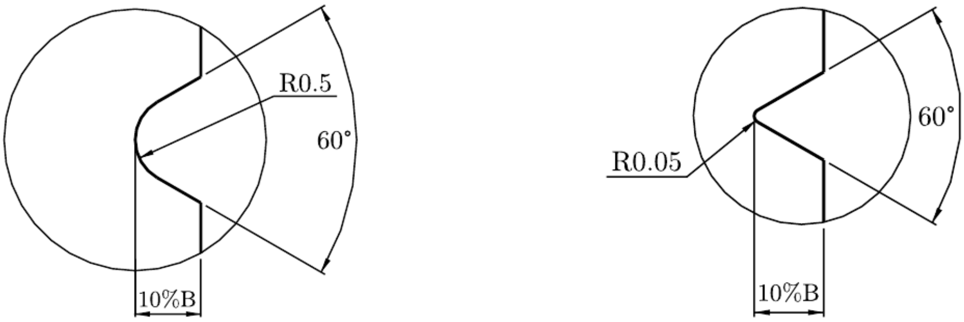

(a) CT.

(b) mDCT.

Figure 6.3: Side-groove dimensions for both macro and sub-size specimens.

6.2.3 Constitutive law identification

To simulate the fracture toughness tests, it is essential to identify a set of coefficients corresponding to the constitutive law. These coefficients involve the hardening law and the damage model. The procedure for determining the hardening law coefficients for both the X52 and E355 mod. steels was previously presented in Section 3.2.2. For details on this procedure, please refer to that section. The GTN model coefficients to be identified are: q_1, q_2, f_c, f_R, A_n^0, and $\bar{\kappa}_c$, which are all material parameters.

X52 steel

Only one type of smooth tensile specimen was employed for the tensile tests with the X52 steel. This condition is not optimal to identify the parameters of the GTN model since several stress triaxiality levels should be analyzed to well estimate the damage model's coefficients. Additionally, this steel exhibited significant dispersion in the experimental results across different tests. Figure 6.4 presents experimental results at various strain rates in the transverse direction, which is the less ductile than the longitudinal orientation of this steel, and to the crack propagation direction of the subsequent fracture toughness tests. All tests were conducted using specimens of identical geometry (see Figure 6.5). The curves reveal a noticeable dispersion in the material's behavior, highlighting the challenges in accurately identifying a constitutive law for this steel. Additionally, the fracture toughness specimens and the disk specimens discussed in Chapter 3 were machined from different tube sections. Consequently, it was decided to identify the model's coefficients by directly simulating the fracture toughness tests using both macro (CT) and sub-size (mDCT) specimens.

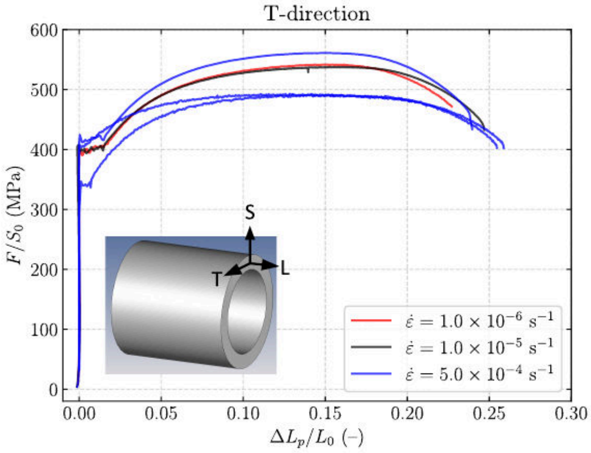

Figure 6.4: Experimental tensile test results for X52 steel at various strain rates in the transverse direction.

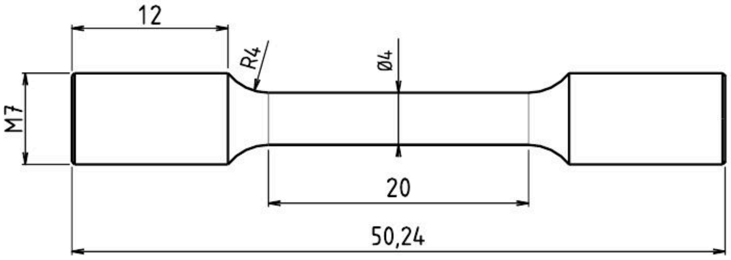

Figure 6.5: Dimensions of the smooth tensile specimens used in the experimental tests.

Table 6.1 lists the fitted coefficients for the studied steel. The fitting process was performed simultaneously for all fracture toughness specimens. The hardening law presented here slightly differs from the one in Chapter 3 for the same material. This variation can be attributed to the observed scatter in the behavior of the X52 steel. The void nucleation coefficients (A_n^0 and $\bar{\kappa_c}$) identified for this material indicate significant secondary void nucleation occurring at low plastic strain values. A comparison between experimental and numerical results employing the coefficients of Table 6.1 will be presented in Section 6.5.

Property	Value	Unit
	Plasticity	
E, ν	200, 0.3	GPa, —
$\sigma_F(\kappa)$	$\max(340,\ 243 + 158(1 - \exp(-28.4\kappa))$ $+400(1 - \exp(-2.7\kappa)))$	MPa
$\dot{\kappa}_0$, K, n	1.0, 52.3, 5.17	s^{-1}, MPa, —
	Ductile damage	
f_0	3×10^{-3}	—
q_1, q_2	1.25, 1.40	—
A_n^0, $\bar{\kappa}_c$	1.0, 0.15	—, —
f_c, f_R	0.05, 0.24	—, —
ℓ_ω, ℓ_κ	100, 33	µm, µm

Table 6.1: Plasticity and ductile damage coefficients identified for the X52 steel.

E355 mod. steel

Unlike the X52 steel, the E355 mod. steel demonstrated consistent and reproducible results with minimal scatter, as shown in Figure 6.6. All tests utilized the same specimen geometry presented in Figure 6.5. The differences observed at varying strain rates are attributed to the material's viscous response, where higher loading rates result in increased stress and strain. Additionally, the strain at failure was identical in both the longitudinal and transverse directions. For this steel, the model coefficients were determined for the longitudinal direction, as crack propagation occurred along this direction for the fracture toughness tests. The same hardening law identified in Chapter 3 was also applied to this analysis, only the damage coefficients were identified in this chapter.

Following the procedure used for the X52 steel, the damage coefficients were fitted directly using the fracture toughness specimens. The optimized material coefficients for the E355 mod. steel are presented in Table 6.2. As a modern steel, it exhibits approximately ten times fewer initial voids (f_0) compared to the X52 steel. Additionally, the secondary void nucleation coefficients (A_n^0 and $\bar{\kappa}_c$) indicate low void nucleation rates, which occur only at high strain values. A comparison between the experimental and numerical results using these identified coefficients is presented in Section 6.5.

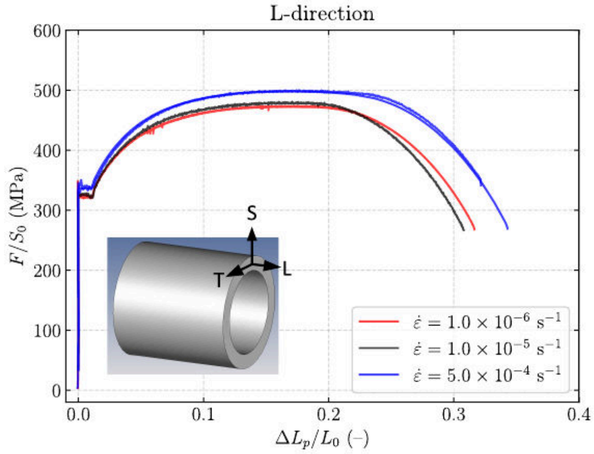

Figure 6.6: Experimental tensile test results for E355 mod. steel at various strain rates in the longitudinal direction.

Property	Value	Unit
	Plasticity	
E, ν	200, 0.3	GPa, —
$\sigma_F(\kappa)$	$\max(325,\ 273 + 214(1 - \exp(-19.29\kappa))$ $+141(1 - \exp(-2.75\kappa)) + 148\kappa)$	MPa
$\dot{\kappa}_0$, K, n	1.0, 213, 4.43	s^{-1}, MPa, —
	Ductile damage	
f_0	4×10^{-4}	—
q_1, q_2	1.5, 1.0	—
A_n^0, $\bar{\kappa}_c$	0.2, 0.8	—, —
f_c, f_R	0.05, 0.35	—, —
ℓ_ω, ℓ_κ	100, 33	µm, µm

Table 6.2: Plasticity and ductile damage coefficients identified for the E355 mod. steel.

6.3 Methodology

This section provides an overview of the experimental methodology used in this study. For detailed information about the procedure, please refer to Madi et al., 2024.

6.3.1 Pre-cracking

The specimens are initially machined without side-grooves and then polished to facilitate the tracking of crack propagation using an optical device. Fatigue pre-cracking is conducted using an electromechanical machine with a force capacity of ±10 kN. Given the reduced size of the mDCT specimens, special care is taken during the pre-cracking process to minimize any impact on the subsequent results. After the pre-cracking steps, side-grooves are machined in both sides of the specimens using Electrical Discharge Machining (EDM). Figure 6.7 contains an example of the left and right sides of the side-grooves machined in a mDCT specimen.

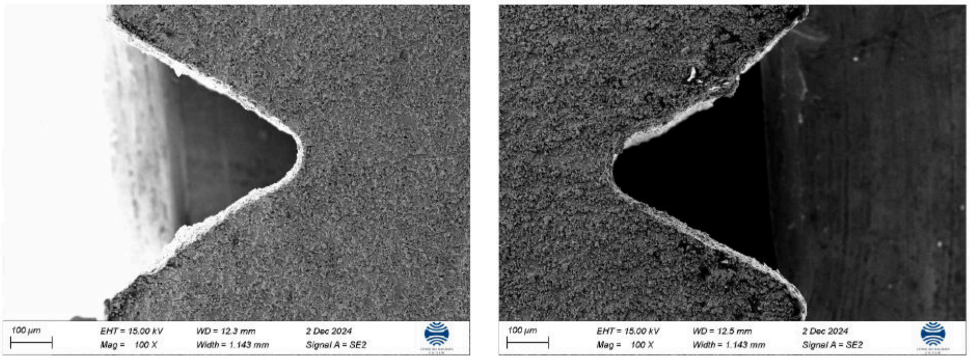

Figure 6.7: Examples of side-grooves machined in a mDCT specimen.

6.3.2 Compliance method

The Edge Trace Techinique (see Figure 6.8) is employed to monitor key parameters, including Load Line Opening Displacement (LLOD) and the Opening Angle (α).

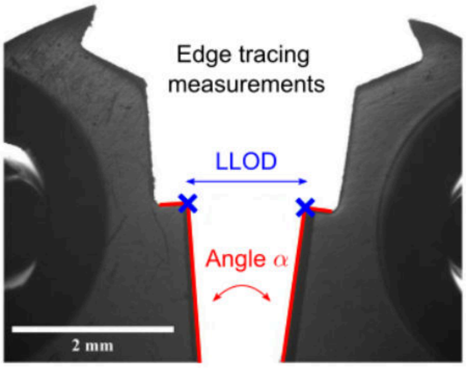

Figure 6.8: Edge trace technique to monitor the Load Line Opening Displacement (LLOD) and the Opening Angle (α).

To assess crack propagation during the test, the elastic compliance method is employed, which involves a loading, holding, and unloading procedure. During the loading phase, a displacement is applied at a low load rate of 100 µm/min until an incremental load line displacement of 50 µm is reached. This displacement is then held for 30 seconds to minimize material relaxation during the subsequent unloading and reloading steps. After the holding period, the specimen is unloaded to 65% of the load achieved at the end of the holding phase and then reloaded to the same force. This process allows for the calculation of crack length using the compliance equations specified in the ASTM E1820 standard. This sequence is repeated until significant crack propagation (approximately 1.3–1.5 mm) is observed. Once the final cycle is completed, the force is returned to zero. Figure 6.9 contains an example of an experimental curve with the compliance method.

6.3.3 CTOD determination

In this study, the Crack Tip Opening Displacement (CTOD or δ) is determined using the Edge Trace (ET) technique, as described in Madi et al., 2024. This method determines δ through straightforward geometric considerations. Figure 6.10 illustrates a schematic representation of the specimen before and

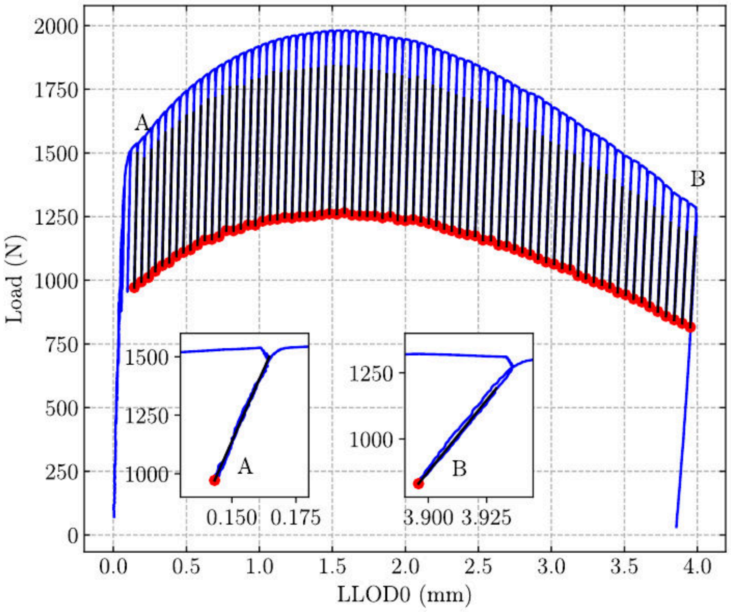

Figure 6.9: Load vs. displacement curve using the compliance method to mesure crack propagation.

after loading. The positions of the four key points shown in Figure 6.10 are defined as follows in the undeformed configuration:

$$P_R = \begin{pmatrix} 0 \\ 0 \end{pmatrix}, \quad P_0 = \begin{pmatrix} 0 \\ D \end{pmatrix}, \quad P_1 = \begin{pmatrix} -H \\ D \end{pmatrix}, \quad P_T = \begin{pmatrix} a_0 \\ 0 \end{pmatrix} \tag{6.2}$$

The reference point (P_R) does not exist in the experiment and is shown in Figure 6.10 only for illustration.

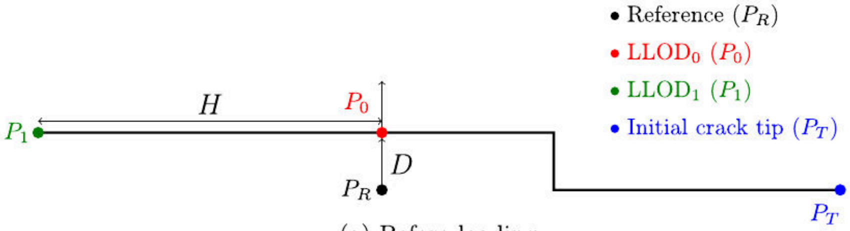

(a) Before loading

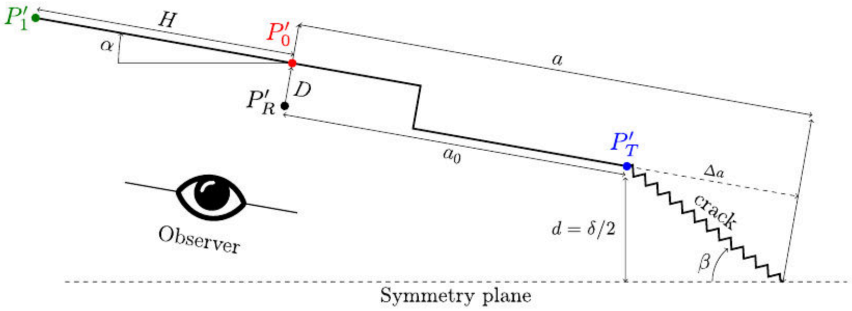

(b) After loading

Figure 6.10: Schematic representation of the measurement of the CTOD using the Edge Trace (ET) technique.

Please note that in the meshes employed in the simulations, $D = 0$. The optical system measures the displacement of points P_0 and P_1. After loading, their positions are defined as follows:

$$P_0' = \begin{pmatrix} u_0 \\ D + \Delta_0 \end{pmatrix}, \quad P_1' = \begin{pmatrix} -H + u_1 \\ D + \Delta_1 \end{pmatrix}, \tag{6.3}$$

Assuming the segment between these two points remains undeformed, the rotation angle can be expressed as:

$$\sin(\alpha) = \frac{\Delta_1 - \Delta_0}{H} \tag{6.4}$$

The positions of points P_R and P_T after loading are then re-expressed as:

$$P_R' = P_0' + \begin{pmatrix} -\sin(\alpha)D \\ -\cos(\alpha)D \end{pmatrix} \tag{6.5}$$

and,

$$P_T' = P_R' + \begin{pmatrix} \cos(\alpha)a_0 \\ -\sin(\alpha)a_0 \end{pmatrix} = \begin{pmatrix} u_0 - \sin(\alpha)D + \cos(\alpha)a_0 \\ D + \Delta_0 - \cos(\alpha)D - \sin(\alpha)a_0 \end{pmatrix} \tag{6.6}$$

It is assumed that the distance between the initial crack tip and the reference point remains constant at a_0. The crack tip opening displacement is defined as twice the vertical displacement of point P_T', and is given by:

$$\delta = \mathrm{LLOD}_0 + 2D(1 - \cos(\alpha)) - 2a_0 \sin(\alpha) \tag{6.7}$$

where $\mathrm{LLOD}_0 \equiv 2\Delta_0$. According to the ASTM E1820 standard, the maximum δ capacity for a specimen is given by:

$$\delta_{max} = \frac{W - a_0}{10m} \tag{6.8}$$

where m depends on the specimen geometry. For CT and mDCT specimens, it is defined as follows:

$$m = 3.62 - 4.21\left(\frac{\sigma_{YS}}{\sigma_{TS}}\right) + 4.33\left(\frac{\sigma_{YS}}{\sigma_{TS}}\right)^2 - 2.00\left(\frac{\sigma_{YS}}{\sigma_{TS}}\right)^3 \tag{6.9}$$

where σ_{YS} and σ_{TS} are respectively the yield strength and the ultimate tensile strength. This calculation requires that the ratio $\sigma_{YS}/\sigma_{TS} \geq 0.5$.

6.4 Simulation model

This section presents the finite element formulation used in the numerical simulations, incorporating both plasticity and damage. Additionally, this section details the numerical procedure employed for for crack advance computation in the simulations.

6.4.1 Finite element formulation

To address the pressure oscillations caused by volumetric locking, a three-field finite element model was employed in Chapter 3. This approach, as illustrated in Figure 3.25, uses quadratic shape functions to interpolate displacements ($\{\boldsymbol{u}\}$) and introduces two additional degrees of freedom: nodal pressure ($\{p\}$) and volume variation ($\{\theta\}$), both interpolated using linear shape functions. While this methodology is effective, it demands high computational costs due to the high number of degrees of freedom of the problem.

For the fracture toughness simulations, another approach was adopted: displacements were interpolated using linear shape functions, and pressure oscillations due to volumetric locking were mitigated using the B-bar formulation (Hughes, 1980, Elguedj et al., 2008). This approach decomposes the strain-displacement matrix $\boldsymbol{B}$ into its deviatoric ($\boldsymbol{B}_d$) and hydrostatic ($\boldsymbol{B}_h$) components, as shown below:

$$\boldsymbol{B} = \boldsymbol{B}_d + \boldsymbol{B}_h \tag{6.10}$$

Subsequently, the hydrostatic term is averaged over the element volume. This averaged term is now denoted as $\bar{\boldsymbol{B}}_h$, allowing the strain-displacement matrix to be recomputed as $\bar{\boldsymbol{B}}$, as follows:

$$\bar{\boldsymbol{B}} = \boldsymbol{B}_d + \bar{\boldsymbol{B}}_h \tag{6.11}$$

Further details regarding this approach can be found in Appendix B.

A comparison of the B-bar and a standard formulation was conducted for a fracture toughness test using a mDCT-2 specimen. This simulation, characterized by high-pressure gradients and a large number of degrees of freedom, served as a benchmark for evaluating the efficiency of the B-bar formulation. Figure 6.11 illustrates the pressure fields obtained with the standard formulation, where fluctuations ahead of the crack tip indicate volumetric locking. This issue is effectively addressed by the B-bar formulation.

(i) Standard formulation

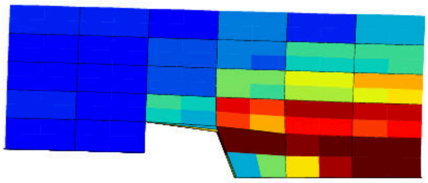

(ii) B-bar formulation

Figure 6.11: Volumetric locking observed ahead of a blunted crack when employing the standard formulation.

Subsequently, a comparison was made between the three-field finite element formulation, which employs quadratic elements with reduced integration, and the B-bar formulation, which uses linear elements with full integration. Figure 6.12 presents the results of this comparison. The simulated force using the B-bar formulation was slightly higher than that obtained with the three-field method. This discrepancy arises because linear elements, having fewer nodes, are inherently stiffer. Nonetheless, the pressure fields showed comparable behavior for both methods.

In the example of Figure 6.12, the three-field method required 1 hour and 40 minutes to complete the simulation, involving 103,762 degrees of freedom. In contrast, the B-bar formulation produced nearly identical results in just 18 minutes, utilizing only 33,974 degrees of freedom. Consequently, the B-bar formulation was selected for the subsequent fracture toughness simulations.

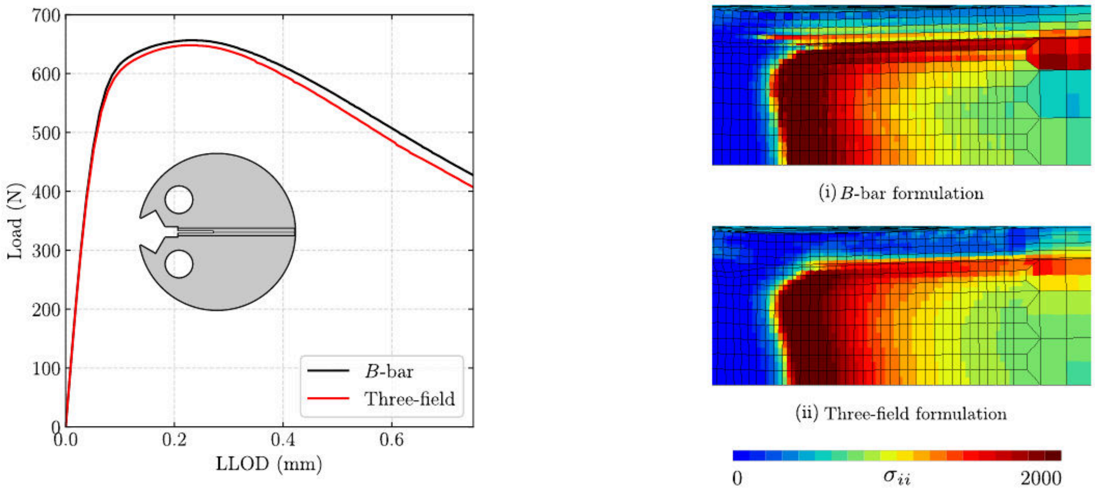

(i) *B*-bar formulation

(ii) Three-field formulation

(a) Load vs. LLOD curve.

(b) Pressure field for both formulations.

Figure 6.12: Comparison between the *B*-bar and the three-field formulations.

6.4.2 Nonlocal GTN model

The damage model employed in this study is the well-known Gurson-Tvergaard-Needleman (GTN) model. To address strain localization and mesh dependence, a nonlocal formulation of the GTN model was utilized. This approach introduces two additional nodal degrees of freedom: the nonlocal plastic volume variation ($\bar{\omega}$) and the nonlocal accumulated plastic strain ($\bar{\kappa}$). A detailed description of the model's formulation and implementation is provided in Section 5.2.

6.4.3 Internal length and mesh discretization

The nonlocal GTN model involves the use of two internal length scales: ℓ_ω and ℓ_κ (see Equations 5.8 and 5.9), associated to the nonlocal variables $\bar{\omega}$ and $\bar{\kappa}$, respectively. The length scale for void growth, ℓ_ω, was set to 100 µm, a value that corresponds to the typical element size used in local models for pipeline steel simulations (Madi et al., 2020). Recognizing that the length scale associated with quasi-cleavage is likely smaller, ℓ_κ was set to approximately 33 µm. Following Tuhami et al., 2022, the mesh size in the crack propagation zone should be less than one-third of the material's internal length. Since void growth is the dominant failure mechanism observed in the fracture toughness tests, a mesh size of around 33 µm was chosen for the simulations. Figure 6.13 provides a schematic representation of the mesh size and its relation to the internal length scale ℓ_ω.

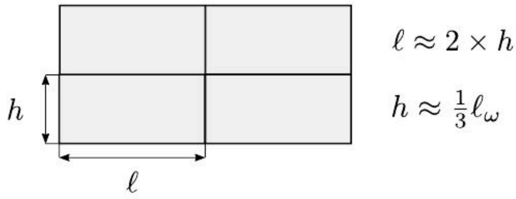

Figure 6.13: Schematic the mesh size and its relation with the characteristic length.

The simulations were performed using 3D meshes, with only one-quarter of each specimen modeled to exploit symmetry. The meshes were refined in the interest region, specifically the crack propagation zone. In this area, the element size matches the dimensions described in Figure 6.13. Figure 6.14 shows the meshes for the mDCT-2 and CT-7.5 specimens. The side-grooves were modeled based on the dimensions provided in Figure 6.3.

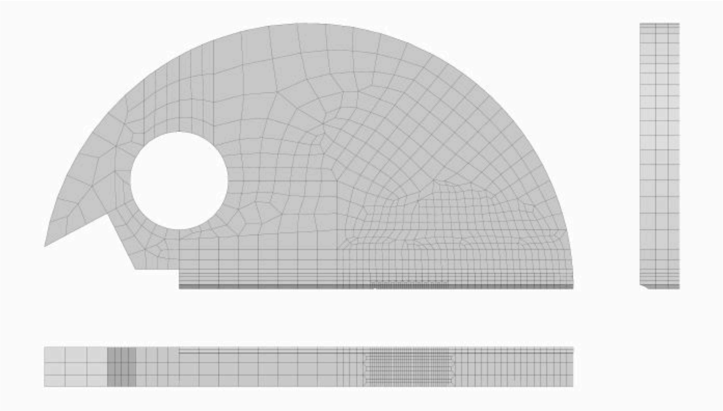

(a) mDCT-2.

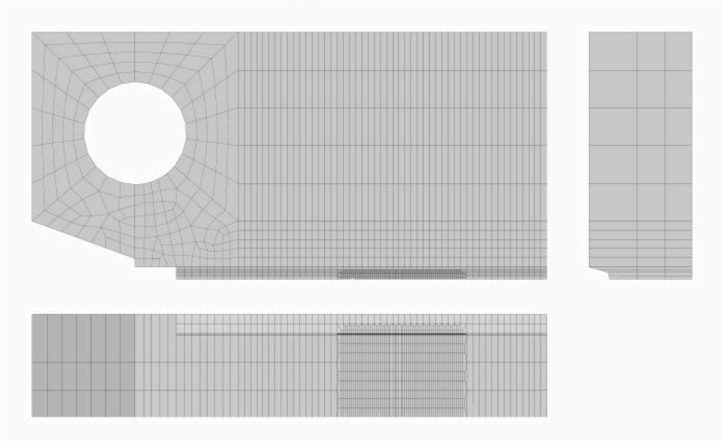

(b) CT-7.5.

Figure 6.14: Meshes employed in the numerical simulations.

Crack propagation in the simulation is modeled using the element removal technique. In this approach, a critical porosity value is defined to represent the porosity at the onset of cracking. This value depends on the material's properties and is expressed as:

$$f_* = 1/q_1 - \epsilon \tag{6.12}$$

where q_1 is a coefficient of the GTN model, and ϵ is a small parameter, typically 10^{-3}. During the simulation, an element is removed when a predefined number of its integration points reach this critical porosity value. In this study, the meshes employ linear hexahedral elements with full integration, which involves eight integration points per element. An element is removed when four of its integration points reach the critical porosity level. Once an element is removed, it is treated as broken, and it is not considered anymore during the simulation. At this point, the nonlocal variables $\bar{\kappa}$ and $\bar{\omega}$ are frozen at their values at the time of element removal. Nodal displacements which are attached to removed elements only are fixed. Similarly, the porosity is set to the porosity at failure and ceases to evolve during the simulation.

6.4.4 Numerical computation of crack advance

Two methodologies were employed to compute the crack advance (Δa) in the fracture toughness test simulations. The first method, based on the elastic compliance technique (see Section 6.3.2), follows a loading, holding, and unloading sequence, which allows the calculation of the crack advance as it is specified in the ASTM E1820 standard. The exact same procedure was applied for the experimental tests. Figure 6.15 contains the comparison between the experiment and the simulation following the compliance technique. The softening observed during the crack propagation decreases the elastic slope of the loading/unloading step. This is numerically reproduced by modifying the Young modulus E into E' as follows:

$$E' = E \times (1 - q_1 f_*) \tag{6.13}$$

where q_1 and f_* are coefficients of the GTN model. As detailed above, elements are removed when $f_* = 1/q_1 - \epsilon$, which also contributes to the specimen compliance increase. Incorporating the load, hold, and unload steps into simulations significantly increases computation time. To avoid these additional steps, an alternative methodology was implemented. This approach uses post-processing to calculate crack propagation based on the material's porosity level. During this post-processing, the elements in the crack propagation zone, highlighted in red in Figure 6.16, are examined.

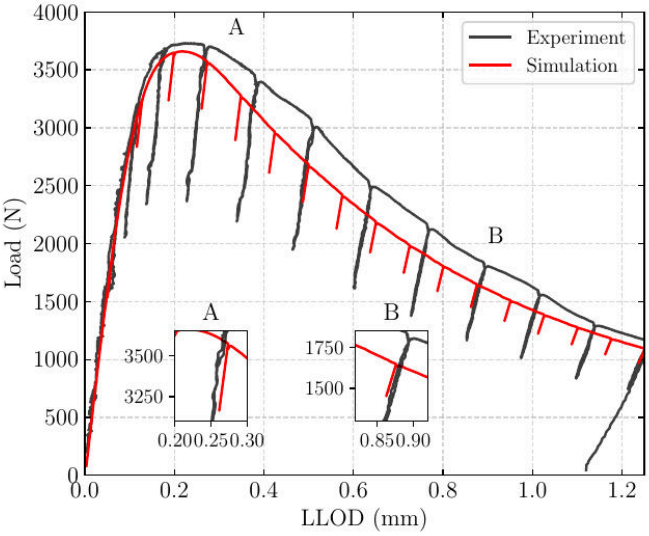

Figure 6.15: Experimental and numerical results based on the elastic compliance technique for the CT-7.5 specimen.

The post-processing procedure begins by identifying the initial crack front (red dots) and analyzing the porosity values at the integration points of elements within the crack propagation zone. Elements that reach the critical porosity value (f_*), which is a material-dependent coefficient, are considered as broken. The updated crack front is then determined after crack propagation, and the crack extension for each point is calculated based on its distance from the load line. To minimize "zig-zag" patterns, the crack extension is averaged using the extensions of neighboring broken points. Figure 6.17 illustrates this process.

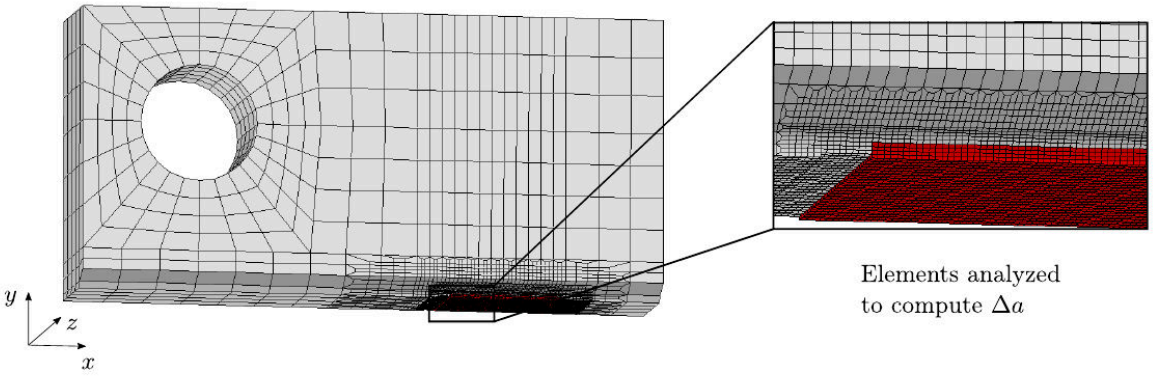

Figure 6.16: Elements analyzed for crack propagation computation.

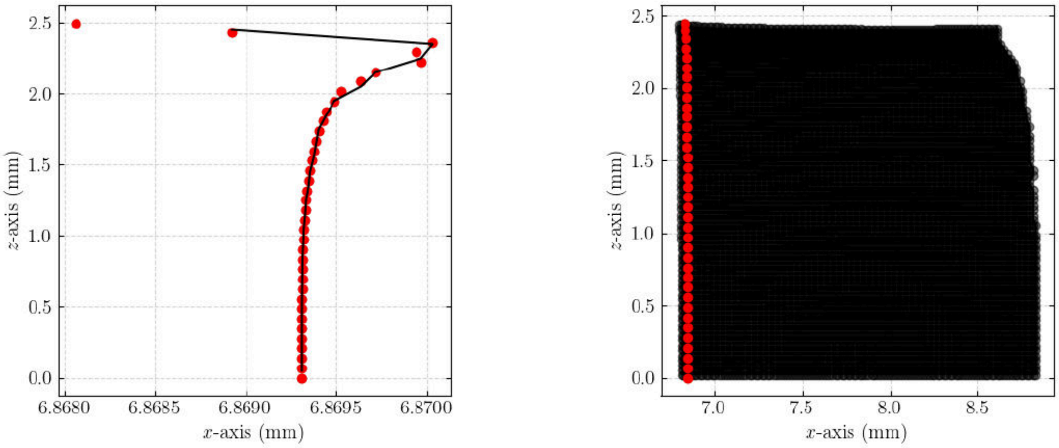

(a)

(b)

Figure 6.17: Numerical computation of crack propagation in a compact tension (CT) specimen at different simulation times. (a) Initial crack front. (b) Final crack extension.

The code applies a correction to the crack extension measurement to account for the specimen's opening angle. Figure 6.18 illustrates the corrected crack length, denoted as a_c. The origin of the coordinate system is defined by the LLOD measurement point (P_0') projected onto the horizontal axis. The position of P_0' is given by:

$$P_0' = \begin{pmatrix} 0 \\ \Delta y \end{pmatrix} \tag{6.14}$$

In this reference frame, the crack tip is located at:

$$P_{CT} = \begin{pmatrix} a_h \\ 0 \end{pmatrix} \tag{6.15}$$

Considering $k = \tan(\alpha)$, the equation of the straight line passing through P_0' with slope α is defined by:

$$y = \Delta y - kx \tag{6.16}$$

The equation of the straight line passing through P_{CT} and perpendicular to the previous one is:

$$y = \frac{1}{k}(x - a_h) \tag{6.17}$$

The horizontal position of the intersection of these two lines is then:

$$x_{CT} = \frac{k\Delta y}{1 + k^2} \tag{6.18}$$

The corresponding y-coordinate can be calculated using one of the line equations. Finally, the distance between P_0' and P_{CT} is computed, providing the "corrected" crack length a_c.

Figure 6.19 compares the $\Delta a - \delta$ curves obtained using the horizontal and the corrected Δa values. It can be observed that, during the blunting phase, the horizontal Δa measure shows a decrease in crack extension, which incorrectly becomes negative. Furthermore, the horizontal measure fails to match the slope of the construction line proposed by the ASTM E1820 standard, where $\delta = 1.4\Delta a$. In contrast, the corrected Δa measure accurately reproduces this relationship.

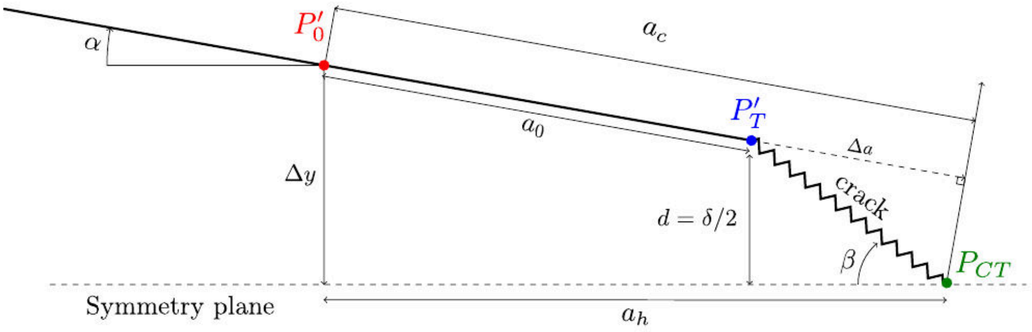

Figure 6.18: Schematization of the numerical procedure for crack advance computation.

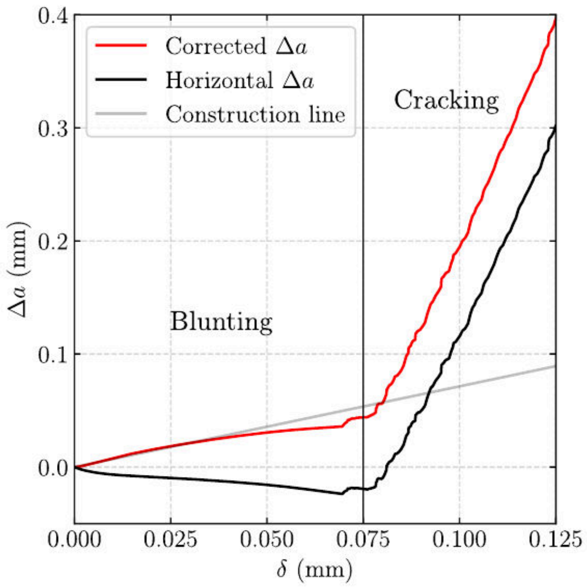

Figure 6.19: Comparison between corrected and horizontal Δa measures.

Figure 6.20 compares the $J - \Delta a$ and $\delta - \Delta a$ curves for a CT specimen, calculated using both the compliance technique and a post-processing methodology to assess crack growth. The J-integral was computed according to the ASTM E1820 standard, as introduced in Section 2.5.1, while the δ values were determined following the procedure in Section 6.3.3. The construction line slopes were calculated as $J = 2\sigma_Y \Delta a$ and $\delta = 1.4\Delta a$, based on the ASTM E1820 recommendations. Results from both methods show close agreement. The post-processing method offers a significant advantage in efficiency, as it eliminates the need for intermediate load, hold, and unload steps required to compute crack growth. Therefore, this methodology will be used in the subsequent simulations.

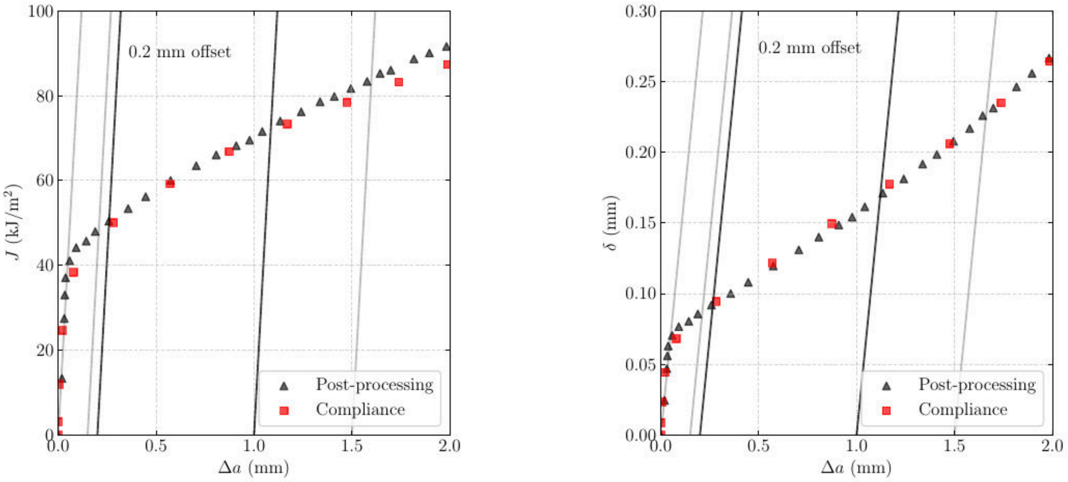

(a) $J - \Delta a$ plot.

(b) $\delta - \Delta a$ plot.

Figure 6.20: Comparison of the results obtained for the CT-7.5 specimen using the compliance technique versus the post-processing method for crack propagation computation.

6.5 Results and discussions

6.5.1 X52 steel

To ensure accuracy and avoid dimensional discrepancies, the meshes for both macro and sub-size specimens (see Figure 6.1 for specimen's geometries) were modeled to precisely match the dimensions of the experimental specimens. Table 6.3 provides the dimensions of each specimen.

Size (mm)	mDCT-2	mDCT-5	CT-7.5
B	2.01	4.96	7.44
B_n	1.61	3.97	5.99
W	10.00	10.00	15.00
a_0	4.82	5.07	7.98

Table 6.3: Dimensions of each fracture toughness specimen of the X52 steel.

In each simulation, a displacement boundary condition was applied to match the loading rate used in the corresponding experimental test. The loading rate was approximately 1.0 µm/s for the sub-size specimens and 1.5 µm/s for the macro specimen. Figure 6.21 compares the experimental and numerical

Load–LLOD curves from the fracture toughness. The simulations were conducted using the constitutive model coefficients listed in Table 6.1 for all specimens. It is evident that the elasto-plastic model fails to accurately represent the fracture toughness test once crack propagation begins, as indicated by the difference between the elasto-plastic curve (black) from the experimental curve (gray). To capture the material softening due to damage and subsequent crack propagation, a damage model such as the GTN model is required. Although the simulations do not perfectly match the maximum load and crack propagation phases in the curves, they show good agreement, considering the scatter observed in the experimental results.

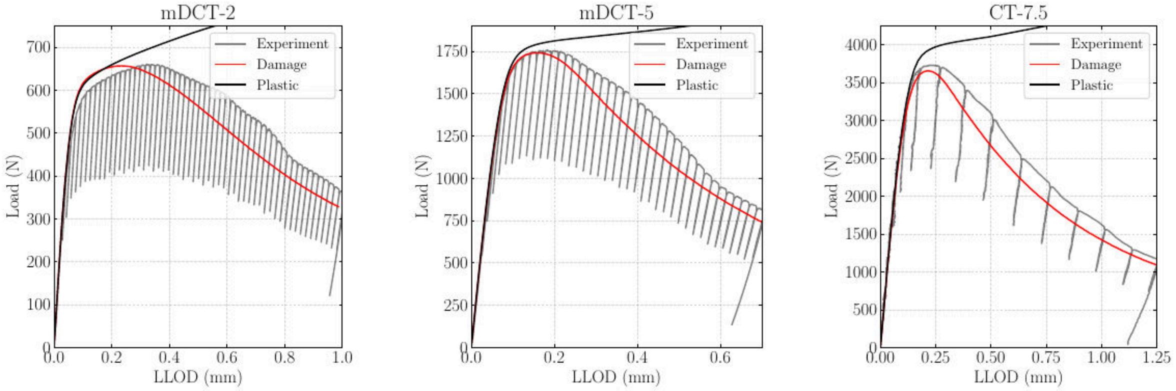

Figure 6.21: Comparison of experimental and numerical Load vs. LLOD curves using macro and sub-size specimens for the X52 steel.

As previously mentioned, a post-processing technique was employed to calculate crack propagation in the simulations. Figure 6.22 compares the experimental and numerical results for both macro and sub-size specimens, where experimental data are shown as symbols and simulation results as lines. Figure 6.22a displays the $J - \Delta a$ curves for the three specimens, while Figure 6.22b presents the $\delta - \Delta a$ results for each specimen.

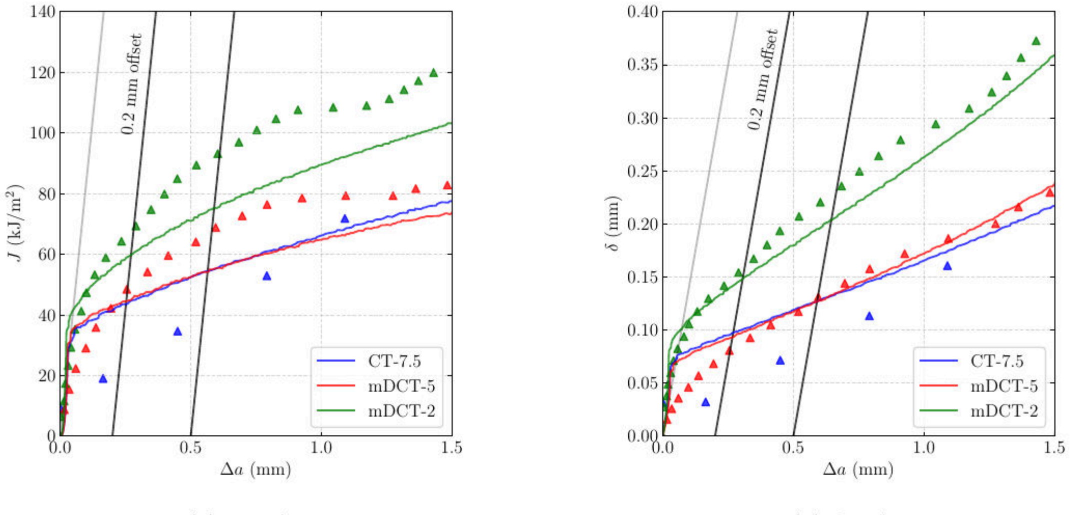

(a) $J - \Delta a$.

(b) $\delta - \Delta a$.

Figure 6.22: Experimental and numerical results for macro and sub-size specimens of the X52 steel.

Figure 6.22 shows that the slopes of the construction lines align well with the numerical results. In the experiments, larger specimens tend to exhibit earlier crack initiation, a trend particularly noticeable for the CT-7.5 specimen. The discrepancy between the onset of the experimental and numerical curves was partially addressed by reducing the strain threshold for void nucleation. However, further reductions had no additional effect, and the model was unable to fully capture the experimental behavior. Moreover, the numerical $\delta - \Delta a$ curve demonstrates better agreement with the experimental results compared to the $J - \Delta a$ curve.

The results also reveal that J and δ values increase as specimen size decreases. The mDCT-5 and CT-7.5 specimens display closer J and δ values, while the smallest specimen, the mDCT-2, exhibits the highest J and δ values. This trend aligns with the end of the transition zone illustrated in Figure 2.19, where fracture toughness decreases with increasing thickness until reaching a plateau for sufficiently thick specimens.

To provide a detailed analysis of each specimen's results, the $J - \Delta a$ curves are presented in Figure 6.23. The J_{max} values were determined using Equation 6.1 and the specimen dimensions listed in Table 6.3. It is important to note that the full range of data for the CT-7.5 and mDCT-5 specimens falls within the validity limits of ASTM E1820. The intersections between the power-law fits (dotted lines) and the 0.2 and 0.5 mm offset lines define the $J_{0.2}$ and $J_{0.5}$ values, respectively. A summary of the results for all specimens is provided in Table 6.4.

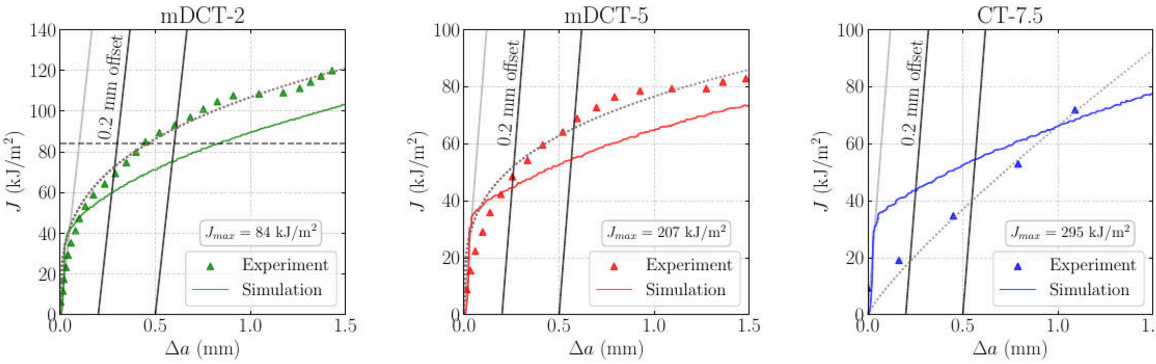

Figure 6.23: $J - \Delta a$ curves for all the specimens.

Specimen	J_{max} (kJ/m^2)	$J_{0.2}$ (kJ/m^2)		$J_{0.5}$ (kJ/m^2)	
		Experiment	Simulation	Experiment	Simulation
mDCT-2	84	73	59	92	76
mDCT-5	207	52	43	65	55
CT-7.5	295	19	40	42	55

Table 6.4: Experimental and numerical J-integral values for the sub-size and macro specimens.

The same approach was applied to the δ measurements. Figure 6.24 presents the experimental and numerical $\delta - \Delta a$ curves for each specimen. The δ_{max} values were calculated following Equation 6.8. Table 6.5 summarizes the experimental and numerical results for each specimen.

To evaluate which measure better aligns with the experimental values, the experimental and numerical results for J and δ from Tables 6.4 and 6.5 were plotted against each other. Figure 6.25 presents these

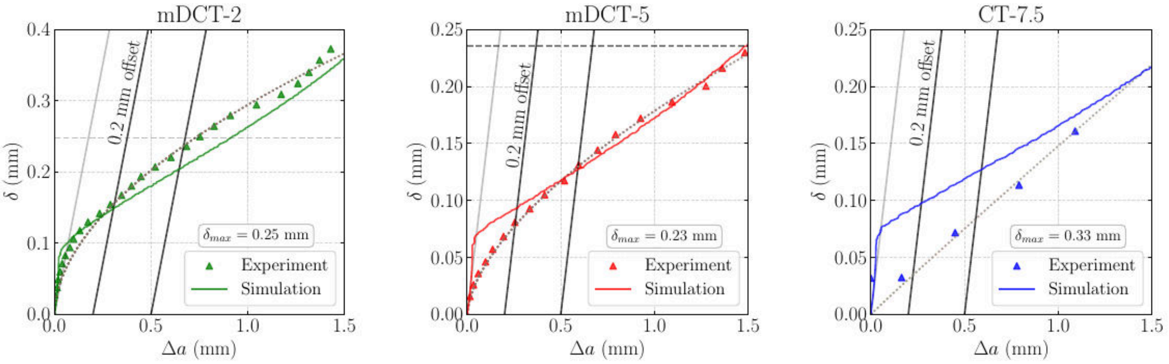

Figure 6.24: $\delta - \Delta a$ curves for all the specimens.

Specimen	δ_{max} (mm)	$\delta_{0.2}$ (mm)		$\delta_{0.5}$ (mm)	
		Experiment	Simulation	Experiment	Simulation
mDCT-2	0.25	0.16	0.12	0.24	0.21
mDCT-5	0.24	0.08	0.08	0.13	0.13
CT-7.5	0.33	0.03	0.08	0.08	0.13

Table 6.5: Experimental and numerical δ values for the sub-size and macro specimens.

results along with the regression line and the coefficient of determination (R^2).

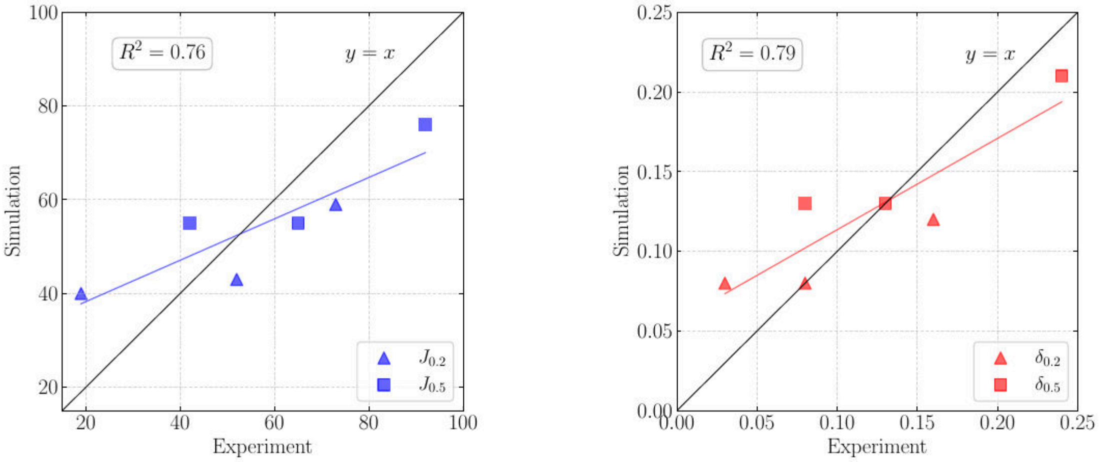

(a) J-values (kJ/m^2).

(b) δ-values (mm).

Figure 6.25: Comparison of the J and δ values obtained from experimental measurements and numerical simulations for each specimen. The black line represent the linear function $y = x$ and the blue and red curves were obtained through linear regression.

The figures indicate that both J and δ provide overall good predictions of the experimental results, with R^2 value equal to 0.76 for J and 0.79 for δ. In experiments, δ is often easier to correlate with observed crack propagation, as it corresponds directly with visual or measured crack opening displacements, whereas the J-integral relies on energy-based calculations that may not always align precisely with observed behavior. Additionally, δ offers a direct, physical measure of crack tip opening displacement, providing a more intuitive understanding of the crack driving force and crack-tip deformation. Finally, the main difference is that one is calculated (J-integral) and the other is measured (δ).

One disadvantage of using the J-integral is that it can introduce inaccuracies in the results due to reliance on formulas derived from strong assumptions, such as plane strain, nonlinear elasticity, and low plasticity, which do not always accurately reflect real conditions. For materials with higher ductility or larger plastic zones, the δ parameter often captures deformation more effectively than the J-integral, which may underestimate the extent of plasticity near the crack tip. The advantage of using δ lies in its ease of application when assessing a pipe with a crack under large deformations. In contrast, the J-integral is not suitable for such conditions, as it was not defined to account for them.

6.5.2 E355 mod. steel

Figure 6.26 compares the Load vs. LLOD curves obtained from experiments and simulations for the fracture toughness tests of the E355 mod. steel. The constitutive law presented in Table 6.2 was identified by considering both the mDCT and CT specimens simultaneously. However, it was not possible to determine a single set of coefficients that could accurately reproduce the results for both sub-size and macro specimens. The results indicate that the set of coefficients listed in Table 6.2 accurately reproduces the behavior of the CT-10 specimen. However, applying the same set of coefficients to the mini specimens results in a more ductile response compared to the experimental observations. No definitive explanation was found for this discrepancy. To address this, a parametric study will be conducted in Section 6.6, exploring variations in specimen size, thickness, and material coefficients to better understand the size effect in fracture toughness tests.

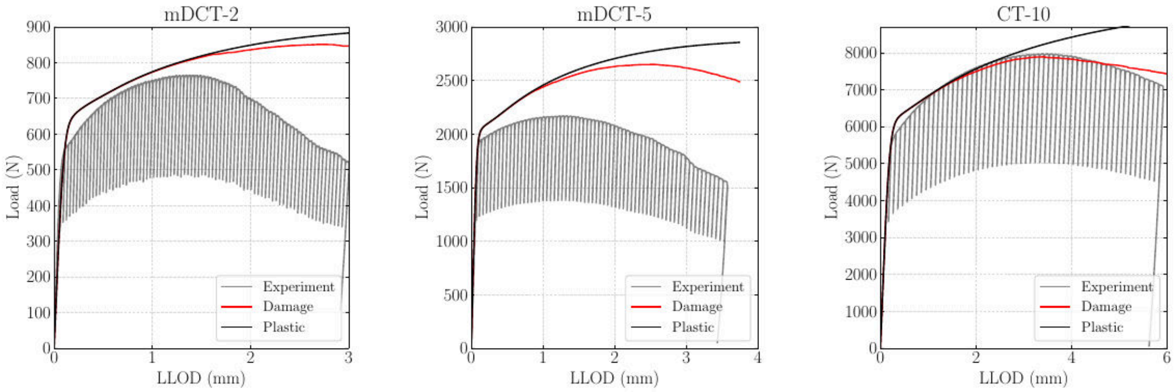

Figure 6.26: Comparison of experimental and numerical Load vs. LLOD curves using macro and sub-size specimens for the E355 mod. steel.

6.6 Parametrical study

The parametric study was conducted using two distinct sets of compact tension (CT) specimens: one consisting of homothetic specimens with systematically scaled dimensions and the other featuring specimens with varying thicknesses. This comprehensive approach enabled a detailed investigation into the influence of both specimen size and thickness on fracture toughness. This section presents the geometries of the specimens used in the study, along with the results obtained for the homothetic and varying-thickness cases across different material configurations.

6.6.1 Specimens' geometries

For the homothetic specimens, five specimens of varying sizes were analyzed, with dimensions scaled systematically from the smallest to the largest. The smallest specimen, labeled CT-3.125, features a thickness (B) of 3.125 mm and a width (W) of 6.25 mm, maintaining the ratios B/W and a_0/W equal to 0.5 and 0.55, respectively. Each specimen includes side-grooves on both sides, equivalent to 10% of B, to promote appropriate stress triaxiality during testing. The initial crack length and overall height of the CT-3.125 specimen are 1.25 mm and 7.5 mm, respectively.

To create larger specimens, all dimensions were scaled by a factor of two for each subsequent specimen, resulting in a series ranging from the smallest (CT-3.125) to the largest (CT-50). It is important to note that this scaling process did not involve simply multiplying the meshes by a factor of two, as this would have made the element size much smaller than the internal length. Instead, each mesh was generated individually, ensuring that the element size, as previously shown in Figure 6.13, was consistent across all cases. Table 6.6 provides detailed dimensions for all specimens, while Figure 6.27 illustrates their geometries.

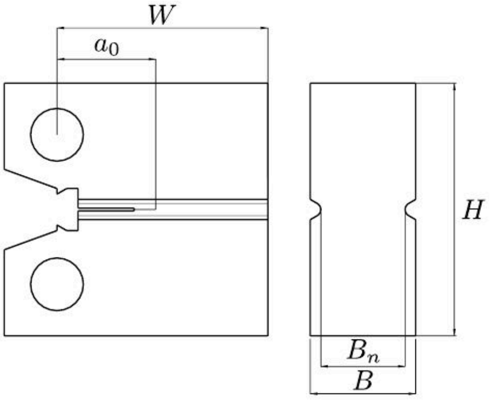

Figure 6.27: Homothetic specimens geometry.

	W (mm)	a_0 (mm)	B (mm)	H (mm)
CT-3.125	6.25	3.4375	3.125	7.5
CT-6.25	12.5	6.875	6.25	15
CT-12.5	25	13.75	12.5	30
CT-20	40	22	20	60
CT-25	50	27.5	25	60
CT-50	100	55	50	120

Table 6.6: Dimensions of the homothetic compact tension (CT) specimens.

The varying-thickness specimens were based on a compact tension (CT) design with dimensions equivalent to the CT-12.5 standard. The investigation systematically varied the thickness to evaluate its influence on fracture behavior. Five thicknesses (B) were tested: 2.5, 5, 7.5, 10, 12.5 and 25 mm. In all cases, side-grooves were included, accounting for 10% of the total thickness. Figure 6.28 illustrates the specimen dimensions, and Table 6.7 provides a summary of the dimensions for all specimens.

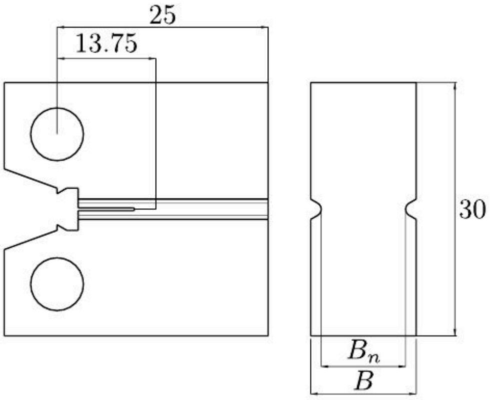

Figure 6.28: Varying thickness specimen geometry.

	W (mm)	a_0 (mm)	B (mm)	H (mm)
CT-2.5	25	13.75	2.5	30
CT-5	25	13.75	5	30
CT-7.5	25	13.75	7.5	30
CT-10	25	13.75	10	30
CT-12.5	25	13.75	12.5	30
CT-25	25	13.75	25	30

Table 6.7: Dimensions of compact tension (CT) specimens for varying thicknesses.

6.6.2 Results and discussions

The initial analysis was conducted using the constitutive law optimized for X52 steel (see Table 6.1). Figure 6.29 shows the $J - \Delta a$ curves for both the homothetic and varying-thickness specimens. The construction line (gray line) was calculated according to the ASTM E1820 standard, defined as $J = 2\sigma_Y \Delta a$. The black lines represent its offset of 0.2 and 0.5 mm.

The standard also recommends a maximum allowable crack propagation length, defined as $\Delta a_{max} = 0.25(W - a_0)$. For the smallest specimen, this limit is equal to 0.7 mm, which is exceeded due to its reduced size. This explains the reduction in J values at higher crack extensions for this specimen.

The results show that $J_{0.2}$ and $J_{0.5}$ values for the homothetic specimens remain relatively constant across different specimen sizes, indicating that specimen size has a minimal effect on fracture toughness for this material. In contrast, the varying-thickness specimens display the opposite trend, with larger thicknesses leading to lower fracture toughness values.

The same analysis was conducted for δ. Figure 6.30 presents the results. The construction lines follows the ASTM E1820, which recommends using $\delta = 1.4\Delta a$. For the homothetic specimen CT-3.125, significant deformation occurs due to its small size and long crack propagation, causing δ to increase rapidly. For the larger specimens, the trend reproduces the results observed in the J curves: the homothetic specimens show relatively stable δ values, while it decreases as thickness increases.

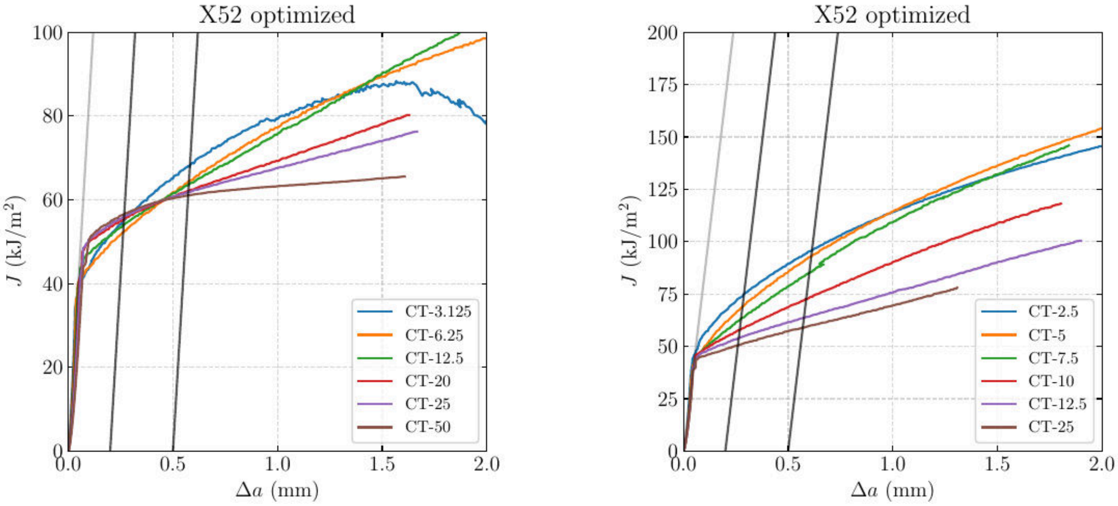

(a) Homothetic specimens.

(b) Varying-thickness.

Figure 6.29: $J - \Delta a$ curves for homothetic and varying-thickness specimens for the X52 steel.

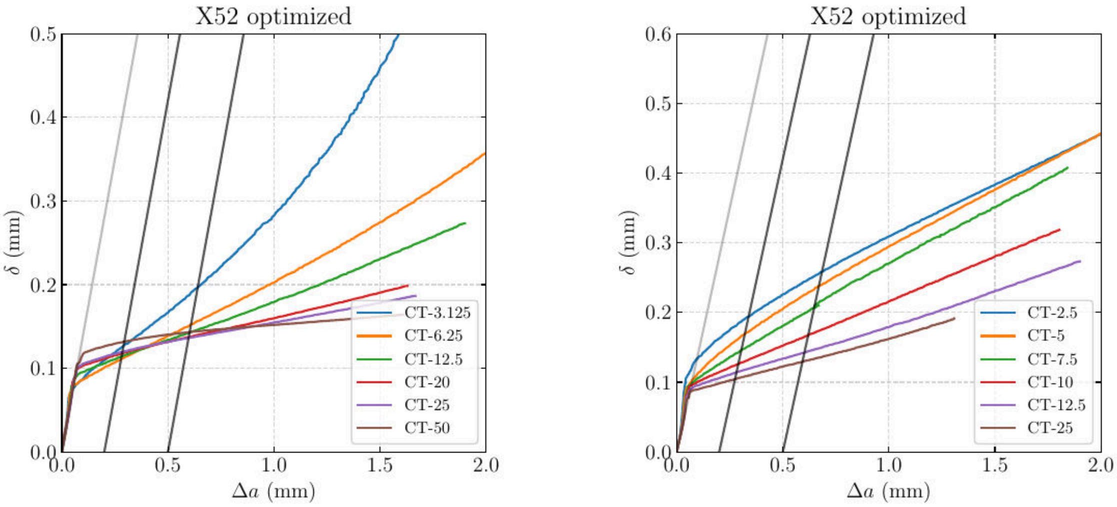

(a) Homothetic specimens.

(b) Varying thickness.

Figure 6.30: $\delta - \Delta a$ curves for homothetic and varying-thickness specimens for the X52 steel.

Figure 6.31 gathers the fracture toughness values obtained for the homothetic and varying-thickness specimens as a function of the specimen's thickness. As previously discussed, the homothetic specimens exhibit stable J values, while the varying-thickness specimens show a rapid decrease in toughness. Specifically, the $J_{0.5}$ curve exhibits a half "bump" shape, which corresponds to the transition zone shown in Figure 2.19. Surprisingly, the δ values for the homothetic specimens initially decrease and then begin to increase again for larger specimens. In contrast, the δ values for the varying-thickness specimens follow the same trend as the J values. Note that, for this case, all J and δ values are inside the range of validity of the ASTM E1820 standard. Thus, even cases considered valid still present a dependence on the specimen's size and thickness.

The same analysis was conducted for the E355 mod. steel, with the optimized coefficients for this material provided in Table 6.2. Figure 6.32 presents the $J - \Delta a$ curves for both the homothetic and varying-thickness specimens. The results demonstrate significantly higher fracture toughness values for

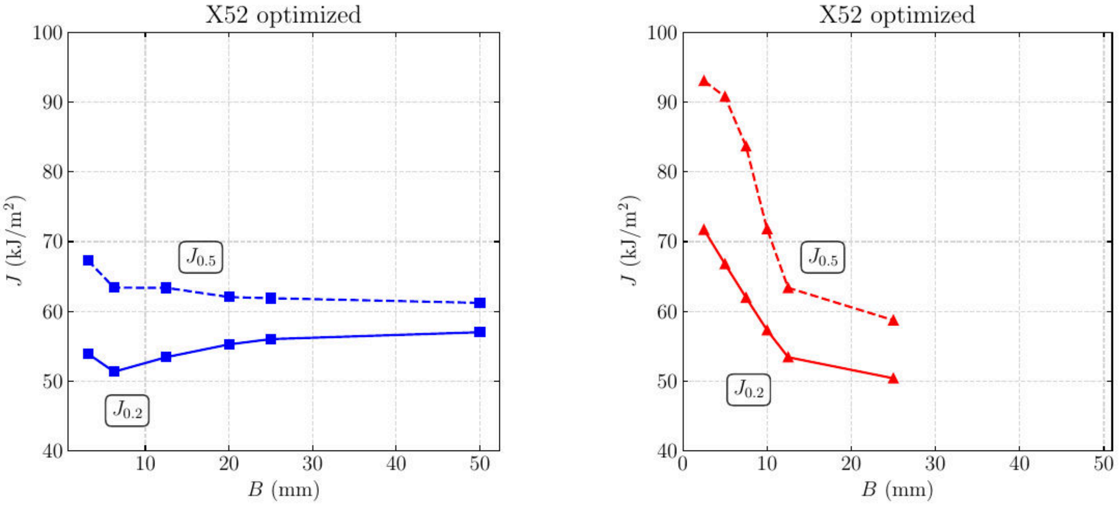

(a) Homothetic specimens.

(b) Varying thickness.

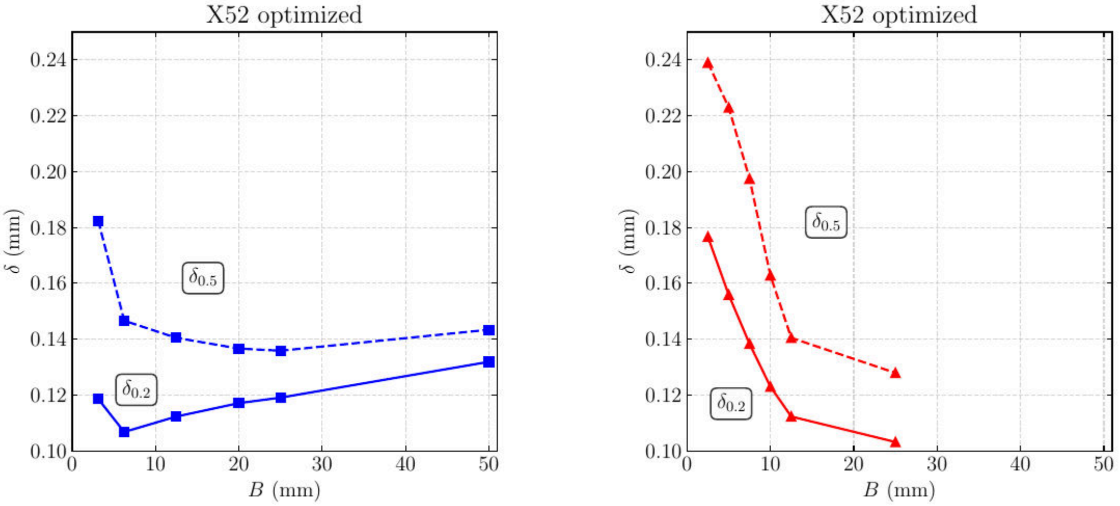

(c) Homothetic specimens.

(d) Varying thickness.

Figure 6.31: Fracture toughness values for homothetic (blue curves) and varying-thickness (red curves) specimens as a function of the specimen's thickness (B).

this steel. Additionally, unlike the X52 steel, a noticeable variation in fracture toughness values is observed even among the homothetic specimens.

Figure 6.33 illustrates the $\delta - \Delta a$ curves for the E355 mod. steel. The high ductility of this material prevented the offset lines from intersecting with the curves, rendering it impossible to determine the $\delta_{0.2}$ and/or $\delta_{0.5}$ values for certain specimens. This issue was particularly evident in the smallest or thinnest specimens, which undergo the most significant deformation.

Figure 6.34 summarizes the fracture toughness values of the E355 mod. steel as a function of thickness. The J values on the right side of the J_{max} curve are considered valid according to the standard. For this material, the "bump" is evident in both the homothetic and varying-thickness specimens, though it is more pronounced in the latter. The J values for the homothetic specimens appear to exhibit less dependence on specimen thickness. The black star on the varying-thickness graph represents experimental results obtained from a specimen with the same geometry as the simulation.

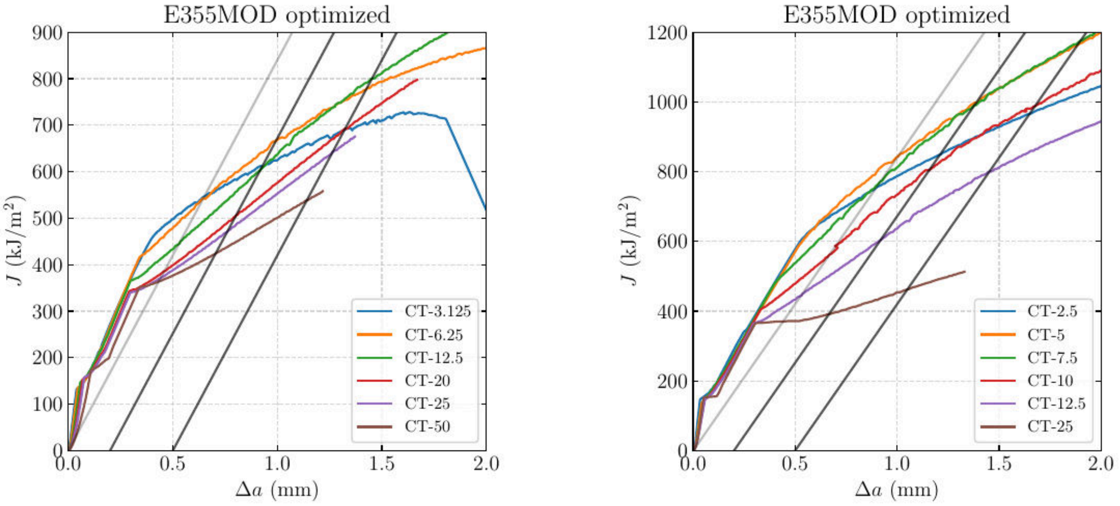

(a) Homothetic specimens.

(b) Varying-thickness.

Figure 6.32: $J - \Delta a$ curves for homothetic and varying-thickness specimens for the E355 mod. steel.

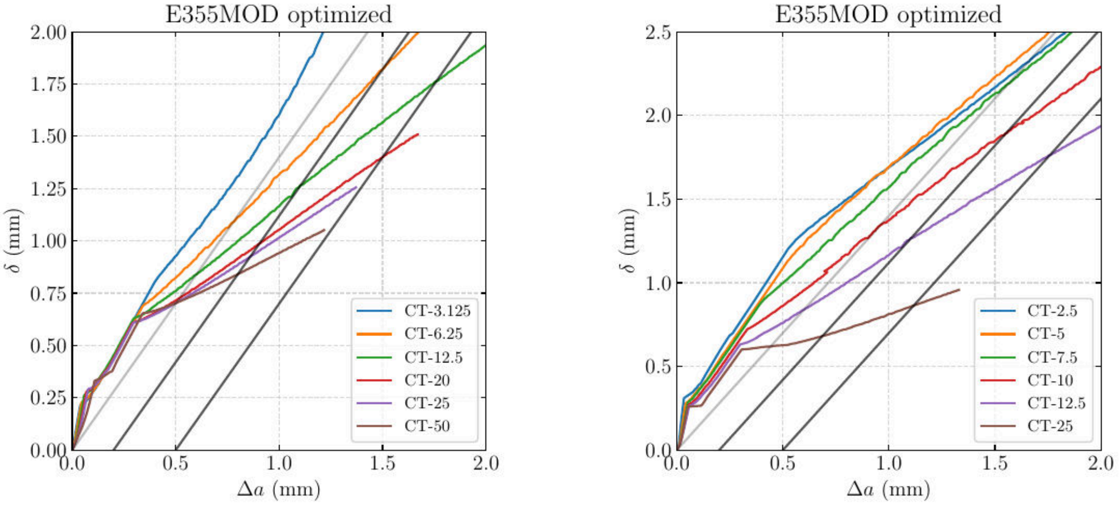

(a) Homothetic specimens.

(b) Varying-thickness.

Figure 6.33: $\delta - \Delta a$ curves for homothetic and varying-thickness specimens for the E355 mod. steel.

As previously mentioned, not all points could be measured for the δ curves. The δ_{max} line indicates the validity range defined by the standard, with points below it considered valid. While no "bump" is observed for δ, a strong dependence between toughness and thickness is evident, particularly for the varying-thickness specimens.

For the last analysis conducted employed an hypothetical material in order to analyze the relation of ductility and size effect. To do so, the hardening law of the X52 steel was employed (see Table 6.1). However, the GTN's coefficients q_1 and q_2 were modified in order to produce different ductility levels.

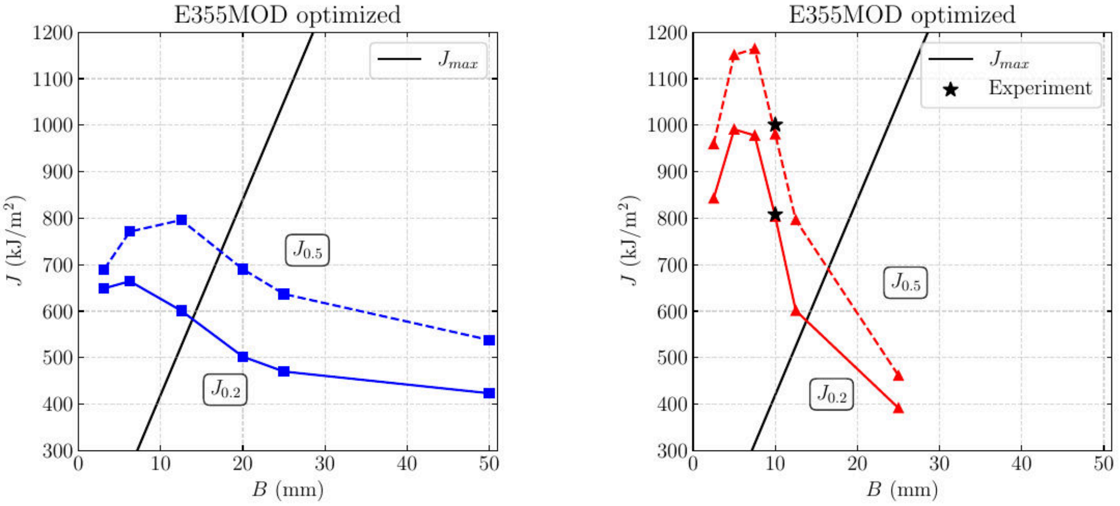

(a) Homothetic specimens.

(b) Varying thickness.

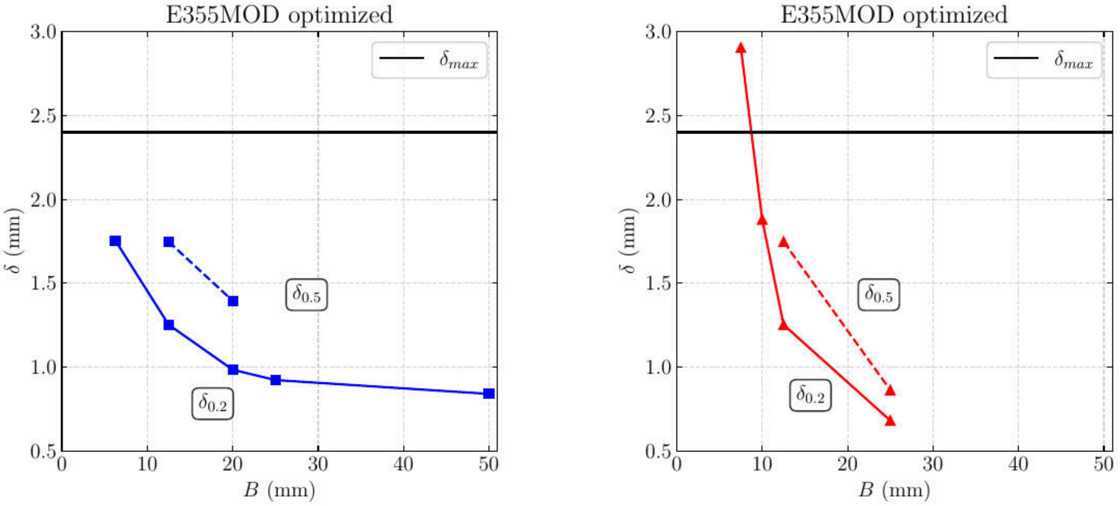

(c) Homothetic specimens.

(d) Varying thickness.

Figure 6.34: Fracture toughness values for homothetic (blue curves) and varying-thickness (red curves) specimens as a function of the specimen's thickness (B).

The following set of coefficients were employed on the simulations:

$$\begin{cases} q_1 = 1.5, \; q_2 = 1.0 \\ q_1 = 1.9, \; q_2 = 1.0 \\ q_1 = 2.0, \; q_2 = 1.5 \end{cases} \tag{6.19}$$

The q_1 and q_2 coefficients in the GTN model (see Equation 2.11) significantly influence the material's ductility and fracture behavior as they control void growth kinetics. The q_1 coefficient controls the contribution of void growth to the overall yield behavior. A higher q_1 increases void growth sensitivity, causing earlier growth and low ductility. In contrast, a lower q_1 reduces void growth, allowing the material to sustain higher strains before failure, thereby increasing ductility. Since voids grow more slowly, the onset of fracture is delayed, resulting in a more ductile behavior.

The q_2 coefficient influences the sensitivity of the yield surface to hydrostatic stress. Higher q_2 values promote faster void growth under triaxial loading conditions, leading to reduced ductility. In contrast, a lower q_2 results in slower void growth, allowing for more plastic deformation before fracture. Thus, high values of both coefficients significantly reduce ductility, while lower values tend to enhance it.

For this configuration, a low level of void nucleation is considered, thus $A_n^0 = 0.2$ and $\bar{\kappa}_c = 0.8$ in order to have minor influence of void nucleation on the results. Figure 6.35 contains the $J_{0.2}$ and $J_{0.5}$ values for the homothetic and varying-thickness specimens for the three set of coefficients q_1 and q_2.

The configuration $q_1 = 1.5$ and $q_2 = 1.0$ represents the most ductile scenario, while $q_1 = 2.0$ and $q_2 = 1.5$ corresponds to the least ductile. From the results, it is evident that for all three cases, the homothetic specimens exhibit more stable toughness values compared to the varying-thickness specimens. This stability suggests that homothetic specimens are less sensitive to size variations.

However, as previously observed, even tests considered valid according to the standard can still display size effects, highlighting the limitations of current validation criteria. The “bump” in the J curves is more pronounced in the varying-thickness specimens, particularly for the most ductile configuration ($q_1 = 1.5$ and $q_2 = 1.0$). This behavior indicates that ductility amplifies the dependence of toughness on thickness, likely due to increased deformation and plastic zone development in the more ductile material configurations.

Figure 6.36 compares the $J_{0.5}$ values for the three sets of damage coefficients (q_1 and q_2). The results clearly highlight the influence of ductility on fracture toughness, particularly for the varying-thickness specimens

The last analysis focused on examining the effect of the void nucleation threshold on fracture toughness. In this study, the coefficients optimized for E355 mod. steel were used, with a void nucleation rate of $A_n^0 = 0.2$ and the nucleation threshold $\bar{\kappa}_c$ varied across values of 0.8, 0.6, 0.4, and 0.2. It is worth noting that for E355 mod. steel, the optimized coefficients ($A_n^0 = 0.2$ and $\bar{\kappa}_c = 0.8$) correspond to a low nucleation rate that initiates at high strain levels. Figure 6.37 presents the $J_{0.5}$ values for both the homothetic and varying-thickness specimens under these four threshold conditions.

The results show that as the nucleation threshold ($\bar{\kappa}_c$) increases, fracture toughness also increases, as void nucleation is delayed. The bump is more noticeable in the varying-thickness specimens, and it becomes more pronounced as $\bar{\kappa}_c$ increases. This result means that the later void nucleation starts, the higher is the size effect, specially for the varying thickness specimens. It is worthy noting that for the varying-thickness specimens, the majority of the tests fail to meet the validity criteria specified by the standard.

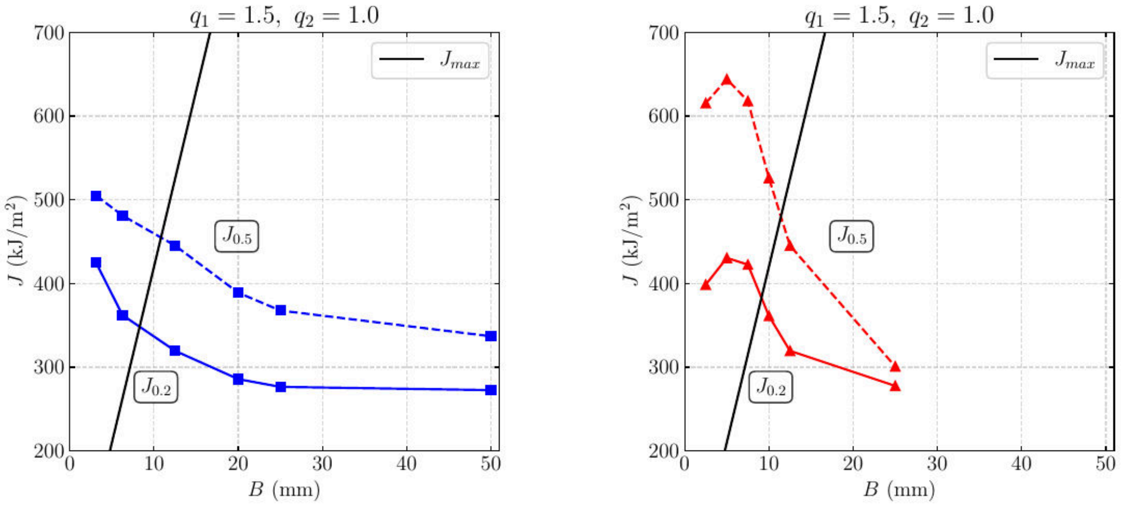

(a) Homothetic specimens.

(b) Varying thickness.

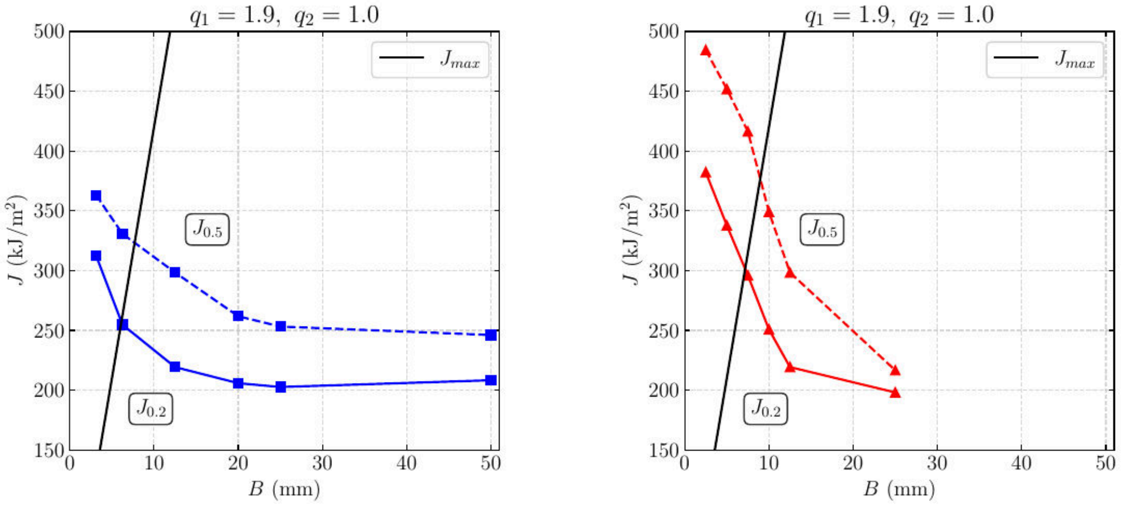

(c) Homothetic specimens.

(d) Varying thickness.

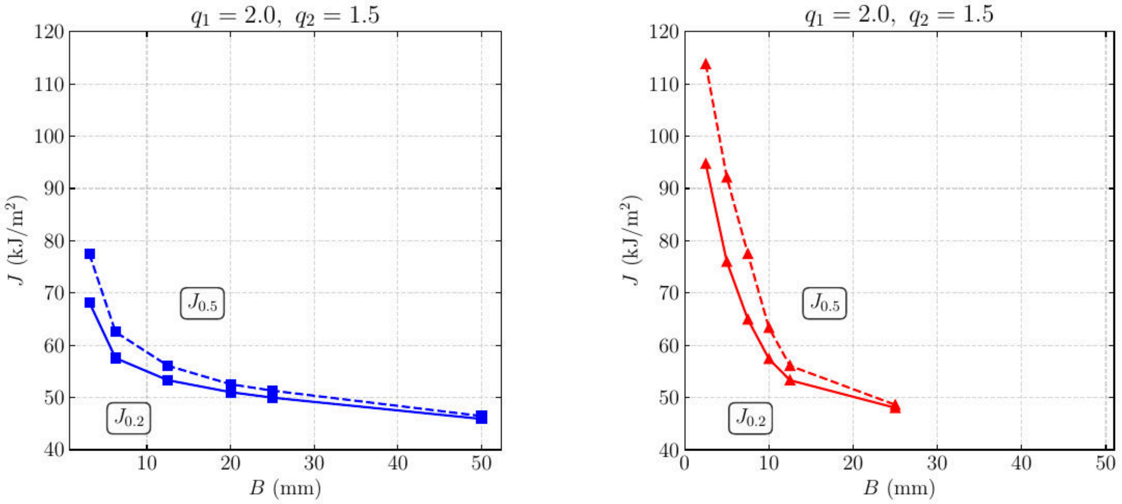

(e) Homothetic specimens.

(f) Varying thickness.

Figure 6.35: Fracture toughness values for homothetic (blue curves) and varying-thickness (red curves) specimens as a function of the specimen's thickness (B).

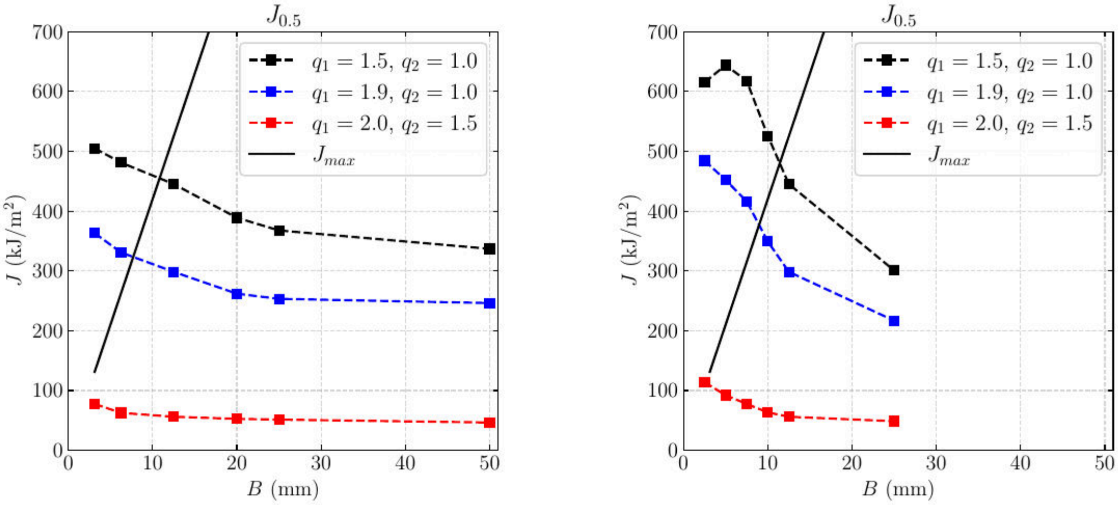

(a) Homothetic specimens.

(b) Varying-thickness.

Figure 6.36: Fracture toughness values for homothetic and varying-thickness specimens with different ductility levels.

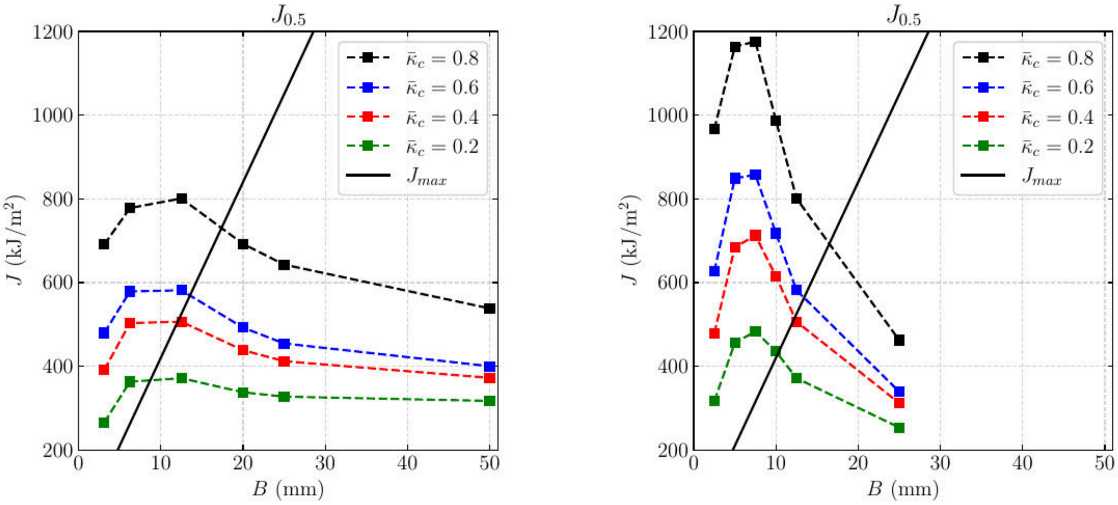

(a) Homothetic specimens.

(b) Varying-thickness.

Figure 6.37: Fracture toughness values for homothetic and varying-thickness specimens with different void nucleation thresholds.

6.7 Conclusions

This chapter presented a comprehensive investigation of fracture toughness of two steel grades: a vintage X52 pipeline steel and a modern E355 modified steel (E355 mod.). Using both standard and sub-size specimens, including Compact Tension (CT) and mini-Disk Compact Tension (mDCT) geometries, the study examined the effects of material properties, specimen size, and geometry on fracture behavior.

A comparison of compliance-based and post-processing methods for crack propagation calculations highlighted the efficiency and accuracy of the latter, establishing it as a reliable alternative for future simulations. The numerical simulations employed a nonlocal GTN model with two internal length scales; pressure is controlled by the B-bar formulation. This approach effectively addressed volumetric locking and reduced computational costs by enabling the use of linear elements with fewer degrees of freedom. Despite the anisotropic behavior and experimental result variability observed for the X52 steel, the numerical model demonstrated overall good agreement with the experimental data. Notably, the X52 steel results indicated that the Crack Tip Opening Displacement provided a more precise prediction of experimental behavior compared to the J-integral. However, the model was not able to accurately capture the ductile response of the E355 mod. steel.

The parametric study further enlightened the complex relation between ductility, void nucleation thresholds, and size effects. Varying-thickness specimens exhibited a pronounced size effect on fracture toughness, with toughness values strongly dependent on thickness, forming a characteristic “bump” shape. In contrast, homothetic specimens displayed a more consistent behavior, though not entirely stable, even when some tests met the validity criteria of the ASTM E1820 standard. The findings also revealed that more ductile materials exhibit stronger size effects and that delaying void nucleation increases the magnitude of these effects for a given nucleation rate.

Overall, the findings contribute to a deeper understanding of size and thickness effects on fracture toughness through a combination of experimental tests and numerical simulations. Future work could focus on implementing local remeshing techniques for crack propagation, which may help mitigate mesh distortions in highly ductile materials like the E355 mod. steel, thereby improving numerical accuracy. While some tests were considered invalid by ASTM standards, they still provided valuable insights for comparing test conditions and material properties, advancing the fracture mechanics understanding of pipeline steels.

7

Conclusions and perspectives

Summary of main results

This thesis focused on the modeling of Hydrogen Embrittlement (HE) in pipeline steels, developing a comprehensive numerical framework that integrates hydrogen diffusion, plasticity, and damage. The model considers a local equilibrium between lattice and trapped hydrogen concentrations, with the hydrogen flux driven by pressure states and directed towards high-stress zones. It also accounts for multiple types of hydrogen traps, whose evolution can be influenced by plastic strain. HE is modeled through a modification of the GTN model, which includes hydrogen-enhanced decohesion (HEDE), leading to increased material damage due to local hydrogen concentrations.

The framework was applied to various experimental test conditions, including pressurized disks, tensile tests, and fracture toughness tests, using different pipeline steel grades. Experimental data from both the literature and tests conducted within this project were used to calibrate the material coefficients and validate the numerical model.

In Chapter 3, the focus was on the Disk Pressure Test (DPT), where two innovative disk geometries were designed using finite element modeling to control failure locations and optimize the test configuration for studying HE. The experimental and numerical results demonstrated that, under the studied conditions, HE intensity was not significantly affected by pressure rise rate, with constant embrittled depths observed across varying rates. The integration of hydrogen-plasticity interactions in the numerical framework was validated, offering valuable insights into the mechanical effects of hydrogen embrittlement.

Chapter 4 addressed hydrogen uptake during tensile tests in a gaseous hydrogen atmosphere. The experimental tests explored the effects of strain level, strain rate, and exposure time on hydrogen absorption and desorption in steels, serving as a benchmark for fitting the numerical model coefficients. The simulations accurately replicated experimental trends, confirming the model's predictive ability under different conditions. Strain levels and exposure times were found to significantly influence hydrogen concentration and uptake, highlighting the role of plasticity in hydrogen absorption.

Chapter 5 introduced the complete model formulation with a modified nonlocal GTN model for simulating hydrogen embrittlement, incorporating hydrogen diffusion effects. This framework effectively captured the degradation effects of HE, accelerating damage evolution and leading to premature failure. A mixed formulation addressed volumetric locking and ensured mesh independence through an implicit gradient model. Validation with literature data for pipeline steel demonstrated the model's accuracy in predicting failure initiation under varying strain rates, toughness reduction in compact tension specimens, and loading rate effects in pressurized disk tests. The model also accounted for ductile fracture and quasi-cleavage mechanisms, though fitting the parameters remains challenging due to the complexity of hydrogen diffusion and trapping interactions.

Finally, Chapter 6 focused on fracture toughness tests using both sub-size and standard specimens. A comparison of crack propagation methods demonstrated the efficiency and accuracy of post-processing techniques for future simulations. The nonlocal GTN model and B-bar formulation were employed to address volumetric locking and reduce computational costs. The study revealed pronounced size effects on fracture toughness in varying-thickness specimens, with more ductile materials exhibiting stronger size effects influenced by void nucleation thresholds.

This work provides a robust framework for simulating hydrogen embrittlement in pipeline steels, offering insights into the mechanical and material behaviors under hydrogen exposure and advancing the understanding of size effects and hydrogen-related damage mechanisms.

Perspectives

This work has raised several open questions and opportunities for further research. Below is a non-exhaustive list of suggestions for future studies:

- Conduct an additional campaign of Thermal Desorption Spectroscopy (TDS) tests to better identify the various trap sites and their associated parameters, such as trap binding energies and trap densities.
- Simulation of desorption curves from the TDS test for 3D specimens under varying conditions, such as specimen shape and heating rate. Figure 7.1 illustrates an example of preliminary simulations performed for different trap binding energies.

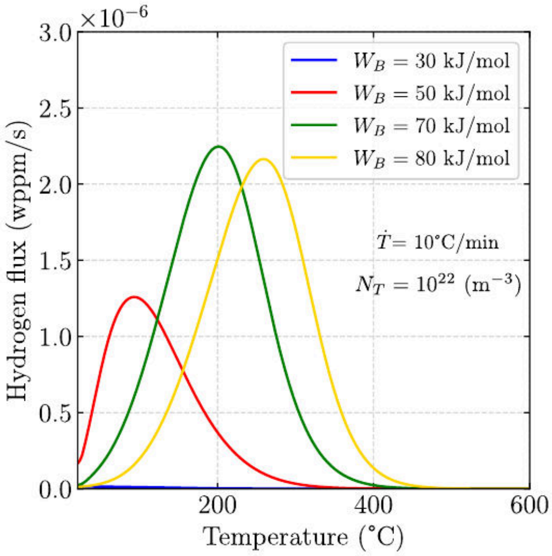

Figure 7.1: TDS desorption curves for different trap binding energies.

- To accurately model the desorption hydrogen peaks observed in TDS tests, consider implementing the McNabb-Foster model (McNabb and Foster, 1963), which accounts for the kinetics of hydrogen trapping and detrapping.
- When a new crack is formed and exposed to hydrogen, hydrogen can enter the material through the newly created crack surfaces. In the current approach, this effect is modeled by locally increasing the lattice diffusion coefficient (D_L) in the regions where the material is broken. An alternative improvement to this method involves implementing a new boundary condition that accounts for the newly created surfaces during crack propagation. These surfaces would allow hydrogen to diffuse through them directly, as illustrated in Figure 7.2.

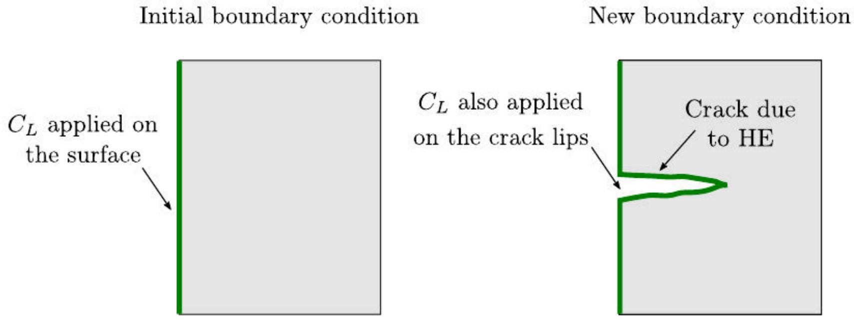

Figure 7.2: New boundary condition for hydrogen diffusion through cracked surfaces.

- Adapt the hydrogen boundary conditions to account for scenarios where gaseous hydrogen is mixed with other gases that inhibit hydrogen penetration, such as carbon monoxide (CO). Carbon monoxide can lead to the oxidation of the pipeline surface, forming a protective layer that reduces the effective hydrogen flux into the material.
- Incorporate hydrogen transport by mobile dislocations into the numerical model. This phenomenon was first proposed by Bastien and Azou, 1951 and has been supported by several experimental observations (Hwang and Bernstein, 1986; Kurkela and Latanision, 1979; Nagao et al., 1998). These findings have inspired the development of dislocation transport models (Dadfarnia et al., 2015; Tien et al., 1975), which predict significantly faster diffusion rates compared to lattice diffusion. These models suggest moving dislocations represent moving traps that carry hydrogen atoms deep into the specimen's gauge section or plastic zone, even at ambient temperatures.
- Enhance the existing remeshing framework for simulations of long crack propagation, as proposed by El Ouazani Tuhami, 2022, to reduce mesh distortion in highly ductile materials and improve the accuracy of crack propagation modeling during fracture toughness tests. The current method performs well for axisymmetric cases, as demonstrated in Figure 7.3. However, for 3D non-axisymmetric specimens, such as compact tension (CT) specimens, there are still numerical challenges related to crack insertion and crack front identification that need to be addressed. The remeshing technique refines only the process zone, which helps reduce simulation time.
- Figure 7.4 presents experimental results from fracture toughness tests using an mDCT specimen under both air and hydrogen pressures. The results show a significant reduction in fracture toughness due to hydrogen embrittlement (HE). The next step is to incorporate the effects of HE into fracture toughness tests with sub-size specimens, in order to investigate the combined influence of size effects and HE.

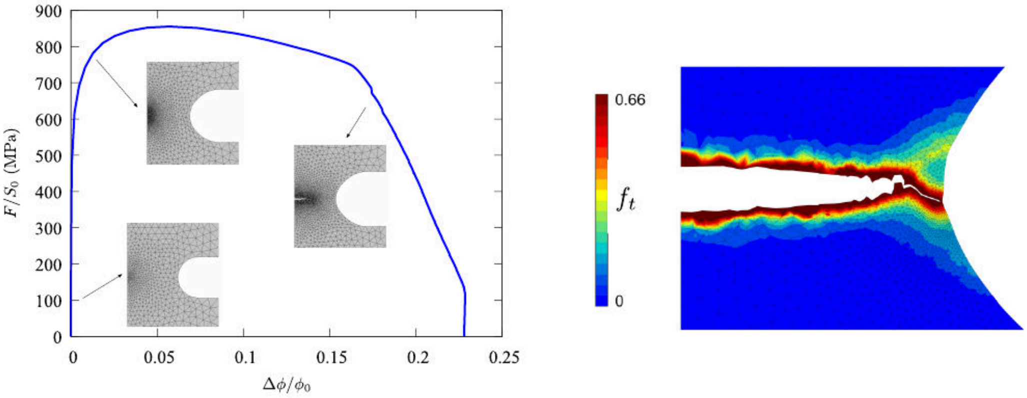

Figure 7.3: Remeshing technique for an axisymmetric tensile specimen.

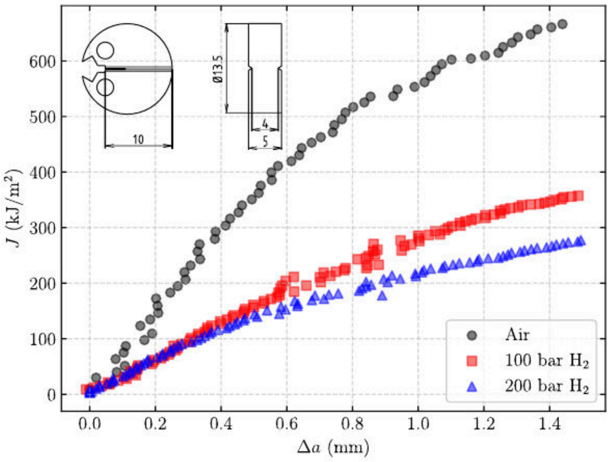

Figure 7.4: Experimental results of a fracture toughness test under air and hydrogen using a mDCT specimen.

Valorization

This work led to the publication of two articles, corresponding to Chapters 3 and 5:

- L.M. Santana, **D. Lopes Pinto**, N. Osipov, J. Furtado, F. Bourguignon, P.J. Marchais, Y. Madi, J. Besson. Study of hydrogen embrittlement in steels using modified pressurized disks, *International Journal of Hydrogen Energy*, 2024.
- **D. Lopes Pinto**, A. El Ouazani Tuhami, N. Osipov, Y. Madi, J. Besson. Simulation of hydrogen embrittlement of steel using mixed nonlocal finite elements, *European Journal of Mechanics / A Solids*, 2024.

The research findings were presented at several conferences and workshops:

- International Conference on Metals & Hydrogen (*SteelyHydrogen*): October 11–13, 2022, Ghent, Belgium. Poster presentation.
- National Mécamat Symposium: January 23–27, 2023, Aussois, France. Poster presentation.
- ESIS Technical Meeting on Numerical Methods: February 6–7, 2023, Belgrade, Serbia. Oral presentation.

- Hydrogen and Materials Integrity Workshop: June 6–8, 2023, Trondheim, Norway. Oral presentation.
- International Conference on Fracture: June 11–16, 2023, Atlanta, United States. Oral presentation.
- Summer School MEALOR II (*Damage Mechanics and Local Approach to Fracture*): August 21–September 1, 2023, Banyuls-sur-Mer, France. Poster presentation (awarded best poster prize).
- European Mechanics of Materials Conference: May 29–31, 2024, Madrid, Spain. Oral presentation.
- Transvalor International Simulation Days: September 30–October 2, 2024, Cannes, France. Oral presentation.

A

Pressurized disk tests

MAT	TYPE	ENV	$\dot{P}_a$ (MPa/min)	P'_r (MPa)	Displacement (mm)
X52	Standard	He	0.03	53.74	4.57
		H_2	0.25	42.44	6.12
		H_2	0.27	24.28	3.61
		H_2	2.44	16.77	3.08
	Cup	He	0.08	71.68	4.89
		H_2	0.21	64.10	3.58
		H_2	0.21	66.79	3.09
		H_2	35.28	67.56	3.96
	Notched	He	0.28	49.54	2.94
		H_2	0.03	70.36	2.27
		H_2	0.27	30.56	1.02
		H_2	2.52	27.70	1.82
		H_2	21.81	28.95	2.17
E355 mod.	Standard	He	0.03	46.12	7.94
		H_2	0.26	45.60	8.61
		H_2	0.24	18.96	8.79
		H_2	2.38	20.19	2.99
	Cup	He	0.26	77.14	5.89
		H_2	0.12	73.05	5.78
		H_2	0.07	69.55	8.39
		H_2	0.29	67.33	3.91
		H_2	20.92	63.43	3.60
	Notched	He	0.06	52.41	4.17
		H_2	0.21	35.93	2.24
		H_2	0.47	29.11	2.29
		H_2	3.10	27.02	2.13
		H_2	22.60	28.34	2.16

Table A.1: Test results for X52 and E355 mod. steels under helium (He) and hydrogen (H_2) environments, $\dot{P}_a$ is the Pressure Rise Rate, P'_r is the corrected rupture pressure, and the displacement is measured in mm.

B

B-bar formulation

The $\boldsymbol{B}$-bar (ou $\bar{\boldsymbol{B}}$) formulation was introduced by Hughes, 1980 and later applied in Elguedj et al., 2008. In the context of a standard finite element, the strain-displacement matrix $\boldsymbol{B}$ establishes a relationship between strains and the nodal displacements interpolated at each node. This strain-displacement matrix can be represented as a concatenation of nodal sub-matrices:

$$\boldsymbol{B} = [\boldsymbol{B}_1, \boldsymbol{B}_2, \ldots, \boldsymbol{B}_n] \tag{B.1}$$

where n is the number of element nodes. In a three-dimensional analysis, the typical sub-matrix $\boldsymbol{B}_a$, where $1 \leq a \leq n$, can be expressed as:

$$\boldsymbol{B}_a = \begin{bmatrix} B_1 & 0 & 0 \\ 0 & B_2 & 0 \\ 0 & 0 & B_3 \\ B_2 & B_1 & 0 \\ 0 & B_3 & B_2 \\ B_3 & 0 & B_1 \end{bmatrix} \tag{B.2}$$

The components of $\boldsymbol{B}_a$ are derived from the derivatives of the shape functions, as defined by the following:

$$B_i = \frac{\partial N_a}{\partial x_i}, \quad 1 \leq i \leq 3 \tag{B.3}$$

where N_a is the shape function associated with node a, and x_i represents the i-th Cartesian coordinate. The previous expressions need to be modified to address volumetric locking, a numerical issue in finite element analysis (FEA) discussed in Section 2.3. To achieve this, it is necessary to first define the hydrostatic component of $\boldsymbol{B}_a$, which is expressed as follows:

$$\boldsymbol{B}_a^h = \frac{1}{3} \begin{bmatrix} B_1 & B_2 & B_3 \\ B_1 & B_2 & B_3 \\ B_1 & B_2 & B_3 \\ 0 & 0 & 0 \\ 0 & 0 & 0 \\ 0 & 0 & 0 \end{bmatrix} \tag{B.4}$$

The deviatoric part of $\boldsymbol{B}_a$ can then be defined as:

$$\boldsymbol{B}_a^d = \boldsymbol{B}_a - \boldsymbol{B}_a^h \tag{B.5}$$

To develop an effective formulation for nearly incompressible applications, $\boldsymbol{B}_a^h$ must be replaced with an averaged hydrostatic contribution. In this context, this averaged contribution is represented as $\bar{\boldsymbol{B}}_a^h$ and is defined as follows:

$$\bar{\boldsymbol{B}}_a^h = \begin{bmatrix} \bar{B}_1 & \bar{B}_2 & \bar{B}_3 \\ \bar{B}_1 & \bar{B}_2 & \bar{B}_3 \\ \bar{B}_1 & \bar{B}_2 & \bar{B}_3 \\ 0 & 0 & 0 \\ 0 & 0 & 0 \\ 0 & 0 & 0 \end{bmatrix} \tag{B.6}$$

where $\bar{\boldsymbol{B}}_a^h$ can be computed as an average over the element volume Ω_e, as follows:

$$\bar{\boldsymbol{B}}_a^h = \frac{\int_{\Omega_e} \boldsymbol{B}_a^h d\Omega}{\int_{\Omega_e} d\Omega} \tag{B.7}$$

Thus, $\boldsymbol{B}_a$ is also modified to take into account the previous modification of $\bar{\boldsymbol{B}}_a^h$. It is now expressed as:

$$\bar{\boldsymbol{B}}_a = \boldsymbol{B}_a^d + \bar{\boldsymbol{B}}_a^h \tag{B.8}$$

As outlined in Elguedj et al., 2007, the $\boldsymbol{B}$-bar approach provides a straightforward method for achieving the performance of mixed methods without introducing unwanted degrees of freedom, applicable to both axisymmetric and anisotropic cases. This characteristic is likely a primary reason why these techniques are widely adopted in large-scale commercial codes (*LS-DYNA Keyword User's Manual*, 2007; Maker, 1995).

C

Details on the model implementation

C.1 Jacobian matrix computation

The Jacobian matrix is defined as $\boldsymbol{J} = \dfrac{\partial \boldsymbol{R}}{\partial \boldsymbol{V}_{int}}$, where:

$$\boldsymbol{R} = (\boldsymbol{R}_e, R_{f_g}, R_{f_n}, R_\omega, R_\kappa) \tag{C.1}$$

$$\boldsymbol{V}_{int} = (\boldsymbol{\varepsilon}_e, f_g, f_n, \omega, \kappa) \tag{C.2}$$

Then, the $\boldsymbol{J}$ matrix is organized as follows. The gray terms are equal to zero.

$$\boldsymbol{J} = \begin{pmatrix}
\frac{\partial \boldsymbol{R}_e}{\partial \varepsilon_e} & \frac{\partial \boldsymbol{R}_e}{\partial f_g} & \frac{\partial \boldsymbol{R}_e}{\partial f_n} & {\color{gray}\frac{\partial \boldsymbol{R}_e}{\partial \omega}} & \frac{\partial \boldsymbol{R}_e}{\partial \kappa} \\
{\color{gray}\frac{\partial R_{f_g}}{\partial \varepsilon_e}} & \frac{\partial R_{f_g}}{\partial f_g} & {\color{gray}\frac{\partial R_{f_g}}{\partial f_n}} & {\color{gray}\frac{\partial R_{f_g}}{\partial \omega}} & {\color{gray}\frac{\partial R_{f_g}}{\partial \kappa}} \\
{\color{gray}\frac{\partial R_{f_n}}{\partial \varepsilon_e}} & {\color{gray}\frac{\partial R_{f_n}}{\partial f_g}} & \frac{\partial R_{f_n}}{\partial f_n} & {\color{gray}\frac{\partial R_{f_n}}{\partial \omega}} & {\color{gray}\frac{\partial R_{f_n}}{\partial \kappa}} \\
\frac{\partial R_\omega}{\partial \varepsilon_e} & \frac{\partial R_\omega}{\partial f_g} & \frac{\partial R_\omega}{\partial f_n} & \frac{\partial R_\omega}{\partial \omega} & \frac{\partial R_\omega}{\partial \kappa} \\
\frac{\partial R_\kappa}{\partial \varepsilon_e} & \frac{\partial R_\kappa}{\partial f_g} & \frac{\partial R_\kappa}{\partial f_n} & {\color{gray}\frac{\partial R_\kappa}{\partial \omega}} & \frac{\partial R_\kappa}{\partial \kappa}
\end{pmatrix} \tag{C.3}$$

- Derivatives of $\boldsymbol{R}_e$:

$$\boxed{\boldsymbol{R}_e = \boldsymbol{\varepsilon}_e + (1 - f_g)\kappa \boldsymbol{n} - \boldsymbol{\varepsilon}} \tag{C.4}$$

$$\frac{\partial \boldsymbol{R}_e}{\partial \varepsilon_e} = \mathbb{1} + (1 - f_g)\kappa \mathbb{N} : \mathbb{E} \quad \text{with} \quad \mathbb{N} = \frac{\partial \boldsymbol{n}}{\partial \boldsymbol{\sigma}} \tag{C.5}$$

$$\frac{\partial \boldsymbol{R}_e}{\partial f_g} = (1 - f_g)\kappa \boldsymbol{n}_f - \kappa \boldsymbol{n} \quad \text{with} \quad \boldsymbol{n}_f = \frac{\partial \boldsymbol{n}}{\partial f} \tag{C.6}$$

$$\frac{\partial \boldsymbol{R}_e}{\partial f_n} = (1 - f_g)\kappa \boldsymbol{n}_f \tag{C.7}$$

$$\frac{\partial \boldsymbol{R}_e}{\partial \kappa} = (1 - f_g)\boldsymbol{n} \tag{C.8}$$

- Derivatives of R_{f_g}:

$$\boxed{R_{f_g} = f_g - (1 - f_g)\bar{\omega}} \tag{C.9}$$

$$\frac{\partial R_{f_g}}{\partial f_g} = 1 + \bar{\omega} \tag{C.10}$$

$$\frac{\partial R_{f_g}}{\partial f_n} = \bar{\omega} \tag{C.11}$$

$$ \tag{C.12}$$

- Derivatives of R_{f_n}:

$$\boxed{R_{f_n} = f_n - A_n\bar{\kappa}} \tag{C.13}$$

$$\frac{\partial R_{f_n}}{\partial f_n} = 1 \tag{C.14}$$

$$ \tag{C.15}$$

- Derivatives of R_ω:

$$\boxed{R_\omega = \omega - (1 - f_g)\kappa \mathrm{trace}(\boldsymbol{n})} \tag{C.16}$$

$$\frac{\partial R_\omega}{\partial \varepsilon_e} = -(1 - f_g)\kappa \mathbb{1} : \mathbb{N} : \mathbb{E} \tag{C.17}$$

$$\frac{\partial R_\omega}{\partial f_g} = \kappa \mathrm{trace}(\boldsymbol{n}) - (1 - f_g)\kappa \mathrm{trace}(\boldsymbol{n}_f) \tag{C.18}$$

$$\frac{\partial R_\omega}{\partial f_n} = -(1 - f_g)\kappa \mathrm{trace}(\boldsymbol{n}_f) \tag{C.19}$$

$$\frac{\partial R_\omega}{\partial \omega} = 1 \tag{C.20}$$

$$\frac{\partial R_\omega}{\partial \kappa} = -(1 - f_g)\mathrm{trace}(\boldsymbol{n}) \tag{C.21}$$

- Derivatives of R_κ:

$$\boxed{R_\kappa = \kappa - \mathcal{F}(\Phi)t} \tag{C.22}$$

$$\frac{\partial R_\kappa}{\partial \varepsilon_e} = -t\mathcal{F}'(\Phi)\boldsymbol{n} : \mathbb{E} \quad \text{with} \quad \mathcal{F}'(\Phi) = \frac{\partial \mathcal{F}(\Phi)}{\partial \Phi} \tag{C.23}$$

$$\frac{\partial R_\kappa}{\partial f_g} = -t\mathcal{F}'(\Phi)\sigma^\star_f \quad \text{with} \quad \sigma^\star_f = \frac{\partial \sigma^\star}{\partial f} \tag{C.24}$$

$$\frac{\partial R_\kappa}{\partial f_n} = -t\mathcal{F}'(\Phi)\sigma^\star_f \tag{C.25}$$

$$\frac{\partial R_\kappa}{\partial \kappa} = 1 + t\mathcal{F}'(\Phi)H \quad \text{with} \quad H = \frac{d\sigma_F}{d\kappa} \tag{C.26}$$

C.2 Consistent tangent matrix computation

Tangent operators play a crucial role in evaluating the element stiffness matrix. For the material model presented in this study, the input, output, and state (integrated) variables used to compute the tangent operators are as follows:

$$\boldsymbol{V}_{IN} = (\boldsymbol{\varepsilon}, \bar{\omega}, \bar{\kappa}, C_L, \boldsymbol{\nabla} C_L, \boldsymbol{\nabla} p) \tag{C.27}$$

$$\boldsymbol{V}_{OUT} = (\boldsymbol{\sigma}, \omega, \kappa, \boldsymbol{J}, h, H_{C_L}) \tag{C.28}$$

$$\boldsymbol{V}_{int} = (\boldsymbol{\varepsilon}_e, f_g, f_n, \omega, \kappa) \tag{C.29}$$

For any small variation in the input variables ($\boldsymbol{V}_{IN}$), the state variables ($\boldsymbol{V}_{int}$) are updated so that the residual equations remain zero. Thus:

$$\boldsymbol{R} = \frac{\partial \boldsymbol{R}}{\partial \boldsymbol{V}_{int}} \boldsymbol{V}_{int} + \frac{\partial \boldsymbol{R}}{\partial \boldsymbol{V}_{IN}} \boldsymbol{V}_{IN} = \boldsymbol{0} \tag{C.30}$$

where $\dfrac{\partial \boldsymbol{R}}{\partial \boldsymbol{V}_{int}}$ is the Jacobian matrix ($\boldsymbol{J}$), previously defined in Section C.1. Thus:

$$\boldsymbol{V}_{int} = -\boldsymbol{J}^{-1} \frac{\partial \boldsymbol{R}}{\partial \boldsymbol{V}_{IN}} \boldsymbol{V}_{IN} \tag{C.31}$$

where $-\boldsymbol{J}^{-1} \dfrac{\partial \boldsymbol{R}}{\partial \boldsymbol{V}_{IN}}$ gives an evaluation of $\dfrac{\partial \boldsymbol{V}_{int}}{\partial \boldsymbol{V}_{IN}}$. The output variables are expressed as a function of the input and state variables, so that $\boldsymbol{V}_{OUT}$ is computed as:

$$\boldsymbol{V}_{OUT} = \frac{\partial \boldsymbol{V}_{OUT}}{\partial \boldsymbol{V}_{int}} \boldsymbol{V}_{int} + \frac{\partial \boldsymbol{V}_{OUT}}{\partial \boldsymbol{V}_{IN}} \boldsymbol{V}_{IN} \tag{C.32}$$

Substituting Equation C.31 into C.32, one finds:

$$\boldsymbol{V}_{OUT} = -\frac{\partial \boldsymbol{V}_{OUT}}{\partial \boldsymbol{V}_{int}} \boldsymbol{J}^{-1} \frac{\partial \boldsymbol{R}}{\partial \boldsymbol{V}_{IN}} \boldsymbol{V}_{IN} + \frac{\partial \boldsymbol{V}_{OUT}}{\partial \boldsymbol{V}_{IN}} \boldsymbol{V}_{IN} \tag{C.33}$$

By reorganizing the terms of the previous equation, one gets:

$$\boldsymbol{V}_{OUT} = \left[-\frac{\partial \boldsymbol{V}_{OUT}}{\partial \boldsymbol{V}_{int}} \boldsymbol{J}^{-1} \frac{\partial \boldsymbol{R}}{\partial \boldsymbol{V}_{IN}} + \frac{\partial \boldsymbol{V}_{OUT}}{\partial \boldsymbol{V}_{IN}} \right] \boldsymbol{V}_{IN} \tag{C.34}$$

where the consistent tangent matrix is equal to:

$$\boldsymbol{M} = -\frac{\partial \boldsymbol{V}_{OUT}}{\partial \boldsymbol{V}_{int}} \boldsymbol{J}^{-1} \frac{\partial \boldsymbol{R}}{\partial \boldsymbol{V}_{IN}} + \frac{\partial \boldsymbol{V}_{OUT}}{\partial \boldsymbol{V}_{IN}} \tag{C.35}$$

As it can be seen, the calculation of the consistent matrix requires the calculation of the following three matrices: $\dfrac{\partial \boldsymbol{V}_{OUT}}{\partial \boldsymbol{V}_{int}}$, $\dfrac{\partial \boldsymbol{R}}{\partial \boldsymbol{V}_{IN}}$ and $\dfrac{\partial \boldsymbol{V}_{OUT}}{\partial \boldsymbol{V}_{IN}}$. These matrices can be computed as block-matrices as follows:

- Computation of $\partial \boldsymbol{V}_{OUT}/\partial \boldsymbol{V}_{int}$:

$$\frac{\partial \boldsymbol{V}_{OUT}}{\partial \boldsymbol{V}_{int}} = \begin{pmatrix} \boldsymbol{\frac{\partial \sigma}{\partial \varepsilon_e}} & \frac{\partial \boldsymbol{\sigma}}{\partial f_g} & \frac{\partial \boldsymbol{\sigma}}{\partial f_n} & \frac{\partial \boldsymbol{\sigma}}{\partial \omega} & \frac{\partial \boldsymbol{\sigma}}{\partial \kappa} \\ \frac{\partial \omega}{\partial \varepsilon_e} & \frac{\partial \omega}{\partial f_g} & \frac{\partial \omega}{\partial f_n} & \boldsymbol{\frac{\partial \omega}{\partial \omega}} & \frac{\partial \omega}{\partial \kappa} \\ \frac{\partial \kappa}{\partial \varepsilon_e} & \frac{\partial \kappa}{\partial f_g} & \frac{\partial \kappa}{\partial f_n} & \boldsymbol{\frac{\partial \kappa}{\partial \kappa}} & \frac{\partial \kappa}{\partial \kappa} \\ \frac{\partial \boldsymbol{J}}{\partial \varepsilon_e} & \frac{\partial \boldsymbol{J}}{\partial f_g} & \frac{\partial \boldsymbol{J}}{\partial f_n} & \frac{\partial \boldsymbol{J}}{\partial \kappa} & \frac{\partial \boldsymbol{J}}{\partial \kappa} \\ \frac{\partial h}{\partial \varepsilon_e} & \frac{\partial h}{\partial f_g} & \frac{\partial h}{\partial f_n} & \frac{\partial h}{\partial \kappa} & \frac{\partial h}{\partial \kappa} \\ \frac{\partial H_{C_L}}{\partial \varepsilon_e} & \frac{\partial H_{C_L}}{\partial f_g} & \frac{\partial H_{C_L}}{\partial f_n} & \frac{\partial H_{C_L}}{\partial \kappa} & \frac{\partial H_{C_L}}{\partial \kappa} \end{pmatrix} \tag{C.36}$$

Most of the terms of this matrix are equal to zero (gray terms in C.36). So, for simplicity, they were omitted from the following:

$$\frac{\partial \boldsymbol{\sigma}}{\partial \varepsilon_e} = \mathbb{E} \tag{C.37}$$

$$\frac{\partial \omega}{\partial \omega} = 1 \tag{C.38}$$

$$\frac{\partial \kappa}{\partial \kappa} = 1 \tag{C.39}$$

- Computation of $\partial \boldsymbol{R}/\partial \boldsymbol{V}_{IN}$:

$$\frac{\partial \boldsymbol{R}}{\partial \boldsymbol{V}_{IN}} = \begin{pmatrix} \boldsymbol{\frac{\partial R_e}{\partial \varepsilon}} & \frac{\partial R_e}{\partial \bar{\omega}} & \frac{\partial R_e}{\partial \bar{\kappa}} & \frac{\partial R_e}{\partial C_L} & \frac{\partial R_e}{\partial (\nabla C_L)} & \frac{\partial R_e}{\partial (\nabla p)} \\ \frac{\partial R_{f_g}}{\partial \varepsilon} & \boldsymbol{\frac{\partial R_{f_g}}{\partial \bar{\omega}}} & \frac{\partial R_{f_g}}{\partial \bar{\kappa}} & \frac{\partial R_{f_g}}{\partial C_L} & \frac{\partial R_{f_g}}{\partial (\nabla C_L)} & \frac{\partial R_{f_g}}{\partial (\nabla p)} \\ \frac{\partial R_{f_n}}{\partial \varepsilon} & \frac{\partial R_{f_n}}{\partial \bar{\omega}} & \boldsymbol{\frac{\partial R_{f_n}}{\partial \bar{\kappa}}} & \frac{\partial R_{f_n}}{\partial C_L} & \frac{\partial R_{f_n}}{\partial (\nabla C_L)} & \frac{\partial R_{f_n}}{\partial (\nabla p)} \\ \frac{\partial R_{\omega}}{\partial \varepsilon} & \frac{\partial R_{\omega}}{\partial \bar{\omega}} & \frac{\partial R_{\omega}}{\partial \bar{\kappa}} & \frac{\partial R_{\omega}}{\partial C_L} & \frac{\partial R_{\omega}}{\partial (\nabla C_L)} & \frac{\partial R_{\omega}}{\partial (\nabla p)} \\ \frac{\partial R_{\kappa}}{\partial \varepsilon} & \frac{\partial R_{\kappa}}{\partial \bar{\omega}} & \frac{\partial R_{\kappa}}{\partial \bar{\kappa}} & \frac{\partial R_{\kappa}}{\partial C_L} & \frac{\partial R_{\kappa}}{\partial (\nabla C_L)} & \frac{\partial R_{\kappa}}{\partial (\nabla p)} \end{pmatrix} \tag{C.40}$$

$$\frac{\partial R_e}{\partial \varepsilon} = -\mathbb{1} \tag{C.41}$$

$$\frac{\partial R_{f_g}}{\partial \bar{\omega}} = -(1 - f_g) \tag{C.42}$$

$$\frac{\partial R_{f_n}}{\partial \bar{\kappa}} = -A_n - A_n' \bar{\kappa} \quad \text{with} \quad A_n' = \frac{\partial A_n}{\partial \bar{\kappa}} \tag{C.43}$$

Similarly to the previous case, all the gray terms are null.

- Computation of $\partial \boldsymbol{V}_{OUT}/\partial \boldsymbol{V}_{IN}$:

$$\frac{\partial \boldsymbol{V}_{OUT}}{\partial \boldsymbol{V}_{IN}} = \begin{pmatrix} \frac{\partial \boldsymbol{\sigma}}{\partial \varepsilon} & \frac{\partial \boldsymbol{\sigma}}{\partial \bar{\omega}} & \frac{\partial \boldsymbol{\sigma}}{\partial \bar{\kappa}} & \frac{\partial \boldsymbol{\sigma}}{\partial C_L} & \frac{\partial \boldsymbol{\sigma}}{\partial (\nabla C_L)} & \frac{\partial \boldsymbol{\sigma}}{\partial (\nabla p)} \\ \frac{\partial \omega}{\partial \varepsilon} & \frac{\partial \omega}{\partial \bar{\omega}} & \frac{\partial \omega}{\partial \bar{\kappa}} & \frac{\partial \omega}{\partial C_L} & \frac{\partial \omega}{\partial (\nabla C_L)} & \frac{\partial \omega}{\partial (\nabla p)} \\ \frac{\partial \kappa}{\partial \varepsilon} & \frac{\partial \kappa}{\partial \bar{\omega}} & \frac{\partial \kappa}{\partial \bar{\kappa}} & \frac{\partial \kappa}{\partial C_L} & \frac{\partial \kappa}{\partial (\nabla C_L)} & \frac{\partial \kappa}{\partial (\nabla p)} \\ \frac{\partial \boldsymbol{J}}{\partial \varepsilon} & \frac{\partial \boldsymbol{J}}{\partial \bar{\omega}} & \frac{\partial \boldsymbol{J}}{\partial \bar{\kappa}} & \frac{\partial \boldsymbol{J}}{\partial C_L} & \boldsymbol{\frac{\partial J}{\partial (\nabla C_L)}} & \boldsymbol{\frac{\partial J}{\partial (\nabla p)}} \\ \frac{\partial h}{\partial \varepsilon} & \frac{\partial h}{\partial \bar{\omega}} & \frac{\partial h}{\partial \bar{\kappa}} & \boldsymbol{\frac{\partial h}{\partial C_L}} & \frac{\partial h}{\partial (\nabla C_L)} & \frac{\partial h}{\partial (\nabla p)} \\ \frac{\partial H_{C_L}}{\partial \varepsilon} & \frac{\partial H_{C_L}}{\partial \bar{\omega}} & \frac{\partial H_{C_L}}{\partial \bar{\kappa}} & \boldsymbol{\frac{\partial H_{C_L}}{\partial C_L}} & \frac{\partial H_{C_L}}{\partial (\nabla C_L)} & \frac{\partial H_{C_L}}{\partial (\nabla p)} \end{pmatrix} \tag{C.44}$$

The remaining terms that have not been computed yet are the ones related to diffusion, which are:

$$\frac{\partial \boldsymbol{J}}{\partial (\nabla C_L)} = \frac{D_L \nabla P V_H}{RT} \tag{C.45}$$

$$\frac{\partial \boldsymbol{J}}{\partial (\nabla p)} = \frac{D_L C_L V_H}{RT} \tag{C.46}$$

$$\frac{\partial h}{\partial C_L} = \frac{N_T \mu' \dot{T} (1 - \mu C_L)}{(1 + \mu C_L)^3} \quad \text{with} \quad \mu' = \frac{d\mu}{dT} \tag{C.47}$$

$$\frac{\partial H_{C_L}}{\partial C_L} = -\frac{2 N_T \mu^2}{(1 + \mu C_L)^3} \tag{C.48}$$

where $\frac{\partial h}{\partial C_L}$ is necessary only for cases where there is a temperature variation, otherwise its derivative is null.

C.3 Global system

C.3.1 Elementary reactions

The elementary reactions associated to the unknowns are:

$$\{\boldsymbol{F}\}_u = \int_{\Omega^e} \boldsymbol{B}^T \cdot \{\boldsymbol{\sigma}\} \, d\Omega = \int_{\Omega_0^e} J \boldsymbol{B}^T \cdot \{\boldsymbol{\sigma}\} \, d\Omega_0 \tag{C.49}$$

$$\{\boldsymbol{F}\}_p = \int_{\Omega^e} (\text{trace}(\varepsilon) - \theta) \boldsymbol{N}_l \, d\Omega \tag{C.50}$$

$$\{\boldsymbol{F}\}_\theta = \int_{\Omega^e} \left(\frac{1}{3} \text{trace}(\sigma^\star) - p \right) \boldsymbol{N}_l \, d\Omega \tag{C.51}$$

$$\{\boldsymbol{F}\}_{\bar{\omega}} = \int_{\Omega^e} ((\bar{\omega} - \omega) \boldsymbol{N}_l + \ell_\omega^2 \boldsymbol{G}^T \cdot \boldsymbol{G} \cdot \{\bar{\omega}\}) \, d\Omega \tag{C.52}$$

$$\{\boldsymbol{F}\}_{\bar{\kappa}} = \int_{\Omega^e} ((\bar{\kappa} - \kappa) \boldsymbol{N}_l + \ell_\kappa^2 \boldsymbol{G}^T \cdot \boldsymbol{G} \cdot \{\bar{\kappa}\}) \, d\Omega \tag{C.53}$$

$$\{\boldsymbol{F}\}_{C_L} = \int_{\Omega^e} \left[\left((1 + H_{C_L}) \frac{C_L}{t} + h \right) \boldsymbol{N}_l - \boldsymbol{G}^T \cdot \boldsymbol{J} \right] d\Omega \tag{C.54}$$

where J in Equation C.49 is defined as $J = \det(\boldsymbol{F})$, the Jacobian determinant that transforms integrals from the deformed configuration (Ω^e) to the reference configuration (Ω_0^e). The integrations are performed using standard Gauss integration methods.

The function $\boldsymbol{M}_R$ is introduced so that the product $\boldsymbol{c}$ of two second-order tensors $\boldsymbol{a}$ and $\boldsymbol{b}$, typically written as $\boldsymbol{c} = \boldsymbol{a} \cdot \boldsymbol{b}$, can be expressed in Voigt notation as:

$$\{\boldsymbol{c}\} = \{\boldsymbol{a} \cdot \boldsymbol{b}\} = \boldsymbol{M}_R(\boldsymbol{b}) \cdot \{\boldsymbol{a}\} \tag{C.55}$$

where the matrix $\boldsymbol{M}_R(\boldsymbol{b})$ depends linearly on $\boldsymbol{b}$.

C.3.2 Elementary stiffness matrix

The elementary stiffness matrix is defined as:

$$\boldsymbol{K} = \begin{pmatrix} \boldsymbol{K}_{uu} & \boldsymbol{K}_{up} & \boldsymbol{K}_{u\theta} & \boldsymbol{K}_{u\bar{\omega}} & \boldsymbol{K}_{u\bar{\kappa}} & \boldsymbol{K}_{uC_L} \\ \boldsymbol{K}_{pu} & \boldsymbol{K}_{pp} & \boldsymbol{K}_{p\theta} & \boldsymbol{K}_{p\bar{\omega}} & \boldsymbol{K}_{p\bar{\kappa}} & \boldsymbol{K}_{pC_L} \\ \boldsymbol{K}_{\theta u} & \boldsymbol{K}_{\theta p} & \boldsymbol{K}_{\theta\theta} & \boldsymbol{K}_{\theta\bar{\omega}} & \boldsymbol{K}_{\theta\bar{\kappa}} & \boldsymbol{K}_{\theta C_L} \\ \boldsymbol{K}_{\bar{\omega}u} & \boldsymbol{K}_{\bar{\omega}p} & \boldsymbol{K}_{\bar{\omega}\theta} & \boldsymbol{K}_{\bar{\omega}\bar{\omega}} & \boldsymbol{K}_{\bar{\omega}\bar{\kappa}} & \boldsymbol{K}_{\bar{\omega}C_L} \\ \boldsymbol{K}_{\bar{\kappa}u} & \boldsymbol{K}_{\bar{\kappa}p} & \boldsymbol{K}_{\bar{\kappa}\theta} & \boldsymbol{K}_{\bar{\kappa}\bar{\omega}} & \boldsymbol{K}_{\bar{\kappa}\bar{\kappa}} & \boldsymbol{K}_{\bar{\kappa}C_L} \\ \boldsymbol{K}_{C_Lu} & \boldsymbol{K}_{C_Lp} & \boldsymbol{K}_{C_L\theta} & \boldsymbol{K}_{C_L\bar{\omega}} & \boldsymbol{K}_{C_L\bar{\kappa}} & \boldsymbol{K}_{C_LC_L} \end{pmatrix} \tag{C.56}$$

where each term can be computed as the derivative of the elementary reactions with respect to the nodal unknowns. The following will introduce the computation of the matrix terms line by line. The gray terms are equal to zero.

- Computation of $\boldsymbol{K}_{uu}$, $\boldsymbol{K}_{up}$, $\boldsymbol{K}_{u\theta}$, $\boldsymbol{K}_{u\bar{\omega}}$, $\boldsymbol{K}_{u\bar{\kappa}}$:

$$\boxed{\{\boldsymbol{F}\}_u = \int_{\Omega^e} \boldsymbol{B}^T \cdot \{\boldsymbol{\sigma}\}\, d\Omega = \int_{\Omega_0^e} J\boldsymbol{B}^T \cdot \{\boldsymbol{\sigma}\}\, d\Omega_0} \tag{C.57}$$

The temporal derivative of $\boldsymbol{F}_u$ is then given by:

$$\dot{\boldsymbol{F}}_u = \boldsymbol{K}_{uu} \cdot \dot{\boldsymbol{u}}^e \tag{C.58}$$

where,

$$\dot{\boldsymbol{F}}_u = \int_{\Omega_0^e} \dot{\boldsymbol{J}}\boldsymbol{B}^T \cdot \{\boldsymbol{\sigma}\} + \boldsymbol{J}\dot{\boldsymbol{B}}^T \cdot \{\boldsymbol{\sigma}\} + \boldsymbol{J}\boldsymbol{B}^T \cdot \{\dot{\boldsymbol{\sigma}}\}\, d\Omega_0 \tag{C.59}$$

To compute $\boldsymbol{K}_{uu}$, variations with respect to $\boldsymbol{u}_e$ are first considered. It is then shown that:

$$\{\boldsymbol{L}\} = \boldsymbol{B} \cdot \dot{\boldsymbol{u}}^e = \{\dot{\boldsymbol{F}} \cdot \boldsymbol{F}^{-1}\} = \boldsymbol{M}_R(\boldsymbol{F}^{-1}) \cdot \{\dot{\boldsymbol{F}}\} = \boldsymbol{M}_R(\boldsymbol{F}^{-1}) \cdot \boldsymbol{B}_F \cdot \dot{\boldsymbol{u}}^e \tag{C.60}$$

where $\boldsymbol{B}$ represents the matrix of derivatives of the quadratic shape functions ($\boldsymbol{N}_q$) with respect to the final configuration, and $\boldsymbol{B}_F$ refers to derivatives of the shape functions with respect to the initial configuration. It follows that:

$$\boldsymbol{B}^T = \boldsymbol{B}_F^T \cdot \boldsymbol{M}_R^T(\boldsymbol{F}^{-1}) = \boldsymbol{B}_F^T \cdot \boldsymbol{M}_R(\boldsymbol{F}^{-T}) \tag{C.61}$$

The product $\dot{\boldsymbol{B}}^T \cdot \{\boldsymbol{\sigma}\}$ from Equation C.59 can be written as:

$$\dot{\boldsymbol{B}}^T \cdot \{\boldsymbol{\sigma}\} = \boldsymbol{B}_F^T \cdot \boldsymbol{M}_R(\dot{\boldsymbol{F}^{-T}}) \cdot \{\boldsymbol{\sigma}\} = \boldsymbol{B}_F^T \cdot \{\boldsymbol{\sigma} \cdot \dot{\boldsymbol{F}^{-T}}\} \tag{C.62}$$

To proceed, it is noted that:

$$\dot{\boldsymbol{F}^{-T}} = -(\boldsymbol{F}^{-T} \underline{\otimes} \boldsymbol{F}^{-1}) : \dot{\boldsymbol{F}}^T = -F_{ik}^{-T} F_{jl}^{-1} \dot{F}_{kl}^T = -F_{ik}^{-T} \dot{F}_{kl}^T F_{lj}^{-T} = -\boldsymbol{L}^T \cdot \boldsymbol{F}^{-T} \tag{C.63}$$

Thus, $\boldsymbol{\sigma} \cdot \dot{\boldsymbol{F}^{-T}}$ can be written as:

$$\{\boldsymbol{\sigma} \cdot \dot{\boldsymbol{F}^{-T}}\} = -\{\boldsymbol{\sigma} \cdot \boldsymbol{L}^T \cdot \boldsymbol{F}^{-T}\} = -\boldsymbol{M}_R(\boldsymbol{F}^{-T}) \cdot \{\boldsymbol{\sigma} \cdot \boldsymbol{L}^T\} \tag{C.64}$$

As a result, $\dot{\boldsymbol{B}}^T \cdot \{\boldsymbol{\sigma}\}$ is expressed as:

$$\dot{\boldsymbol{B}}^T \cdot \{\boldsymbol{\sigma}\} = -\boldsymbol{B}_F^T \cdot \boldsymbol{M}_R(\boldsymbol{F}^{-T}) \cdot \{\boldsymbol{\sigma} \cdot \boldsymbol{L}^T\} = -\boldsymbol{B}^T \cdot \{\boldsymbol{\sigma} \cdot \boldsymbol{L}^T\} \tag{C.65}$$

With $\dot{J} = J\mathrm{trace}(\boldsymbol{L})$, $\dot{\boldsymbol{F}}_u$ can be formulated as:

$$\dot{\boldsymbol{F}}_u = \int_{\Omega_0^e} J\boldsymbol{B}^T \cdot \{-\boldsymbol{\sigma} \cdot \boldsymbol{L}^T + \dot{\boldsymbol{\sigma}} + \mathrm{trace}(\boldsymbol{L})\boldsymbol{\sigma}\}\, d\Omega_0 \tag{C.66}$$

The Truesdall rate of the Cauchy stress tensor $\boldsymbol{\sigma}$ is defined as:

$$\boldsymbol{\sigma}^\tau = \dot{\boldsymbol{\sigma}} - \boldsymbol{L} \cdot \boldsymbol{\sigma} - \boldsymbol{\sigma} \cdot \boldsymbol{L}^T + \mathrm{trace}(\boldsymbol{L})\boldsymbol{\sigma} \tag{C.67}$$

Then,

$$\dot{\boldsymbol{F}}_u = \int_{\Omega_0^e} J\boldsymbol{B}^{\boldsymbol{T}} \cdot \{\boldsymbol{\sigma}^\tau + \boldsymbol{L} \cdot \boldsymbol{\sigma}\}\, d\Omega_0 \tag{C.68}$$

$$= \int_{\Omega_0^e} J\boldsymbol{B}^{\boldsymbol{T}} \cdot \{\mathbb{C}^\tau : \boldsymbol{L} + \boldsymbol{L} \cdot \boldsymbol{\sigma}\}\, d\Omega_0 \tag{C.69}$$

$$= \int_{\Omega_0^e} J\boldsymbol{B}^{\boldsymbol{T}} \cdot \{\mathbb{C}^\tau \cdot \{\boldsymbol{L}\} + \boldsymbol{M}_R(\boldsymbol{\sigma}) \cdot \boldsymbol{L}\}\, d\Omega_0 \tag{C.70}$$

$$= \int_{\Omega_0^e} J\boldsymbol{B}^{\boldsymbol{T}} \cdot \{\mathbb{C}^\tau + \boldsymbol{M}_R(\boldsymbol{\sigma})\} \cdot \{\boldsymbol{L}\}\, d\Omega_0 \tag{C.71}$$

$$= \int_{\Omega_0^e} J\boldsymbol{B}^{\boldsymbol{T}} \cdot \{\mathbb{C}^\tau + \boldsymbol{M}_R(\boldsymbol{\sigma})\} \cdot \boldsymbol{B} \cdot \dot{\boldsymbol{u}}^e\, d\Omega_0 \tag{C.72}$$

$$= \int_{\Omega_0^e} J\boldsymbol{B}^{\boldsymbol{T}} \cdot \{\mathbb{C}^\tau + \boldsymbol{M}_R(\boldsymbol{\sigma})\} \cdot \boldsymbol{B} \cdot\, d\Omega_0 \dot{\boldsymbol{u}}^e \tag{C.73}$$

$$\tag{C.74}$$

where $\{\mathbb{C}^\tau\}$ represents the tangent operator associated with the Truesdell rate, defined as:

$$\mathbb{C}^\tau = \mathbb{C}^J - \frac{1}{2}(\boldsymbol{\sigma} \underline{\otimes} \mathbb{1} + \boldsymbol{\sigma} \overline{\otimes} \mathbb{1} + \mathbb{1} \underline{\otimes} \boldsymbol{\sigma} + \mathbb{1} \overline{\otimes} \boldsymbol{\sigma}) + \boldsymbol{\sigma} \otimes \mathbb{1} \tag{C.75}$$

where $\{\mathbb{C}^J\}$ is associated with the Jaumann rate of the stress tensor $\boldsymbol{\sigma}$. Thus, $\boldsymbol{K}_{uu}$ is defined as:

$$\boldsymbol{K}_{uu} = \int_{\Omega^e} \boldsymbol{B}^{\boldsymbol{T}} \cdot \{\mathbb{C}^{\tau}\} \cdot \boldsymbol{B}\, d\Omega + \int_{\Omega^e} \boldsymbol{B}^{\boldsymbol{T}} \cdot \boldsymbol{M}_R(\boldsymbol{\sigma}) \cdot \boldsymbol{B} \cdot d\Omega \tag{C.76}$$

$$= \boldsymbol{K}_{uu}^{M} + \boldsymbol{K}_{uu}^{G} \tag{C.77}$$

where $\boldsymbol{K}_{uu}^{M}$ represents the contribution from material nonlinearity, and $\boldsymbol{K}_{uu}^{G}$ represents the contribution from geometrical nonlinearity. Knowing that $\boldsymbol{\sigma} = \mathbb{K} : \boldsymbol{\sigma}^\star + p\mathbb{1}$, the term $\boldsymbol{K}_{up}$ is computed as:

$$\boldsymbol{K}_{up} = \frac{\partial\{\boldsymbol{F}\}_u}{\partial\{p^e\}} = \int_{\Omega^e} \boldsymbol{B}^T \cdot \mathbb{1} \otimes \boldsymbol{N}_l\, d\Omega \tag{C.78}$$

The modified strain is defined as $\boldsymbol{\varepsilon}^\star = \mathbb{K} : \boldsymbol{\varepsilon} + \frac{1}{3}\theta\mathbb{1}$. Then, $\boldsymbol{K}_{u\theta}$ is expressed as:

$$\boldsymbol{K}_{u\theta} = \frac{\partial\{\boldsymbol{F}\}_u}{\partial\{\theta^e\}} = \int_{\Omega^e} \boldsymbol{B}^T \cdot \frac{\partial\boldsymbol{\sigma}}{\partial\theta}\, d\Omega \tag{C.79}$$

$$= \int_{\Omega^e} \boldsymbol{B}^T \cdot \frac{\partial\boldsymbol{\sigma}}{\partial\boldsymbol{\sigma}^\star} \cdot \frac{\partial\boldsymbol{\sigma}^\star}{\partial\boldsymbol{\varepsilon}^\star} \cdot \frac{\partial\boldsymbol{\varepsilon}^\star}{\partial\theta} \cdot \frac{\partial\theta}{\partial\theta^e}\, d\Omega \tag{C.80}$$

$$= \frac{1}{3}\int_{\Omega^e} \boldsymbol{B}^T \cdot \left(\mathbb{K} : \frac{\partial\boldsymbol{\sigma}^\star}{\partial\boldsymbol{\varepsilon}^\star} : \mathbb{1}\right) \otimes \boldsymbol{N}_l\, d\Omega \tag{C.81}$$

where $\mathbb{K}$ is the fourth-order tensor that associates a second-order tensor to its deviator, $\partial\boldsymbol{\sigma}^\star/\partial\boldsymbol{\varepsilon}^\star$ was previously computed by the consistent tangent matrix in Section C.2 and $\mathbb{1}$ is the unit second-order tensor. $\boldsymbol{K}_{u\bar{\omega}}$ is computed as:

$$\boldsymbol{K}_{u\bar{\omega}} = \frac{\partial\{\boldsymbol{F}\}_u}{\partial\{\bar{\omega}^e\}} = \int_{\Omega^e} \boldsymbol{B}^T \cdot \frac{\partial\boldsymbol{\sigma}}{\partial\boldsymbol{\sigma}^\star} \cdot \frac{\partial\boldsymbol{\sigma}^\star}{\partial\bar{\omega}} \cdot \frac{\partial\bar{\omega}}{\partial\bar{\omega}^n}\, d\Omega \tag{C.82}$$

$$= \int_{\Omega^e} \boldsymbol{B}^T \cdot \left(\mathbb{K} : \frac{\partial\boldsymbol{\sigma}^\star}{\partial\bar{\omega}}\right) \otimes \boldsymbol{N}_l\, d\Omega \tag{C.83}$$

In a similar way, $\boldsymbol{K}_{u\bar{\kappa}}$ is computed as:

$$\boldsymbol{K}_{u\bar{\kappa}} = \frac{\partial\{\boldsymbol{F}\}_u}{\partial\{\bar{\kappa}^e\}} = \int_{\Omega^e} \boldsymbol{B}^T \cdot \left(\mathbb{K} : \frac{\partial\boldsymbol{\sigma}^\star}{\partial\bar{\kappa}}\right) \otimes \boldsymbol{N}_l\, d\Omega \tag{C.84}$$

The remaining derivative terms in Equations C.82 and C.84 were previously computed in Section C.2.

- Computation of $\boldsymbol{K}_{pu}$, $\boldsymbol{K}_{pp}$, $\boldsymbol{K}_{p\theta}$, $\boldsymbol{K}_{p\bar{\omega}}$, $\boldsymbol{K}_{p\bar{\kappa}}$:

$$\boxed{\{\boldsymbol{F}\}_p = \int_{\Omega^e} (\mathrm{trace}(\varepsilon) - \theta)\boldsymbol{N}_l\, d\Omega} \tag{C.85}$$

$$\boldsymbol{K}_{pu} = \frac{\partial\{\boldsymbol{F}\}_p}{\partial\{\boldsymbol{u}^e\}} = \boldsymbol{K}_{up}^T \tag{C.86}$$

(C.87)

In theory, $\boldsymbol{K}_{pp}$ should be equal to zero. However, this consideration causes convergence problems. Thus, $\boldsymbol{K}_{pp}$ is expressed as follows, where K_{pen} is a infinitesimal constant, such as 1×10^{-12}.

$$\boldsymbol{K}_{pp} = \frac{\partial\{\boldsymbol{F}\}_p}{\partial\{p^e\}} = \int_{\Omega^e} K_{pen} \cdot \boldsymbol{N}_l \otimes \boldsymbol{N}_l \, d\Omega \tag{C.88}$$

$$\boldsymbol{K}_{p\theta} = \frac{\partial\{\boldsymbol{F}\}_p}{\partial\{\theta^e\}} = \int_{\Omega^e} -\boldsymbol{N}_l \otimes \boldsymbol{N}_l \, d\Omega \tag{C.89}$$

- <u>Computation of $\boldsymbol{K}_{\theta u}$, $\boldsymbol{K}_{\theta p}$, $\boldsymbol{K}_{\theta\theta}$, $\boldsymbol{K}_{\theta\bar{\omega}}$, $\boldsymbol{K}_{\theta\bar{\kappa}}$:</u>

$$\boxed{\{\boldsymbol{F}\}_\theta = \int_{\Omega^e} \left(\frac{1}{3}\text{trace}(\sigma^\star) - p\right) \boldsymbol{N}_l \, d\Omega} \tag{C.90}$$

$$\boldsymbol{K}_{\theta u} = \frac{\partial\{\boldsymbol{F}\}_\theta}{\partial\{\boldsymbol{u}^e\}} = \boldsymbol{K}_{u\theta}^T \tag{C.91}$$

$$\boldsymbol{K}_{\theta p} = \frac{\partial\{\boldsymbol{F}\}_\theta}{\partial\{p^e\}} = \boldsymbol{K}_{p\theta}^T \tag{C.92}$$

$$\boldsymbol{K}_{\theta\theta} = \frac{\partial\{\boldsymbol{F}\}_\theta}{\partial\{\theta^e\}} = \frac{1}{9}\int_{\Omega_e} \left(\mathbb{1} : \left(\frac{\partial \boldsymbol{\sigma}^\star}{\partial \boldsymbol{\varepsilon}^\star} : \mathbb{1}\right)\right) \boldsymbol{N}_l \otimes \boldsymbol{N}_l \, d\Omega \tag{C.93}$$

$$\boldsymbol{K}_{\theta\bar{\omega}} = \frac{\partial\{\boldsymbol{F}\}_\theta}{\partial\{\bar{\omega}^e\}} = \frac{1}{3}\int_{\Omega^e} \left(\text{trace}\left(\frac{\partial \boldsymbol{\sigma}}{\partial \bar{\omega}}\right)\right) \boldsymbol{N}_l \otimes \boldsymbol{N}_l \, d\Omega \tag{C.94}$$

$$\boldsymbol{K}_{\theta\bar{\kappa}} = \frac{\partial\{\boldsymbol{F}\}_\theta}{\partial\{\bar{\kappa}^e\}} = \frac{1}{3}\int_{\Omega^e} \left(\text{trace}\left(\frac{\partial \boldsymbol{\sigma}}{\partial \bar{\kappa}}\right)\right) \boldsymbol{N}_l \otimes \boldsymbol{N}_l \, d\Omega \tag{C.95}$$

- <u>Computation of $\boldsymbol{K}_{\bar{\omega}u}$, $\boldsymbol{K}_{\bar{\omega}\theta}$, $\boldsymbol{K}_{\bar{\omega}\bar{\omega}}$, $\boldsymbol{K}_{\bar{\omega}\bar{\kappa}}$:</u>

$$\boxed{\{\boldsymbol{F}\}_{\bar{\omega}} = \int_{\Omega^e} \left((\bar{\omega} - \omega)\boldsymbol{N}_l + \ell_\omega^2 \boldsymbol{G}^T \cdot \boldsymbol{G} \cdot \{\bar{\omega}\}\right) d\Omega} \tag{C.96}$$

$$\boldsymbol{K}_{\bar{\omega}u} = \frac{\partial\{\boldsymbol{F}\}_{\bar{\omega}}}{\partial\{\boldsymbol{u}^e\}} = -\int_{\Omega^e} \boldsymbol{N}_l \otimes \left(\frac{\partial \omega}{\partial \varepsilon} \cdot \boldsymbol{B}\right) \, d\Omega \tag{C.97}$$

$$\boldsymbol{K}_{\bar{\omega}\theta} = \frac{\partial\{\boldsymbol{F}\}_{\bar{\omega}}}{\partial\{\theta^e\}} = -\frac{1}{3}\int_{\Omega^e} \text{trace}\left(\frac{\partial \omega}{\partial \boldsymbol{\varepsilon}^\star}\right) \boldsymbol{N}_l \otimes \boldsymbol{N}_l \, d\Omega \tag{C.98}$$

$$\boldsymbol{K}_{\bar{\omega}\bar{\kappa}} = \frac{\partial\{\boldsymbol{F}\}_{\bar{\omega}}}{\partial\{\bar{\kappa}^e\}} = -\int_{\Omega^e} \frac{\partial \omega}{\partial \bar{\kappa}} \boldsymbol{N}_l \otimes \boldsymbol{N}_l \, d\Omega \tag{C.99}$$

$$\boldsymbol{K}_{\bar{\omega}\bar{\omega}} = \frac{\partial\{\boldsymbol{F}\}_{\bar{\omega}}}{\partial\{\bar{\omega}^e\}} = \int_{\Omega^e} \left(1 - \frac{\partial \omega}{\partial \bar{\omega}}\right) \boldsymbol{N}_l \otimes \boldsymbol{N}_l + \ell_w^2 \boldsymbol{G}^T \cdot \boldsymbol{G} \, d\Omega \tag{C.100}$$

- Computation of $\boldsymbol{K}_{\bar{\kappa}u}$, $\boldsymbol{K}_{\bar{\kappa}\theta}$, $\boldsymbol{K}_{\bar{\kappa}\bar{\omega}}$, $\boldsymbol{K}_{\bar{\kappa}\bar{\kappa}}$:

$$\boxed{\{\boldsymbol{F}\}_{\bar{\kappa}} = \int_{\Omega^e} ((\bar{\kappa} - \kappa)\boldsymbol{N}_l + \ell_\kappa^2 \boldsymbol{G}^T \cdot \boldsymbol{G} \cdot \{\bar{\kappa}\})\, d\Omega} \tag{C.101}$$

$$\boldsymbol{K}_{\bar{\kappa}u} = \frac{\partial \{\boldsymbol{F}\}_{\bar{\kappa}}}{\partial \{\boldsymbol{u}\}} = -\int_{\Omega^e} \boldsymbol{N}_l \otimes \left(\frac{\partial \kappa}{\partial \varepsilon} \cdot \boldsymbol{B} \right)\, d\Omega \tag{C.102}$$

$$\boldsymbol{K}_{\bar{\kappa}\theta} = \frac{\partial \{\boldsymbol{F}\}_{\bar{\kappa}}}{\partial \{\theta\}} = -\frac{1}{3} \int_{\Omega^e} \operatorname{trace}\left(\frac{\partial \kappa}{\partial \boldsymbol{\varepsilon}^\star} \right) \boldsymbol{N}_l \otimes \boldsymbol{N}_l \, d\Omega \tag{C.103}$$

$$\boldsymbol{K}_{\bar{\kappa}\bar{\omega}} = \frac{\partial \{\boldsymbol{F}\}_{\bar{\kappa}}}{\partial \{\bar{\omega}\}} = -\int_{\Omega^e} \frac{\partial \kappa}{\partial \bar{\omega}} \boldsymbol{N}_l \otimes \boldsymbol{N}_l \, d\Omega \tag{C.104}$$

$$\boldsymbol{K}_{\bar{\kappa}\bar{\kappa}} = \frac{\partial \{\boldsymbol{F}\}_{\bar{\kappa}}}{\partial \{\bar{\kappa}\}} = \int_{\Omega^e} \left(1 - \frac{\partial \kappa}{\partial \bar{\kappa}} \right) \boldsymbol{N}_l \otimes \boldsymbol{N}_l + \ell_w^2 \boldsymbol{G}^T \cdot \boldsymbol{G} \, d\Omega \tag{C.105}$$

$$\tag{C.106}$$

- Computation of $\boldsymbol{K}_{C_L C_L}$, $\boldsymbol{K}_{C_L p}$:

$$\boxed{\{\boldsymbol{F}\}_{C_L} = \int_{\Omega^e} \left[\left((1 + H_{C_L}) \frac{C_L}{t} + h \right) \boldsymbol{N}_l - \boldsymbol{G}^T \cdot \boldsymbol{J} \right]\, d\Omega} \tag{C.107}$$

$\boldsymbol{K}_{C_L C_L}$ is defined as the derivative of $\{\boldsymbol{F}\}_{C_L}$ with respect to $\{C_L\}$ and consists of several components, as follows:

$$\boldsymbol{K}_{C_L C_L} = \frac{\partial \{\boldsymbol{F}\}_{C_L}}{\partial \{C_L\}} = \int_{\Omega^e} \left((1 + H_{C_L}) \frac{1}{t} \right) \boldsymbol{N}_l \otimes \boldsymbol{N}_l \, d\Omega \tag{C.108}$$

$$- \int_{\Omega^e} \boldsymbol{G}^T \cdot \frac{\partial \boldsymbol{J}}{\partial \nabla C_L} \cdot \boldsymbol{G} \, d\Omega \tag{C.109}$$

$$- \int_{\Omega^e} \left(\boldsymbol{G}^T \cdot \frac{\partial \boldsymbol{J}}{\partial C_L} \right) \otimes \boldsymbol{N}_l \, d\Omega \tag{C.110}$$

$$+ \int_{\Omega^e} \left(\frac{\partial H_{C_L}}{\partial C_L} \cdot \frac{C_L}{t} + \frac{\partial h}{\partial C_L} \right) \boldsymbol{N}_l \otimes \boldsymbol{N}_l \, d\Omega \tag{C.111}$$

$$+ \int_{\Omega^e} \left(\frac{\partial H_{C_L}}{\partial C_L} \cdot \frac{C_L}{t} \right) \boldsymbol{N}_l \otimes \boldsymbol{N}_l \, d\Omega \tag{C.112}$$

$$+ \int_{\Omega^e} \left(\frac{\partial h}{\partial C_L} \right) \boldsymbol{N}_l \otimes \boldsymbol{N}_l \, d\Omega \tag{C.113}$$

$$\boldsymbol{K}_{C_L p} = \frac{\partial \{\boldsymbol{F}\}_{C_L}}{\partial \{p\}} = -\int_{\Omega^e} \boldsymbol{G}^T \cdot \frac{\partial \boldsymbol{J}}{\partial \nabla p} \cdot \boldsymbol{G} \, d\Omega \tag{C.114}$$

Bibliography

Abbas, M., Ern, A., & Pignet, N. (2018). Hybrid high-order methods for finite deformations of hyperelastic materials. *Computational Mechanics*, *62*, 909–928. https://doi.org/10.1007/s00466-018-1538-0

Abbas, M., Ern, A., & Pignet, N. (2019a). A hybrid high-order method for finite elastoplastic deformations within a logarithmic strain framework. *Numerical Methods for Engineering*. https://doi.org/10.1002/nme.6137

Abbas, M., Ern, A., & Pignet, N. (2019b). A hybrid high-order method for incremental associative plasticity with small deformations. *Computer Methods in Applied Mechanics and Engineering*, *346*, 891–912. https://doi.org/https://doi.org/10.1016/j.cma.2018.08.037

Abbasi, T., & Abbasi, S. A. (2011). "Renewable" hydrogen: Prospects and challenges. *Renewable and Sustainable Energy Reviews*, *15*, 3034–3040. https://doi.org/10.1016/j.rser.2011.02.026

Ahn, D., Sofronis, P., & Dodds, R. (2007). On hydrogen-induced plastic flow localization during void growth and coalescence. *International Journal of Hydrogen Energy*, *32*(16), 3734–3742. https://doi.org/https://doi.org/10.1016/j.ijhydene.2006.08.047

Al Akhrass, D., Bruchon, J., Drapier, S., & Fayolle, S. (2014). Integrating a logarithmic-strain based hyperelastic formulation into a three-field mixed finite element formulation to deal with incompressibility in finite-strain elastoplasticity. *Finite Elements in Analysis and Design*, *86*, 61–70. https://doi.org/https://doi.org/10.1016/j.finel.2014.04.004

Ambati, M., Gerasimov, T., & De Lorenzis, L. (2015). Phase-field modeling of ductile fracture. *Computational Mechanics*, *55*, 1017–1040. https://doi.org/10.1007/s00466-015-1151-4

Anderson, T. L. (2017). *Fracture mechanics: Fundamentals and applications, fourth edition* (4th). CRC Press. https://doi.org/10.1201/9781315370293

Ardon, K., Gasperini, M., Charles, Y., & Furtado, J. (2013). Failure mechanisms of an aisi 4135 steel submitted to the disk pressure test under helium and hydrogen gas. *Key Engineering Materials*, *592-593*, 291–294. https://doi.org/10.4028/www.scientific.net/KEM.592-593.291

Barnoush, A., & Vehoff, H. (2010). Recent developments in the study of hydrogen embrittlement: Hydrogen effect on dislocation nucleation. *Acta Materialia*, *58*(16), 5274–5285. https://doi.org/https://doi.org/10.1016/j.actamat.2010.05.057

Barsom, J., & Rolfe, S. (1987). *Fracture and fatigue control in structures* (2nd). Prentice-Hall.

Bastien, P., & Azou, P. (1951). Effect of hydrogen on the deformation and fracture of iron and steel in simple tension. In W. M. Baldwin (Ed.), *Proceedings of the first world metallurgical congress* (pp. 535–552). ASM.

Bažant, Z. P., Belytschko, T. B., & Chang, T.-P. (1984). Continuum theory for strain-softening. *Journal of Engineering Mechanics*, *110*(12), 1666–1692. https://doi.org/10.1061/(ASCE)0733-9399(1984)110:12(1666)

Bažant, Z. P., & Pijaudier-Cabot, G. (1988). Nonlocal Continuum Damage, Localization Instability and Convergence. *Journal of Applied Mechanics*, *55*(2), 287–293. https://doi.org/10.1115/1.3173674

Beachem, C. D. (1972). A new model for hydrogen-assisted cracking (hydrogen "embrittlement"). *Metallurgical Transactions*, *3*, 441–455. https://doi.org/10.1007/BF02642048

Beghini, M., Benamati, G., & Bertini, L. (1996). Hydrogen embrittlement characterization by disk pressure tests: Test analysis and application to high chromium martensitic steels. *Journal of Engineering Materials and Technology*, *118*(2), 179–185. https://doi.org/10.1115/1.2804884

Bellet, M. (1999). Finite element analysis of compressible viscoplasticity using a three-field formulation: Application to metal powder hot compaction. *Computer Methods in Applied Mechanics and Engineering*, *175*(1), 19–40. https://doi.org/https://doi.org/10.1016/S0045-7825(98)00317-X

Benzerga, A. A. (2000). *Rupture ductile des tôles anisotropes. simulation de la propagation longitudinale dans un tube pressurisé* (Doctoral dissertation) [2000ENMP1067]. http://www.theses.fr/2000ENMP1067

Besson, J. (2010). Continuum models of ductile fracture: A review. *International Journal of Damage Mechanics*, *19*(1), 3–52. https://doi.org/10.1177/1056789509103482

Besson, J. (2021). Chapitre I : Méthodes numériques pour la rupture ductile.

Besson, J., Moinereau, D., & Steglich, D. (2006). *Local approach to fracture*. Presses des MINES.

Besson, J., Steglich, D., & Brocks, W. (2001). Modeling of crack growth in round bars and plane strain specimens. *International Journal of Solids and Structures*, *38*(46), 8259–8284. https://doi.org/https://doi.org/10.1016/S0020-7683(01)00167-6

Besson, J., Bleyer, J., Feld-Payet, S., Gourgues-Lorenzon, A.-F., Hannard, F., Helfer, T., Hure, J., Kondo, D., Lazarus, V., Le Bourlot, C., Maitournam, H., Maurini, C., Moes, N., Morgeneyer, T., Morin, L., Petit, T., & Simar, A. (2023). *MEALOR II Damage Mechanics and Local Approach to Fracture*. Zenodo. https://doi.org/10.5281/zenodo.10125169

Birnbaum, H., & Sofronis, P. (1994). Hydrogen-enhanced localized plasticity—a mechanism for hydrogen-related fracture. *Materials Science and Engineering: A*, *176*(1), 191–202. https://doi.org/https://doi.org/10.1016/0921-5093(94)90975-X

Bockris, J. O., McBreen, J., & Nanis, L. (1965). The hydrogen evolution kinetics and hydrogen entry into a-iron. *Journal of The Electrochemical Society*, *112*(10), 1025. https://doi.org/10.1149/1.2423335

Bourdin, B., Francfort, G., & Marigo, J.-J. (2000). Numerical experiments in revisited brittle fracture. *Journal of the Mechanics and Physics of Solids*, *48*, 797–826. https://doi.org/10.1016/S0022-5096(99)00028-9

Brass, A., Chene, J., & Coudreuse, L. (2000). Fragilisation des aciers par l'hydrogène : Mécanismes. *Techniques de l'ingénieur*, *176*, 1–12. https://doi.org/https://doi.org/10.51257/a-v2-m176

Brepols, T., Wulfinghoff, S., & Reese, S. (2017). Gradient-extended two-surface damage-plasticity: Micromorphic formulation and numerical aspects. *International Journal of Plasticity*, *97*, 64–106.

Briottet, L., Moro, I., & Lemoine, P. (2012). Quantifying the hydrogen embrittlement of pipeline steels for safety considerations. *International Journal of Hydrogen Energy*, *37*(22), 17616–17623. https://doi.org/https://doi.org/10.1016/j.ijhydene.2012.05.143

Bron, F., Besson, J., & Pineau, A. (2004). Ductile rupture in thin sheets of two grades of 2024 aluminum alloy. *Materials Science and Engineering: A*, *380*(1), 356–364. https://doi.org/https://doi.org/10.1016/j.msea.2004.04.008

Brun, K., & Allison, T. C. (2022). *Machinery and energy systems for the hydrogen economy*. Elsevier.

Cao, T.-S., Mazière, M., Danas, K., & Besson, J. (2015). A model for ductile damage prediction at low stress triaxialities incorporating void shape change and void rotation. *International Journal of Solids and Structures*, *63*, 240–263. https://doi.org/10.1016/j.ijsolstr.2015.03.003

Cervera, M., Chiumenti, M., & Codina, R. (2010). Mixed stabilized finite element methods in nonlinear solid mechanics: Part i: Formulation. *Computer Methods in Applied Mechanics and Engineering*, *199*(37), 2559–2570. https://doi.org/https://doi.org/10.1016/j.cma.2010.04.006

Charles, Y., Gaspérini, M., Disashi, J., & Jouinot, P. (2012). Numerical modeling of the disk pressure test up to failure under gaseous hydrogen. *Journal of Materials Processing Technology*, *212*(8), 1761–1770. https://doi.org/https://doi.org/10.1016/j.jmatprotec.2012.03.022

Charles, Y., Gaspérini, M., Fagnon, N., Ardon, K., & Duhamel, A. (2019). Finite element simulation of hydrogen transport during plastic bulging of iron submitted to gaseous hydrogen pressure. *Engineering Fracture Mechanics*, *218*, 106580. https://doi.org/https://doi.org/10.1016/j.engfracmech.2019.106580

Chen, Y., Lorentz, E., & Besson, J. (2020). Crack initiation and propagation in small-scale yielding using a nonlocal gtn model. *International Journal of Plasticity*, *130*, 102701. https://doi.org/https://doi.org/10.1016/j.ijplas.2020.102701

Chu, C. C., & Needleman, A. (1980). Void Nucleation Effects in Biaxially Stretched Sheets. *Journal of Engineering Materials and Technology*, *102*(3), 249–256. https://doi.org/10.1115/1.3224807

Corporation, L. S. T. (2007). *Ls-dyna keyword user's manual*.

Dadfarnia, M., Martin, M. L., Nagao, A., Sofronis, P., & Robertson, I. M. (2015). Modeling hydrogen transport by dislocations. *Journal of the Mechanics and Physics of Solids*, *78*, 511–525. https://doi.org/https://doi.org/10.1016/j.jmps.2015.03.002

Dalloz, A., Besson, J., Gourgues-Lorenzon, A.-F., Sturel, T., & Pineau, A. (2009). Effect of shear cutting on ductility of a dual phase steel [MatModels 2007]. *Engineering Fracture Mechanics*, *76*(10), 1411–1424. https://doi.org/https://doi.org/10.1016/j.engfracmech.2008.10.009

Danas, K., & Castañeda, P. (2009). A finite-strain model for anisotropic viscoplastic porous media: I – theory. *European Journal of Mechanics - A/Solids*, *28*, 387–401. https://doi.org/10.1016/j.euromechsol.2008.11.002

Daw, M. S., & Baskes, M. I. (1987). Application of the embedded atom method to hydrogen embrittlement. In R. M. Latanision & R. H. Jones (Eds.), *Chemistry and physics of fracture* (pp. 196–218). Springer Netherlands. https://doi.org/10.1007/978-94-009-3665-2_12

de Souza Neto, E., Perić, D., Dutko, M., & Owen, D. (1996). Design of simple low order finite elements for large strain analysis of nearly incompressible solids. *International Journal of Solids and Structures*, *33*(20), 3277–3296. https://doi.org/https://doi.org/10.1016/0020-7683(95)00259-6

del Busto, S., Betegón, C., & Martínez-Pañeda, E. (2017). A cohesive zone framework for environmentally assisted fatigue [XVIII International Colloquium Mechanical Fatigue of Metals]. *Engineering Fracture Mechanics*, *185*, 210–226. https://doi.org/https://doi.org/10.1016/j.engfracmech.2017.05.021

Depover, T., Pérez Escobar, D., Wallaert, E., Zermout, Z., & Verbeken, K. (2014). Effect of hydrogen charging on the mechanical properties of advanced high strength steels. *International Journal of Hydrogen Energy*, *39*(9), 4647–4656. https://doi.org/https://doi.org/10.1016/j.ijhydene.2013.12.190

Depover, T., & Verbeken, K. (2016). The effect of tic on the hydrogen induced ductility loss and trapping behavior of fe-c-ti alloys. *Corrosion Science*, *112*, 308–326. https://doi.org/https://doi.org/10.1016/j.corsci.2016.07.013

Depover, T., & Verbeken, K. (2021). Hydrogen diffusion in metals: A topic requiring specific attention from the experimentalist. *Hydrogen Storage for Sustainability 2*, 247–280.

Depraetere, R., De Waele, W., Cauwels, M., Depover, T., Verbeken, K., Boone, M., & Hertelé, S. (2023). Influence of stress triaxiality on hydrogen assisted ductile damage in an x70 pipeline steel. *Materials Science and Engineering: A*, *864*, 144549. https://doi.org/https://doi.org/10.1016/j.msea.2022.144549

Depraetere, R., De Waele, W., & Hertelé, S. (2021). Fully-coupled continuum damage model for simulation of plasticity dominated hydrogen embrittlement mechanisms. *Computational Materials Science*, *200*, 110857. https://doi.org/https://doi.org/10.1016/j.commatsci.2021.110857

Di Pietro, D. A., & Ern, A. (2015). A hybrid high-order locking-free method for linear elasticity on general meshes. *Computer Methods in Applied Mechanics and Engineering*, *283*, 1–21. https://doi.org/https://doi.org/10.1016/j.cma.2014.09.009

Diamantopoulou, E., Liu, W., Labergere, C., Badreddine, H., Saanouni, K., & Hu, P. (2017). Micromorphic constitutive equations with damage applied to metal forming. *International Journal of Damage Mechanics*, *26*(2), 314–339. https://doi.org/10.1177/1056789516684650

Díaz, A., Alegre, J., Cuesta, I., & Zhang, Z. (2019). Numerical study of hydrogen influence on void growth at low triaxialities considering transient effects. *International Journal of Mechanical Sciences*, *164*, 105176. https://doi.org/https://doi.org/10.1016/j.ijmecsci.2019.105176

Dillard, T., Forest, S., & Ienny, P. (2006). Micromorphic continuum modelling of the deformation and fracture behaviour of nickel foams. *European Journal of Mechanics - A/Solids*, *25*(3), 526–549. https://doi.org/https://doi.org/10.1016/j.euromechsol.2005.11.006

Doherty, W. P., Wilson, E. L., & Taylor, R. L. (1969). Stress analysis of axisymmetric solids utilizing higher-order quadrilateral finite elements [Microforme, English].

Drexler, A., Bergmann, C., Manke, G., Kokotin, V., Mraczek, K., Leitner, S., Pohl, M., & Ecker, W. (2021). Local hydrogen accumulation after cold forming and heat treatment in punched advanced high strength steel sheets. *Journal of Alloys and Compounds*, *856*, 158226. https://doi.org/https://doi.org/10.1016/j.jallcom.2020.158226

Drexler, A., Siegl, W., Ecker, W., Tkadletz, M., Klösch, G., Schnideritsch, H., Mori, G., Svoboda, J., & Fischer, F. (2020). Cycled hydrogen permeation through armco iron – a joint experimental and modeling approach. *Corrosion Science*, *176*, 109017. https://doi.org/https://doi.org/10.1016/j.corsci.2020.109017

Drexler, A., Depover, T., Leitner, S., Verbeken, K., & Ecker, W. (2020). Microstructural based hydrogen diffusion and trapping models applied to fe–cx alloys. *Journal of Alloys and Compounds*, *826*, 154057. https://doi.org/https://doi.org/10.1016/j.jallcom.2020.154057

Drexler, A., Depover, T., Verbeken, K., & Ecker, W. (2019). Model-based interpretation of thermal desorption spectra of fe-c-ti alloys. *Journal of Alloys and Compounds*, *789*, 647–657. https://doi.org/https://doi.org/10.1016/j.jallcom.2019.03.102

Drexler, A., Vandewalle, L., Depover, T., Verbeken, K., & Domitner, J. (2021). Critical verification of the kissinger theory to evaluate thermal desorption spectra. *International Journal of Hydrogen Energy*, *46*(79), 39590–39606. https://doi.org/https://doi.org/10.1016/j.ijhydene.2021.09.171

El Ouazani Tuhami, A., Feld-Payet, S., Quilici, S., Osipov, N., & Besson, J. (2023). Simulations of complex crack paths using a robust and cost-efficient continuous–discontinuous approach. *International Journal of Solids and Structures*, *274*, 112199. https://doi.org/https://doi.org/10.1016/j.ijsolstr.2023.112199

El Ouazani Tuhami, A. (2022). *Étude et modélisation de la rupture ductile en conditions de chargement complexes : Application à l'endommagement en cisaillement* (Thèse de doctorat) [Soutenance le 12/05/2022]. Université Paris sciences et lettres. Paris, France.

Eldahshan, H., Bouchard, P. O., Alves, J., Perchat, E., & Pino Munoz, D. (2021). Phase field modeling of ductile fracture at large plastic strains using adaptive isotropic remeshing. *Computational Mechanics*, *67*, 763–783. https://doi.org/10.1007/s00466-020-01962-7

Elguedj, T., Bazilevs, Y., Calo, V. M., & Hughes, T. J. R. (2007). *B and f projection methods for nearly incompressible linear and nonlinear elasticity and plasticity using higher-order nurbs elements* (tech. rep.). Defense Technical Information Center. Fort Belvoir, VA. https://doi.org/10.21236/ADA478310

Elguedj, T., Bazilevs, Y., Calo, V., & Hughes, T. (2008). B and f projection methods for nearly incompressible linear and non-linear elasticity and plasticity using higher-order nurbs elements. *Computer Methods in Applied Mechanics and Engineering*, *197*(33), 2732–2762. https://doi.org/https://doi.org/10.1016/j.cma.2008.01.012

Enakoutsa, K., Leblond, J., & Perrin, G. (2007). Numerical implementation and assessment of a phenomenological nonlocal model of ductile rupture. *Computer Methods in Applied Mechanics and Engineering*, *196*(13), 1946–1957. https://doi.org/https://doi.org/10.1016/j.cma.2006.10.003

Engelen, R. A., Geers, M. G., & Baaijens, F. P. (2003). Nonlocal implicit gradient-enhanced elasto-plasticity for the modelling of softening behaviour. *International Journal of Plasticity*, *19*(4), 403–433. https://doi.org/https://doi.org/10.1016/S0749-6419(01)00042-0

Eringen, A., & Edelen, D. (1972). On nonlocal elasticity. *International Journal of Engineering Science*, *10*(3), 233–248. https://doi.org/https://doi.org/10.1016/0020-7225(72)90039-0

Ernst, H., Paris, P., & Landes, J. (1981). Estimations on J-Integral and Tearing Modulus T from a Single Specimen Test Record. In *Fracture Mechanics*. ASTM International. https://doi.org/10.1520/STP28814S

Faleskog, J., Gao, X., & Shih, C. F. (1998). Cell model for nonlinear fracture analysis – i. micromechanics calibration. *International Journal of Fracture*, *89*, 355–373. https://doi.org/10.1023/A:1007421420901

Feaugas, X., & Delafosse, D. (2019). 9 - hydrogen and crystal defects interactions: Effects on plasticity and fracture. In C. Blanc & I. Aubert (Eds.), *Mechanics - microstructure - corrosion coupling* (pp. 199–222). Elsevier. https://doi.org/https://doi.org/10.1016/B978-1-78548-309-7.50009-0

Feld-Payet, S., Besson, J., & Feyel, F. (2011). Finite element analysis of damage in ductile structures using a nonlocal model combined with a three-field formulation. *International Journal of Damage Mechanics*, *20*(5), 655–680. https://doi.org/10.1177/1056789511405935

Feld-Payet, S., Chiaruttini, V., Besson, J., & Feyel, F. (2015). A new marching ridges algorithm for crack path tracking in regularized media. *International Journal of Solids and Structures*, *71*, 57–69. https://doi.org/https://doi.org/10.1016/j.ijsolstr.2015.04.043

Ferreira, P., Robertson, I., & Birnbaum, H. (1999). Hydrogen effects on the character of dislocations in high-purity aluminum. *Acta Materialia*, *47*(10), 2991–2998. https://doi.org/https://doi.org/10.1016/S1359-6454(99)00156-1

Fidelle, J., Broudeur, R., Pirrovani, C., & Roux, C. (1974). Disk pressure technique. In *Special technical publication 543* (pp. 34–47). American Society for Testing; Materials.

Fidelle, J., Broudeur, R., & Roux, C. (1975). Hydrogen gas embrittlement under the influence of strain rate, temperature and thickness effects: Relationship with delayed failure. *Proceedings of the International Conference on the Effect of Hydrogen on Materials*.

Foerch, R., Besson, J., Cailletaud, G., & Pilvin, P. (1997). Polymorphic constitutive equations in finite element codes. *Computer Methods in Applied Mechanics and Engineering*, *141*(3), 355–372. https://doi.org/https://doi.org/10.1016/S0045-7825(96)01111-5

Forest, S. (2009). Micromorphic approach for gradient elasticity, viscoplasticity, and damage. *Journal of Engineering Mechanics*, *135*(3), 117–131. https://doi.org/10.1061/(ASCE)0733-9399(2009)135:3(117)

Forest, S. (2018). Micromorphic approach to materials with internal length. In H. Altenbach & A. Öchsner (Eds.), *Encyclopedia of continuum mechanics* (pp. 1–11). Springer Berlin Heidelberg. https://doi.org/10.1007/978-3-662-53605-6_150-1

Francfort, G., & Marigo, J.-J. (1998). Revisiting brittle fracture as an energy minimization problem. *Journal of the Mechanics and Physics of Solids*, *46*(8), 1319–1342. https://doi.org/https://doi.org/10.1016/S0022-5096(98)00034-9

Fried, I., & Malkus, D. S. (1975). Finite element mass matrix lumping by numerical integration with no convergence rate loss. *International Journal of Solids and Structures*, *11*(4), 461–466. https://doi.org/https://doi.org/10.1016/0020-7683(75)90081-5

Gallon, N. (2021). *Hydrogen pipelines - design and materials challenges and mitigations* (Tech. rep.). N. Gallon.

Gangloff, R. P. (2008). Critical issues in hydrogen assisted cracking of structural alloys. In S. Shipilov, R. Jones, J.-M. Olive, & R. Rebak (Eds.), *Environment-induced cracking of materials* (pp. 141–165). Elsevier. https://doi.org/https://doi.org/10.1016/B978-008044635-6.50015-7

García-Macías, E., Harris, Z., & Martínez-Pañeda, E. (2024). Tds simulator: A matlab app to model temperature-programmed hydrogen desorption [In Press]. *International Journal of Hydrogen Energy*.

Gerberich, W., Marsh, P., & Hoehn, J. (2013). Hydrogen induced cracking mechanisms - are there critical experiments? *Hydrogen Effects in Materials*, 539–554. https://doi.org/10.1002/9781118803363.ch47

Germain, P., Nguyen, Q., & Suquet, P. (1983). Continuum thermodynamics ASME. *Journal of Applied Mechanics*, *105*, 1011–1020. https://doi.org/10.1115/1.3167184

Guo, L., Su, J., Wang, Z., Shi, J., Guan, X., Cao, W., & Ou, Z. (2024). Hydrogen safety: An obstacle that must be overcome on the road towards future hydrogen economy. *International Journal of Hydrogen Energy*, *51*, 1055–1078. https://doi.org/https://doi.org/10.1016/j.ijhydene.2023.08.248

Gurson, A. L. (1977). Continuum Theory of Ductile Rupture by Void Nucleation and Growth: Part I—Yield Criteria and Flow Rules for Porous Ductile Media. *Journal of Engineering Materials and Technology*, *99*(1), 2–15. https://doi.org/10.1115/1.3443401

Hahn, G. T., & Rosenfield, A. R. (1975). Metallurgical factors affecting fracture toughness of aluminum alloys. *Metallurgical Transactions A*, *6*, 653–668. https://doi.org/10.1007/BF02672285

Herrmann, L. R. (2012). Elasticity equations for incompressible and nearly incompressible materials by a variational theorem. *Journal of Applied Mechanics*. https://doi.org/10.2514/3.3277

Hirth, J. P. (1980). Effects of hydrogen on the properties of iron and steel. *Metallurgical Transactions A*, *11*, 861–890. https://doi.org/10.1007/BF02654700

Hoagland, R. G., & Heinisch, H. L. (1992). An atomic simulation of the influence of hydrogen on the fracture behavior of nickel. *Journal of Materials Research*, *7*, 2080–2088. https://doi.org/https://doi.org/10.1557/JMR.1992.2080

Huespe, A., Needleman, A., Oliver, J., & Sánchez, P. (2009). A finite thickness band method for ductile fracture analysis. *International Journal of Plasticity*, *25*(12), 2349–2365. https://doi.org/https://doi.org/10.1016/j.ijplas.2009.03.005

Huespe, A., Needleman, A., Oliver, J., & Sánchez, P. (2012). A finite strain, finite band method for modeling ductile fracture. *International Journal of Plasticity*, *28*(1), 53–69. https://doi.org/https://doi.org/10.1016/j.ijplas.2011.05.010

Hughes, T. J. R. (2012). *The finite element method: Linear static and dynamic finite element analysis*. Courier Corporation.

Hughes, T. J. R. (1980). Generalization of selective integration procedures to anisotropic and nonlinear media. *International Journal for Numerical Methods in Engineering*, *15*, 1419–1430. https://doi.org/10.1002/nme.1620150914

Hütter, G., Linse, T., Mühlich, U., & Kuna, M. (2013). Simulation of ductile crack initiation and propagation by means of a non-local gurson-model. *International Journal of Solids and Structures*, *50*(5), 662–671. https://doi.org/https://doi.org/10.1016/j.ijsolstr.2012.10.031

Hwang, C., & Bernstein, I. (1986). Dislocation transport of hydrogen in iron single crystals. *Acta Metallurgica*, *34*(6), 1001–1010. https://doi.org/https://doi.org/10.1016/0001-6160(86)90209-9

International Organization for Standardization. (2023). *ISO/DIS 11114: Gas Cylinders — Compatibility of Cylinder and Valve Materials with Gas Contents*.

Javani, H. R., Peerlings, R. H. J., & Geers, M. G. D. (2016). Three-dimensional finite element modeling of ductile crack initiation and propagation. *Advances in Modeling and Simulation in Engineering Sciences*, *3*, 19. https://doi.org/10.1186/s40323-016-0071-y

Jemblie, L., Olden, V., & Akselsen, O. (2017). A coupled diffusion and cohesive zone modelling approach for numerically assessing hydrogen embrittlement of steel structures. *International Journal of*

Hydrogen Energy, *42*(16), 11980–11995. https://doi.org/https://doi.org/10.1016/j.ijhydene.2017.02.211

Johnson, W. H., & Thomson, W. (1875). Ii. on some remarkable changes produced in iron and steel by the action of hydrogen and acids. *Proceedings of the Royal Society of London*, *23*(156-163), 168–179. https://doi.org/10.1098/rspl.1874.0024

Kachanov, L. M. (1958). Time of the rupture process under creep conditions. *Isv. Akad. Nauk. SSR. Otd Tekh. Nauk.*, *8*, 26–31.

Kailasam, M., & Castañeda, P. (1998). A general constitutive theory for linear and nonlinear particulate media with microstructure evolution. *Journal of the Mechanics and Physics of Solids*, *46*(3), 427–465. https://doi.org/https://doi.org/10.1016/S0022-5096(97)00095-1

Kasper, E. P., & Taylor, R. L. (2000). A mixed-enhanced strain method part ii: Geometrically nonlinear problems. *Computers & Structures*, *75*, 251–260. https://doi.org/10.1016/S0045-7949(99)00135-2

Kasuya, T., Yokobori, A. T., Ozeki, G., Ohmi, T., & Enoki, M. (2021). Modelling of hydrogen diffusion in a weld cold cracking test: Part 1, experimental determinations of apparent diffusion coefficient and boundary condition. *ISIJ International*, *61*(4), 1245–1253. https://doi.org/10.2355/isijinternational.isijint-2020-523

Kholtobina, A. S., Pippan, R., Romaner, L., Scheiber, D., Ecker, W., & Razumovskiy, V. I. (2020). Hydrogen trapping in bcc iron. *Materials*, *13*(10). https://doi.org/10.3390/ma13102288

Knott, J. F. (1994). Fracture toughness and hydrogen-assisted crack growth in engineering alloys. In A. W. Thompson & N. R. Moody (Eds.), *Environment-induced cracking of metals* (pp. 901–916). Wiley. https://doi.org/10.1002/9781118803363.ch36

Koplik, J., & Needleman, A. (1988). Void growth and coalescence in porous plastic solids. *International Journal of Solids and Structures*, *24*(8), 835–853. https://doi.org/10.1016/0020-7683(88)90051-0

Krom, A., Koers, R., & Bakker, A. (1999). Hydrogen transport near a blunting crack tip. *Journal of the Mechanics and Physics of Solids*, *47*(4), 971–992. https://doi.org/https://doi.org/10.1016/S0022-5096(98)00064-7

Kumar, K., Madhusoodanan, K., & Singh, R. (2017). Miniature test techniques for life management of operating equipment. *Nuclear Engineering and Design*, *323*, 345–358. https://doi.org/10.1016/j.nucengdes.2017.03.007

Kumnick, A., & Johnson, H. (1980). Deep trapping states for hydrogen in deformed iron. *Acta Metallurgica*, *28*(1), 33–39. https://doi.org/https://doi.org/10.1016/0001-6160(80)90038-3

Kurkela, M., & Latanision, R. (1979). The effect of plastic deformation on the transport of hydrogen in nickel. *Scripta Metallurgica*, *13*(10), 927–932. https://doi.org/https://doi.org/10.1016/0036-9748(79)90322-3

Laureys, A., Depraetere, R., Cauwels, M., Depover, T., Hertelé, S., & Verbeken, K. (2022). Use of existing steel pipeline infrastructure for gaseous hydrogen storage and transport: A review of factors affecting hydrogen induced degradation. *Journal of Natural Gas Science and Engineering*, *101*, 104534. https://doi.org/https://doi.org/10.1016/j.jngse.2022.104534

Laveissiere, B., Philippart, J., & Pagetti, J. (1991). Etude de la diffusion de l'hydrogene atomique dans le fer et le platine en milieu acide. *Electrochimica Acta*, *36*(3), 615–620. https://doi.org/https://doi.org/10.1016/0013-4686(91)85148-Z

Leclerc, J., Nguyen, V., Pardoen, T., & Noels, L. (2020). A micromechanics-based non-local damage to crack transition framework for porous elastoplastic solids. *International Journal of Plasticity*, *127*, 102631. https://doi.org/https://doi.org/10.1016/j.ijplas.2019.11.010

Lemaitre, J., & Desmorat, R. (2005). *Engineering damage mechanics*. Springer.

Lemaitre, J., Desmorat, R., & Sauzay, M. (2000). Anisotropic damage law of evolution. *European Journal of Mechanics - A/Solids*, *19*(2), 187–208. https://doi.org/https://doi.org/10.1016/S0997-7538(00)00161-3

Lemaître, J. (1985). A continuous damage mechanics model for ductile fracture. *Journal of Engineering Materials and Technology*, *107*(1), 83–89. https://doi.org/10.1115/1.3225775

Li, H., Fu, M., Lu, J., & Yang, H. (2011). Ductile fracture: Experiments and computations. *International Journal of Plasticity*, *27*(2), 147–180. https://doi.org/https://doi.org/10.1016/j.ijplas.2010.04.001

Li, M., Chaouadi, R., Uytdenhouwen, I., Pardoen, T., & Bonny, G. (2023). The effect of loss of constraint on the initiation of ductile fracture in a mini-CT. *Proceedings of the ASME Pressure Vessels & Piping Conference*, V001T01A035. https://doi.org/10.1115/PVP2023-106216

Li, X., Ma, X., Zhang, J., & et al. (2020). Review of hydrogen embrittlement in metals: Hydrogen diffusion, hydrogen characterization, hydrogen embrittlement mechanism and prevention. *Acta Metallurgica Sinica (English Letters)*, *33*(6), 759–773. https://doi.org/10.1007/s40195-020-01039-7

Lin, M., Yu, H., Ding, Y., Wang, G., Olden, V., Alvaro, A., He, J., & Zhang, Z. (2022a). A predictive model unifying hydrogen enhanced plasticity and decohesion. *Scripta Materialia*, *215*, 114707. https://doi.org/https://doi.org/10.1016/j.scriptamat.2022.114707

Lin, M., Yu, H., Ding, Y., Wang, G., Olden, V., Alvaro, A., He, J., & Zhang, Z. (2022b). Simulation of ductile-to-brittle transition combining complete gurson model and czm with application to hydrogen embrittlement. *Engineering Fracture Mechanics*, *268*, 108511. https://doi.org/https://doi.org/10.1016/j.engfracmech.2022.108511

Linse, T., Hütter, G., & Kuna, M. (2012). Simulation of crack propagation using a gradient-enriched ductile damage model based on dilatational strain [Cracks in Microstructures and Engineering Components]. *Engineering Fracture Mechanics*, *95*, 13–28. https://doi.org/https://doi.org/10.1016/j.engfracmech.2012.07.004

Liu, Q., Atrens, A. D., Shi, Z., Verbeken, K., & Atrens, A. (2014). Determination of the hydrogen fugacity during electrolytic charging of steel. *Corrosion Science*, *87*, 239–258. https://doi.org/https://doi.org/10.1016/j.corsci.2014.06.033

Looney, C. P., Hagan, Z. M., Connolly, M. J., Bradley, P. E., Slifka, A. J., & Amaro, R. L. (2020). Modelling the test methods used to determine material compatibility for hydrogen pressure vessel service. *International Journal of Fatigue*, *132*, 105339. https://doi.org/https://doi.org/10.1016/j.ijfatigue.2019.105339

Lopes Pinto, D., El Ouazani Tuhami, A., Osipov, N., Madi, Y., & Besson, J. (2023). Simulation of hydrogen embrittlement of steel using mixed nonlocal finite elements. *European Journal of Mechanics - A/Solids*, 105116. https://doi.org/https://doi.org/10.1016/j.euromechsol.2023.105116

Lord, J. D., Roebuck, B., Morrell, R., & Lube, T. (2010). 25 year perspective aspects of strain and strength measurement in miniaturised testing for engineering metals and ceramics. *Mater. Sci. Technol.*, *26*(2), 127–148. https://doi.org/10.1179/026708309X12584564052012

Lorentz, E. (2005). Ill-posed boundary conditions encountered in 3d and plate finite element simulations. *Finite Elements in Analysis and Design*, *41*(11), 1105–1117. https://doi.org/https://doi.org/10.1016/j.finel.2005.01.002

Lorentz, E., & Andrieux, S. (1999). A variational formulation for nonlocal damage models. *International Journal of Plasticity*, *15*(2), 119–138. https://doi.org/https://doi.org/10.1016/S0749-6419(98)00057-6

Lorentz, E., Besson, J., & Cano, V. (2008). Numerical simulation of ductile fracture with the rousselier constitutive law. *Computer Methods in Applied Mechanics and Engineering*, *197*(21), 1965–1982. https://doi.org/https://doi.org/10.1016/j.cma.2007.12.015

Lorentz, E., & Godard, V. (2011). Gradient damage models: Toward full-scale computations. *Computer Methods in Applied Mechanics and Engineering*, *200*(21), 1927–1944. https://doi.org/https://doi.org/10.1016/j.cma.2010.06.025

Lu, H., Guo, B., Chen, X., Yao, J., & Liu, B. (2024). Numerical investigation on leakage and diffusion characteristics of buried hydrogen-blended natural gas pipelines. *International Journal of Hydrogen Energy*, *59*, 1491–1506. https://doi.org/10.1016/j.ijhydene.2024.02.075

Luu, T. T. (2006). *Déchirure ductile des aciers à haute résistance pour gazoducs (X100)* (Theses). École Nationale Supérieure des Mines de Paris. https://pastel.hal.science/tel-00142118

Lynch, S. (1979). Hydrogen embrittlement and liquid-metal embrittlement in nickel single crystals. *Scripta Metallurgica*, *13*(11), 1051–1056. https://doi.org/https://doi.org/10.1016/0036-9748(79)90202-3

Lynch, S. (2011). *Hydrogen embrittlement (he) phenomena and mechanisms* (V. Raja & T. Shoji, Eds.). Woodhead Publishing. https://doi.org/https://doi.org/10.1533/9780857093769.1.90

Madi, Y., Belhadj, C., van Gorp, A., Dodelin, L., Polo, M., Goti, R., Soret, C., Besson, J., & Dupoiron, F. (2021). Caractérisation de la température de transition et de la ténacité sur prélèvements quasi non destructifs. *Symposium Scientifique Et Technique Esope, FCTM-ESOPE*. https://hal.science/hal-03691096

Madi, Y., Santana, L., Belkacemi, S., Farrugia, V., Meddour, A., Marchais, P.-J., Bertin, M., & Furtado, J. (2024). Mechanical characterization of hydrogen embrittlement in a gaseous environment: An innovative test setup using sub-size specimens. *Engineering Failure Analysis*, *162*, 108362. https://doi.org/https://doi.org/10.1016/j.engfailanal.2024.108362

Madi, Y., Shinohara, Y., & Besson, J. (2020). Effect of prestrain on ductility and toughness in a high-strength line pipe steel. *International Journal of Fracture*, *224*, 15–29. https://doi.org/10.1007/s10704-020-00442-6

Maker, B. (1995). *Nike3d: A non-linear, implicit, three-dimensional finite element code for solid and structural mechanics* (tech. rep. UCRL-MA-105268 Rev. 1). Lawrence Livermore National Laboratory, University of California, Livermore.

Marchi, C. S., Somerday, B., & Robinson, S. (2007). Permeability, solubility and diffusivity of hydrogen isotopes in stainless steels at high gas pressures. *International Journal of Hydrogen Energy*, *32*(1), 100–116. https://doi.org/https://doi.org/10.1016/j.ijhydene.2006.05.008

Marini, B., Mudry, F., & Pineau, A. (1985). Experimental study of cavity growth in ductile rupture. *Engineering Fracture Mechanics*, *22*(6), 989–996. https://doi.org/https://doi.org/10.1016/0013-7944(85)90038-4

Martin, M., Connolly, M., DelRio, F., & Slifka, A. (2020). Hydrogen embrittlement in ferritic steels. *Applied Physics Reviews*, *7*(4), 10.1063/5.0012851. https://doi.org/10.1063/5.0012851

Martínez-Pañeda, E., Golahmar, A., & Niordson, C. F. (2018). A phase field formulation for hydrogen assisted cracking. *Computer Methods in Applied Mechanics and Engineering*, *342*, 742–761. https://doi.org/https://doi.org/10.1016/j.cma.2018.07.021

Martínez-Pañeda, E., Harris, Z. D., Fuentes-Alonso, S., Scully, J. R., & Burns, J. T. (2020). On the suitability of slow strain rate tensile testing for assessing hydrogen embrittlement susceptibility. *Corrosion Science*, *163*, 108291. https://doi.org/https://doi.org/10.1016/j.corsci.2019.108291

Martínez-Pañeda, E., Niordson, C. F., & Gangloff, R. P. (2016). Strain gradient plasticity-based modeling of hydrogen environment assisted cracking. *Acta Materialia*, *117*, 321–332. https://doi.org/https://doi.org/10.1016/j.actamat.2016.07.022

Mazière, M., & Forest, S. (2015). Strain gradient plasticity modeling and finite element simulation of lüders band formation and propagation. *Continuum Mechanics and Thermodynamics*, *27*(1-2), 83–104. https://doi.org/10.1007/s00161-013-0331-8

McNabb, A., & Foster, P. (1963). A new analysis of diffusion of hydrogen in iron and ferritic steels. *Transactions of the Metallurgical Society of AIME*, *227*(3), 618–627.

Mediavilla, J., Peerlings, R., & Geers, M. (2006). A nonlocal triaxiality-dependent ductile damage model for finite strain plasticity. *Computer Methods in Applied Mechanics and Engineering*, *195*(33), 4617–4634. https://doi.org/https://doi.org/10.1016/j.cma.2005.10.001

Meibom, P., & Karlsson, K. (2010). Role of hydrogen in future north european power system in 2060. *International Journal of Hydrogen Energy*, *35*(5), 1853–1863. https://doi.org/https://doi.org/10.1016/j.ijhydene.2009.12.161

Miehe, C., Aldakheel, F., & Raina, A. (2016). Phase field modeling of ductile fracture at finite strains: A variational gradient-extended plasticity-damage theory. *International Journal of Plasticity*, *84*, 1–32. https://doi.org/https://doi.org/10.1016/j.ijplas.2016.04.011

Miura, N., & Soneda, N. (2012). Evaluation of fracture toughness by master curve approach using miniature C(T) specimens. *Journal of Pressure Vessel Technology*, *134*(2). https://doi.org/10.1115/1.4005751

Moran, B., Ortiz, M., & Shih, C. F. (1990). Formulation of implicit finite element methods for multiplicative finite deformation plasticity. *International Journal for Numerical Methods in Engineering*, *29*(3), 803–822. https://doi.org/10.1002/nme.1620290304

Moro, I., Briottet, L., Lemoine, P., Andrieu, E., Blanc, C., & Odemer, G. (2010). Hydrogen embrittlement susceptibility of a high strength steel x80. *Materials Science and Engineering: A*, *527*(27), 7252–7260. https://doi.org/https://doi.org/10.1016/j.msea.2010.07.027

Moro, I. (2009). *Fragilisation par l'hydrogène gazeux d'un acier ferrito-perlitique de grade API X80* (Doctoral dissertation 2009INPT032G). Institut National Polytechnique de Toulouse - INPT. https://theses.hal.science/tel-04382243

Motarjemi, A. K., Koçak, M., & Ventzke, V. (2002). Mechanical and fracture characterization of a bi-material steel plate. *Int. J. Press. Vessels Pip.*, *79*(3), 181–191. https://doi.org/10.1016/S0308-0161(02)00012-1

Murali, J., Adler, T., Sudarshan, T., Louthan, M., & McNitt, R. (1980). Testing for hydrogen—a-106 steel compatibility. *International Journal of Hydrogen Energy*, *5*(6), 597–608. https://doi.org/https://doi.org/10.1016/0360-3199(80)90038-5

Nagao, A., Kuramoto, S., & Kanno, M. (1998). Hydrogen microprint technique applied to observe impurity hydrogen in aluminum during deformation. In B. Mishra (Ed.), *Proceedings of the 1998 tms annual meeting* (pp. 867–875). TMS.

Nagumo, M. (2004). Hydrogen related failure of steels – a new aspect. *Materials Science and Technology*, *20*(8), 940–950. https://doi.org/10.1179/026708304225019687

Nagumo, M., Nakamura, M., & Taka, K. (2001). Hydrogen thermal desorption relevant to delayed-fracture susceptibility of high-strength steels. *Metallurgical and Materials Transactions A*, *32*, 339–347. https://doi.org/https://doi.org/10.1007/s11661-001-0265-9

Nahshon, K., & Hutchinson, J. (2008). Modification of the gurson model for shear failure. *European Journal of Mechanics - A/Solids*, *27*(1), 1–17. https://doi.org/https://doi.org/10.1016/j.euromechsol.2007.08.002

Nanninga, N. E., Somerday, B. P., Piraino, A. D., & Fekete, J. M. (2012). Comparison of hydrogen embrittlement in three pipeline steels in high pressure gaseous hydrogen environments. *Corrosion Science*, *59*, 1–9.

Newman, J., & Shreir, L. (1969). Role of hydrides in hydrogen entry into steel from solutions containing promoters. *Corrosion Science*, *9*(8), 631–641. https://doi.org/https://doi.org/10.1016/S0010-938X(69)80117-4

Nguyen, T. T., Tak, N., Park, J., Nahm, S. H., & Beak, U. B. (2020). Hydrogen embrittlement susceptibility of x70 pipeline steel weld under a low partial hydrogen environment. *International Journal of Hydrogen Energy*, *45*(43), 23739–23753. https://doi.org/https://doi.org/10.1016/j.ijhydene.2020.06.199

Nguyen, V., Pardoen, T., & Noels, L. (2020). A nonlocal approach of ductile failure incorporating void growth, internal necking, and shear dominated coalescence mechanisms. *Journal of the Mechanics and Physics of Solids*, *137*, 103891. https://doi.org/https://doi.org/10.1016/j.jmps.2020.103891

Nielsen, K. L., & Tvergaard, V. (2009). Effect of a shear modified gurson model on damage development in a fsw tensile specimen. *International Journal of Solids and Structures*, *46*(3), 587–601. https://doi.org/https://doi.org/10.1016/j.ijsolstr.2008.09.011

Olden, V., Thaulow, C., Johnsen, R., Ostby, E., & Berstad, T. (2008). Application of hydrogen influenced cohesive laws in the prediction of hydrogen induced stress cracking in 25%cr duplex stainless steel. *Engineering Fracture Mechanics*, *75*(8), 2333–2351. https://doi.org/https://doi.org/10.1016/j.engfracmech.2007.09.003

Ono, H., Kasada, R., & Kimura, A. (2004). Specimen size effects on fracture toughness of jlf-1 reduced-activation ferritic steel. *Journal of Nuclear Materials*, *329-333*, 1117–1121. https://doi.org/https://doi.org/10.1016/j.jnucmat.2004.04.034

Oriani, R. (1970). The diffusion and trapping of hydrogen in steel. *Acta Metallurgica*, *18*(1), 147–157. https://doi.org/https://doi.org/10.1016/0001-6160(70)90078-7

Peerlings, R. H. J., de Borst, R., Brekelmans, W. A. M., de Vree, J. H. P., & Spee, I. (1996). Some observations on localisation in non-local and gradient damage models. *European Journal of Mechanics. A, Solids*, *15*, 937–953.

Peerlings, R., Poh, L., & Geers, M. (2012). An implicit gradient plasticity–damage theory for predicting size effects in hardening and softening [Cracks in Microstructures and Engineering Components]. *Engineering Fracture Mechanics*, *95*, 2–12. https://doi.org/https://doi.org/10.1016/j.engfracmech.2011.12.016

Petit, T., Besson, J., Ritter, C., Colas, K., Helfen, L., & Morgeneyer, T. F. (2019). Effect of hardening on toughness captured by stress-based damage nucleation in 6061 aluminum alloy. *Acta Materialia*, *180*, 349–365. https://doi.org/https://doi.org/10.1016/j.actamat.2019.08.055

Pfeil, L. (1926). The effect of occluded hydrogen on the tensile strength of iron. *Proc. R. Soc. (London)*, *A112*, 128–195. https://doi.org/https://doi.org/10.1098/rspa.1926.0103

Pietro, D. A. D., Ern, A., & Lemaire, S. (2014). An arbitrary-order and compact-stencil discretization of diffusion on general meshes based on local reconstruction operators. *Comput. Methods Appl. Math.*, *14*, 461–472. https://doi.org/10.1515/cmam-2014-0018

Pijaudier-Cabot, G., & Bažant, Z. P. (1987). Nonlocal damage theory. *Journal of Engineering Mechanics*, *113*(10), 1512–1533. https://doi.org/10.1061/(ASCE)0733-9399(1987)113:10(1512)

Pineau, A. (2006). Development of the local approach to fracture over the past 25 years: Theory and applications. *International Journal of Fracture*, *138*(1), 139–166. https://doi.org/10.1007/s10704-006-0035-1

Pleshivtseva, Y., Derevyanov, M., Pimenov, A., & Rapoport, A. (2023). Comprehensive review of low carbon hydrogen projects towards the decarbonization pathway. *International Journal of Hydrogen Energy*, *48*(10), 3703–3724. https://doi.org/https://doi.org/10.1016/j.ijhydene.2022.10.209

Prat, F., Besson, J., Grange, M., et al. (1998). Behavior and rupture of hydrided zircaloy-4 tubes and sheets. *Metallurgical and Materials Transactions A*, *29*, 1643–1651. https://doi.org/10.1007/s11661-998-0087-0

Rice, J. R. (1968). A path independent integral and the approximate analysis of strain concentration by notches and cracks. *Journal of Applied Mechanics*, *35*(2), 379–386. https://doi.org/10.1115/1.3601206

Rice, J. R. (1976). The localisation of plastic deformation. In W. T. Koiter (Ed.), *Proc. 14th int. conf. theoretical and applied mechanics*. North-Holland.

Rice, J. R. (1980). The mechanics of earthquake rupture. *Proceedings of the International School of Physics "Enrico Fermi"*, 555–649.

Rice, J., & Tracey, D. (1969). On the ductile enlargement of voids in triaxial stress fields∗. *Journal of the Mechanics and Physics of Solids*, *17*(3), 201–217. https://doi.org/https://doi.org/10.1016/0022-5096(69)90033-7

Riks, E. (1979). An incremental approach to the solution of snapping and buckling problems. *International Journal of Solids and Structures*, *15*(7), 529–551. https://doi.org/https://doi.org/10.1016/0020-7683(79)90081-7

Robertson, I., Sofronis, P., Nagao, A., & et al. (2015). Hydrogen embrittlement understood. *Metallurgical and Materials Transactions B*, *46*, 1085–1103. https://doi.org/10.1007/s11663-015-0325-y

Rousselier, G. (1987). Ductile fracture models and their potential in local approach of fracture. *Nuclear Engineering and Design*, *105*(1), 97–111. https://doi.org/https://doi.org/10.1016/0029-5493(87)90234-2

Rousselier, G. (2001). Dissipation in porous metal plasticity and ductile fracture. *Journal of the Mechanics and Physics of Solids*, *49*(8), 1727–1746. https://doi.org/https://doi.org/10.1016/S0022-5096(01)00013-8

Rudnicki, J., & Rice, J. (1975). Conditions for the localization of deformation in pressure-sensitive dilatant materials. *Journal of the Mechanics and Physics of Solids*, *23*(6), 371–394. https://doi.org/https://doi.org/10.1016/0022-5096(75)90001-0

Ruggieri, C., & Dodds, R. H. (1996). A transferability model for brittle fracture including constraint and ductile tearing effects: A probabilistic approach. *International Journal of Fracture*, *79*, 309–340. https://doi.org/10.1007/BF00018594

Santana, L., Pinto, D. L., Osipov, N., Furtado, J., Bourguignon, F., Marchais, P.-J., Madi, Y., & Besson, J. (2024). Study of hydrogen embrittlement in steels using modified pressurized disks. *International Journal of Hydrogen Energy*, *88*, 498–514. https://doi.org/https://doi.org/10.1016/j.ijhydene.2024.09.165

Scheider, I., Brocks, W., & Cornec, A. (2004). Procedure for the determination of true stress-strain curves from tensile tests with rectangular cross-section specimens. *J. Engng Mater. Technol.*, *126*(1), 70–76.

Scherer, J.-M., Phalke, V., Besson, J., Forest, S., Hure, J., & Tanguy, B. (2020). Lagrange multiplier based vs micromorphic gradient-enhanced rate-(in)dependent crystal plasticity modelling and simulation. *Computer Methods in Applied Mechanics and Engineering*, *372*, 113426. https://doi.org/https://doi.org/10.1016/j.cma.2020.113426

Scibetta, M., Lucon, E., & van Walle, E. (2002). Optimum use of broken charpy specimens from surveillance programs for the application of the master curve approach. *International Journal of Fracture*, *116*, 231–244. https://doi.org/10.1023/A:1020165900918

Seupel, A., Hütter, G., & Kuna, M. (2020). On the identification and uniqueness of constitutive parameters for a non-local gtn-model. *Engineering Fracture Mechanics*, *229*, 106817. https://doi.org/https://doi.org/10.1016/j.engfracmech.2019.106817

Shinohara, Y., Madi, Y., & Besson, J. (2016). Anisotropic ductile failure of a high-strength line pipe steel. *International Journal of Fracture*, *197*, 127–145. https://doi.org/10.1007/s10704-015-0054-x

Shinohara, Y., Besson, J., & Madi, Y. (2012). Anisotropic damage behavior in high-strength line pipe steels. *International Journal of Offshore and Polar Engineering*, *22*(1), 83–89. https://www.scopus.com/inward/record.uri?eid=2-s2.0-84863922046&partnerID=40&md5=0d4740df0b8ff594212f7ffff26005eb

Shokeir, Z., Besson, J., Belhadj, C., Petit, T., & Madi, Y. (2022). Edge tracing technique to study post-necking behavior and failure in al alloys and anisotropic plasticity in line pipe steels. *Fatigue & Fracture of Engineering Materials & Structures*, *45*. https://doi.org/10.1111/ffe.13754

Sicsic, P., Marigo, J.-J., & Maurini, C. (2014). Initiation of a periodic array of cracks in the thermal shock problem: A gradient damage modeling. *Journal of the Mechanics and Physics of Solids*, *63*, 256–284. https://doi.org/https://doi.org/10.1016/j.jmps.2013.09.003

Simo, J., & Taylor, R. (1991). Quasi-incompressible finite elasticity in principal stretches: Continuum basis and numerical algorithms. *Computer Methods in Applied Mechanics and Engineering*, *85*(3), 273–310. https://doi.org/10.1016/0045-7825(91)90100-K

Simo, J., Taylor, R., & Pister, K. (1985). Variational and projection methods for the volume constraint in finite deformation elasto-plasticity. *Computer Methods in Applied Mechanics and Engineering*, *51*(1), 177–208. https://doi.org/https://doi.org/10.1016/0045-7825(85)90033-7

Sofronis, P., Liang, Y., & Aravas, N. (2001). Hydrogen induced shear localization of the plastic flow in metals and alloys. *European Journal of Mechanics - A/Solids*, *20*(6), 857–872. https://doi.org/https://doi.org/10.1016/S0997-7538(01)01179-2

Sofronis, P., & McMeeking, R. (1989). Numerical analysis of hydrogen transport near a blunting crack tip. *Journal of the Mechanics and Physics of Solids*, *37*(3), 317–350. https://doi.org/https://doi.org/10.1016/0022-5096(89)90002-1

Standard test method for linear-elastic plane-strain fracture toughness K_{IC} of metallic materials [ASTM E399-22]. (2022). ASTM International. https://www.astm.org/e0399-22.html

Standard test method for measurement of fracture toughness [ASTM E1820-23]. (2023). ASTM International. https://www.astm.org/e1820-23.html

Steglich, D., & Brocks, W. (1997). Micromechanical modelling of the behaviour of ductile materials including particles. *Computational Materials Science*, *9*(1), 7–17. https://doi.org/https://doi.org/10.1016/S0927-0256(97)00053-0

Steglich, D., Siegmund, T., & Brocks, W. (1999). Micromechanical modeling of damage due to particle cracking in reinforced metals. *Computational Materials Science*, *16*(1), 404–413. https://doi.org/https://doi.org/10.1016/S0927-0256(99)00083-X

Steigerwald, E. (1969). Plane strain fracture toughness of high strength materials. *Engineering Fracture Mechanics*, *1*(3), 473–494. https://doi.org/https://doi.org/10.1016/0013-7944(69)90006-X

Sumpter, J. (1993). An Experimental Investigation of the T Stress Approach. In *Constraint Effects in Fracture*. ASTM International. https://doi.org/10.1520/STP18042S

Tabata, T., & Birnbaum, H. (1983). Direct observations of the effect of hydrogen on the behavior of dislocations in iron. *Scripta Metallurgica*, *17*(7), 947–950. https://doi.org/https://doi.org/10.1016/0036-9748(83)90268-5

Tanguy, B., Luu, T., Perrin, G., Pineau, A., & Besson, J. (2008). Plastic and damage behaviour of a high strength x100 pipeline steel: Experiments and modelling. *International Journal of Pressure Vessels and Piping*, *85*(5), 322–335. https://doi.org/https://doi.org/10.1016/j.ijpvp.2007.11.001

Tanguy, B. (2001). *Modélisation de l'essai charpy par l'approche locale de la rupture : Application au cas de l'acier 16mnd5 dans le domaine de transition* (Doctoral dissertation). http://www.theses.fr/2001ENMP1042

Tanné, E., Li, T., Bourdin, B., Marigo, J.-J., & Maurini, C. (2018). Crack nucleation in variational phase-field models of brittle fracture. *Journal of the Mechanics and Physics of Solids*, *110*, 80–99. https://doi.org/https://doi.org/10.1016/j.jmps.2017.09.006

Taylor, R. L. (2000). A mixed-enhanced formulation tetrahedral finite elements. *International Journal for Numerical Methods in Engineering*, *47*(1-3), 205–227. https://doi.org/10.1002/(SICI)1097-0207(20000110/30)47:1/3<205::AID-NME768>3.0.CO;2-J

Tien, J. K., Richards, R. J., Buck, O., & Marcus, H. L. (1975). Model of dislocation sweep-in of hydrogen during fatigue crack growth. *Scripta Metallurgica*, *9*(10), 1097–1101. https://doi.org/https://doi.org/10.1016/0036-9748(75)90287-2

Trasatti, S. P., Sivieri, E., & Mazza, F. (2005). Susceptibility of a X80 steel to hydrogen embrittlement. *Materials and Corrosion*, *56*(2), 111–117. https://doi.org/https://doi.org/10.1002/maco.200403821

Troiano, A. (2016). The role of hydrogen and other interstitials in the mechanical behavior of metals, edward de mille campbell memorial lecture. *Trans ASM*, *52*, 147–157. https://doi.org/10.1007/s13632-016-0319-4

Tuhami, A. E. O., Feld-Payet, S., Quilici, S., Osipov, N., & Besson, J. (2022). A two characteristic length nonlocal gtn model: Application to cup–cone and slant fracture. *Mechanics of Materials*, *171*, 104350. https://doi.org/https://doi.org/10.1016/j.mechmat.2022.104350

Turnbull, A. (1995). Factors affecting the reliability of hydrogen permeation measurement. In *Materials science forum* (pp. 63–78). Trans Tech Publ.

Tvergaard, V., & Needleman, A. (1984). Analysis of the cup-cone fracture in a round tensile bar. *Acta Metallurgica*, *32*(1), 157–169. https://doi.org/https://doi.org/10.1016/0001-6160(84)90213-X

Tvergaard, V. (1981). Influence of voids on shear band instabilities under plane strain conditions. *International Journal of Fracture*, *17*(4), 389–407. https://doi.org/10.1007/BF00036191

Tvergaard, V. (1982). Influence of void nucleation on ductile shear fracture at a free surface. *Journal of the Mechanics and Physics of Solids*, *30*(6), 399–425. https://doi.org/https://doi.org/10.1016/0022-5096(82)90025-4

Tvergaard, V., & Needleman, A. (1995). Effects of nonlocal damage in porous plastic solids. *International Journal of Solids and Structures*, *32*(8), 1063–1077. https://doi.org/https://doi.org/10.1016/0020-7683(94)00185-Y

Van den Eeckhout, E., Verbeken, K., & Depover, T. (2023). Methodology of the electrochemical hydrogen permeation test: A parametric evaluation. *International Journal of Hydrogen Energy*, *48*(78), 30585–30607. https://doi.org/https://doi.org/10.1016/j.ijhydene.2023.04.211

Verbeken, K. (2012). Analysing hydrogen in metals: Bulk thermal desorption spectroscopy (tds) methods. In R. P. Gangloff & B. P. Somerday (Eds.), *Gaseous hydrogen embrittlement of materials in energy technologies* (pp. 27–55). Woodhead Publishing. https://doi.org/https://doi.org/10.1533/9780857095374.1.27

Wang, T., Fang, X., Lv, W., Zhang, H., Luo, Y., Zheng, L., & Liang, W. (2022). Effect of hydrogen on the mechanical properties and fracture modes of annealed 430 ferritic stainless steel. *Materials Science and Engineering: A*, *832*, 142491. https://doi.org/https://doi.org/10.1016/j.msea.2021.142491

Xia, Z., Zhang, J., Tong, Q., & Ding, S. (2019). Multi-physics modeling of delayed hydride cracking in zirconium alloys. *Journal of the Mechanics and Physics of Solids*, *132*, 103677. https://doi.org/https://doi.org/10.1016/j.jmps.2019.07.020

Xu, K. (2012). 14 - hydrogen embrittlement of carbon steels and their welds. In R. P. Gangloff & B. P. Somerday (Eds.), *Gaseous hydrogen embrittlement of materials in energy technologies* (pp. 526–561). Woodhead Publishing. https://doi.org/https://doi.org/10.1533/9780857093899.3.526

Xue, L. (2008). Constitutive modeling of void shearing effect in ductile fracture of porous materials [Local Approach to Fracture (1986–2006): Selected papers from the 9th European Mechanics of Materials Conference]. *Engineering Fracture Mechanics*, *75*(11), 3343–3366. https://doi.org/https://doi.org/10.1016/j.engfracmech.2007.07.022

Yu, H., He, J., Morin, D. D., Ortiz, M., & Zhang, Z. (2025). A self-consistent void-based rationale for hydrogen embrittlement. *Scripta Materialia*, *255*, 116403. https://doi.org/https://doi.org/10.1016/j.scriptamat.2024.116403

Yu, H., Olsen, J. S., Alvaro, A., Qiao, L., He, J., & Zhang, Z. (2019). Hydrogen informed gurson model for hydrogen embrittlement simulation. *Engineering Fracture Mechanics*, *217*, 106542. https://doi.org/https://doi.org/10.1016/j.engfracmech.2019.106542

Yu, H., Olsen, J. S., He, J., & Zhang, Z. (2018). Hydrogen-microvoid interactions at continuum scale. *International Journal of Hydrogen Energy*, *43*(21), 10104–10128. https://doi.org/https://doi.org/10.1016/j.ijhydene.2018.04.064

Zafra, A., Harris, Z., Sun, C., & Martínez-Pañeda, E. (2022). Comparison of hydrogen diffusivities measured by electrochemical permeation and temperature-programmed desorption in cold-rolled pure iron. *Journal of Natural Gas Science and Engineering*, *98*, 104365. https://doi.org/https://doi.org/10.1016/j.jngse.2021.104365

Zhang, W., & Zhao, G. (2024). Leakage and diffusion characteristics of underground hydrogen pipeline. *Petroleum*, *10*(2), 319–325. https://doi.org/10.1016/j.petlm.2023.06.002

Zhang, Y., Lorentz, E., & Besson, J. (2017). Ductile damage modelling with locking-free regularized gtn model. *International Journal for Numerical Methods in Engineering*, *113*. https://doi.org/10.1002/nme.5722

Zhang, Z., Thaulow, C., & Ødegård, J. (2000). A complete gurson model approach for ductile fracture. *Engineering Fracture Mechanics*, *67*(2), 155–168. https://doi.org/https://doi.org/10.1016/S0013-7944(00)00055-2

Zhu, Y., Engelhardt, M. D., & Pan, Z. (2019). Simulation of ductile fracture initiation in steels using a stress triaxiality–shear stress coupled model. *Acta Mechanica Sinica*, *35*, 600–614. https://doi.org/10.1007/s10409-018-0825-5

Zienkiewicz, O. (1977). *The finite element method*. McGraw-Hill.

Zienkiewicz, O., Taylor, R., & Too, J. (1971). Reduced integration technique in general analysis of plates and shells. *International Journal for Numerical Methods in Engineering*, *3*(2), 275–290. https://doi.org/10.1002/nme.1620030211

Zvirko, O., Dzioba, I., Hredil, M., Pała, R., Oliynyk, O., & Furmańczyk, P. (2023). Specimen size effect on the tensile properties of rolled steel of long-term-operated portal crane. *Materials*, *16*(8), 3017. https://doi.org/10.3390/ma16083017

RÉSUMÉ

Les structures industrielles de production d'énergie et de transport, généralement conçues pour une durée de vie pouvant atteindre 40 ans, nécessitent une compréhension approfondie du comportement des matériaux à long terme afin de garantir leur sécurité et leur fiabilité. Face à la demande croissante en énergie, l'hydrogène se présente comme un vecteur énergétique prometteur dans le cadre de la décarbonisation des sources d'énergie. Cependant, sa capacité à diffuser dans les matériaux peut entraîner des ruptures prématurées, caractérisées par une ductilité et une ténacité réduites, un phénomène connu sous le nom de fragilisation par l'hydrogène. Ce mécanisme complexe résulte d'interactions entre contraintes mécaniques et chimiques.

Cette étude propose une méthode d'éléments finis (FEM) pour simuler la fragilisation par l'hydrogène en intégrant plasticité et endommagement associés à la diffusion de l'hydrogène. Pour corriger le verrouillage volumique, des méthodes d'intégration mixtes et sélectives ont été mises en œuvre. Un modèle d'endomagemment de Gurson-Tvergaard-Needleman (GTN), fondé sur une formulation nonlocale à gradient implicite avec deux longueurs internes, permet de régulariser la croissance des porosités ainsi que la nucléation contrôlée par la déformation. Dans ce cadre, l'évolution de l'endommagement est augmentée par la concentration d'hydrogène, ce qui réprésente efficacement la décohésion favorisée par l'hydrogène (HEDE) et la rupture prématurée qui en résulte.

Le modèle développé a été appliqué à diverses simulations, notamment des disques pressurisés, des essais de traction et des tests de ténacité avec des éprouvettes de tailles standard et sous-dimensionnées. Les résultats numériques montrent une bonne concordance avec les données expérimentales, soulignant la capacité du modèle à estimer la distribution de l'hydrogène dans le métal, en tenant compte de la diffusion, du piégeage, de l'initiation de fissures en surface et de la rupture prématurée. Ce cadre numérique non seulement améliore la compréhension de la fragilisation par l'hydrogène, mais constitue également un outil précieux pour l'interprétation des résultats expérimentaux.

MOTS CLÉS

Rupture ductile, modèle GTN nonlocal, fragilisation par l'hydrogène, ténacité à la rupture, effet d'échelle, modélisation par éléments finis.

ABSTRACT

Industrial power generation and transportation structures, typically designed for a service life of up to 40 years, require a deep understanding of long-term material behavior to ensure safety and reliability. With increasing demand for energy, hydrogen is emerging as a promising energy vector in the decarbonization of energy sources. However, the ability of hydrogen to diffuse into materials can lead to premature failure characterized by reduced ductility and toughness, a phenomenon known as hydrogen embrittlement (HE). This complex mechanism involves both mechanical and chemical stresses.

This study presents a finite element method (FEM) strategy to simulate HE by integrating plasticity and damage with hydrogen diffusion. To address volumetric locking, mixed and selective integration methods were employed. The Gurson-Tvergaard-Needleman (GTN) model, enhanced by an implicit gradient nonlocal formulation with two internal lengths, enabling the regularization of void growth and strain-controlled nucleation. In this model, damage evolution is increased by hydrogen concentration, effectively modeling hydrogen-enhanced decohesion (HEDE) and subsequent premature failure.

The developed framework was applied to various simulations, including pressurized disks, tensile tests, and fracture toughness tests with standard and sub-size specimens. Numerical results demonstrated good agreement with experimental data, demonstrating the model's capacity to estimate hydrogen distribution within the metal, accounting for diffusion, trapping, multi-crack initiation, and premature failure. This numerical framework not only allows better understanding of hydrogen embrittlement but also serves as a valuable tool for interpreting experimental results.

KEYWORDS

Ductile failure, nonlocal GTN model, hydrogen embrittlement, fracture toughness, size effect, finite element modeling.